annual progress

HIGH STRENGTH WEIGHT REDUCTION MATERIALS

FREEDOMCAR AND VEHICLE TECHNOLOGIES PROGRAM

Less dependence on foreign oil today, and transition to a petroleum-free, emissions-free vehicle tomorrow.

U.S. Department of Energy
Energy Efficiency and Renewable Energy
Bringing you a prosperous future where energy is clean, abundant, reliable, and affordable

FreedomCAR & Fuel Partnership

21st CENTURY TRUCK PARTNERSHIP

U.S. Department of Energy
Office of FreedomCAR and Vehicle Technologies
1000 Independence Avenue S.W.
Washington, DC 20585-0121

FY 2006

Progress Report for High Strength Weight Reduction Materials

Energy Efficiency and Renewable Energy
Office of FreedomCAR and Vehicle Technologies
Advanced Materials Technologies

Edward Wall	**Program Manager, OFCVT**
Rogelio Sullivan	**Advanced Materials Technologies Team Leader**
James Eberhardt	**Chief Scientist**

March 2006

CONTENTS

1. INTRODUCTION

The energy consumption of on-road heavy trucks has been increasing because of the growth in demand for freight delivery as the U.S. economy continues to expand. The recent rapid rise in fuel prices has elevated fuel costs to the number one concern of the trucking industry. Owners and operators of trucks and truck fleets have been operating on razor-thin margins, and increasing the fuel economy of their vehicles is one way of reducing their fuel costs to remain viable as a business. One way of achieving heavy vehicle fuel economy improvements, without sacrificing revenue earnings limited by maximum allowable vehicle weight or volume, is through the use of high-strength weight reduction materials for the tractor or trailer or both. Vehicle weight reduction results in reduced parasitic energy losses and improved overall vehicle fuel efficiency by enabling more ton-miles per gallon of fuel consumed. In addition, it is recognized that improved materials may enable the implementation of other technologies that can further improve the fuel efficiency of heavy vehicles.

The High-Strength Weight Reduction (HSWR) Materials Technology activity of the U.S. Department of Energy's (DOE's) Office of FreedomCAR and Vehicle Technologies (OFCVT) Program seeks to reduce the weight of heavy vehicles without reducing vehicle functionality, durability, reliability, or safety and to do so cost-effectively. Work has been focused on developing advanced materials and materials processing technologies that can be applied to a wide array of heavy vehicle body, chassis, and suspension components to achieve weight reduction. Research is focused on overcoming barriers to the widespread introduction of lightweight materials in the heavy vehicle industry. Major barriers include cost; design and simulation technologies; manufacturability; prototyping and tooling; joining and assembly; and maintenance, repair, durability, and recycling. Priority materials include advanced high-strength steels, aluminum, magnesium, titanium, and composites such as metal matrix materials and glass- and carbon-fiber-reinforced thermosets and thermoplastics. The research required to develop these technologies is too high-risk to be pursued independently by the heavy vehicle industry because of substantial return-on-investment uncertainties. In addition, the relatively low volume of truck components makes it difficult for any individual truck manufacturer to develop on its own a new production/fabrication process using new kinds of materials such as composites.

Research and development (R&D) activities were conducted through a variety of contractual mechanisms. These include cooperative research and development agreements (CRADAs), university grants, R&D subcontracts, and directed research. Research partners include heavy vehicle manufacturers (including member companies of the government/industry 21st Century Truck Partnership), first-tier component manufacturers and materials suppliers, national laboratories, and other non-profit technology organizations. Laboratories include Argonne National Laboratory (ANL), Idaho National Engineering and Environmental Laboratory (INEEL), Los Alamos National Laboratory (LANL), Oak Ridge National Laboratory (ORNL), and Pacific Northwest National Laboratory (PNNL).

Among the several goals established for this development area, one is to enable at least a 22% reduction in the weight of an unloaded tractor-trailer combination and about a 10–33% reduction in the weight of other classes of heavy vehicles, depending on performance requirements and duty cycles. With the completion and issuance of this final High Strength Weight Reduction Materials report, most of these goals have been accomplished. Technology R&D results have been made available to industry for further development and commercialization. Some of these results are discussed in this final annual report.

2. MATERIALS DEVELOPMENT

A. Advanced Materials for Friction Brakes

Principal Investigator: P. J. Blau
Oak Ridge National Laboratory
P.O. Box 2008, Oak Ridge, TN 37831-6063
(865) 574-5377; fax: (865) 574-6918; e-mail:blaupj@ornl.gov

Technology Development Area Specialist: James J. Eberhardt
(202) 586-9837; fax: (202) 587-2476; e-mail: james.eberhardt@ee.doe.gov
Field Technical Manager: Philip S. Sklad
(865) 574-5069; fax: (865) 574-6098; e-mail: skladps@ornl.gov

---

Contractor: Oak Ridge National Laboratory
Contract No.: DE-AC05-00OR22725

Objectives

- Determine the feasibility of using advanced, lightweight materials and surface treatments for truck disk brake surfaces and develop the friction, wear, and performance data needed to promote their introduction. Materials of interest include titanium alloys and their composites, carbon-based materials, and novel surface treatments and coatings that enhance both durability and frictional stability over a range of temperatures.

Approach

- Design and build a subscale brake material testing apparatus to conduct friction and frictional-heating studies of advanced materials at speeds and pressures similar to those of full-sized truck brakes.
- Characterize changes to the surfaces of materials that occur as a result of frictional contact under braking conditions. Relate these changes to material properties and frictional performance.
- Investigate the effects of speed, contact pressure, and temperature on the frictional response of candidate brake rotor materials, such as titanium alloys, thermally sprayed coatings, ceramic composites, and carbon materials, and apply that knowledge to identify which of them seem most promising for further development.
- Identify and test friction materials (pads) that work well with the advanced brake rotor materials.
- Work with trucking industry partners and commercial dynamometer test laboratories to evaluate advanced candidate materials under established testing conditions, such as standard American equivalent (SAE) procedures and federal test methods.

Accomplishments

- Designed and built an instrumented, subscale brake materials friction and wear testing system.
- Investigated the effects of wet and dry braking conditions on frictional behavior.
- Published a review of the compositions of friction materials that includes thermo-physical properties data.
- Characterized wear particles that are generated in tests of candidate advanced brake materials.
- Published a study of the effects of the wear test method on relative rankings of commercial brake linings.

- Published a technical report that summarizes current ORNL research on nontraditional brake materials, such as ceramic composites, titanium alloys, and titanium composites.
- Friction-tested nontraditional brake materials on a titanium (Ti)-based composite that was produced using low-cost Ti powder and compared the results to tests using a novel thermal diffusion treatment to harden the surface of a traditional ingot metallurgy Ti alloy.
- Worked with a commercial truck industry supplier to test thermally sprayed Ti rotors in a full-scale dynamometer and captured thermal images to compare their heating response to traditional cast iron.
- Prepared new carbon-based brake composites for friction testing on the subscale brake tester (SSBT).

Future Direction

- Complete industry testing protocols on full-scale, thermally sprayed coated titanium truck brake rotors.
- Complete tests on densified carbon-based disk materials and on a novel surface treatment for Ti-based rotors.

Introduction

New, aerodynamic designs for energy-efficient heavy trucks and advanced tires with lower rolling resistance can markedly improve fuel economy. However, as parasitic losses and the drag on trucks decrease, the demands on brakes increase. Braking systems include hardware design, instrumentation and control, and friction materials that dissipate energy as the vehicle decelerates. This project specifically addresses the latter. Friction brake materials must exhibit a combination of characteristics, including

- frictional stability over a wide range of temperatures
- good frictional heat removal and dissipation
- dimensional stability to avoid vibrations
- corrosion resistance to road de-icing compounds
- durability and wear resistance
- lightweight and cost competitiveness

Opportunities exist to utilize advanced materials to improve the fuel efficiency without compromising vehicle safety and reliability.

The goal of this project is to characterize newly developed materials and surface treatments that show significant potential as truck brake rotor materials. The approach is first to characterize and friction test small specimens of candidate materials in the laboratory and then progress to full-scale component tests using standard industry procedures. For laboratory testing, an instrumented, SSBT was built and used to evaluate a wide variety of advanced materials, including ceramic composites, intermetallic alloys, titanium alloys, metal matrix composites, and hard-coated titanium. A summary of the test results was prepared and distributed to U.S. truck manufacturers and braking system component suppliers.

Friction and wear testing is coupled with microstructural studies of surface films generated during braking and correlated with measurements of physical properties. A thermal efficiency parameter that expresses the rise in surface temperature per unit of frictional work was developed to assess the extent to which brake design features, such as vents, must be taken into account when replacing traditional cast iron rotors. During this reporting period, a full-scale, titanium alloy truck brake rotor was tested for the first time in a commercial truck component manufacturer's facility (Figure 1). Results were particularly promising in terms of the resistance of the surfaces to fade at high temperatures.

Materials of Current Interest

A number of candidate materials were tested and then eliminated from further consideration due either to their low melting points, brittleness, sensitivity to corrosion, or wear-particle characteristics. Those of current interest are shown in Table 1.

Figure 1. One of the first four full-scale, thermally sprayed titanium truck brake rotors to be produced. It was prepared for this project by Red Devil Brakes, Inc., of Pennsylvania.

Table 1. Candidate materials of current interest for friction studies on the SSBT apparatus

Rotor materials	Source
Titanium alloy, thermally sprayed with a proprietary friction-control coating	Red Devil Brakes, Inc., Mount Pleasant, Pennsylvania
Titanium powder composite with hard particles in the surface layers	C. Blue and W. Peter, ORNL, in collaboration with International Titanium Powder Corporation
Oxygen diffusion-treated titanium alloy	A process being developed for improving the tribology of titanium surfaces by J. Qu, ORNL
Densified carbon material	Developed by J. Klett, ORNL

The thermally sprayed and powder metallurgy Ti materials have been described in earlier reports. The coating consists of a proprietary blend of metallic and ceramic particles. The substrate is Ti-6Al-4V alloy.

The densified carbon materials were prepared during this reporting period at ORNL. Plates were produced in two forms: a two-dimensional (2-D) compressed structure (Figure 2) and a three-dimensional (3-D) weave (Figure 3). One of the principal differences in these structures is in the heat flow. The 3-D material tends to remove heat from the surface somewhat better, but the 2-D structure has better in-plane conduction. After preparation, they were machined to fit the mounting hardware in the SSBT. The initial selection of counterface (pad) materials for the carbon disk specimens was based on prior experience in testing C-SiC composite disks in a project with GE Power Systems (formerly Honeywell Advanced Composites, Inc.). In that work, it was found that the best performance involved testing with self-mated materials. However, a commercial, semimetallic pad material may also be tried, depending on the results of the first friction test trials on the SSBT.

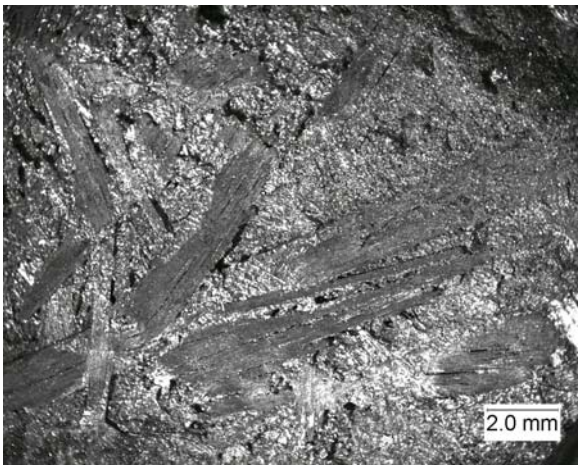

Figure 2. Surface of the 2-D structure, as finished.

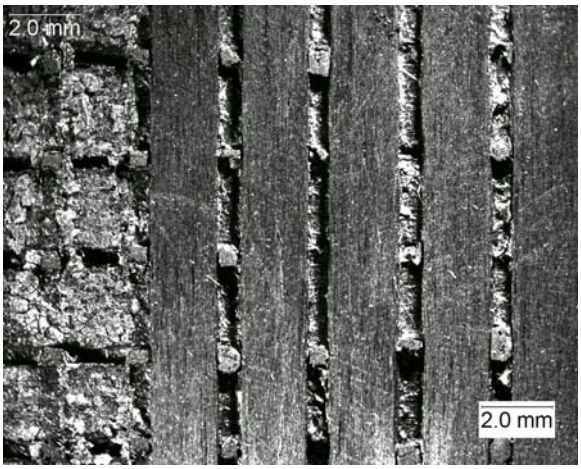

Figure 3. Surface of the 3-D structure, as finished.

Dynamometer Tests and Thermal Imaging

One of the four thermally sprayed Ti rotors (shown in Figure 1) was shipped to a major truck

component manufacturer for dynamometer testing in comparison with a standard cast iron rotor of the same type. J. Martino, of Red Devil Brakes, prepared the brake pads for that test. In addition to a modified version of a federal testing protocol, a series of rapid decelerations ("snubs") from equivalent highway speeds of 50 mph down to 15 mph, were performed. R. Dinwiddie, of ORNL, was present to record calibrated thermal images of the cast iron rotor and the Ti rotor using a high-speed, rotation-synchronized infrared camera.

A thermal image of the Ti rotor after a series of five snubs is shown in Figure 4. The maximum heating seemed to occur about four seconds after the brake pads were applied. Figure 5 compares these maximum temperatures for the Ti and cast iron discs.

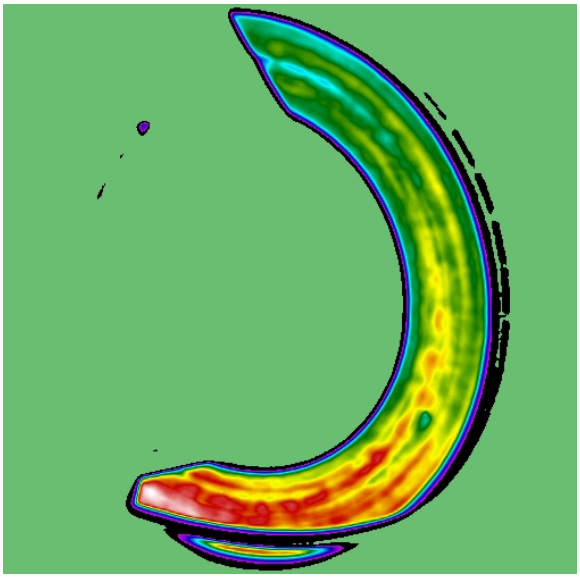

Figure 4. Infrared (IR) thermal image of the Ti rotor during the sixth snub stop. Red represents a temperature of about 1600ºF and dark blue about 1200ºF. Dashed dark streaks at the right edge of the disk are cooling vents.

As Figure 5 data show, the Ti disc ran several hundred degrees hotter than the cast iron disk, but it retained its frictional capabilities at these higher temperatures, an important consideration in emergency stops, repeated brake application during long hills, and in the kind of service that requires frequent stops, such as school buses, delivery trucks, and trash haulers.

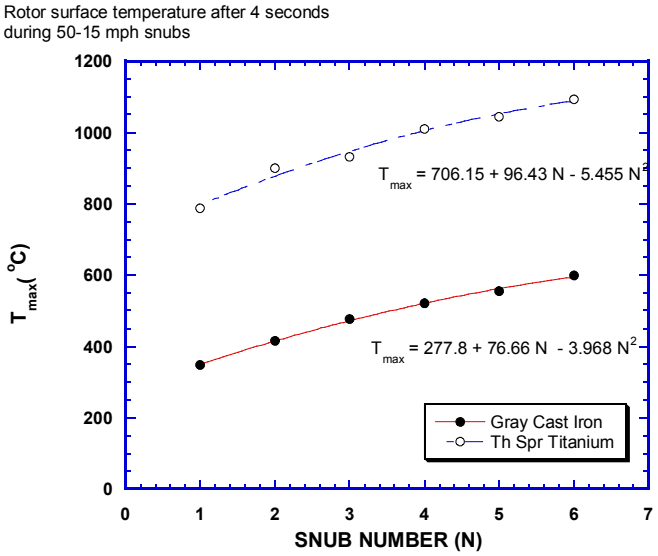

Figure 5. Friction coefficients (μ_{ave}) after four seconds of sliding for cast iron and Ti brake rotors.

Oxygen Diffusion Treatment Appears Promising

In addition to thermal spraying and the addition of hard-particles, a novel process called thermal diffusion has been used to improve the frictional characteristics of Ti-6Al-4V alloy surfaces. Preliminary SSBT experiments, conducted during this period, show excellent frictional behavior over a range of testing speeds and temperatures. A patent disclosure has been filed and details will be reported later.

Future Plans. Testing of carbon-based brake disc materials. SSBT friction tests of the two forms of densified carbon described earlier in this report will be performed in the fall of 2006 and results are expected to be available by the end of CY 2006. Additional analysis of the test data for thermal oxidation will be performed, and a paper comparing it to alternative treatments is planned.

Conference Paper. A summary of the past two years of research on Ti-based materials for disc brakes has been submitted to the 16th International Conference on Wear of Materials (2007) . Plans for the conference include a special session on brake materials and that will be an excellent forum for the presentation of the current results.

Conclusions

The friction and frictional-heating response of several Ti-based brake rotor materials have been

evaluated. The materials' excellent retention of stopping capabilities at elevated temperature ("fade resistance") was demonstrated both in the laboratory and in full-scale tests of a thermally sprayed truck brake rotor.

Publications/Presentations/Patents

Peter J. Blau, Brian C. Jolly, William H. Peter, and Craig A. Blue, "Tribiological Investigation of Titanium-Based Materials for Brakes," accepted for *Wear of Materials '07*, Montreal, Canada, April 15–19, 2007.

Patent disclosure: "Oxygen-Diffused Titanium for Engine and Other Bearing Applications."

B. Integrated Approach for Development of Energy-Efficient Steel Components for Heavy Vehicle and Transportation Applications

Co-Principal Investigator: Leo Chuzhoy
Caterpillar, Inc.
P.O. Box 1875, Peoria, IL 61656-1875
(309) 578-6621; fax: (309) 578-2953; e-mail: chuzhoy_leo@cat.com

Co-Principal Investigator: Gerard Ludtka
Oak Ridge National Laboratory
P.O. Box 2008, Oak Ridge, TN 37831-6064
(865) 574-5098; fax: (865) 574-3940; e-mail: ludtkagm1@ornl.gov

Co-Principal Investigator: Alan Needleman
Brown University
Box D, Brown University, Providence, RI 02912-D
(401) 863-2863; fax: 401-863-1157; e-mail: alan_needleman@brown.edu

Chief Scientist: James J. Eberhardt
(202) 586-9837; fax: (202) 587-2476; e-mail: james.eberhardt@ee.doe.gov
Field Technical Manager: Philip S. Sklad
(865) 574-5069; fax:(865) 574-6098; e-mail:skladps@ornl.gov

Contractor: Caterpillar Corp., ORNL, Brown University
Contract No.: DE-AC05-00OR22726, DE-AC05-00OR22725, 4000023957

Objective

- Develop microstructure-level (often called mesoscale) simulation (MLS) tools to capture the formation and influence of inhomogeneous (real life) microstructures in steel processing.
- Use the tools to understand and predict microstructure evolution during processing and ultimately to predict the resultant component performance.
- Use the information gained to design steel microstructures and develop process roadmaps.
- Demonstrate the developed techniques on a pilot project at Caterpillar involving a defined structural component, a track roller shaft, that represents a steel component with high production volume that could benefit from microstructure-level improvements.

Approach

- Develop microstructure-level models to accurately predict the evolution and behavior of steel microstructures during component processing and performance.
- Characterize thermomechanical properties of microstructural constituents as a function of temperature and composition for exact chemistries.
- Develop tools to assess required environmental resources and integrate them into the simulation.

Accomplishments

- Developed and validated specific MLS models for at least one experimental case:
  - — Developed the first reported quenching model for the transformation of austenite to lath martensite.
  - — Obtained predicted transformation rates in general agreement with experimental results.
  - — Used the model to show the dynamic microstructure evolution during quenching and the effect of process variables on microstructure evolution.
  - — Developed a microstructure solidification model to predict MnS inclusion forming during solidification.
  - — Developed a damage evolution model at the microstructure level to predict damage initiation and cyclic fatigue failure.
  - — Developed a microstructure evolution model during induction heating to predict grain size and austenitization fraction.

Future Direction

- Fully couple the phase transformation and evolution prediction of the heat treatment module with mechanical property evolution and stress state evolution.
- Build links to transfer the microstructure information combined with mechanical properties and stress into the microstructure-level failure model.
- Develop a microstructure-level model that fully couples phase transformation, mechanical property evolution, and residual stress evolution.
- Establish an integrated method to take microstructure information from the manufacturing process into failure analysis.

Introduction

Product cost and performance are two major pressures influencing the acceptance of energy savings technologies by manufacturers, suppliers, and users in the heavy vehicle and transportation industries. Energy cost has become a significant portion of total product cost for steel applications. Major reductions in energy use are potentially achievable for the transportation and heavy vehicle industries through development and optimization of cost-effective fabrication processes and enhanced product performance. The key enabling technologies to achieve these benefits are improved materials and realistic, microstructure-level simulations to predict manufacturability and life-cycle performance. Over the past two decades, steel mills and forge shops have successfully implemented numerous energy-efficient processes. The next logical step is to focus on the development of steel microstructures produced in such a way that they are energy-efficient and environmentally benign over the entire manufacturing cycle.

Structural materials used in critical steel components of machines have evolved to the point where further improvements in the performance can be achieved only through a fundamental understanding of the mechanisms driving material behavior during processing and service. Microstructural elements such as grain size, inclusion and precipitate distributions, and chemistry control the performance of engineering materials. Variation in these microstructural elements leads to variation in such critical properties as fatigue life, toughness, and wear resistance. Therefore, understanding and developing the capability to control the formation of steel microstructures and predicting the functional and environmental performance is critical to moving the industry closer to its energy-efficiency, resource-efficiency, and pollution-prevention goals. The full realization of these benefits, however, requires a design tool that optimizes the microstructure with respect to the mechanical and environmental performance throughout the life cycle of a particular steel component.

To apply an integrated approach to the development of energy-efficient steel components, the development of three major areas of research needs to be completed:

- microstructure-level models to accurately predict the evolution and behavior of steel microstructures during component processing and performance

- thermomechanical properties of microstructural constituents as a function of temperature and composition for exact chemistries
- tools to assess required environmental resources

This project addresses activities required for the first of these three areas. The second and third tasks are either supported by current funding through the National Science Foundation or are expected to be funded through the DOE Initiative for Proliferation Prevention. Through these integrated efforts, a design tool will be developed that optimizes the microstructure, manufacturability, and performance of components with respect to the mechanical and environmental performance required throughout the components' life cycles. The overall benefit of this research will be the development and demonstration of a design methodology that will enable the domestic transportation and heavy vehicle industries to compete effectively in future worldwide markets through improved product performance and energy savings. Furthermore, the proposed design tool can be extended to other materials—i.e., cast iron, aluminum, titanium, magnesium, nickel-based alloys, ceramics, and composites—thus impacting virtually all industries.

In addition to significant energy and cost savings benefits to the transportation and steel industries through microstructure-level modeling, virtually all industries will be impacted. Examples include aerospace (engines, transmissions, structural), marine (engines and drives), agricultural and construction equipment, oil and chemical processing (pumps and gear boxes), military vehicles, mining machinery, appliances (compressors, motors, gear boxes, shafts), power tools, and automotive aftermarket.

Project-end Deliverables

The deliverables for the project will be the following:

- Microstructure-level methods for simulating the manufacturing cycle of steel products coupled with material performance computations (Tasks 1, 2, and 3)
- A specific chemical composition and processing map for a 1500-series steel and a micro-alloyed steel suitable for the application under consideration (Task 4)
- Energy and environmental resources required to produce the selected steel component using at least two steels and processing schemes (Task 4)

The project tasks will focus on three critical areas in the development of these models: heat treatment processing, machining, and materials performance in specific applications. These three processes have been chosen because they are critical steps in reaching the goal of being able to develop a specific steel for a particular application with a heavy reliance on modeling and with energy requirements optimized as an integral part of the development process. Modeling of casting and forming processing has been performed under other programs, and Caterpillar has shown successful application and commercialization of these models. These existing models will be used along with the heat treatment, machining, and specific applications models described in this report to complete a suite of models for the manufacture of micro-alloyed steels.

To accomplish the project objectives, a multidisciplinary team consisting of a national laboratory, a university, and a steel end user has been assembled. The team will be supported by an international research institute for material characterization and by experts in environmental impact assessment. The following section describes each of the technical tasks to be performed.

Semiannual Period Report Topics

Model development and results for the following two topics were reported in detail in the 2006 semiannual report and therefore will not be duplicated in this annual report:

- The first reported quenching model for the transformation of austenite to lath martensite has been developed.
- The predicted transformation rates are in general agreement with experimental results.
- The model can show the dynamic microstructure evolution during quenching and the effect of process variables on microstructure evolution.

Modeling of Fatigue Life Prediction Based on Continuum Damage Mechanics

Background

Fracture and fatigue failures are always important issues to be considered by the engineers in designing engineering components. About 80–90% of all engineering failures relate to fracture and fatigue for different length scales and different material systems

Investigations of failure and crack growth related to fatigue have been a challenge to scientists for decades. Classical linear elastic fracture mechanics has been successful in dealing with fracture problems with a negligible nonlinear zone ahead of the crack tip. However, the concepts of fracture mechanics present difficulty when the nonlinear process zone is relatively large compared with the crack length or the size of the structure, or on a microstructural length scale.

Void nucleation and growth has been recognized as a key micromechanism of rupture for ductile metals. In a continuum damage mechanics (CDM) approach, damage is assumed to be one of the internal constitutive variables that account for the effects on the material associated with a given damage condition through the definition of a state variable of damage. Damage not only affects the material's yield function but also reduces the stiffness through the equation of effective stresses with cyclic loading. In addition, the fatigue properties of metals are quite microstructure sensitive. The CDM approach is promising for investigating the relationship between the fatigue damage properties and microstructure.

Objective

The goal of the project is to develop a microstructure-level material simulation model based on metal plasticity and CDM by accounting for the material degradation during cyclic loading to predict the fatigue failure and service life of components. The material properties are related to the microstructure of the material. An MLS is developed to consider the void nucleation stage from inclusions and porosity through void growth and coalescence and ultimately to the final material failure stage. This simulation technique clearly addresses the link between macro-level failure and microstructure-level defects. Microstructure changes during the manufacturing process then can be integrated into the failure prediction further. A more accurate life prediction based on developed CDM based modeling is achieved.

The occurrence of plastic deformation and accumulation with loading cycles is a main cause of damage development that will lead the material to fail later. Under cyclic loading, irreversible microstructure changes occur in the following forms: persistent slip bands, rearrangement of dislocation systems into cell structures, and void nucleation and growth at secondary phase inclusions. The latter is one cause of the high strain, which is expected to result in a short life.

The major advantage of the approaches based on continuum mechanics is the transferability from specimen to structure, since model parameters should be geometry-independent.

Methodology

This model development consisted of the following steps:

- Development of a damage evolution law for steel under cyclic plastic flows
- Development of the approach to extract the material parameter from the experimental data
- Design of a program to simulate the damage evolution during the cyclic loading and a damage-driven fatigue model
- Validate the model and the accuracy of the simulation results by comparing them with the experimental S-N curve

Results

The described methodology was used to characterize the material parameter in the derived damage evolution fatigue model (specifics will be published in a subsequent report) for a gray iron material (class 40 B). A typical testing curve is shown in Figure 1. To clearly see the loading-unloading curve for different hysteresis loops during multiple fatigue cycles, successive curves are offset by 0.005 strain in Figure 2. The test was conducted at room temperature and was controlled by a constant strain amplitude condition.

In Figure 3, the elastic modulus regression is plotted with the increasing number of cycles. It can be seen clearly that the modulus under the tension portion of the curve keeps dropping with increasing

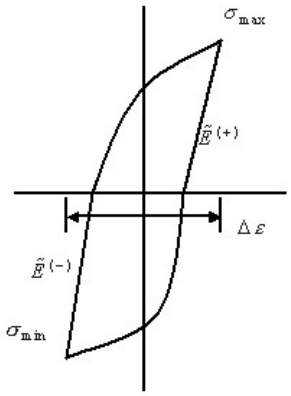

Figure 1. Schematic drawing to calculate the increment of the plastic strain.

number of cycles, which means more damage accumulation. Also, the modulus regression data show that the effect of damage to modulus regression under compression is not as much as the effect under tension.

The corresponding damage evolution with number of cycles is shown in Figure 4. It can be seen that at the beginning, the damage accumulates slowly. With an increasing number of cycles, more damage accumulated; and after the damage reached the critical damage value Dc=0.3, the damage growth rate increased suddenly and material rupture occurred.

Verification

Using the material parameters obtained as described above, the damage model was used to calculate the fatigue life for a different loading range and compare it with the experimental S-N curve. Both the calculation results and the experimental results were plotted on the same graph, Figure 5. The fatigue cycles ranged from 100 to 100000 cycles corresponding to different strain levels. The calculated data agree well with the experimental S-N curve. This also proves that the CDM approach is applicable to different load levels and fatigue life ranges.

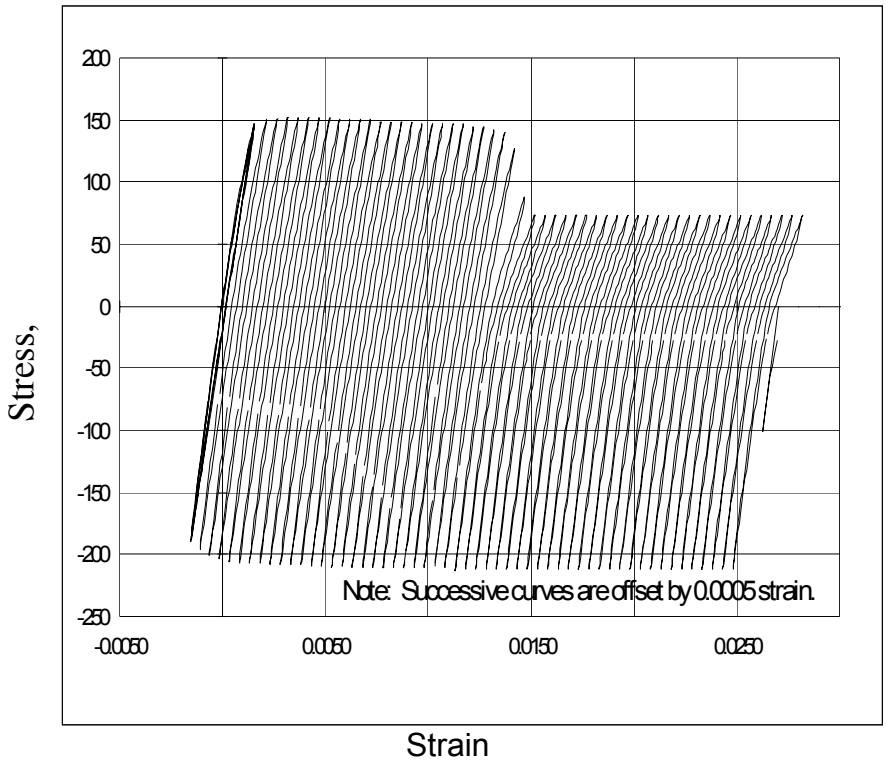

Figure 2. Fatigue test stress strain curve.

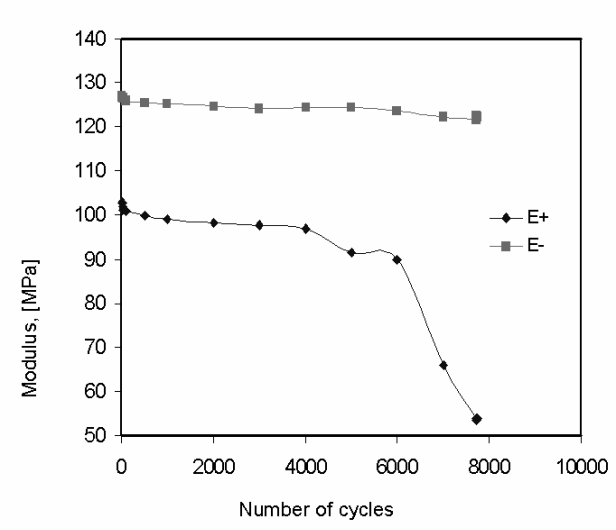

Figure 3. Elastic modulus regression during the cyclic loading condition.

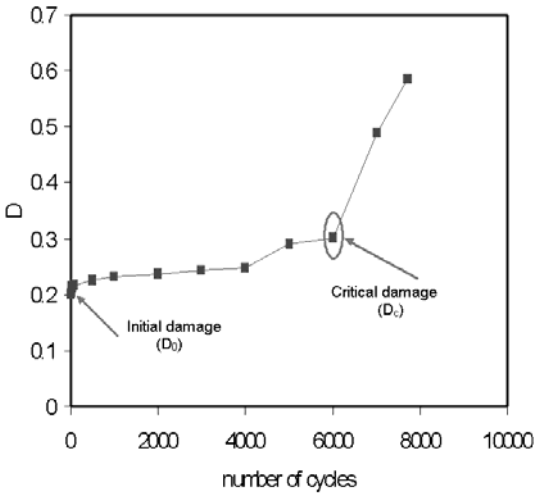

Figure 4. Damage evolution for the fatigue test.

Conclusion

A material model based on CDM was developed. In this model, the damage is coupled with plastic strain and provides more accuracy to the damage evolution. An approach to calibrate the material parameter was developed for this model. The material damage properties (such as initial damage, critical damage, and crack closure factor) were extracted from the cyclic fatigue loading test data for gray iron. Then, in the simulation, the fatigue model was used with the measured damage properties to estimate the fatigue life by considering the cyclic damage accumulation under cyclic fatigue loading.

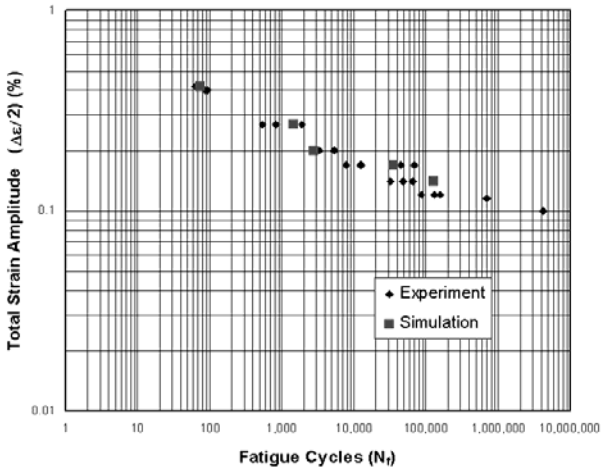

Figure 5. The comparison of experimental and calculated S-N curve.

The life prediction from the simulation shows very good agreement with the experimental results. The predicted S-N curves (ranging from 100 to 100000 cycles) agree with the experimental data. This proved that this model is robust at different load levels as well as in different ranges of cycles in fatigue life. This model can be applied to different types of metals and materials based on the damage evolution constitution.

Presentations and Publications

Adrian V. Catalina, Doru M. Stefanescu, Leo Chuzhoy, and Michael L. Johnson, "A Solid Fraction Evolution Approach for Modeling of Dendritic Growth in Multicomponent Alloys," presented at the TMS Annual Meeting, San Antonio, March 13–16, 2006.

Don Sherman, "Characterization of the Carbon and Retained Austenite Distributions in Martensitic Medium Carbon, High Silicon Steel," submitted for publication in Metallurgical and Materials Transactions A in October 2006.

B. J. Yang, Leo Chuzhoy, and Mike Johnson, "Modeling of Reaustenitization of Hypoeutectoid Fe-C Steels with a Cellular Automaton Method," presented at the TMS Annual Meeting, San Antonio, March 13–16, 2006.

B. J. Yang, Leo Chuzhoy, and Mike Johnson, "Modeling of Reaustenitization of Hypoeutectoid Steels with Cellular Automaton method," submitted to *Journal of Acta Mater.* in August 2006.

C. Development of Technologies for the Application of Magnesium Metal Matrix Composites for Heavy Vehicles

Principal Investigator: Adam R. Loukus
GS Engineering, Inc.
101 West Lakeshore Drive
(906) 482-1235; fax: (906) 482-1236; e-mail; adam.loukus@gsengineering.com

Chief Scientist: James J. Eberhardt
(202) 586-9837; fax: (202) 587-2476; e-mail: james.eberhardt@ee.doe.gov
Field Technical Manager: Philip S. Sklad
(865) 574-5069; fax:(865) 574-6098; e-mail:skladps@ornl.gov

Participants
Glen Simula, Andrew Halonen, Tom Wood, GS Engineering, Inc.
Josh Loukus, Gary Pennala, REL Machine, Inc.
Robert Hathaway, Chad Johnson, Vadim Pikhovich, Oshkosh Truck Corp.
Dave Weiss, Eck Industries
Bob Coleman, Engineered Fiber Solutions

Contractor: GS Engineering, Inc.
Contract No.: WR10637

Objective

- Analyze different casting processes before designing and building process-controlled squeeze casting equipment. Use this equipment to cast metal matrix composite (MMC) components with mechanical properties adequate to replace heavier materials used in Class 8 vehicles.

Approach

- Infiltrate several preforms with the magnesium (Mg) alloy AZ91 using different casting processes: pressureless infiltration (PLI), squeeze casting, and pressure infiltration vacuum-assisted casting (PIVAC).
- Evaluate the microstructural features in the composite structures and evaluate the interactions of the Mg alloy and the reinforcement. Follow a parallel path of process simulation to optimize material flow into preforms.
- Use MAGMAsoft® simulations to assist in the die design, machine a casting die, and make preliminary castings.
- Pursue further Mg components casting.

Accomplishments

- Analyzed the differences in material characteristics, such as the strength, stiffness, grain size, and interfacial reactions, as functions of casting processes.
- Designed and simulated mold filling with a preform in a connecting rod component.
- Built a casting die and performed initial infiltration trials on a GSE press with aluminum alloys to streamline the casting system.

Future Direction

- Milestone 1—Cast magnesium MMC connecting rods.
- Milestone 2—Evaluate components in bench and field tests.

Introduction

The microstructural features of the Mg composites castings done in year 1 have been studied in some depth in the past few months. Significant understanding of the interfaces has been developed in the past months that has reemphasized the goals and route that have been chosen. A clean, inert environment during casting is crucial for the matrix-to-reinforcement bonding and hence a high-integrity casting. The GSE squeeze casting press is operational, and casting trials are scheduled as the materials arrive to determine the effects of the casting parameters on component strength, stiffness, and porosity. MAGMAsoft software was used to aid in process and die design to minimize the chances of porosity in the cast components. A detailed plan for the remainder of year 2 funds is included in the future work section.

Grain Structure Analysis

The squeeze cast trials were run on a production caster on which monitoring and control of parameters necessary for consistent quality were not available. PLI studies were performed in order to clarify the infiltration potential of various preform materials. Using the PLI process also provided evidence of the effects of infiltration velocity and cooling rate on microstructure. The controllable casting atmosphere in the process eliminates rapid oxide formation that is prevalent with the squeeze casting process.

Metallographic analysis shows the advantages of squeeze casting over a PLI process. The cycle time for squeeze casting is shorter; hence the cooling rate will be higher than for a PLI process. This differential in cooling rate and applied pressure is illustrated in the corresponding metallographic structures (Figures 1 and 2).

The finer grain size achievable with the squeeze casting process (Figure 1) should result in greater ductility, toughness, and strength compared with the PLI process (Figure 2) where the grain size is 3 times larger.

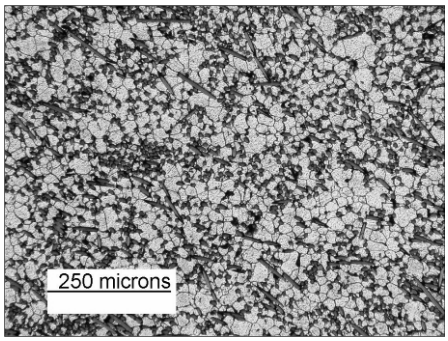

Figure 1. Carbon fiber 25% (compacted), AZ91D-T6 squeeze cast (SC) process, 100×. Etched with 10% citric acid. ASTM E112 grain size 7.

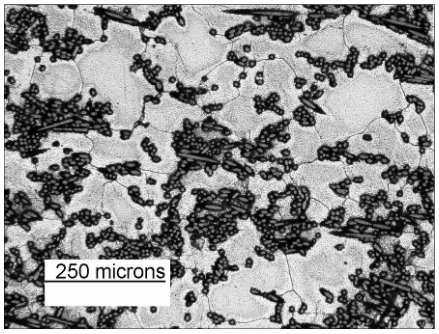

Figure 2. Carbon fiber 25%, AZ91D-as cast, PLI process 100×. Etched with 10% citric acid. ASTM E112 grain size 2.

SEM/Auger Analysis

The intent of the following analysis was to examine the carbon fiber in two orientations so as to identify the reaction products at the interface. Using focused ion beam (FIB), Mg from the matrix surrounding the fiber was removed. A sputter profile was used to establish how much sputter cleaning needed to be done to remove the contaminant and native oxide layers formed on the polished surface.

The data indicated that at least 2 min of sputtering at an etch rate of ~200 nm/min is required. To create a smooth sample surface, it was necessary to argon-ion sputter while rotating the specimen for approximately 3 min.

Figure 3 is an scanning electron microscopy (SEM) image of an area of the sample that was analyzed to identify reactions along the length of an individual carbon fiber. Table 1 shows the atomic concentration of the areas analyzed. as indicated in Figure 3. All values are relative, not absolute, since no standards were used. The spectral data were taken after mapping; i.e. the surface had time to adsorb a lot of residual gas (e.g., water, CO, CO_2). In fact, a comparison of points 3 and 5 shows that there are nearly equal amounts of oxygen, although area 3 is clearly a reaction product. The material in area 3 is an oxide reaction product while the oxygen seen in area 5 is adsorbed oxygen on the Mg-matrix surface.

Table 1. Atomic concentration survey spectra from the points shown in Figure 3 and resulting compositions

Area	C	O	Mg	Al
1	4.78	25.07	25.71	44.43
2	14.28	27.20	35.01	23.51
3	5.10	34.44	55.64	4.81
4	73.11	4.51	15.98	6.40
5	5.02	31.28	59.43	4.27
6	8.68	30.75	43.08	17.49

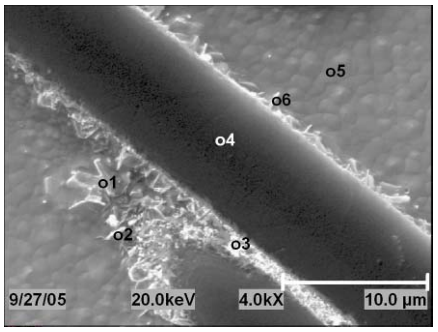

Figure 3. SEM image of a longitudinal view of fibers in the matrix. The indicated points are where spectral analysis was performed.

Figure 4 is an on-end SEM image of an area of the sample that was analyzed to identify reactions around the circumference of an individual carbon fiber. Table 2 shows the atomic concentration levels from the spectral analysis of the areas identified in Figure 4. The analysis shows that the reaction products have high levels of oxygen.

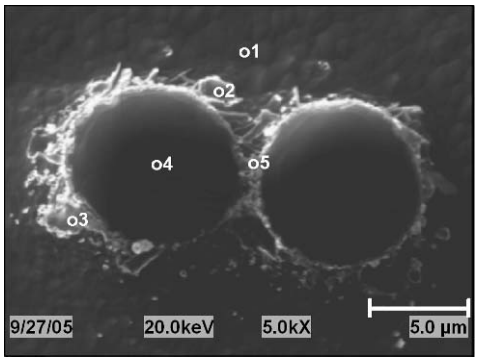

Figure 3. SEM image of a longitudinal view of fibers in the matrix. The indicated points are where spectral analysis was performed.

Table 2. Atomic concentration of the indicated points from Figure 4

Area	C	O	Mg	Al
1	2.19	5.46	89.85	2.49
2	3.95	9.86	67.21	18.98
3	7.07	27.26	24.14	41.53
4	75.96	3.16	16.05	4.83
5	9.26	31.85	56.86	2.03

The use of auger electron spectroscopy (AES) elemental mapping highlights the composition of the interfacial constituents. Figure 5 shows that oxide-rich areas surround the fiber. Together, the two maps show that Mg-O and Al-O reaction products are formed at the fiber/matrix interface.

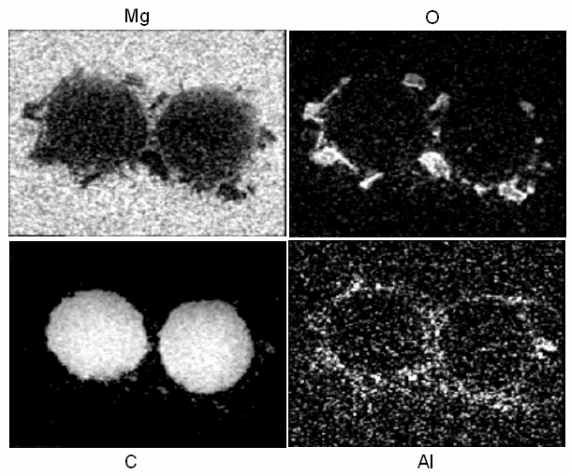

Figure 5. Individual gray-scale AES maps of Mg, carbon, aluminum, and oxygen. These maps correspond to the SEM image in Figure 3.

At high magnification, the reaction zone at the interface is observed. This zone is critical to the ultimate characteristics of the engineering component. In Figure 6, we see the interface containing silicates and oxides that can prove detrimental to the material's mechanical properties.

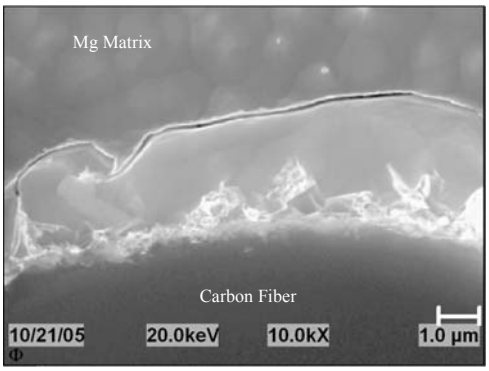

Figure 6. SEM showing the interfacial reaction between the carbon fiber and the magnesium matrix with a sample produced by PLI.

From the AES analysis, it is apparent that essentially four main elements are present in the interfacial regions. Magnesium, oxygen, aluminum and silicon have all been mapped as shown in Figure 7. It is then of practical and scientific use to determine which compounds are present in the casting, as we know the constituents. Therefore, some samples were scanned using X-ray diffraction to conduct this analysis.

To positively identify secondary phases, the samples as identified in Table 3 below were analyzed using X-ray diffraction. Samples were metallographically prepared and etched with 3% nital to minimize cold work effects due to polishing. The analysis was accomplished using a Scintag XDS-2000 θ/θ diffractometer. The X-ray diffraction results confirm the presence of magnesium oxide (MgO) and magnesium silicide (Mg_2Si) at the fiber/matrix interface that was observed in the AES analysis of the interface region in the PLI sample.

Mold Flow Analysis and Die Design

Simulation of castings before die building has become a common practice in the last decade as a result of the increasing speed of computers and the accuracy predicted by mold flow programs such as

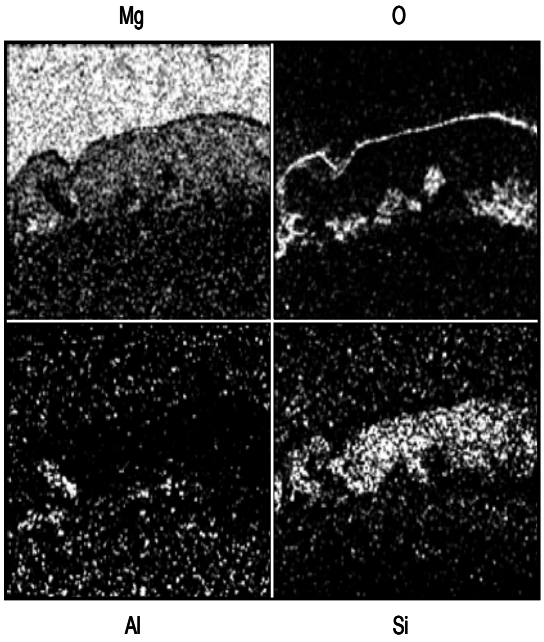

Figure 7. Individual gray-scale AES maps of Mg, oxygen, aluminum, and silicon. These maps correspond to the SEM in Figure 6.

Table 3. Summary of secondary phases identified with X-ray diffraction with various performs and processes. PIVAC samples are in T4 condition. All others are as-cast

Alloy/Process	Secondary Phases Identified w/ XRD		Approx. MgO particle size (nm)
AZ91D/ CF25 PIVAC		MgO	11 +/- 2
AZ91D/ CF10 SiC15 PIVAC	Mg_2Si	MgO	10 +/- 2
AZ91D/ SiC25 CF3 Squeeze Cast	Mg_2Si	MgO	19 +/- 5
AZ91D/ SiC25 CF3 PLI	Mg_2Si	MgO	79 +/- 5

MAGMAsoft. MAGMAsoft casting simulation software, developed by MAGMA GmbH, of Aachen, Germany, is a widely used software package that enables foundries and casting users to simulate filling and solidification processes. The program allows for prediction of potential casting defects associated with incomplete filling and/or lack of feeding during solidification stages. The software is driven by an advanced set of algorithms based on laws of physics, thermodynamics, and computational fluid dynamics and is capable of simulating a wide variety of casting processes such as vertical/horizontal sand casting of ferrous and non-

ferrous alloys; low-pressure, permanent mold and die casting of non-ferrous alloys; investment casting of ferrous and non-ferrous alloy, etc. The well-developed filling and solidification algorithms consider a variety of factors and parameters that may be used in a particular casting process. One such advanced feature of MAGMAsoft is the capability it provides to simulate filling of a runner system that contains a filter.

The purpose of this activity is to simulate, using MAGMAsoft, the infiltration of a carbon fiber/SiC particulate preform with molten Mg. Using a modified squeeze cast process, the intent is to push the molten metal through the preform to produce a lightweight component with a high specific strength. Because of their high density, preforms obstruct the flow of molten metal in the mold cavity, often causing the formation of unfilled pockets and microporosity within the casting. Understanding flow mechanisms during infiltration is essential to obtaining optimum pouring temperature, filling rate, backpressure, and other parameters that define a robust process capable of consistently producing 100% infiltrated, sound Mg squeeze cast composites.

The objectives of this portion of the work are as follows.

Step 1. Explore the possibilities of using casting simulation software to model infiltration of preforms with Mg during the squeeze casting process.

Step 2. Understand flow mechanisms during filling of the mold and attempt to predict potential defects that may result from incomplete infiltration of the preform.

Step 3. Model different mold cavity configurations containing preforms of varying geometries.

Results and conclusions obtained from the work described are communicated to GS Engineering and REL Machine to assist them with setup parameters during their experimental work.

Step 1

A typical setup of a squeeze cast process consists of a sprue through which molten metal is delivered either directly into the cavity or through runners, a mold cavity, and vents. In the Mg squeeze cast process explored by GS Engineering and REL, the sprue is positioned vertically (Z direction) and metal is delivered into the mold cavity from the bottom of the mold. The schematic of the setup is shown in Figure 8.

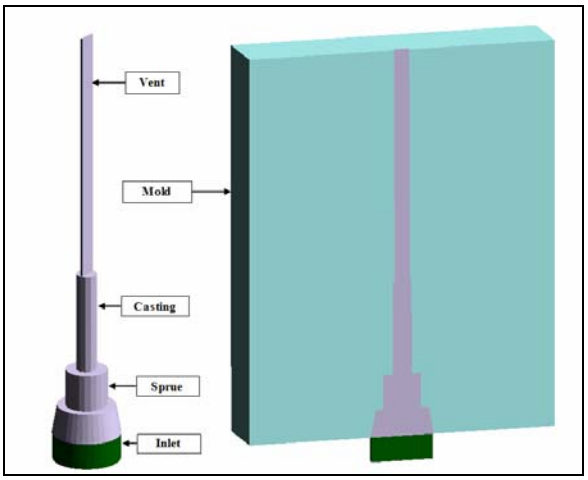

Figure 8. Typical setup of squeeze cast process.

Based on the functionality description of MAGMAsoft, the program is fully capable of simulating a vertical casting process, including modeling the flow of metal through the filter. Therefore, it was thought possible to model infiltration of a preform during the filling stage of a squeeze casting process.

In order to model the filling stage of the process, a certain amount of freedom was used with the MAGMAsoft package, including these examples:

1. The formulas used in MAGMAsoft that describe the flow of metal through the filter are based on the pressure drop data vs stream velocity. The drop in pressure in the stream of metal as it flows through the filter largely depends of the permeability of the filter and its size. To run simulations, researchers at GS Engineering and REL experimentally derived pressure drop curves for each type of preform based on its density and size. These pressure drop curves were imported into the MAGMAsoft filter database to be used during experimental simulation runs.

2. Modeling of the flow of metal through the preform-filter does not consider the complex internal topography of pores. In addition, the simulation is carried out assuming the absence of interaction between molten metal and the residual binder compounds remaining on the surfaces of preform fibers and particles. The potential lack of wetting of particles and fibers that may exist during the actual infiltration process is not ac-

counted for in the simulation because of the extreme complexity of mechanisms describing this phenomenon.

Step 2

The concept of modeling the infiltration of the preform in a squeeze casting process was tested in the following setup (Figure 9):

1. A cylindrical cavity was set in a steel mold.
2. A rectangular preform with a square cross-section was placed in the cavity.
3. An inlet was placed at the bottom of the mold in immediate contact with the preform.
4. A vent was added to the system to provide an outlet for gases pushed out of the mold cavity by the metal during infiltration.

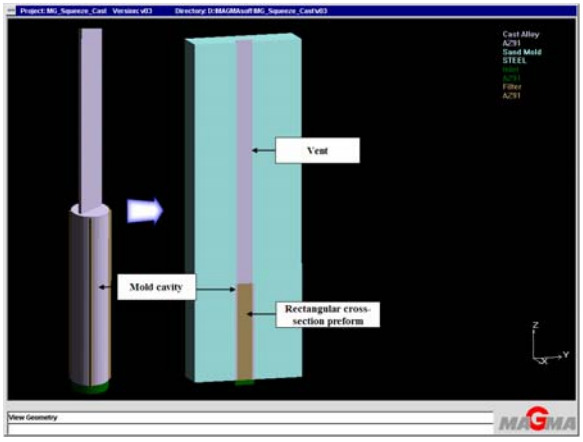

Figure 9. Infiltration of a rectangular 35% SiC–3% carbon fiber preform.

Additional setup parameters used in the simulation are as follows:

1. Mg alloy used in simulation: AZ91
2. Alloy pouring temperature: 725°C
3. Preform used: 35% SiC, 3% carbon fiber
4. Temperature to which mold was preheated: 300°C.
5. Total fill time predicted by this simulation run: 4 s.

The results of the simulation showed several prevailing filling patterns:

1. Because of the difference in cross-section geometry of the mold cavity and the preform, the setup allowed the molten metal to flow through the gaps between the mold and the preform. As a result, the alloy quickly enveloped the preform and entered the vent before complete infiltration of the preform.

2. The infiltration of the preform proceeds from the bottom up. However, once the entire preform is enveloped by the alloy, additional infiltration is observed with the metal moving from the sidewall toward the centerline of the preform.

The final stages of filling indicate that there exists a high potential for formation of center line porosity or areas of incomplete infiltration, as shown in Figure 10.

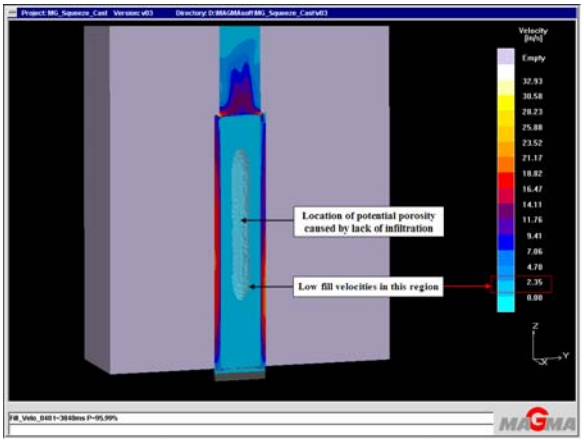

Figure 10. Melt velocity distribution at 96% of fill time.

Melt pressure distribution in the mold at 96% of filling supports this prediction—low melt pressures (14.9 ~ 76.1 psi) in the vicinity of a porosity pocket indicate that the flow of metal is reduced to the point of a complete halt.

The main conclusion reached based on the results of this simulation is that the gap between the mold and the preform allows a fraction of the melt front to follow the path of least resistance. This creates a condition in which the metal envelopes the preform long before it is fully infiltrated. Subsequent infiltration of the mold may be impeded by the gases trapped inside the preform. Following this modeling run, it was recommended that a setup be explored in which the gap between the mold and the preform is eliminated by matching the cavity of the mold to the geometry of the preform, i.e the final geometry of the casting.

Step 3

The setup modeled in Step 3 is depicted in Figure 11. The mold cavity precisely matches the geometry of a preform that when fully infiltrated would result in a Mg squeeze-cast connecting rod casting. The goal of the setup is to force the metal directly through the preform by eliminating any gaps between the mold and the preform. This simulation was carried out using the same process parameters as those in step 2. The stages of the filling sequence are shown in Figure 12.

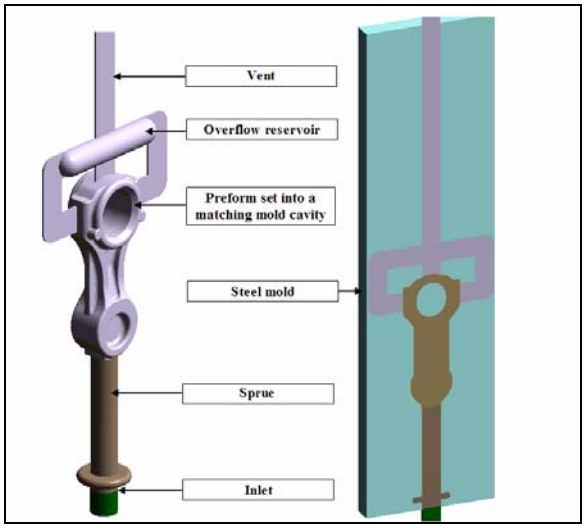

Figure 11. Mold set up to squeeze-cast a preform reinforced AZ91 Mg connecting rod casting.

Filling of casting reinforced by preform

The results of this modeling run demonstrate a generally good pattern of filling. The entire cross-section of the preform was filled without the formation of visible pockets of porosity. The problem arises at the final stages, around 94 to 100% of filled volume. A large pocket of porosity was formed at the very top of the connecting rod casting, as shown in Figure 12.

Full infiltration is observed throughout the volume of the preform up to ~94% of fill. However, beyond this point, an apparent pocket of porosity is formed at the top of the rod casting. Higher melt pressures noted around the pocket point to the fact

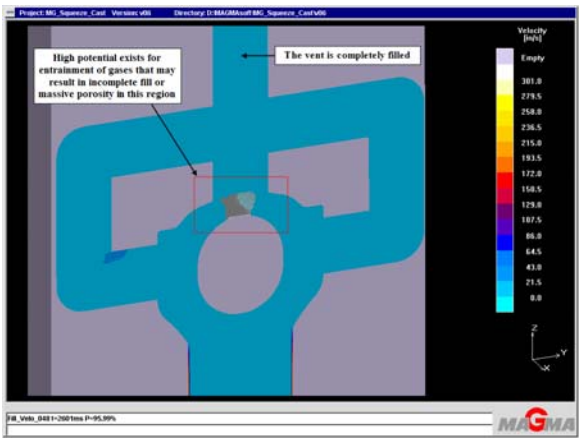

Figure 12. Mold flow simulation 94% complete showing potential filling issues.

that the flow of metal is slowed or halted by trapped gases.

The distribution of melt pressure results provides another valuable bit of information on the potential problems that may arise during the infiltration stage. A rapid increase in back-pressure is observed in the sprue as infiltration proceeds beyond 50% of total fill. Pressure in the sprue reaches as high as 23,730 psi at 96% of total fill. It is suggested that these pressure values be compared with the compression strength of the preform to make sure that the preforms are not cracked or crushed during infiltration. The total fill time of this system was predicted at 2.65 s.

Based on the velocity and pressure results, it is believed that the lack of infiltration at the top of the casting is caused by incorrect design of the overflow/venting system. This flaw can be fixed by a relatively simple redesign of the venting system. It is suggested that two of the three overflow outlets be eliminated, leaving only one outlet at the top of the casting. This outlet would connect with a large overflow reservoir that would branch into two vertical vents.

Also, the contact with the sprue at the bottom of the casting was widened to increase the amount of metal entering the mold. The modified mold layout is shown in Figure 13.

The setup with the suggested modification in the venting system was simulated to verify that the change would improve infiltration at the top of the casting. The casting process parameters were kept unchanged to maintain consistency between simulations. Infiltration progressed through the cross-

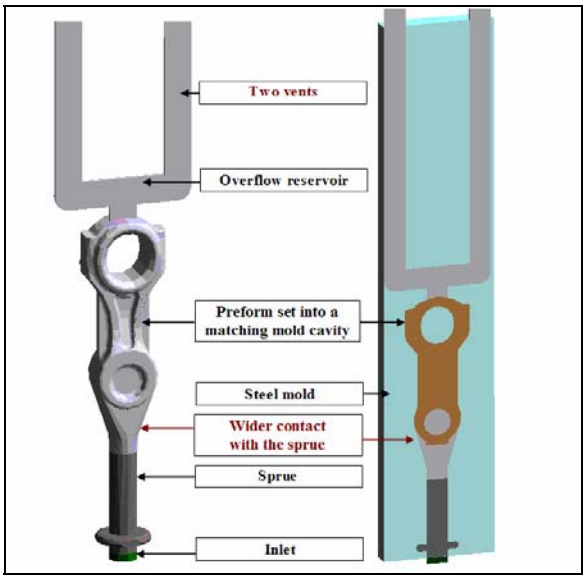

Figure 13. Modified layout to improve venting.

section unobstructed and completed at the top of the connecting rod casting without any indications of potential porosity pockets.

Similarly, pressure distribution results did not contain any signs that would mark potential insufficient infiltration. However, the back-pressure in the sprue rapidly rose as the melt front moved through the preform to the top of the casting. Steps may be needed to measure the actual back-pressure during experimental runs, and the head pressure may need to be adjusted to prevent damage to the preform.

Computer modeling of fiber/particulate pre-form infiltration with molten Mg using MAGMAsoft provided sensible results that gave insight into the filling mechanisms taking place during the filling stage of the process. The following conclusions were drawn from the simulation results:

1. Infiltration may be improved when the preform comes into direct contact with the mold wall, thus eliminating gaps and forcing the metal to flow through the preform instead of around it.

2. The back-pressure of the melt built up in the sprue may need to be controlled to avoid exerting excessive compressive forces on the preform that might damage its structural integrity.

3. The venting system is a critical element to successful infiltration. It must be designed to avoid entrainment of gases that will impede the progress of metal through the preform.

It is highly recommended that each setup modeled with MAGMAsoft be experimentally tested to draw correlations between results.

Die Fabrication and Casting Trials

From the iterations in the MAGMAsoft model, a good feel for the metal flow through the preform was realized. These steps eliminated costly die reworking, as the design of the die was altered to enhance metal flow. The die, shown in Figure 14, is the result of a collaborative effort ranging from the die designer to the mold flow analyst to the machinist cutting the final dies.

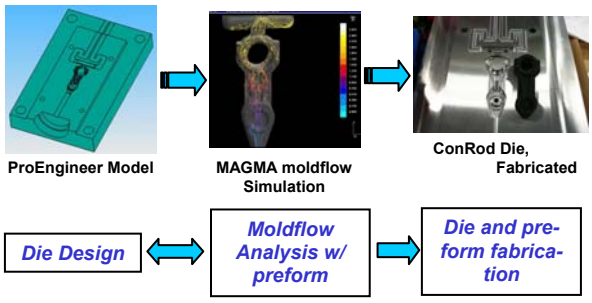

Figure 14. The process diagram of the connecting rod die build.

Aluminum connecting rods were the first components cast in the new die to ensure a good seal was obtained before switching to the more volatile metal Mg. Initial experiments were performed. The final casting is seen in Figure 15.

Validation of Model with Experiments

Model validation is ongoing, but some preliminary data indicate that the model predictions and casting observations do agree with each other. CT scans of a conrod cast with an aluminum alloy indicate good filling of the cavity (Figure 16). Issues arise at the thick-to-thin transitions, as is expected in many castings. These issues can be overcome with adjustment of casting process conditions.

Press Validation

A series of infiltration trials were cast on the GSE press to narrow process parameter windows

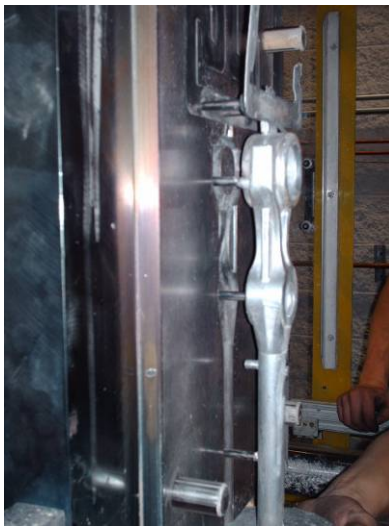

Figure 15. Initial magnesium connecting rod casting in die.

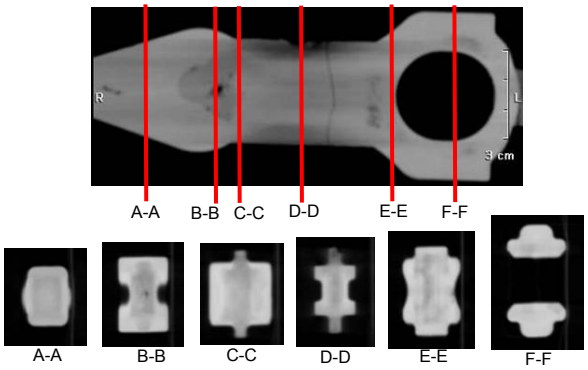

Figure 16. CT scan of a reinforced connecting rod showing the degree of aluminum infiltration of the preform.

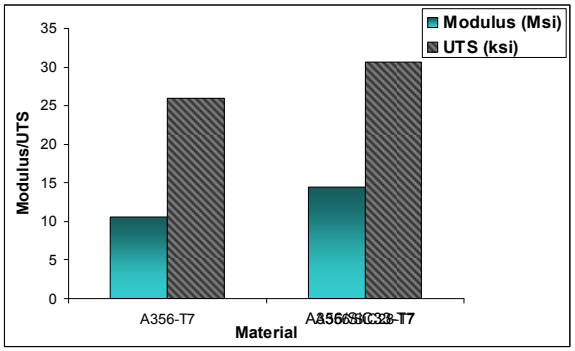

Figure 17. Comparison of A356 and A356-33SiC.

and to compare mechanical properties achieved with listed data on MMCs. Figure 17 indicates strength and stiffness values achieved in the casting of A356 into a 33 vol % SiC preform. It also compares the pure alloy with the MMC. A 36% increase in stiffness and an 18% increase in ultimate tensile strength was noticed with the reinforcement.

Initial casting with A356 and A356-33SiC showed the mechanical properties achieved compare very well with published data. That raises our confidence in our casting system. Our initial trials with Mg look promising, as we were able to infiltrate our CF25 preforms with some success. This work will continue in the coming months, as our molten metal transfer system is currently functional.

Conclusions

Process control in Mg MMCs is complicated by the reactive nature of the molten metal. Interactions between the metal and the preforms can be positive for good fiber-matrix bonding, but too much of these reaction products can produce unwanted intermetallics and oxides in the matrix. The reaction products of the Mg alloy reacting with the silica binder have been tabulated and the amounts can be seen from the X-ray diffraction data. The quantities of Mg_2Si and MgO change with the casting speed and solidification times; therefore, contact time between the molten metal and the preform must be optimized to obtain good bonding between the two without degradation of the reinforcement or the overproduction of excess constituents. In light of these observations, process conditions are precisely controlled to optimize the casting of selectively reinforced Mg composites and will be reported in future publications.

Future Work

Future work will focus on refining the materials, i.e., matrix/reinforcement, and process parameters for a production-capable casting system through a series of casting trials on the GSE casting press with microstructural analysis of micro and macro interfaces. Mechanical testing will be performed in bench and field testing, which will give feedback to optimize process and materials based on those results. The Gantt chart in Figure 18 details the work and timeline for year 2 of the project.

Acknowledgements

The authors would like to thank DOE and Oak Ridge National Laboratory (ORNL) for the funding

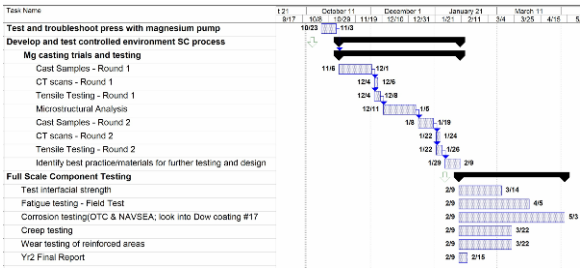

Figure 18. Project plan for remaining work to be completed.

to perform this research. Also, thanks are due to Harry Meyer of ORNL for the AES analysis of cast samples, Edward Laitila (Michigan Technological University) for assistance in performing the X-ray diffraction analysis, and GOM Technologies for the pressureless infiltration trials.

Presentations/Publications

R. Hathaway, A. Loukus, C. Johnson, T. Wood, J. Loukus, A. Halonen, G. Simula, V. Pikhovich, B. Coleman, and D. Weiss, "Manufacturing Process Influence on Microstructural Features of Selectively Reinforces Magnesium Metal Matrix Composites," in *TMS Proceedings*, San Antonio, 2006.

J. E. Loukus, A. Loukus, A. Halonen, "The Effects of Processing Methods on the Mechanical Properties of Cast Magnesium Metal Matrix Composites," AFS International Conference on High Integrity Light Metal Castings, Indianapolis, October 31–November 1, 2005.

3. MATERIALS PROCESSING TECHNOLOGIES

A. Development of an Advanced Squeeze Casting Process for Producing High-Integrity Truck Components

Principal Investigator: David C. Weiss
Eck Industries, Incorporated
1602 North 8th Street, Manitowoc, WI 54221-0967
(920) 682-4618; fax: (920) 682-9298; e-mail: dweiss@eckindustries.com

Chief Scientist: James J. Eberhardt
(202) 586-9837; fax: (202) 587-2476; e-mail: james.eberhardt@ee.doe.gov
Field Technical Manager: Philip S. Sklad
(865) 574-5069; fax: (865) 574-6098; e-mail:skladps@ornl.gov

Contractor: Eck Industries, Incorporated
Contract No.: 4000022893

Objective

- Develop the equipment and process technology for an advanced squeeze casting (ASC) process to enable production of high-integrity cast metal components.
  - — Integrate the advantages of two casting methods—low-pressure permanent mold (LPPM) and direct squeeze casting —to attain non-turbulent fill of the die, high solidification rates to refine microstructural features, and solidification under pressure to minimize microporosity.
  - — Design and build a new kind of casting machine and develop process technologies needed to cast high-integrity truck components from nonferrous alloys.

Approach

- Design and construct a casting machine that integrates a low-pressure metal delivery system suitable for either aluminum or magnesium alloys, reliable gate shut-off technology, and direct application of squeeze pressures up to 103 MPa (15,000 psi). This machine is intended for production.
- Develop a gate shut-off mechanism that will operate reliably in a production environment.
- Select a casting that will be produced in the casting machine built for this project.
- Use fluid-flow and solidification analysis to predict optimum flow conditions for metal entering the mold and differential squeeze pressure requirements.
- Design and build cast tooling
- Develop process technologies for the low-pressure/squeeze casting of aluminum alloys and evaluate the effect of various process parameters on casting integrity.
- Apply developed technologies to the production of a selected automotive component.

Accomplishments

- Designed, built, and installed ASC machine at Eck Industries.
- Designed and fabricated squeeze cast tooling .
- Developed process parameters for prototype production of B356-T6 connecting rods.
- Produced ASC and LPPM castings for determination of static and dynamic properties of ASC-processed B356-T6.

Future Direction

- Determine static and dynamic properties of ASC-processed B356-T6.
- Demonstrate production viability of ASC casting machine and process.

Introduction

Squeeze casting is the solidification of liquid metal under pressure in a closed metal die. The casting produced has improved properties and a more uniform microstructure compared with those produced by traditional molten metal fabrication techniques. The improved properties are achieved through controlled entry of the metal into the die through large gates, which reduces turbulence, and high solidification rates with resulting refinement of microstructural features.

There are two squeeze casting methods—direct and indirect. The method and efficiency of pressure application distinguish the two processes. Direct squeeze casting applies pressure directly on the casting. Indirect squeeze casting applies pressure indirectly via the gating system. The length of the gating system and any partial solidification prior to complete solidification of the part reduces the magnitude of the pressure applied and may result in casting porosity. For the indirect method, the dimensions of the die cavity control part dimensions. For the direct method, the part dimensions are controlled by the die cavity dimensions and the finish position of the top die. Thus direct squeeze casting requires precise machine control to attain the desired part dimensions. In addition, the direct method requires in-gate shut-off technology to control pressure during cavity pressurization. Both methods suffer from poor metal handling from the furnace into the mold or gating system. Inadequate control of pouring speed generates turbulence and casting defects such as oxide inclusions that reduce fatigue properties.

Earlier attempts to improve the squeeze casting process by combining the advantages of low-pressure die fill with those of squeeze casting demonstrated substantial mechanical property improvement and reduced component porosity. However, continuous production operation of the equipment was not achieved. The machines used were not specifically designed to meet the needs of the process.

Technical Approach

The results of this project will provide (1) a production-viable ASC machine, (2) process technology that will improve the strength and reliability of cast automotive components, and (3) demonstrated production viability of the equipment and process.

Machine design. Previous efforts demonstrated that modification of current cast machine designs would not provide a production-capable ASC machine. An assessment of the capabilities and limitations of current machine designs demonstrated that

- Low-pressure cast equipment typically does not have the structural rigidity needed to withstand the high pressures required of squeeze casting.
- Die-casting and currently available squeeze casting machines are not designed for proper (non-turbulent) molten metal entry into the die cavity.
- Neither type of equipment is typically available with the hydraulic and electronic controls necessary to attain the die cavity motions required for the direct squeeze casting process.

After much consideration, the project team decided it was easier and more cost-effective to build a machine from the ground up than to modify an existing cast machine design. To facilitate the design and construction, the team partnered with Empire Castings, Inc., an experienced producer of low-pressure casting equipment.

Process development. Bendix, Inc., is an industrial manufacturer of truck components with an interest in reducing manufacturing cost by the use of high-quality castings. Consultation with Bendix led to the selection of an air compressor connecting rod for prototype production in the ASC machine. This component has a level of complexity that can demonstrate the production capability of the ASC machine and process, show the need for mechanical properties higher than those attainable with commercially available castings, and provide an opportunity for production with the ASC process.

The cast part will be modeled for fluid flow and solidification. This work will be done in parallel with equipment design. Simulation will provide an understanding of optimum metal flow conditions and squeeze requirements, if any, to contend with solidification shrinkage. This is very important to the success of the program and, potentially, to the details of the machine design. The ASC machine will have two mechanisms to feed the casting—low-pressure, nonturbulent fill of the die cavity and high-pressure, direct squeeze to minimize solidification shrinkage. Modeling experiments will explore the interaction of the two feed mechanisms and select process parameters that lead to process optimization. Modeling results will be used to refine the die design and select initial casting process parameters.

After tooling construction and ASC machine delivery, castings will be made under the range of process conditions anticipated during modeling. The alloy to be used for development is the cast alloy B356. Evaluation of those castings will include radiography, die penetrant inspection, and tensile testing. It is anticipated that this part of the program will require multiple iterations to produce the desired product quality. Some equipment and tooling modification may be required during this part of the program.

After successful production of development castings, the production viability of the equipment and process will be demonstrated by

- Production of a connecting rod with reduced porosity and improved mechanical properties compared with the current die-cast connecting rod used by Bendix.
- Continuous production with the ASC machine and connecting rod tooling to include at least one 5-h continuous run with the equipment running at least 3 days in a week.

The goal of the project team is to implement commercial part production on an ongoing basis.

Program Schedule

The revised scheduled start and end dates for the various program tasks are listed in Table 2.

Table 2. Overall program schedule (revised)

Program Task	Start date	Finish date
Machine design	June 2003	Feb. 2004
Machine build	Mar. 2004	Nov. 2004
Tooling design	July 2003	Oct. 2003
Tooling build	Nov. 2003	Mar. 2004
Process model	Oct. 2004	Dec. 2004
In-gate SO development	Nov. 2003	Dec. 2003
Machine install	Nov. 2004	Nov. 2004
Casting development	Dec. 2004	Dec. 2005
Evaluation and testing	July 2006	Dec. 2006
Final report	Nov. 2006	Jan. 2007

Program Status

ASC machine. The 600-ton-capacity ASC casting machine is installed at Eck Industries (Figure 1) and has been used to cast tensile bar specimens and prototype connecting rods (Figure 2).

Data acquisition system. The computerized data acquisition system has worked flawlessly. The pressure, displacement, and temperature data have been used to understand the operation of the ASC process and establish process parameters. A plot of a typical data set is shown in Figure 3.

Process development. Modification of the machine's PLC program to use timers instead of temperature data for controlling start and stop of machine operations was proved successful by the sequential accomplishment of 40 castings. A typical

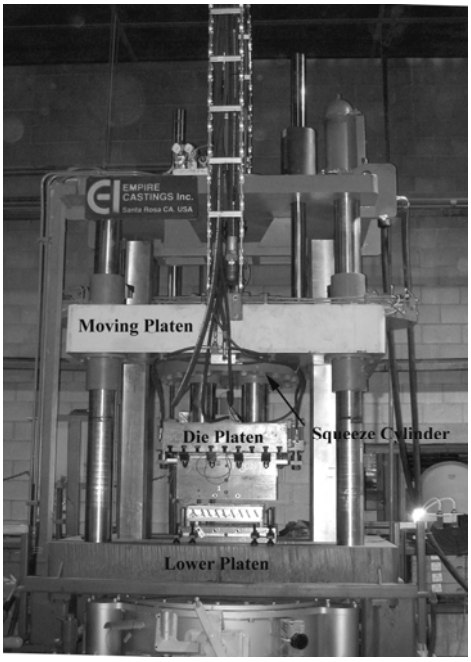

Figure 1. ASC machine installed at Eck Industries.

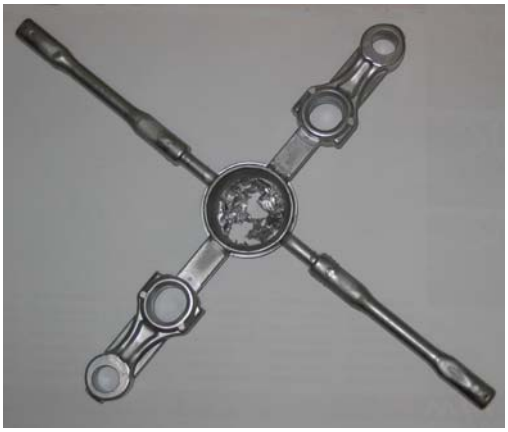

Figure 2. Typical casting from 40 shot run.

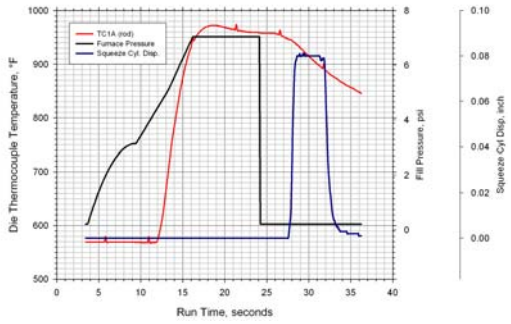

Figure 3. Typical data obtained from data collection system during casting runs.

casting is shown in Figure 2. Subsequently the four-cavity mold designed and fabricated for the program was used to make two sets of castings—one set by squeeze casting and the other via the conventional permanent mold process. The two sets of tensile bar castings were machined and are being used to determine tensile and fatigue properties of B356-T6 castings. Subsequent data analysis, fractography and image analysis will determine the quality and property enhancement attainable to the ASC process.

Conclusions

Consistent operation of the ASC machine has been obtained. Fatigue and tensile specimens have been machined and evaluated for quality level via radiography. The determination of static and fatigue properties at room temperature has been started and completion is scheduled for December 2006. As shown in Table 2, the schedule has been revised to reflect expected completion dates.

Prototype Production for Industry

Eck Industries is working with an industrial customer to determine the viability of the ASC process for the production of a transmission hub (see Figure 4). When it is produced via die casting, the rejection rate for this part is higher than desired.

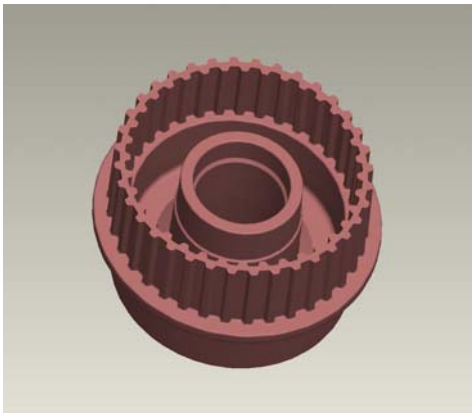

Figure 4. Transmission hub for automotive application.

Casting simulation predicts that both die and LPPM casting will contain porosity in areas that need to be "porosity free." Use of the ASC process is expected to provide the desired "porosity free" casting, reduce the rejection rate, and reduce overall manufacturing costs. Lower porosity levels are also

expected to increase the fatigue life of the component. Prototype casting of this component is scheduled for early December 2006. Successful prototype casting is expected to lead to a production contract for this and other similar components.

Presentations and Publications

D. C. Weiss, "Design and Fabrication of a Machine for an Advanced Squeeze Casting (ASC) Process," presented at the AFS International Conference on High Integrity Light Metal Castings, Indianapolis, October 31–November 1, 2005, and published in *Proceedings of the AFS International Conference on High Integrity Light Metal Castings*, American Foundry Society, Schaumberg, IL, 2005.

B. Counter-Gravity (Hitchiner) and Pressure-Assisted Lost Foam Magnesium Casting

Principal Investigator: Qingyou Han
Oak Ridge National Laboratory
Oak Ridge, TN 37831-6083
(865) 574-4352; fax: (865) 574-4357; e-mail: hanq@ornl.gov

Chief Scientist: James J. Eberhardt
(202) 586-9837; fax: (202) 587-2476; e-mail: james.eberhardt@ee.doe.gov
Field Technical Manager: Philip S. Sklad
(865) 574-5069; fax: (865) 574-6098; e-mail: skladps@ornl.gov

Participants:
Ralph B. Dinwiddie, Oak Ridge National Laboratory
Pete Angelini, Oak Ridge National Laboratory
Graham V. Walford, Walford Technologies
Ken Currie, Tennessee Technological University
Mohamed Abdelrahman, Tennessee Technological University
Fred Vondra, Tennessee Technological University

Contractor: Oak Ridge National Laboratory
Contract No.: DE-AC05-00OR22725

Objective

Evaluate the Hitchiner process and pressure-assisted lost foam casting of magnesium (Mg) alloys. In particular,

- Develop the casting system.
- Develop low-density foams and appropriate coatings.
- Establish casting parameters for selected Mg alloys.
- Conduct computer simulations of the process to be used to generate design guidelines.
- Validate the process by characterizing microstructure and properties of castings.

Approach

- Compare lost foam casting characteristics of Mg and aluminum (Al) at 1 atmosphere
- Castability/integrity/mechanical properties
- Compare lost foam Mg casting with Hitchiner lost foam Mg casting and pressure-assisted casting
  - — Castability/integrity/mechanical properties
- Document the features of the Hitchiner lost foam Mg casting
  - — Possible applications, typical features of casting that are suitable for the Hitchiner process, and limitations of the Hitchiner process

Accomplishments

- Developed melting and casting capabilities at Tennessee Technological University (TTU) and Oak Ridge National Laboratory (ORNL).
- Observed significant difference between Mg lost foam casting and Al lost foam casting in mold filling and molten metal/foam interaction.
- Developed a system for the selection of foam materials and coatings.
- Carried out experiments to develop baseline data and to evaluate the Hitchiner process for lost foam casting

Future Direction

- Select/develop coatings and foams for the Hitchiner process for lost foam magnesium casting.
- Complete the design of a parametric study of the parameters affecting the castability of Mg alloys under the Hitchiner process conditions.
- Start the simulation of the Hitchiner/lost foam process.
- Document the features of Hitchiner lost foam Mg casting.

Introduction

The last 10 years have seen dramatic increase in the production and utilization of Mg. This demand is primarily due to an increase of 20% annually in the use of Mg in the automobile industry driven by the desire to increase vehicle fuel efficiency by reducing vehicle weight. Magnesium has found uses in several automotive components because of its low density and high strength-to-weight ratio compared with conventional automotive materials. More recently, Mg castings have been introduced into pickup trucks and vans, such as the standard size Ford F-150. Additional opportunities exist for the use of Mg casting in these vehicles, as well as in heavier trucks. Even with these successes, however, Mg has not been as widely accepted as it might have been for the following reasons: the cost of the alloys, the lack of long-term field validation or controlled fleet testing data for powertrain components, and lack of a technological base for foundry casting of Mg alloys.

Magnesium castings are traditionally produced by die casting or precision sand casting. Each of these processes has its advantages and disadvantages for producing components. The major disadvantage of conventional die casting processes is that certain geometries cannot be produced using steel die sections and are limited by moving cores. In addition, die casting often results in unacceptable levels of porosity. On the other hand, precision sand casting can produce a wide range of shapes with high levels of soundness, but at an unacceptable cost. Although successful castings can be manufactured, continuing problems experienced during the casting of the Mg alloys include porosity formation, oxidation, and hot tearing/cracking formation.

In order to take greater advantage of the attractive properties of Mg, alternative approaches that promise to be more robust and lead to the development and fabrication of larger, thinner wall castings must be considered. Lost foam castings can be competitive with other casting techniques for applications with complex internal passages (coring) and can reduce machining, save space, and/or integrate multiple complex features or components into a single casting.

Previous studies at ORNL on gravity lost foam casting of Al have determined that many factors affect the quality of the casting outcome. In particular, the metal filling process of the lost foam pattern is greatly influenced by the pattern properties. The advancing metal front decomposes the foam into gaseous and liquid decomposition products that must be eliminated from the casting volume to complete the process. Pattern density and the pattern gas permeability arising from the combination of the foam and ceramic coating are critical factors in the process, yet they are not

measured on any commercial process line. Variances in these properties are difficult to control and result in variance in the metal filling behavior. The physical properties of Mg would increase this problem further. In particular, the low density, latent heat, and high reactivity of the molten Mg alloy are serious issues for its castability under lost foam casting conditions.

These problems can be overcome by making use of pressure-/vacuum-assisted mold filling together with closed-loop process control. The Hitchiner process, which uses vacuum as a driving force for mold filling, is a logical choice for lost foam casting of Mg alloys. The change of pressure across the advancing metal front can be used to accommodate variances in the gas permeability of the foam and coating for the whole pattern and for local variations in the pattern. Pressure can also be used to assist in mold filling.

The challenges of using the Hitchiner process and pressure-assisted lost foam Mg casting are in the areas of setting up the experimental equipment for the research; parametric study of the parameters affecting the processes; development of low-density foams for the casting of Mg alloys; control of permeability of the sand, foam and foam coatings; and the use of controlled atmospheres for reducing metals reactance, chemistry, and the thermal profile of the pattern to be cast. This article is the second-year report for this project. The goal of the second-year research was to develop the Hitchiner casting process and evaluate this process for Mg casting.

The Casting Systems

The existing metalcasting facilities at TTU have been modified for handling molten Mg alloys and for using the Hitchiner process for lost foam casting of Mg alloys. A Thermtronix solid state Al/ Mg electric resistance furnace has been purchased and facilitated for use. It has a 200–300 lb charge capability (depending on whether it is used for Mg or Al), and a special-purpose cover made from mild steel has been added to the furnace to allow for introduction of a cover gas to prevent the molten Mg alloys from reacting with the atmosphere. The cover also has a hinged lid on the very top to facilitate direct insertion of the counter-gravity sprue. The Hitchiner counter-gravity casting system, shown in Figure 1, has been successfully tested for Mg castings and Al castings. Both a simple flat plate pattern (provided by GM) and a widget pattern (provided by Foseco Morval) were successfully cast using Mg alloy AM60B and Al alloy 319. A 1% sulfur hexafluoride/99% carbon dioxide cover gas was used over the molten Mg either in the crucible or in the furnace. A set of safe operating procedures were adopted to safely handle and cast Mg alloys in the current casting facility.

Figure 1. The Hitchiner casting system is being tested by TTU and ORNL researchers for lost foam casting of Mg alloys.

Foam Development and Selection

A broader study of foam decomposition has been undertaken that seeks to develop a kinetic and thermochemical model that describes polystyrene foam decomposition for a broad range of heating rates for oxidizing and non-oxidizing environments. Understanding the foam decomposition processes under different process conditions, including foam decomposition in the presence of molten Mg, served as the motivation behind this work. This effort might help in improving casting quality in ways such as reducing residue entrainment.

Based on a thorough literature search on appropriate kinetic models applicable to the polystyrene foam decomposition phenomena encountered in the lost foam casting process, experiments have been designed and carried out to investigate the foam degradation kinetics under the process conditions. The main purpose of this experimentation is to obtain data on the composition of polystyrene

foam degradation products as a function of melt temperatures and processing times.

Initially, a simple burn chamber using an infra-red heat source was constructed for these experiments, but a more precise reactor concept was conceived. Figure 2 shows the burn chamber used. The reactor consists of a heater maintained at a constant surface temperature and an automatic feeder that feeds the foam at a velocity "v"' from the automatic feeder, which simulate the actual metal temperature and melt flow rate, respectively, in the commercial casting process. When the foam impinges on the heater surface, it decomposes and forms various products. These liquid and gaseous products are collected and analyzed for their composition. Decomposition data could be collected as a function of both foam push rate and metal temperature. A schematic of the proposed reactor is shown in the figure.

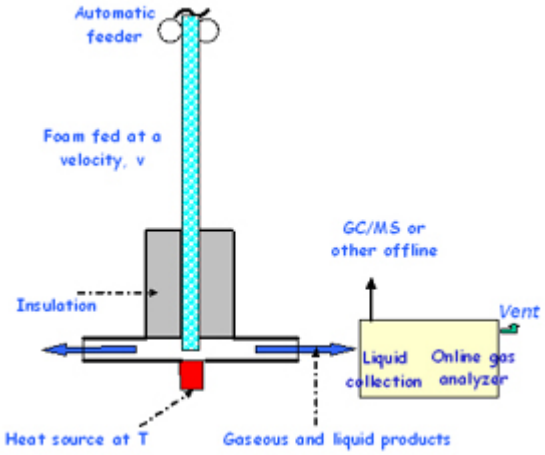

Figure 2. The burn chamber for characterizing foam decomposition.

In addition to analyzing and modeling the foam decomposition products, another important aspect is the characterization of the foam pattern. Walford Technologies, Inc. (WTI) has expanded its pattern quantification system to provide measurement of density, sonic propagation surface finish, and dimension profiles for patterns up to 36 in. in length. Figure 3 shows the setup of the infrared camera at a molding operation. The

Figure 3. Infrared camera installation at a molding operation.

camera is targeted to observe the expanded polystyrene (EPS) foam part.

Further work is required to correlate the properties of the EPS part as measured at the time of molding with the properties of a part that is suitable for casting. However, effective control of any process, and in particular of the process of using EPS in Mg casting operations, requires real time control and assessment of the part. This has not been previously accomplished.

Experimental Results on Castability

Castability experiments have been carried out at ORNL and TTU. Three types of patterns were used: a simple flat plate, the GM window pattern, and a widget pattern. The plate pattern was used for observing mold filling and for evaluating porosity distribution. The window pattern and the widget pattern were used for evaluating the castability of alloys. Five types of foam materials from Styrochem were tested: type A (T-17-170, ventless tool), type B1 (T-185, vented tool), type B2 (T-185, ventless tool), type C (T-170, vented tool), and type E (T-185 with bromated additive, ventless tool). A high-permeability coating was used for the testing. Castings of an A356 alloy and an AM60B alloy were made.

Casting temperature has a significant effect on the castability of the Mg AM60B alloy. Castings were made using the GM window patterns made of B1 foam. A cold shut defect occurred at the corner where the metal filled last when the pouring temperatures were around 1400 to 1450°F. Increasing the pouring temperature reduced the

cold shut defect. When the pouring temperature was 1500°F, the cold shut defect was eliminated. However, 1500 °F is about 355°F higher than the liquidus temperature of the alloy. At such a high temperature, oxidation and dross formation can be a significant problem. A similar casting can be made at 1300°F using the Al alloy A356, indicating it is more difficult to cast Mg alloys than Al alloys.

The Hitchiner process enhances the castability of Mg alloys significantly. Figure 4 shows a widget Mg casting made using the Hitchiner process. The casting was cast at 1300°F and had no cold shut defect. Considering that the widget casting is more complex in geometry than a window casting, a higher pouring temperature would be required in order to make a casting without cold shut defect if the widget casting were made under the normal lost foam casting conditions. The use of the Hitchiner process makes it possible to produce geometrically perfect castings at a much lower pouring temperature. The results also suggest opportunities for using this process for making a casting larger than that made by using the normal lost foam casting process.

Figure 4. A geometrically perfect Mg alloy lost foam casting made using the Hitchiner process.

A systematic research plan was developed using a mixed-level Taguchi design program and a random number generator. The research evaluates the effects of the key parameters or factors of the Hitchiner process on the castability and mechanical properties of AM60B alloys. These parameters include the pouring temperature, the pressure or vacuum, the coating, and the types of foams. The experimental studies are still under way.

Experimental Results for Porosity Formation

The porosity distributions in flat plate castings of A356 and AM60B made using the lost foam casting process were characterized. The effect of degassing on the porosity distribution in the flat plate casting was also investigated. Castings of A356 alloy and AM60B alloy were made using a flat plate pattern of 76.2×152.4 mm and 12.7 mm thick (3×6 in. and 0.5 in. thick). The use of a simple geometry plate casting eliminated the effect of geometry on porosity formation. The casting was bottom-gated. A large fiber downsprue was used, which provided the pressure head and served as a riser for feeding the macro shrinkage. The flat plate castings were cut into small specimens. Each specimen was used for density measurement using the apparent density measurement method.

The measured density distribution of the AM60B plate casting is shown in Figure 5a and 5b for degassed and non-degassed molten metal, respectively. The density distribution in the AM60B castings is fairly uniform, varying between 1.775 and 1.778 g/cm^3. This small variation in the density data is within experimental error. Degassing did not affect the density or porosity formation much. No interdendritic pores were found in the casting, indicating the downsprue was large enough to avoid the formation of macro-porosity.

Figure 6a and 6b illustrate the density distribution in the flat plate casting of A356 with and without rotary degassing. The in-gate location is in the middle at the right side of the diagram (x=35 mm and y=0 mm). Comparing Figure 6a and 6b, the density of the degassed casting is higher than that of the un-degassed one. The density value varies from 2.634 to 2.654 g/cm^3 for the degassed casting, but it varies from 2.60 to 2.625 g/cm^3 for the un-degassed casting. The density data strongly suggest that degassing is an effective means of reducing porosity in Al lost foam castings.

The trend of porosity distribution in both castings, degassed and un-degassed, is identical. The local density of the alloy was higher near the gate

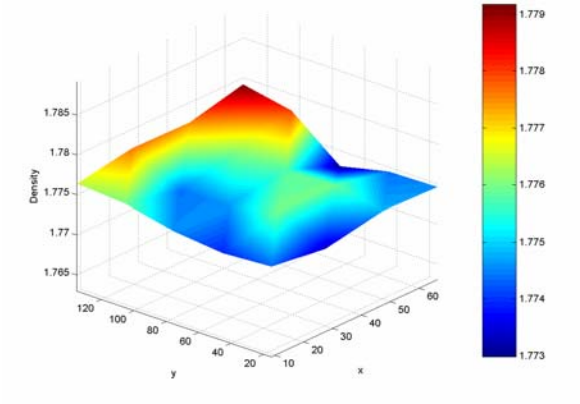

(a)

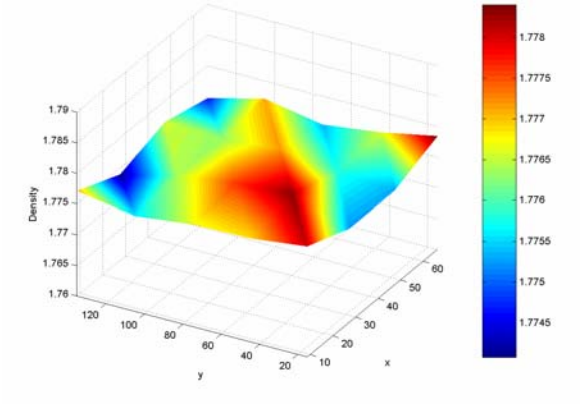

(b)

Figure 5. The measured density distribution in Mg AM60B alloy castings (a) degassed, and (b) un-degassed. The casting was gated at the middle on the right side of the plot.

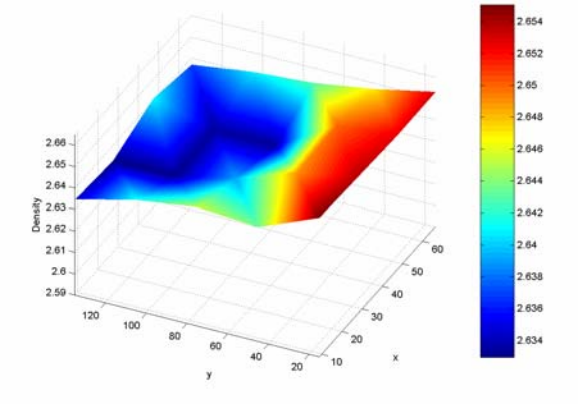

(a)

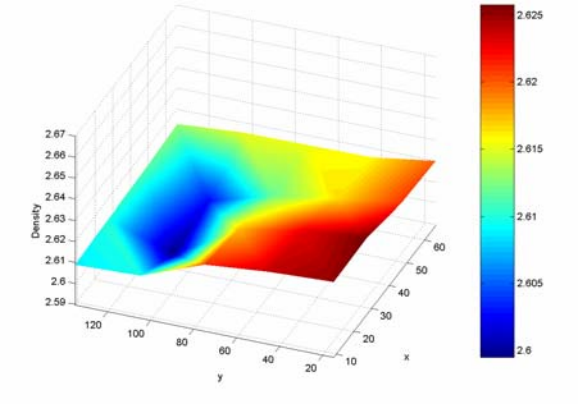

(b)

Figure 6. The measured density distribution in Al A356 castings (a) degassed, and (b) un-degassed. The casting was gated at the right side. A low-density region was identified near the left side of the Al casting.

and lower away from the gate. The lowest-density region occurred in the middle near the end of the plate casting. A significant amount of porosity existed in this region. Figure 7 shows the microstructure of the Al plate casting near the region where the density is the lowest. The pores there are interdendritic, rather than isolated spherical as usually seen in the regions near the gate of the casting.

The mechanism of the porosity formation in Al lost foam casting was investigated using an infrared camera to observe mold filling during the lost foam process. The metal advanced faster near the edge of the plate casting because the decomposition product of the foam could easily escape from the edges. As a result, the flow front was V-shaped. The low-porosity region occurred at the center of the V-shape partly because of entrapped foam residues and partly because the metal front in that area collected more hydrogen because it was in contact with the decomposition atmosphere for a longer time than was the metal near the edges.

This study on porosity distributions in Mg alloy and Al alloy lost foam casting showed that porosity formation is less an issue in Mg lost foam casting than in Al lost foam casting. Most likely that is due to the fact that hydrogen has a higher solubility in the solid Mg alloys than in the solid Al alloys. Less porosity formation is one of the benefits of using the lost foam process for making Mg castings.

Conclusions

The objectives of the second-year research in this project have been met. Melting and lost foam

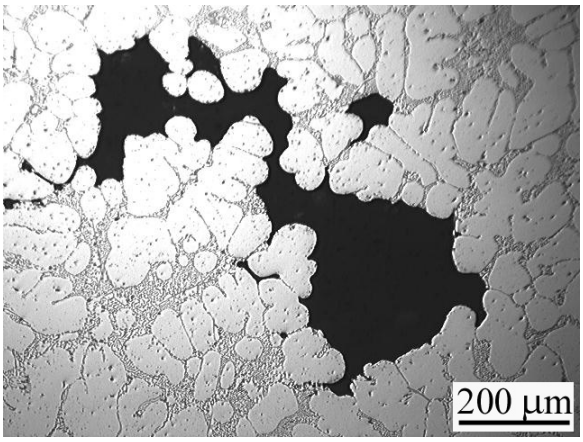

Figure 7. Interdendritic porosity occurred in the region where the density is the lowest on the Al plate casting.

casting capabilities have been developed at TTU and ORNL. The Hitchiner process has been established at TTU for testing counter-gravity and pressure-assisted lost foam Mg casting. A burn chamber has been modified for studying polystyrene foam decomposition for a broad range of heating rates for oxidizing and non-oxidizing environments.

High-quality lost foam castings of Mg and Al alloys have been made using both the conventional lost foam and the Hitchiner processes. The castability of Mg alloys under Hitchiner conditions (vacuum-assisted lost foam conditions) is much better than that under conventional lost foam casting conditions.

The porosity distribution in lost foam casting of Mg alloy is significantly different from that in Al alloys. Uniform distribution of porosity is observed in lost foam Mg casting, whereas the porosity distribution in Al alloy casting is highly nonuniform. The application of these experimental results will be explored in the third-year research.

Publications

Q. Han and H. Xu, "Fluidity of Alloys under High Pressure Die Casting Conditions," *Scripta Materialia*, **53**, 7–10 (2005).

Q. Han, R. Dinwiddie, P. K. Sklad, K. Currie, F. Vondra, M. Abdelrahman, G. Walford, D. Nolan, and T. Nedkova, "Lost Foam Casting of Magnesium Alloys," in *Magnesium Technology 2007*, TMS, in press.

Q. Han, R. Dinwiddie, P. K. Sklad, K. Currie, F. Vondra, M. Abdelrahman, G. Walford, D. Nolan, and T. Nedkova, "Comparison of Lost Foam Casting of AM60B Alloy and A356 Alloy," *Transactions of AFS 2007*, in press.

C. Wrought Magnesium Alloy/Process Development

Principal Investigator: J. A. Horton
Oak Ridge National Laboratory
P.O. Box 2008, Oak Ridge, TN 37831-6115
(865) 574-5575; fax: (865) 574-825; e-mail: hortonja@ornl.gov

Principal Investigator: S. R. Agnew
University of Virginia
116 Engineer's Way
P.O. Box 400745, Charlottesville, VA 22904-4745

Chief Scientist: James J. Eberhardt
(202) 586-9837; fax: (202) 587-2476; e-mail: james.eberhardt@ee.doe.gov
Field Technical Manager: Philip S. Sklad
(865) 574-5069; fax: (865) 574-6098; e-mail:skladps@ornl.gov

Contractor: Oak Ridge National Laboratory
Contract No.: DE-AC05-00OR22725

Objectives

- Develop wrought magnesium (Mg) alloys with better formability than current Mg alloys.
- Investigate new processing techniques for cost reduction and formability improvement.
- Contribute to basic understanding of deformation, processing, and alloy behavior for this lightweight metal.

Approach

- Explore new processing schemes for Mg alloy sheets, evaluate the practical formability of new alloys and alloys subjected to new processes, determine deformation mechanisms using experimentation and simulation.

Accomplishments

- Presented and published roll bonding paper.
- Published paper on deep drawing of sheet Mg.
- Presented and published paper on alloying for texture modification; it demonstrates new path to enhanced formability.
- Initiated rolling studies of new set of alloys cast by MEL.

Future Direction

- Interact with an industrial partner to advance commercialization of infrared processing for cost reduction.
- Define further correlations of microstructure, mechanisms, and anisotropy. In particular, define the kinetics and crystallography of recrystallization in Mg alloys.
- Further explore superplastic-type behavior observed at warm forming temperatures.

Introduction

Magnesium, with a density that is 66% of that of aluminum, has obvious advantages for use as a structural material in the transportation industry. Magnesium castings are steadily growing in use in automobiles and trucks. However, wrought applications are held back by the high cost of sheet due to the large number of processing steps. This project is currently focusing on processing techniques and issues to reduce the cost of sheet Mg. In addition, we continue to investigate means to improve the formability of wrought Mg alloys.

During this period, we have finished and submitted several publications based on work largely performed last year with details presented earlier.

Rolling Studies of New Alloy Compositions Cast at MEL for Cost Reduction

Wrought alloy costs have several components, including starting alloy composition and original ingot casting procedures. A collaborative effort with MEL is aimed at addressing this issue in conjunction with tailoring an alloy for a continuous cast and rolling line. Ninety small slabs were cast at MEL for rolling and characterization studies at Oak Ridge National Laboratory (ORNL) (see Figure 1). Both normal rolling schedules and schedules amenable to an infrared reheat continuous process are being investigated. Previous work at ORNL has shown that infrared reheat yields similar results to current commercial practice suggesting that, in conjunction with twin roll casting, it presents a possibility for a continuous production line.

Figure 1. An initial rolling attempt at a new composition alloy.

Deformation Behavior of a Twin-roll-cast Alloy

Mechanical properties of a twin-roll-cast $Mg_6Zn_{0.5}Mn_{0.3}Cu_{0.02}Zr$ with a grain size of ~15 μm were measured at temperatures from 423 to 523 K. Constant strain rate, strain rate change, and temperature change tests (strain rates from 5×10^{-7} to 3.3×10^{-3}/ s^{-1}) were employed to characterize the plastic flow behavior of the alloy (Figure 2). It was observed that, at low strain rates and high temperatures, the alloy followed a power law behavior; but the power law breaks down at high strain rates and low temperatures. Transient behavior was also characterized to identify the dominant deformation mechanism in the alloy.

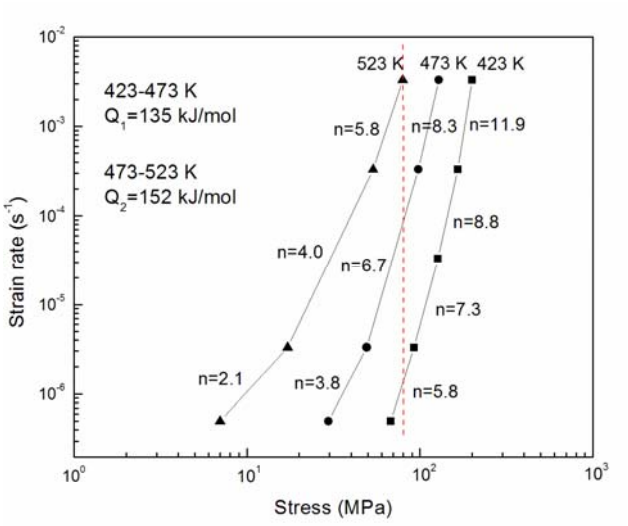

Figure 2. Strain rate vs steady state flow stress for a twin-roll-cast Mg alloy.

Roll Bonding

The process of accumulative roll bonding (ARB) has been applied to wrought Mg alloy AZ31. Accumulative roll bonding results in severe plastic deformation of sheet material. In AZ31, this process leads to the refinement of the microstructure by dynamic recrystallization. The refinement of the microstructure results in an improvement in mechanical properties with the potential for producing materials for superplastic forming. In this work, AZ31 was bonded with up to 64 layers and the potential of roll cladding with aluminum was investigated. The development of microstructure and the mechanical properties are reported in this document.

The conclusions of the paper:

- Successful ARB of AZ31-H24 sheets was achieved by rolling at 400ºC.
- It was possible to roll Mg clad with aluminum alloy 6061.

- ARB results in significant grain refinement by dynamic recrystallization. This refinement of the microstructure leads to significant improvements in the high-temperature ductility (Table 1) and indicates the possibility for this processing route to be used to produce sheet amenable to superplastic forming.

and Prangnell.[1] Samples were deformed in plane strain compression to prescribed strain levels at temperatures high enough to prevent cracking and then were recrystallized. The deformation texture was very similar to that observed after plane strain compression (e.g., rolling) of other Mg alloys, such as common AZ31 (Figure 5). However, the texture can radically evolve during recrystallization. Annealing above the precipitate solvus temperature results in a nearly random recrystallization texture where the initially strong basal texture is completely eliminated. Annealing below the solvus temperature produces a recrystallized texture similar to that of conventional Mg alloys, i.e., a weakened basal texture. If this same material is then annealed above the solvus to promote grain growth, a randomized texture evolves, similar to that of samples simply recrystallized above the solvus. It is hypothesized that a sort of preferred growth mechanism, whereby grains with random orientation grow faster than those with the original basal texture, contributes significantly to the texture randomization observed in wrought Mg alloys containing rare earth elements.

Table 1. Mechanical properties of roll-bonded AZ31

	Condition	Grain size (μ m)	RMT		400°C	
			Elongation (%)	UTS (MPa)	Elongation (%)	UTS (MPa)
AZ31	H24	~10	12.2	294.5	37.9	20.5
ARB1	64 layers	Min. 1	9.0	234.0	137.9	22.6
ARB2	A1'-Mg'-'A1	Mg-5	15.2	199.5	64.8	29.5
ARB3	AZ31-70%	5	21.8	288.0	126.9	21.5

Unlike aluminum alloys, the texture of ARB Mg alloy AZ31 is very similar to the texture of conventional hot-rolled AZ31.

Deep Drawing

The sheet formability of current Mg alloys at ambient temperatures is poor; however, the formability at moderately elevated temperatures can be excellent. Cylindrical cup drawing tests are used to compare the warm forming characteristics of conventional alloy AZ31B with those of alloys containing lithium or yttrium solid solutions. While both types of experimental alloy may have better room temperature ductility (e.g., $\varepsilon_f \sim 25–30\%$) than AZ31B, only the lithium alloy has comparable or better deep drawing capacity. The results are discussed in terms of the sheet anisotropy, and attention is drawn to the fact that Mg alloys exhibit an unusual bending response because of mechanical twinning. The analysis has further shown that the strength of the Mg sheet is sufficient to pull the sheet into the die; however, difficulties reside in the bend/unbend and ironing operations that occur at the radius of the top edge of the die. (See Figures 3 and 4.)

Alloy Development

A Mg alloy modeled after the commercial alloy WE54 was thermomechanically processed and characterized to elucidate the mechanisms by which its texture can be randomized, as reported by Ball

Mechanical Modeling of Forming

O-temper AZ31B Mg sheet was deformed under large-strain tension/compression. The effects of twinning and untwinning, which are responsible for asymmetric yield and hardening evolution, were revealed by metallography, acoustic emission (AE), and texture measurements (Figure 6). Predominant deformation mechanisms were revealed: basal slip for initial tension, twinning for initial compression, and untwinning for tension following compression. A working model consistent with microscopic and macroscopic behavior was constructed.

Figure 3. Effect of temperature on drawing operations.

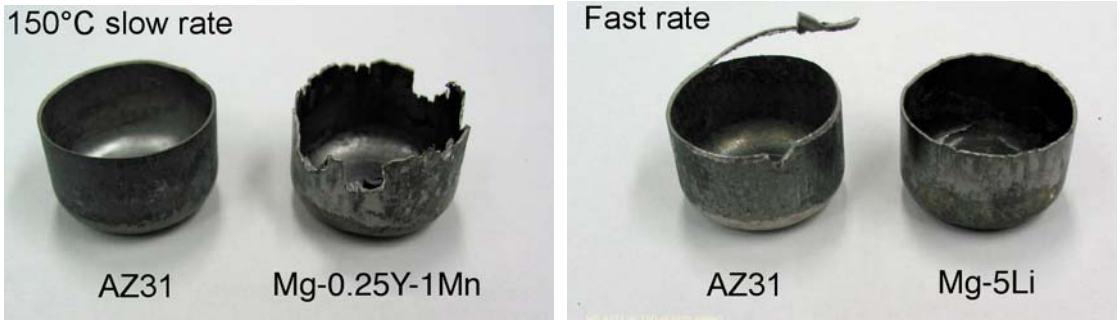

Figure 4. Rate effects on drawing on Mg alloys.

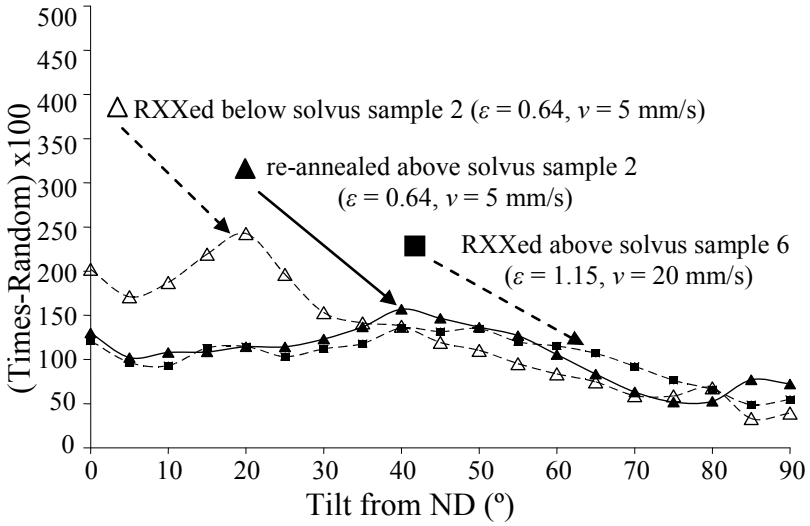

Figure 5. Plot of basal intensity vs tilt showing how texture was eliminated during recrystallization of the $Mg_5Y_3Nd_1Zr$ alloy.

Reference

1. E. A. Ball and P. B. Prangnell, *Scripta Metall. Mater.* **31,** 111–116 (1994) .

New Publications and Presentations

S. X. Song, J. A. Horton, N. J. Kim, and T. G. Nieh, "Deformation Behavior of a Twin-roll-cast Mg-6Zn-0.5Mn-0.3Cu-0.02Zr Alloy at Elevated Temperatures" submitted to *Script Met.*

A. L. Bowles and J. A. Horton, "Accumulative Roll Bonding of Magnesium Alloy AZ31," *CIM-TMS Symposium on Magnesium Technology in the Global Age*, Montreal, Canada, October 1–4, 2006.

S. R. Agnew, J. W. Senn, and J. A. Horton, "Mg Sheet Metal Forming: Lessons Learned from Deep

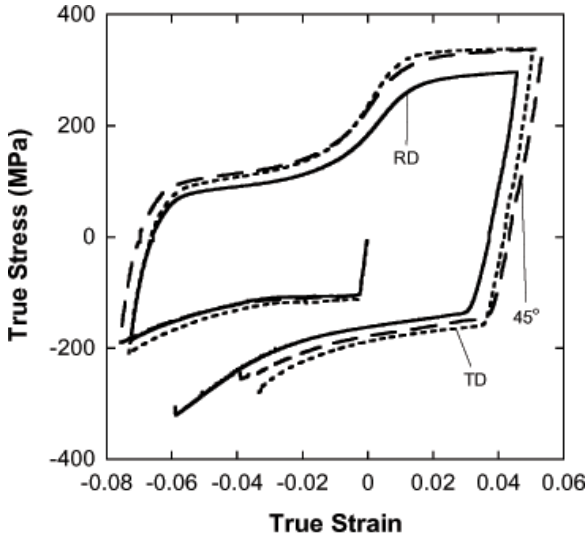

(a) Compression-Tension-Compression (C-T-C)

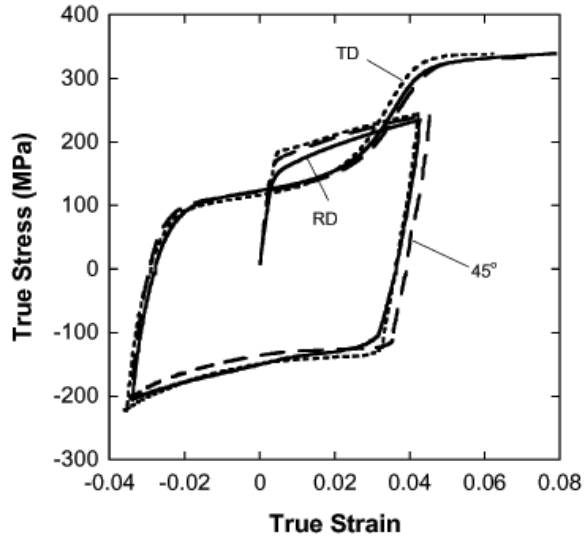

(b) Tension-Compression-Tension (T-C-T)

Figure 6. Large strain tension/compression curves of AZ31 used for forming/springback models.

Drawing Li and Y Solid-Solution Alloys," *JOM* **58**(5), 62–69 (2006).

S. R. Agnew, D. W. Brown, and C. N. Tomé, "Validating a Polycrystal Model for the Elasto-plastic Response of Magnesium Alloy AZ31 Using In-situ Neutron Diffraction," *Acta Materialia* **54**, 4841–4852 (2006).

J. W. Senn and S. R. Agnew, "Texture Randomization during Thermomechanical Processing of a Mg-Y-Nd Alloy," *Proceedings of the Magnesium Technology in the Global Age Symposium*, Montreal, Canada, October 2006.

J. Bohlen, M. R. Nürnberg, J. W. Senn, D. Letzig, and S. R. Agnew, "The Texture and Anisotropy of Magnesium-Zinc-Rare Earth Alloy Sheets," *Acta Mater.*, in press.

X. Y. Lou, M. Li, R. K. Boger, S. R. Agnew, and R. H. Wagoner, "Hardening Evolution of AZ31B Mg Sheet," *Inter. J. Plasticity* **23**, 44–86.6 (2007).

Previously Reported Publications and Presentations

A. L. Bowles, Q. Han, J. A. Horton, "Castability of Magnesium Alloys" pp. 99–104 in *Magnesium Technology 2005,* eds. N. R. Nelameggham, H. I. Kaplan, and B. R. Powell, TMS, 2005.

J. A. Horton, C. A. Blue, T. Muth, A. L. Bowles, S. R. Agnew, "Infrared Processing of Magnesium Wrought Alloys" 155–158 in *Magnesium Technology 2005,* eds. N. R. Neelameggham, H. I. Kaplan, and B. R. Powell, TMS, 2005.

S. R. Agnew and O. Duygulu, "Plastic Anisotropy and the Role of Non-basal Slip in Magnesium Alloy AZ31," *Inter. J. Plasticity* **21**, 1161–1193 (2005).

S. R. Agnew, D. W. Brown, and C. N. Tomé, "Validating a Polycrystal Model for the Elasto-Plastic Response of Magnesium Alloy AZ31 Using In-situ Neutron Diffraction," submitted to *Acta Mater.*

S. R. Agnew, P. Mehrotra, and T. M. Lillo, "Equal Channel Angular Extrusion of a Heat Treatable Magnesium Alloy," *Scripta Mater.*, in revision.

S. R. Agnew, P. Mehrotra, T. M. Lillo, G. M. Stoica, and P. K. Liaw, "Crystallographic Texture Evolution of Three Wrought Magnesium Alloys during Equal Channel Angular Extrusion," *Mat. Sci. Eng. A* **408**, 72–78 (2005).

S. R. Agnew, P. Mehrotra, T. M. Lillo, G. M. Stoica, and P. K. Liaw, "Texture Evolution of Five Wrought Magnesium Alloys during Route A Equal Channel Angular Extrusion: Experiments and Simulations" *Acta Mater.* **53**, 3135–3146 (2005).

D. W. Brown, S. R. Agnew, M. A. M. Bourke, T. M. Holden, S. C. Vogel and C. N. Tomé, "Internal Strain and Texture Evolution during Deformation Twinning in Magnesium," *Mat. Sci. Eng. A*. **399**, 1–12 (2005).

D. W. Brown, S. R. Agnew, S. Abeln, W. Blumenthal, M. A. M. Burke, M. Mataya, C. N. Tome, and S. C. Vogel, "The Role of Texture, Temperature

and Strain-rate in the Activity of Deformation Twinning," *Mat. Sci. Eng. A* **495–497**, 1037–1042 (2005).

A. Jain and S. R. Agnew, "Modeling the Temperature Dependent Effect of Twinning on Mechanical Behavior of Magnesium," in *Tenth Inter. Symp. on the Physics of Materials*, Prague, Czech Republic, August 2005 (in press*, Mat. Sci. Eng. A*)

S. R. Agnew, O. Duygulu, and A. Jain, "Using Polycrystal Plasticity Simulation to Explore the Behavior of Wrought Magnesium Alloys," presented at Plasticity 2005, Kauai, January 2005.

S. R. Agnew, O. Duygulu, and A. Jain, "Developing Mechanism-Based Models of the Mechanical Behavior of Wrought Magnesium Alloys," presented at the University of Michigan Department of MSE Seminar Series, Ann Arbor, Michigan, February 2005.

O. Duygulu and S.R. Agnew, "Grain Size Effects on Deformation Mechanism Activity in Magnesium Alloy AZ31B," presented at the Magnesium Technology 2005 Symposium, TMS Annual Meeting, San Francisco, February 2005.

S. R. Agnew, D. W. Brown, and C. N. Tomé, "Neutron Diffraction Study of Deformation Mechanisms in Magnesium Alloy AZ31B," presented at the Symposium on Neutron Diffraction Characterization of Mechanical Behavior, TMS Annual Meeting, San Francisco, February 2005.

D. Alloy Design and Thermomechanical Processing of a Beta Titanium Alloy for a Heavy Vehicle Application

Principal Investigator: Craig A. Blue
Oak Ridge National Laboratory
Oak Ridge, TN 37831-8063
(865) 574-4351; fax: (865) 574-4357; e-mail: blueca@ornl.gov

Field Project Manager: William H. Peter
Oak Ridge National Laboratory
Oak Ridge, TN 37831-8063
(865) 241-8113; fax: (865) 574-4357; e-mail: peterwh@ornl.gov

Chief Scientist: James J. Eberhardt
(202) 586-9837; fax: (202) 587-2476; e-mail: james.eberhardt@ee.doe.gov
Field Technical Manager: Philip S. Sklad
(865) 574-5069; fax:(865) 574-6098; e-mail: skladps@ornl.gov

Participants:
Edwin H. Kraft, EHK Technologies
Evan K. Ohriner, Oak Ridge National Laboratory
David C. Harper, Oak Ridge National Laboratory
Jim O. Kiggins, Oak Ridge National Laboratory
Donny McInturff, Oak Ridge National Laboratory
Lance Jacobsen, International Titanium Powder, L.L.C.
Bill Ernst, International Titanium Powder, L.L.C.
Dariusz Kogut, International Titanium Powder, L.L.C.
DOE CRADA Partner–Producer of Heavy Vehicle Components

Contractor: Oak Ridge National Laboratory
Contract No.: DE-AC05-00OR22725

Objectives

- Develop a "low cost" beta titanium (Ti) alloy to reduce the weight of a heavy vehicle component, using a low-cost powder developed by the Defense Advanced Research Projects Agency (DARPA) Titanium Initiative or another low-cost Ti powder.
- Investigate blending procedures for elemental or master alloy additions and homogenization (specifically for solid state processing).
- Develop processing parameters for solution treating, rolling, and aging of the new Ti alloy.
- Evaluate microstructure, mechanical behavior, and chemistry of arc-melt and drop castings of new alloy to compare with existing, expensive beta Ti compositions.
- Demonstrate the ability to extrude rod using powder Ti precursor.
- Demonstrate "low-cost" production of beta Ti alloy component.

Approach

- Collaborate with the rest of the DOE team to develop new alloy compositions specifically geared toward DOE heavy vehicle/truck components. Mechanical properties, similar microstructures to existing beta alloys, and cost are the main parameters that will determine the success of the new alloy.
- Cast the new compositions along with conventional compositions compare cast, solution-treated, cold-worked, and aged microstructures. Tensile properties, microstructures, and cost will determine which composition will ultimately be extruded.
- After down-selecting to one composition, extrude blended powders to full consolidation and product form.
- Develop the necessary thermomechanical processing techniques for the desired properties required for end use.
- Ultimately, produce component from new alloy.

Accomplishments

- Extruded CP Ti, Ti-6Al-4V, and other Ti alloys from low-cost ITP powder with comparable mechanical properties, microstructures, and chemistries to ASTM standards.
- Selected two beta Ti alloy compositions for casting.
- Made several arc-melt castings of a new alloy composition and a conventional beta composition for comparison. Performed differential thermal analysis and chemical analysis on the castings.
- Initiated study of preliminary elemental blending of powders and cold consolidation of powder to increase apparent density.
- Redesigned component to take into consideration Ti beta alloy mechanical properties. CRADA partner initiated studying necessary cold work processing steps for optimum mechanical properties using conventional beta alloy.

Future Direction

- Perform monotonic tensile testing and chemistry analysis on additional castings of new alloy compositions.
- Continue to improve blending techniques while limiting oxygen pickup.
- Extrude new Ti beta alloy powder compositions.
- Optimize thermomechanical processing technique required for component.
- Produce beta Ti alloy component.
- Conduct laboratory and vehicle testing of Ti component.

Introduction

The aircraft industry is currently the single largest market for Ti and Ti alloy products primarily because of the exceptional strength-to-weight ratio, elevated temperature performance, and corrosion resistance. The strong dependence of Ti on the aerospace industry has caused Ti production to be very cyclic. Currently, Ti alloy sheet costs are around $40–50/lb, and lead times for product delivery from time of order can be as long as 18 months. Titanium usage outside the aerospace industry has been limited by its higher cost relative to competing materials, primarily aluminum alloys and steels. Although Ti possesses an attractive set of properties—including high specific strength, corrosion resistance, damage tolerance, low Young's modulus, high strength-to-weight ratio, and biocompatibility—its cost limits its applications to selected markets. Many automotive systems would benefit from the use of Ti products. Automotive exhaust systems could save as much as 50% of their current weight by integrating Ti parts.[1,2,3] Titanium valves and valve springs, connecting rods, suspension springs, wheels, drive shafts, underbody panels, side impact

bars, and half shafts are just some of the automotive applications that could benefit from the use of Ti.

A recent market comparison for the use of engineering materials shows that steel is the most widely used material, with 725 million tons used each year.[4] Aluminum, stainless steel, and copper are used at a rate of 20 million tons, 14.5 million tons, and 11 million tons, respectively.[4] Titanium is much less widely used at 0.04 million tons per year.[4] Government studies have shown that Ti enjoys only 1/20th of its potential usage.[5]

Technical problems preventing the integration of Ti, apart from the cost of manufacturing, include wear resistance, a lower modulus than steel, and machining difficulties. Wear resistance can be addressed by coatings, reinforcements, and compositing, as has been shown in preliminary work performed by Blau et al.[6] Low modulus is a benefit in some applications; when required, modulus can be increased by reinforcing the part with a second material. The machining difficulties can be reduced by the production of near-net-shape parts. The major problem is that Ti costs substantially more than competing materials.

Although the cost of Ti ore is significantly more than that of other competing materials, the difference in the cost of sheet, plate, and most other Ti and Ti alloy product forms is a result of secondary processing or milling operations (Figure 1). For example, processing of Ti from ingot to 1-in.plate accounts for 47% of the total cost of the material.[7,8] Thinner plate and sheet gauge sections increase the production costs, the amount of production waste, and the percentage of total production costs.

Current melting techniques include vacuum arc remelting (VAR), electron beam melting, and plasma arc single-melt processes. VAR is used to consolidate feedstocks, improve homogeneity, and refine grain size. To VAR-cast an ingot, a dc arc is struck between a Ti electrode and a base plate. The intense heat melts the electrode, and the Ti is cast into an ingot. VAR requires 20 hours and large-scale equipment.

Electron beam and plasma arc single-melt processes have the advantage over VAR in increased use of low-cost scrap and improved removal of high-density and low-density inclusions. In these two

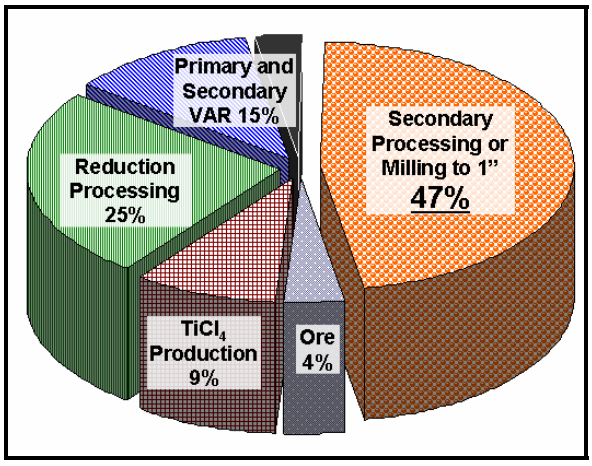

Figure 1. Breakdown of cost in the production of 1-in. CP Ti plate.

processes, ingots are cast directly from melted feed sponge, alloy additions and scrap. But the cast ingot still requires post-processing, which accounts for 47% of the total cost.[7,8]

Although much time and effort has been invested in the development of these processing techniques, the cost of Ti still remains high because of yield losses and the cost of raw materials and post-processing. In an ongoing effort to reduce the cost of Ti and Ti alloy production, Oak Ridge National Laboratory (ORNL) has investigated new solid state and melt technologies in producing plate, sheet, and rod. Vacuum hot pressing (VHP), high-density infrared (HDI) processing, roll compaction, and extrusions have been explored at ORNL (Figure 2).[3,9] These methods used DARPA Titanium Initiative "low-cost" powders produced by the Armstrong method and provided by International Titanium Powder (ITP). ITP has produced CP Ti and Ti alloys in its pilot processing facility and has initiated the development of a full-scale production plant to produce CP Ti and Ti alloy powders. Consolidation studies are required to produce consolidated components, parts, and material.

This annual progress report discusses recent studies to develop a low-cost beta Ti alloy for a heavy vehicle component. This work is performed with a vehicle component manufacturer that currently produces the targeted component from steel. The producer has seen the value added by potentially replacing the component with a Ti alloy if

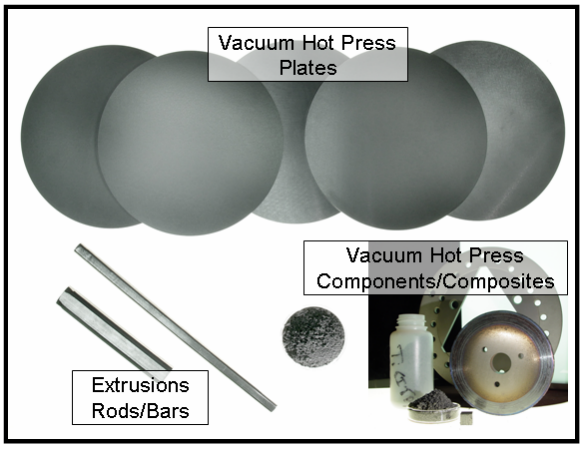

Figure 2. Various product forms of consolidated ITP CP Ti and Ti alloy powder resulting from manufacturing process development at ORNL.

production costs can be minimized. ORNL is collaborating with this company to determine a new alloy composition, lower in price than current aerospace Ti alloy compositions, that is geared toward the mechanical properties of the component. Arc-melted drop castings are produced of the new compositions to evaluate the mechanical characteristics compared with existing expensive compositions. ORNL will then develop a material processing technology that successfully consolidates blended powder, produces the necessary characteristics, and reduces the cost of current Ti production mill processing.

Experimental Procedure

The present scope of work was performed within four tasks: 1, component design; 2, economical modeling; 3, alloy design and verification; and 4, process development. Each task was designed with the ultimate goal of producing a beta Ti alloy component that reduced the weight of a heavy truck component. For ease of discussion, the experimental procedure and the results will be subdivided into the four tasks.

Task 1: Component Design

The identity of the component selected for this CRADA is proprietary. However, certain mechanical/structural considerations had to be taken into account to redesign the component so that a Ti alloy could be successfully implemented. Component design was performed by the CRADA partner, with ORNL providing information on the potential processing routes and thermomechanical history that could influence the resulting product form and component design.

Task 2: Economic Model

A preliminary economic model was constructed based on a "greenfield" production approach. Specific economics were taken into account include labor, price of the Ti powder, price of elemental alloying powders, thermomechanical processing costs, machining, capital costs, and post-aging processing. The model has been modified as the processing development matures. The resulting economic model will be comprehensive.

Task 3: Alloy Design and Verification

The selected component would best use an alloy with the beta (body centered cubic) crystal structure. Beta alloys are normally composed of beta grains with precipitates of the alpha (hexagonal close-packed) phase within the beta grains and at grain boundaries. The application of the selected component will operate at ambient temperatures, so there is no need to provide high-temperature strength, creep resistance, or enhanced oxidation resistance; but Ti corrosion resistance is a benefit. One priority objective of the alloy design is the achievement of a comparable low-cost alloy. Many of the conventional commercial alloys contain significant levels of expensive alloy additions. Since the CRADA project uses powder processing rather than melt metallurgy, issues of melt segregation of elements, such as iron, are not of concern. Therefore, lower-cost beta stabilizing elements can be used in the design of the composition for the heavy vehicle component.

A method of alloy design was used that takes advantage of established tendencies of various elements to stabilize the alpha or beta phases in comparison with the benchmark elements molybdenum (Mo) (beta stabilizer) and aluminum (Al) (alpha stabilizer); these tendencies are known as the Mo equivalence or Al equivalence of each element. A beta stability index for an alloy is then calculated as the sum of the Mo equivalences of all its beta stabilizing constituents, minus the sum of the Al equiva-

lences of all its alpha stabilizing constituents; this is the Mo–Al equivalence. This index was calculated for many commercial beta alloys and for numerous candidate compositions that would contain low levels of expensive elements and could use inexpensive master alloy powders.

One primary and two secondary compositions were selected for further investigation. Transformation diagrams were determined by computer simulation for these three compositions. The primary composition and a conventional beta Ti composition were then arc-melted and drop cast to provide material for preliminary processing. The intense heat of the arc was used to melt the Ti and other constituent elements of the alloy. Elements were thoroughly mixed in a copper crucible and turned over four to five times between arc-melting operations to improve homogeneity. Once mixed, the alloy button was cast in a water-cooled ½×½×3 in. copper mold. Chemical analysis was performed on the Ti alloy ingots, inert gas fusion was used to determine oxygen and nitrogen weight percentages (ASTM E 1409-05), and metal elements were analyzed using direct current plasma emission spectroscopy (ASTM E 1097-03). Micrographs were made of the as-cast microstructure. Small samples (20 to 50 mg) were cut from the castings to perform differential thermal analysis (DTA) measurements using a SDT Q600 from TA Instruments. A heating rate of 20°C/min was used, and the sample was allowed to go a full cycle. A CP Ti sample cast from low-cost ITP Ti was analyzed for comparison. DTA analysis was performed to identify the beta transus.

Task 4: Process Development

A solid state or powder metallurgy processing technique that takes advantage of the new low-cost Ti powders is the objective. The blending of elemental or master alloy powders to form the desired alloy, extrusion parameters and methodology, solution treating temperatures and time intervals, rolling conditions, aging temperature and time intervals, and post-aging conditioning are all thermomechanical variables that must be developed and identified for the realization of the heavy vehicle Ti alloy component. However, identifying these parameters on extruded samples of blended powders initially would be costly and time-prohibitive. Therefore, preliminary solution treating (ST), cold rolling (CR), and aging (A) processes are being performed on drop castings to evaluate the candidate alloys in the required processed state, since cast microstructures will not provide the necessary mechanical properties for the application. Once an alloy composition exhibits the required microstructures, economics, and mechanical properties, extrusions of the alloy will be initiated and thermomechanical processing parameters will be refined for the extruded condition. Process development is being performed in four individual efforts to rapidly develop the processing technology. The four stages include blending of elemental powders (performed at ORNL); extrusion of low-cost Ti powders (performed at ORNL); development of ST, CR, and A (performed at ORNL); and post-aging conditioning of the component (performed at the CRADA partner's facilities). Procedures are identified for blending of elemental powders and development of ST, CR, and A procedures in the following paragraphs. The extrusion procedures for low-cost Ti powder were discussed in the FY 2005 Annual Progress Report.[9] Post-aging conditioning is proprietary to the CRADA partner and will not be discussed.

Blending of elemental powders

The blending of powders to establish the alloy was performed using ITP Ti powder synthesized by the Armstrong process and elemental alloying powders. The alloying powders were not of high purity for the first trials performed in this fiscal year. The initial objective was to blend the powders using attrition methods and observe the degree of mixing or homogenization that occurs. The secondary objective will be to minimize the level of oxygen pickup during blending operations. Once homogenization has been verified, high-purity powders will be used. Two batches of Ti powder with elemental alloying powders were milled, around 128 g for each batch. One batch was dry milled, and the other was wet milled in ethanol to see if one method enabled greater proficiency than the other. A zirconia media at a ball-to-powder weight ratio of 14 to 1 was used to blend the alloy and attrite the ITP Ti powder particles. Milling was performed for 4 hours. The dry-milled bottle was pumped out and backfilled two times with argon. The milling rate was around

100 rps in a 1-L high-density polyethylene container. The material milled in ethanol was dried at 60°C overnight and then oblique blended for 1 h to mix up the powder after settling during the drying process. The blended powders were then compressed into 1.7-cm-diam disks, 3–6 mm thick, at a pressure of 20,000 psi in air. In a similar cold compression process, ITP CP Ti powder, without alloying elements and without milling operations, was also pressed at various pressures to assess compaction versus pressure trends for the ITP powder morphology. The results will later help to develop the pressures required to consolidate powder into cans for extrusion. (The CP Ti powder will have lower densities per a given pressure than a milled and blended powder, but it will provide minimal pressure requirements to obtain desired cross sections in the extruded condition).

Scanning electron microscopy (SEM) and energy-dispersive X-ray (EDX) mapping were performed on the compressed alloy samples to observe homogeneity. Chemical analysis was also performed to assess the accuracy of the chemical composition; inert gas fusion was used to determine oxygen and nitrogen weight percentages (ASTM E 1409-05); and metal elements were analyzed using direct current plasma emission spectroscopy (ASTM E 1097-03).

Development of ST, CR, and A procedures

Development of ST, CR, and A procedures is critical for the resulting mechanical properties of a Ti alloy component. The primary developed alloy and the conventional beta Ti alloy were both studied. ST of the as-drop-cast ingots was performed in a small circular halogen/T3 infrared furnace for 0.5 to 1 h at temperatures above the beta transus in ultra-high-purity argon atmosphere. CR was performed on a 4-high WC roll mill. Multiple passes were performed on the ST samples; 3–5% reductions were taken on every pass. Total CR reductions were up to 50%. Aging was performed in a tungsten-element, vacuum furnace at moderate temperatures for 4 to 30 h. Macro and micro hardness values were measured throughout the processing of both compositions. Hardness values and microstructures were compared.

Results and Discussion

Task 1: Component Design

Initial design of this component in Ti was completed. It was selected to replace a steel vehicle component for a weight savings of 40%, including allowance for the geometric changes required to provide equal mechanical performance. The component is of a bar shape amenable to extrusion, which was selected as the primary process, as well as alternative process methods.

Task 2: Economic Model

A preliminary greenfield model was produced for production of the Ti alloy component. However, after thorough discussion among all parties at the annual review meeting, the approach was modified to focus on the use of existing commercial operations wherever possible. Restructuring of the model to accommodate this change began, and an effort also began to identify potential facilities to use in volume production. A synergistic approach is required for the realization of the Ti component and the economic model, since economics are of primary importance, new production capabilities are continuing to evolve, and Ti solid state processing is a new and rapidly expanding field. The economic model will continue to develop as process development continues.

Task 3: Alloy Design and Verification

As previously indicated, a primary low-cost composition was selected for initial development. The low-cost composition and the conventional beta Ti alloy were first cast into buttons and then successfully drop cast into square cross-sectioned ingots. At least three ingots were produced for each composition. Figure 3 shows a button and drop casting of the new composition, a micrograph of the new composition, and a micrograph of the conventional composition.

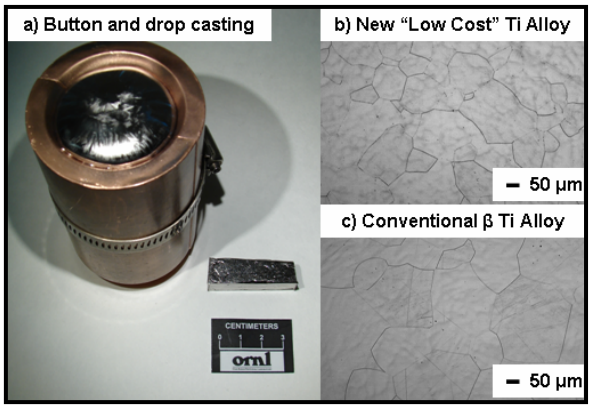

Figure 3. Composite image of (a) button and drop cast ingot, (b) optical micrograph of the new composition, and (c) optical micrograph of conventional beta Ti alloy processed in a similar manner.

The drop cast ingot and button of the conventional beta alloy and the new alloy were similar in color and appearance. The micrographs exhibited equiaxed grains, with the new composition having a similar appearance to the conventional composition. The chemical analysis results were very good for preliminary trials. The conventional alloy contained one alloying element that was off by 1 wt %, and the Ti composition was slightly high. The developed composition was closer to target with alloying elements within 0.3 wt =% of target values. Interstitial elements (e.g., oxygen, nitrogen) were very low for both compositions. The hardness of the as-cast ingots was the only significant difference observed between the two alloys; the hardness value of the new alloy was approximately 40% greater than that of the conventional alloy. The increase in hardness seemed to be based solely on the metal alloying additions, as the oxygen and nitrogen content of both sets of ingots was extremely low. Future castings will use cold-pressed ITP CP Ti powder pellets, as initial castings with pure Ti from an outside source had oxygen values much lower than required. Additionally, a third composition that may eliminate requirements for a powder blending procedure will be investigated.

Task 4: Process Development

Blending of elemental powders

Initial blending efforts focused on the required procedures to homogenize the powders. Preliminary chemical homogenization results were promising; SEM and EDX results exhibited relatively good uniformity to around 50 to 100 µm. Several of the initial powder particles were larger than optimal; this is the main reason chemical uniformity was not observed below 50 µm. However, fine alloying element powder particles exhibited good blending at even very low scales, as can be seen in Figure 4. The chemical analysis results were within 0.6 wt % for each alloying element. Oxygen and nitrogen values were high in the partially consolidated blended powders; this may be a result of initially high oxygen levels in the alloying powders used and oxidation during the ball milling process. Values of zirconium, from the zirconia ball media, were below traceable values in the chemical analysis results.

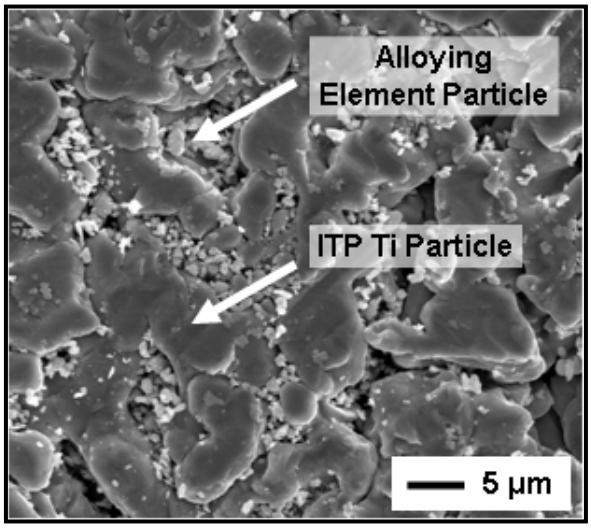

Figure 4. SEM of partially consolidated blended alloy. Fine alloy powder particles were well distributed through ITP Ti particles.

Extrusion procedures

Extrusions for various sizes, shapes, pressures, and compositions have been previously reported. Fully dense, as-extruded samples have exhibited mechanical, chemical, and metallurgical properties similar to those of wrought Ti products. Photos, micrographs, and the resulting mechanical properties are provided in Figure 5.

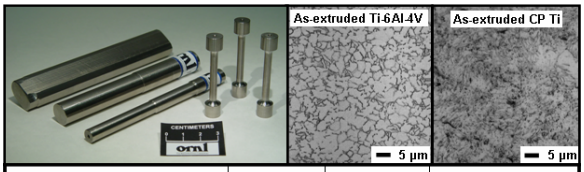

Sample	YS [MPa]	UTS [MPa]	Ductility [%]
As-Extruded Armstrong Ti	407	552	17.0
Ti Grade 2	345	448	20.0
Extruded Ti-6Al-4V	**Insufficient Material:** *Insufficient Ti-6Al-4V material was extruded to provide mechanical results.*		

Figure 5. Photos of CP Ti after removing can and machined into round tensile bars, with mechanical results and micrographs of extruded bars and flat stock.

The next major step in the extrusion process development is the extrusion of the blended alloy powder; this cannot be performed until the blending technique is optimized. However, developing methodologies to increase the tap density of the low-cost Ti powder is an issue that directly influences the possible size of resulting extrusions and is presently under investigation. In FY 2006, cold press consolidation pressures were compared with the resulting apparent densities. Previously, ITP powder was cold pressed in the extrusion can to ~20% of theoretical density. Higher pressures are required to extrude larger cross sections. Figure 6 is a graph illustrating low pressures and the resulting densities; this information will be used in the extrusion of the beta Ti alloys for component fabrication.

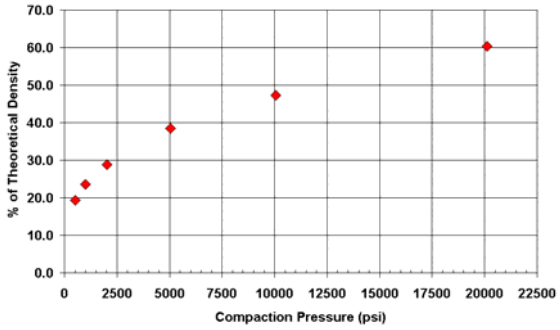

Figure 6. Graph illustrating the resulting density when various compaction pressures are applied to ITP Ti powder in a steel die with lubricated walls.

Development of ST, CR, and A procedures

Castings of the new alloys have made it possible to begin the thermomechanical process development required for the desired mechanical properties prior to extrusion of the blended powders. Therefore, ST, CR, and A procedures were initiated. However, the main intent of the preliminary thermomechanical processing at this stage is to allow for proper alloy selection. Preliminary work was performed mainly on the arc melt castings of the conventional alloy and compared with VAR-melted samples prepared from an outside commercial source using conventional techniques. The new alloy will be processed similarly to the conventional material using the beta transus, acquired from DTA results, as a reference temperature. CR of the cast, conventional alloy was performed; a total reduction of 50% after multiple passes was possible. The cast and ST new alloy will be compared with this amount of cold work. However, the new composition is harder than the conventional alloy, and the total CR reduction may not need to be at 50%. Figure 7 shows the conventional alloy during and after processing with microstructures of the cast material compared with conventional VAR material.

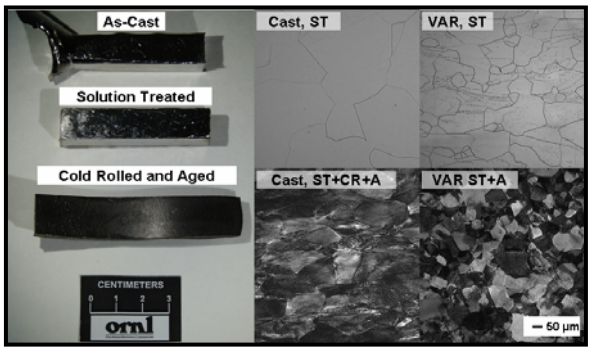

Figure 7. Image of the ORNL conventional alloy as-cast, ST, and CR/A (left) with microstructures of the ST and ST+CR/A conditions (center). For comparison, micrographs of a commercially produced VAR sample are included (right).

Post-aging procedures and development of the component

The CRADA partner performed preliminary final processing on commercial beta C plate material

to begin understanding the effect of this processing on properties. The details of this processing are proprietary. However, the effort resulted in a basic understanding of the relative effect of several process parameters on some critical material properties. These data will be useful in specifying these process parameters for powder-processed material of the finally selected composition.

The CRADA partner also performed aging studies to begin an understanding of the effect of aging time and temperature on properties. Rockwell C hardness was measured after various aging times at four aging temperatures. Yield strength and hardness were then measured for two of the most promising aging conditions.

All partners in this project have also participated in gathering data and literature on the processing, heat treatment, and properties of various beta alloys for use in designing thermomechanical processing and heat treatment of the powder processed alloys.

Summary

The following are highlights of progress in FY 2006.

1. Extrusion of CP Ti, Ti-6Al-4V, and other Ti alloy was performed in the production of rods, bars, and flat stock.
2. A primary alloy composition was developed.
3. An economic model was initiated.
4. Castings of a primary low-cost composition and a conventional alloy for comparison were fabricated. Subsequent ST, CR, and A process development was initiated with promising preliminary results.
5. Blending technique development was initiated.
6. Post-aging procedures are being developed at the CRADA partner's organization.

Conclusions

Although Ti and Ti-6Al-4V have attractive properties that would benefit a great number of engineering applications, their use is limited by the cost of the raw material and the processing necessary to make a usable product. But with recent advancements in low-cost powder production at ITP, in conjunction with processing techniques developed at ORNL in collaboration with industry, the cost of Ti and Ti alloy products could be drastically reduced. Previous extrusions have proved the feasibility of using low-cost powder in new, innovative markets. The preliminary study of CP-Ti extrusions seems to produce mechanical properties similar to those of cast Ti. New alloys have been targeted that could lower the cost of Ti alloys, enabling this class of material to enter new markets. Preliminary arc melt castings have shown promising microstructures and results, and alloy blending practices for the new powders are well under way. Further processing development will lead to new low-cost Ti alloy components for heavy vehicle usage.

References

1. K. Faller and F. H. Froes. "The Use of Titanium in Family Automobiles: Current Trends," *JOM* **53**(4), 27–28 (2001) .
2. F. Froes et al. "Titanium in the Family Automobile: The Cost Challenge," *JOM* **56(**2), 40–44 (2004).
3. J. Rivard et al. "The Thermomechanical Processing of Titanium and Ti-6Al-4V Thin Gage Sheet and Plate," *JOM* **57**(11), 58–61 (2005).
4. J. Kraft, *Summary of Emerging Titanium Cost Reduction Technologies: A Study Performed For U.S. Department of Energy and Oak Ridge National Laboratory*, Subcontract 4000023694, Department of Energy, 2004.
5. B. Hurless et al. "Lowering the Cost of Titanium," *The AMPTIAC Quarterly* **6**(2), 3–9 (2002).
6. P. Blau et al. "Tribological Investigation of Titanium-Based Materials for Brakes," submitted for review.
7. A. Hartman et al., *JOM* **50(**9), 19 (1998).
8. H. Friedrich et al., "Titanium in Automotive Applications—Nightmare, Vision, or Reality," pp. 3393–3402 in *Proceedings, 10th World Conference on Titanium,* ed. G. Lutjering, Weinheim, Germany, Wiley-VCH, 2003.

9. U.S. Department of Energy, *FY 2005 Progress Report for High Strength Weight Reduction Materials*, Office of Energy Efficiency and Renewable Energy, DOE, Washington, D.C., 2006.

E. Durability of Titanium Chassis Components

Principal Investigator: P. J. Blau
Oak Ridge National Laboratory
P.O. Box 2008, Oak Ridge, TN 37831-6063
(865) 574-5377; fax: (865) 574-6918; e-mail:blaupj@ornl.gov

Technology Development Area Specialist: James J. Eberhardt
(202)586-9837; fax: (202)587-2476; e-mail: james.eberhardt@ee.doe.gov
Field Technical Manager: Philip S. Sklad
(865) 574-5069; fax: (865) 574-6098; e-mail: skladps@ornl.gov

---

Contractor: Oak Ridge National Laboratory
Contract No.: DE-AC05-00OR22725

Objectives

- Investigate and develop technology for enhancing the surface durability of titanium (Ti) alloy components, which will, in turn, enable their use in lightweight vehicles.

Approach

- Design and build a system to simulate road-vibration–induced fretting damage in Ti chassis components such as leaf springs.
- Design and conduct experiments that simulate the kinds of random loads to which springs and fasteners are subjected when a vehicle operates.
- Quantify the fretting damage and identify surface engineering treatments that can be applied to mitigate that damage.
- Determine the effects of load, oscillation amplitude, and joint configuration on the fretting response of candidate surface engineering treatments.
- Provide guidelines to designers of lightweight chassis components regarding engineering solutions to address contact damage that can arise when Ti parts are used in wear-critical locations.
- Establish the relationships between the method of machining Ti parts and their resistance to contact damage.

Accomplishments

- Designed and built fixtures on which to conduct fretting tests of flat strips of Ti alloys in a configuration representative of leaf springs.
- Conducted preliminary experiments to develop an understanding of the kinds of damage that can be produced on Ti using the new apparatus.
- Conducted a literature review of fretting-prevention treatments developed for aerospace Ti alloys. The information will be used to devise similar approaches for increasing the durability of Ti chassis components.

Future Direction

- After verifying the characteristics of the testing fixtures and selected protocols, complete baseline studies of untreated Ti alloys to provide a basis on which to compare the relative effectiveness of selected fretting-prevention methods.
- Use Oak Ridge National Laboratory (ORNL) cumulative dissipated energy analyses, developed for fatigue testing, to assess the relationship between the frictional energy dissipated during fretting contact and the degree of damage produced by random-spectrum loading.
- Evaluate the potential for ORNL-developed oxygen thermal-diffusion treatments in reducing or eliminating fretting damage.
- Prepare Ti surfaces by common industrial machining processes and determine the extent to which the artifacts left by those processes can affect the durability of Ti chassis components, both surface treated and untreated.

Introduction

Compared with other lightweight alloys, such as those based on aluminum and magnesium, Ti alloys have higher strength and much greater resistance to the effects of elevated temperatures, sustained loads ("creep"), and corrosion. While not as low in density as aluminum and magnesium alloys, Ti can provide significant lightweighting for fuel-efficient automobiles, trucks, and trailers while offering durability and corrosion resistance as well.

Recent breakthroughs in primary Ti processing and low-cost powder production methods promise to reduce material cost. Therefore, the potential exists to expand the alloys' applications beyond aerospace and into components for ground transportation. Designers of truck and automotive chassis parts such as leaf springs have not considered Ti as a viable candidate in the past largely because of its cost, but as new processing methods bring the price down, it becomes important to establish the technology base needed to support the broader use of Ti alloys.

The goal of this new project is to investigate and develop technology for enhancing the surface durability of Ti components, which will, in turn, expand their applications in lightweight vehicles. While there are a number of areas that could be addressed, the present effort focuses on measuring the resistance of Ti alloys to fretting damage, as might be experienced in Ti leaf springs and mechanical fasteners. Leveraging past work by aerospace engineers, the current approach is to use state-of-the-art surface engineering tools to reduce that damage and demonstrate their feasibility. The results of this work are expected to apply both to the performance of Ti-based components in service and to the manufacturing of Ti parts.

Approach

Fretting is short-amplitude oscillatory motion that results in the generation of minute wear particles. The cumulative effects of fretting damage include the loosening of joints and the initiation of fatigue cracks that can eventually lead to catastrophic failures. There are a number of possible approaches to fretting damage remediation, depending on the kind of mechanical configuration to which the materials are exposed. The approaches include (1) tightening the clamp load on the joint to stop vibration, (2) reducing the load to lower the contact pressure on the mating surfaces, (3) lubricating the contact to lower the shear forces on the surfaces, and (4) substituting more fretting-resistant materials or surface treatments.

Historically, most fretting test apparatuses used in fundamental research either use small pads clamped on the sides of a flat tensile specimen in a fatigue machine or a small sphere of hard material oscillating against a flat coupon. Neither of these configurations simulates the fretting of flat strips against one another, as might be present in leaf springs; therefore, a new test configuration was required.

Once the fixtures were designed and machined, it was necessary to characterize the test method itself and to determine how best to quantify the fretting resistance of selected surface treatments for Ti. The next step was to acquire baseline data against which the effectiveness of the surface treatments will be judged. Work in FY 2006 was therefore focused on preparing the testing equipment and conducting preliminary experiments to establish a testing protocol.

Progress

A flexible test configuration was designed so that several possible fretting geometries could be tested using slight variations of the same system. The basic fixture arrangement is shown in Figure 1. The upper and lower components use attachment hardware that is compatible with servo-hydraulically actuated mechanical testing systems at ORNL. Figure 1 shows a cylindrical upper specimen (viewed end-on) and a cantilevered lower sheet specimen below it. Repetitive vertical displacement of the lower specimen causes fretting to occur on the surfaces of both top and bottom specimens. The relative amount of fretting depends on the applied conditions and whether the mating materials are the same or dissimilar.

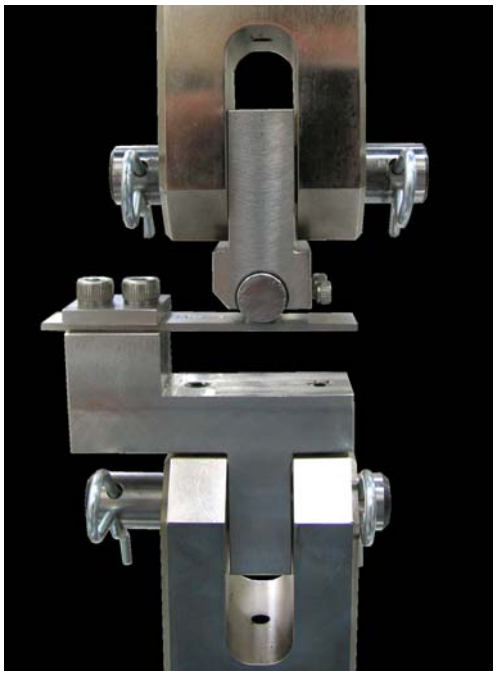

Figure 1. This cylinder-on-flat fretting configuration was designed to fit existing fatigue testing frames. The cylinder specimen diameter is 9.53 mm.

In addition to the cylinder-on-flat contact geometry shown in Figure 1, additional contact configurations shown in Figure 2 are under consideration. These will enable the configuration to simulate either multiple-layer springs or pad-on-sheet configurations that can also occur in various chassis locations, such as leaf spring supports.

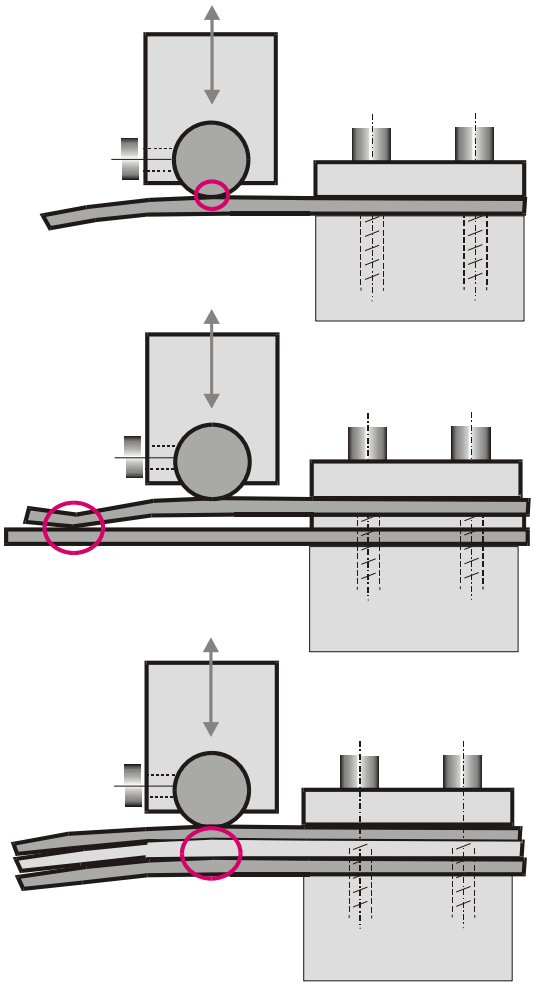

Figure 2. Three fretting configurations that can use the fixture shown in Figure 1. Top: cylinder-on-flat sheet. Center: curved sheet-on-flat sheet. Bottom: laminar stack of flat sheets.

Initial studies used both tool steel and Ti as the upper cylindrical specimens to fret against Ti-6Al-4V sheet specimens. An optical photomicrograph of a sheet specimen (Figure 3), subjected to three million cycles against a Ti cylinder, shows features that are characteristic of oscillatory damage. These include abrasion grooves and localized accumulations of oxidized debris particles. After the standard testing protocol is established, the kinds of damage features will be categorized by optical and scanning electron microscopy, along with the composition of the debris particles.

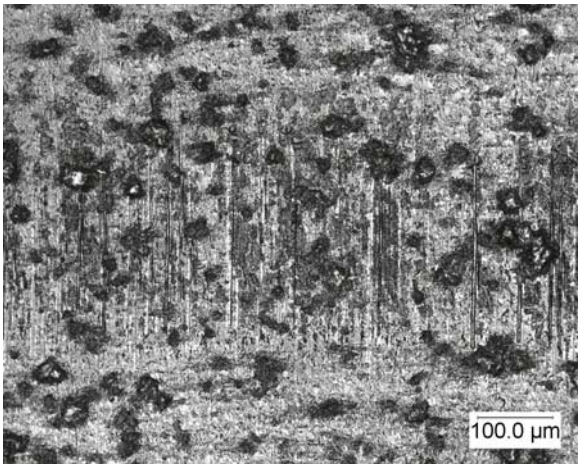

Figure 3. Optical photomicrograph of the fretting surface of a Ti sheet specimen that sustained 3,000,000 cycles. The sliding direction was vertical and the amplitude of sliding was approximately 300 µm.

The spectrum of vibrations to which an on-road vehicle is subjected depends on its weight and suspension design, its vehicle operating profile, and the condition of the tires and road surfaces. Fretting damage can occur in different ways, depending on the interface geometry of the mating parts and the loading conditions. A special software program, developed by Don Erdman of ORNL, produces a random loading spectrum and enables load and displacement data to be obtained. This software will be used to simulate road-induced loading spectra while collecting data on the cumulative energy expended during fretting contact.

After millions of cycles of contact have been applied to the specimens, the resulting surface damage will be correlated with the energy used to create it. Once baseline data are established for untreated Ti alloys, selected surface treatments will be applied to the specimens and the results compared with the baseline. These surface treatments are planned to include a novel diffusion treatment being developed by Jun Qu of ORNL. The objective of this aspect of the work is to identify the most cost-effective treatments that can be used to reduce contact damage on Ti components and share that information with manufacturers who are interested in developing lightweight chassis components.

Effects of Surface Grinding on Durability

The durability of surfaces can be affected not only by their surface finish but also by the machining and finishing processes used to create them. Machining can produce work-hardening of metal surfaces, leave residual stresses in the subsurface regions, and introduce a degree of directionality (texture) to the microstructure that in turn may affect its resistance to contact damage. Therefore, a study of the effects of machining damage on the fretting and wear resistance of Ti surfaces is planned to supplement this effort.

Future Plans

During the coming months, the fretting test protocol and method of quantifying the extent of surface damage will be standardized. Then baseline tests of Ti alloys will be conducted. Surface treatment and coating methods will be selected and test coupons will be obtained. Finally, a study of the effects of grinding conditions on the durability of Ti alloy surfaces will be initiated.

Conclusions

Application of lightweight Ti alloys for chassis components such as leaf springs can be accelerated by using what has been learned from prior aerospace research and development efforts. Multi-configuration fixtures have been prepared, and software to conduct and analyze spectrum loading fretting wear tests has been obtained. Baseline test protocols are being established, and a list of promising candidate surface treatments, including one developed at ORNL, is being prepared.

4. ENABLING TECHNOLOGIES

A. Joining of Advanced Materials by Plastic Deformation

Principal Investigator: J. L. Routbort (co-workers: D. Singh, Cinta Lorenzo-Martin, and G. Chen)
Argonne National Laboratory
9700 S. Cass Avenue, Argonne, IL 60439-4838
630-252-5065 routbort@anl.gov

Chief Scientist: James J. Eberhardt
(202) 586-9837; fax: (202) 587-2476; e-mail: james.eberhardt@ee.doe.gov
Field Technical Manager: Philip S. Sklad
(865) 574-5069; fax: (865) 574-6098; e-mail: skladps@ornl.gov

Contractor: Argonne National Laboratory
Contract No.: W-31-109-Eng-38

Objective

- Join advanced materials such as ceramics, cermets, intermetallics, composites, and biomaterials by plastic deformation and collaborate with industry and universities to produce sensors.
- Investigate grain rotation that is assumed to occur during grain–boundary sliding (GBS), resulting in deformation bonding.

Approach

- Apply a modest compressive load to two pieces of similar or dissimilar materials that have had little surface preparation in the temperature region where the materials are known to deform by grain-boundary sliding.
- Measure the strength of the interface by 4-point bend tests and compare the results with theory.
- Use electron back-scattered diffraction to measure grain rotation as a function of strain.
- Prepare for in-situ Advanced Photon Source (APS) experiment to measure grain rotation during deformation.

Accomplishments

- Made strong, pore-free joints with various ceramics, cermets, intermetallics, composites, and more recently, biomaterials, with and without various interlayers. Fracture occurs away from interface.
- Published 18 journal papers, obtained patent for plastic joining process, filed patent applications for oxygen sensor and joining of advanced materials.
- Won R&D 100 Award for oxygen sensor.

Future Direction

- Join metals and intermetallics to ceramics for solid-oxide fuel cell applications.
- Complete installation of equipment in beamline to use the Advanced Photon Source to measure grain rotation during deformation. We are currently using various routes to produce dense, fine-grained ceramics to deform ex-and in-situ.

Foreword

Progress on this work has not been as rapid as anticipated as a result of decreased funding, the complexities of designing an in-situ experiment to measure grain rotation during deformation of a ceramic at the APS, and repairs on a 30-year old Instron with a high-temperature furnace. However, the MTS machine for the APS has been purchased and is on site, grips are being designed, and the X-ray absorption of a model ceramic has been measured. It was determined that we can use a sample of 5-mm thickness. Preparations to produce a dense, fine-grained NaCl sample continue. These samples will be deformed to determine that GBS occurs, and then deformed in-situ at the APS while the change of grain orientation is measured using diffraction techniques as described in previous annual reports.

The following discussion is taken from a keynote lecture presented at the conference Mechanical Properties in Advanced Materials: Recent Insights, Fuenteheridos, Spain, June 7–11, 2006, to be published in the *Journal of the European Ceramic Society*. It forms the preliminary study for the in-situ experiment at the APS scheduled for Fall 2006.

Introduction

Study of the high-temperature deformation behavior of polycrystalline ceramics is important from several perspectives: (1) high-temperature structural applications of the ceramic,[1] (2) fabrication of the ceramics with improved properties,[1–3] and recently, (3) joining of polycrystalline ceramics by the plastic deformation process.[4–6] In general, high-temperature deformation of polycrystalline ceramic materials, with equiaxed grains, is controlled by a diffusion-controlled GBS mechanism.[7,8] It is expected that if there is no cavitation and no change in grain shape, then the grains must rotate to accommodate the deformation strains.[9]

Understanding grain rotation phenomena during high-temperature deformation has implications for the processing of ceramic materials with enhanced mechanical properties, as well as for the joining of ceramics. It is possible that minimizing GBS and rotation could enhance the creep resistance properties of a material. Recently, it has been demonstrated that various ceramics and intermetallics can be joined by high-temperature plastic deformation that results in interfaces that are indistinguishable from the bulk material.[4–6,8,10] This joining technique operates by interpenetration of grains at joining surfaces as a result of GBS and grain rotation. There are no known experimental studies that have quantified grain rotation in polycrystalline ceramics as a function of deformation strains. Thus a high-temperature deformation study has been conducted on a model material, strontium titanate ($SrTiO_3$). Dense polycrystalline $SrTiO_3$ can be fabricated with relative ease and is easily deformed.

Polycrystalline perovskite materials such as $BaTiO_3$ and $SrTiO_3$ are suitable for applications as capacitor materials because of their ferroelectric behavior.[11] Moreover, the Earth's lower mantle is primarily composed of perovskite (Mg, Fe)SiO_3 and understanding of its plastic deformation behavior is important.[12] High-temperature deformation behavior of $BaTiO_3$ has been extensively studied. Park et al.[13] conducted a high-temperature (1200–1300°C) compressive deformation study on polycrystalline $BaTiO_3$ with fairly large grain sizes ranging from 19–52 μm. Their data indicated a stress exponent of 1 and activation energy of 720 kJ/mol. Moreover, Park et al. concluded that the dominant deformation mechanism was GBS assisted by lattice cation diffusion. Fine-grained (0.45 μm) $BaTiO_3$ deformed superplastically between 1150 and 1250°C with an activation energy of 800–1200 kJ/mol.[14]

High-temperature deformation literature data for SrTiO3 are fairly limited, and most of the studies are conducted on single crystals. Using compressive tests on SrTiO3 single crystals between 1200 and 1520°C, Wang et al.[12] showed power-law creep behaviour in $SrTiO_3$ for samples compressed in the <100> and <110> directions. Creep along the <110> direction was much easier than along the <100> direction. The stress exponent (n) was ≈3.5 and activation energy (Q) ranged from 620 kJ/mol for the <110> samples and was ≈750 kJ/mol for the <100> samples. For the <100> samples, Q was a function of stress and/or temperature.

In this study, we have first investigated the high-temperature compressive deformation behavior of polycrystalline $SrTiO_3$ at various strain rates in the temperature range of 1200–1345°C. Creep deformation data and electron microscopy were used to ascertain that GBS was the dominant deformation mechanism. Subsequently, the electron back-scattered diffraction technique was used to measure grain rotation as a function of applied plastic strain. Measured grain rotations were

compared with a simulation available in the literature.[15]

Experimental Details

The $SrTiO_3$ specimens were fabricated using commercially available 98.5%-pure $SrTiO_3$ powder (#72117, Alfa Aesar, Ward Hill, MA). The $SrTiO_3$ powder compacts were formed by uniaxial pressing (45 kN force) using a hydraulic laboratory press (Carver Laboratory press, Menominee Falls, WI) in a cylindrical hardened steel die. The die formed pellets of 2.2 cm diameter and 2.54 cm length. No binders were added to the powders prior to pressing.

The specimens were fired in a box furnace (Lindberg Furnaces, Asheville, NC) at 1450°C in air for 5 h. The heating rate averaged 3°C/minute, and the cooling rate was approximately 4°C/minute.

The density of the sintered $SrTiO_3$ sample was determined by the Archimedes method. Sample preparation for microstructural examination involved polishing one of the sample surfaces down to a 0.5-µm finish using alumina slurry. To reveal grain boundaries, samples were thermally etched at 1200°C for 0.5 h in air. Subsequently, microstructure was examined in a Hitachi S-4700-II (Tokyo, Japan) field emission scanning electron microscope (FE-SEM). Grain size was measured by the standard linear intercept method[16] using at least 250 intercepts on SEM photomicrographs. Fabricated $SrTiO_3$ samples were analyzed using inductively coupled plasma–atomic emission spectroscopy (ICP-AES) at Argonne's Analytical Chemistry Laboratory to determine the ratio of strontium and titanium.

Samples for high-temperature mechanical testing were cut, ground, and polished to ≈4×5×7 mm parallelepipeds. Constant crosshead-displacement-rate experiments were carried out in an Instron machine (Model 1125, Canton, MA) equipped with an atmosphere-controlled high-temperature furnace. Details of the experimental setup are described elsewhere.[5] The samples were compressed between two alumina platens, with platinum foil used as a diffusion barrier. Temperatures of 1200–1345ºC were used, with initial strain rates ranging between $2\times10^{-6}/\,s^{-1}$ and $5\times10^{-5}/\,s^{-1}$. Prior to the start of the experiment, the chamber was backfilled and flushed with argon gas at least three times. All experiments were conducted in ≈1 atm of high-purity (99.999%) argon atmosphere. At a specific test temperature, for each specimen, crosshead speeds were changed (with and without unloading the sample) to obtain various nominal strain rates. Strain rates were changed only after a steady state (no work hardening) was reached on the load-time trace.

Microstructural analyses of pre- and post-deformed samples were further conducted using SEM and transmission electron microscopy (TEM). TEM foils of samples were prepared by slicing thin sections using a precision diamond saw. Mechanical polishing further thinned samples. Subsequently, samples were ion milled using a Gatan (Pleasanton, CA) Model 691 precision ion polishing system. The microstructural analysis was performed using a Philips CM-200 transmission electron microscope operating at 200 kV in the Electron Microscopy Collaborative Research Center at Argonne National Laboratory.

Quantitative rotations of specific surface grains, as a function of applied strain, were measured using the electron back-scatter diffraction (EBSD) technique.[17] A parallelepiped-shaped $SrTiO_3$ sample, with dimensions similar to those of the deformation study samples, was used. However, in this case, one of the four faces (parallel to the loading direction) was polished to a 0.05-µm finish using alumina polishing solution and then plasma cleaned. A small Vicker's indent was made approximately in the center of the polished face. This was done to provide a reference point so that the grains that were followed as a function of strain could be easily located. Subsequently, the polished surface was coated with a thin layer of carbon.

EBSD pattern acquisition from the $SrTiO_3$ sample was conducted on a field emission electron microscope (Hitachi S-4500, Tokyo, Japan) equipped with an orientation imaging microscopy (TSL, Draper, UT) feature at Northwestern University's Electron Probe Instrumentation Center. A special sample holder was designed so that the sample orientation in the microscope was always kept the same. Sample tilt with respect to the horizontal was 70°. Diffraction patterns or Kikuchi bands were recorded from ≈20 specific grains. To determine the grain rotation, Kikuchi bands were represented by spots using the Hough transform.[18] The principle of the Hough transform is that the intensity at a *point* in the Hough space represents the intensity along a *line* in the original image. The coordinates in Hough space are usually taken as ρ and θ. Here a point (ρ, θ) in the Hough transform represents a line at an angle θ and at a distance ρ from the center of the

original pattern. Thus any rotation in the grains will rotate the Kikuchi bands and spots. Grain rotation was determined by the shift in the position of the spots in θ coordinate in the 2-dimensional Hough image as a function of the applied strain. If we assume the uncertainty of θ in the Hough transformed image is ±1 pixel, the uncertainty in the rotation of the Kikuchi line (and the grain) in the original image will be ±1°. This procedure is automated in the orientation imaging microscope and was individually applied to all the identified grains.

Grain rotation measurement, as a function of applied strain, was conducted in an interrupted test procedure. After ≈20 grains were identified and indexed on the undeformed sample, the sample was plastically deformed in steps of 0.02 strains at 1280°C and at a strain rate of 5×10^{-6}/s. At each step, the sample was removed from the Instron and placed back in the SEM to collect EBSD patterns from the identified grains. This procedure was repeated until the cumulative plastic strain in the sample was 0.08. In addition to tracking the changes in the grain orientation with deformation strains, the form factors [(4p*grain area)/(grain diameter)^2] of the individual grains were tracked with strain. Form factor was determined by using standard imaging software on an SEM image of the specific grain.

Results

The density of the as-fabricated $SrTiO_3$ sample was ≈95% of the theoretical density. Examination of the microstructure indicated that the grains were relatively equiaxed with few entrapped pores. Average grain size was ≈6 μm.

Major impurities were zirconium, silicon, barium, aluminum, and calcium. Based purely on the weight fractions of strontium and titanium, it appears that sintered ceramic is deficient in titanium with an Sr/Ti atomic ratio of 1.015. It should be noted that zirconium is a major impurity (3.9 wt %).

A typical stress-strain profile obtained in compression at 1250°C is presented in Figure 1. For the most part, at each strain rate, the stress reached a steady-state value. Similar responses were obtained in deformation tests conducted at other test temperatures. However, at the highest strain rate of 10^{-4}/s, at 1200°C, there was some evidence of work hardening. In such cases, the stress at which plastic deformation was observed was taken as the flow stress.

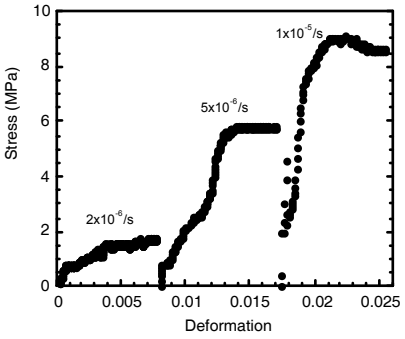

Figure 1. Stress-deformation profile for $SrTiO_3$ obtained during compression testing at 1250°C.

Figure 2 represents the strain-rate dependence of the flow stress on a log-log basis for the four temperatures investigated. Assuming no substantive changes occurred in the microstructures during testing, a steady-state phenomenological creep equation is used to define the dependence of strain rate on the flow stress:[19]

$$\dot{\varepsilon} = A\sigma^n \exp(-Q/RT) \qquad (1)$$

where $\dot{\varepsilon}$ is the strain rate, σ is the flow stress, n is the stress exponent, A is a constant, Q is the activation energy, R is the gas constant, and T is the absolute test temperature. A stress exponent of n=1 indicates that diffusion-controlled viscous flow is the likely deformation process.[1] Values of n, estimated from best fits of the experimental data to Eq. (1), were 0.9 ± 0.1 at 1345ºC, 0.9 ± 0.1 at 1300ºC, 1.0 ± 0.1 at 1250°C, and 1.6 ± 0.1 at 1200ºC, as shown in Figure 2. Within the experimental uncertainties in the stress and strain rates, it is safe to assume that n = 1 for the three test temperatures from 1250 to 1345°C.

At a constant strain rate, activation energy, Q, for the deformation process can be represented as

$$Q = nR \left(\frac{\partial \ln \sigma}{\partial \left(1/T\right)} \right)_{\dot{\varepsilon}} \qquad (2)$$

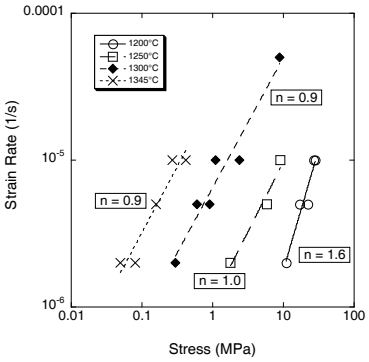

Figure 2. Strain-rate dependency on flow stress for $SrTIO_3$ samples at various test temperatures.

Figure 3 shows the Arrhenius plot of flow stress as a function of reciprocal absolute temperature at four different strain rates tested. Data for tests conducted at temperatures from 1250 to 1345°C were considered. From the slopes of the various lines, the mean activation energy determined was 628 ± 24 kJ/mol. It is assumed that the stress exponent, *n*, is constant over the temperature range, and a value of $n = 1$ was used for the calculation.

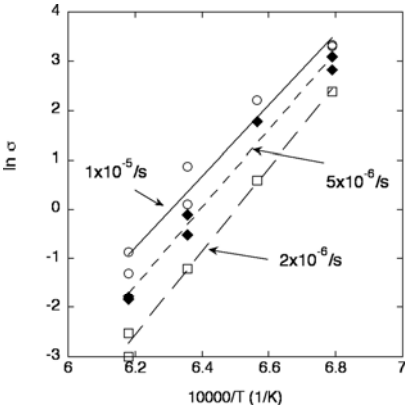

Figure 3. Flow stress in $SrTiO_3$ as a function of test temperature at constant strain rates.

Figure 4 is a typical TEM micrograph of a $SrTiO_3$ sample that was deformed at 1350°C with a total strain of 5%. The grain boundaries are clean with no cavitation observed. No discernible changes in the grain shape were observed. In addition, according to the TEM micrograph, no dislocations are seen in the deformed sample. However, in the deformed samples, there is evidence of twins within the grains.

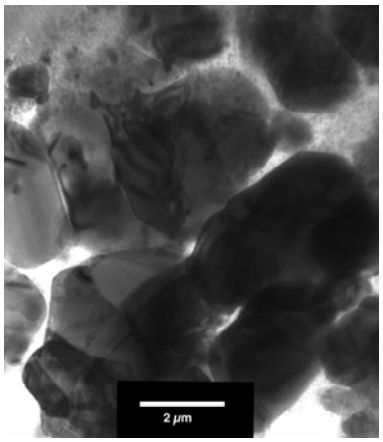

Figure 4. TEM micrograph of $SrTiO_3$ deformed at 1350°C to e = 0.05. Marker is 2 μm.

Figures 5a–c show a series of micrographs of a particular grain (#24) at strains of 0.02, 0.04, and 0.06, respectively. These micrographs demonstrate that the same grain can be located and tracked in the interrupted loading experiment for grain rotation measurements. It is clear from these images that there is no discernible change in the shape of the grain with higher strain. These figures also show the diffraction patterns and their respective Hough transformed images. The rotation of a grain is detected by the shift in the spots in the Hough space. As shown in Figures 5a and 5b, the spot moved by 4 pixels (from 64 to 68) or the grain rotated by 4° as the cumulative strain in the sample was increased from 0.02 to 0.04. Subsequently, from 0.04 to 0.06 strain, the spot shifted by 1 pixel or the corresponding additional grain rotation was ≈1°.

Figure 6 shows the measurable grain rotations, as a function of strain, on 7 grains out of the ≈20 grains that were followed. It is interesting to see that grains rotate in both the positive and negative directions. There is no systematic trend in grain rotation with the applied strain. The maximum rotation measured was 7°. Furthermore, some grains showed immediate rotation at low applied strains and then either did not rotate further or rotated back with increasing strains. Form factors measured on some of these grains as a function of applied strain indicated that there was no significant change in the form factors, within the error of measurement of ±5%, which indicates no obvious grain shape change.

(a)

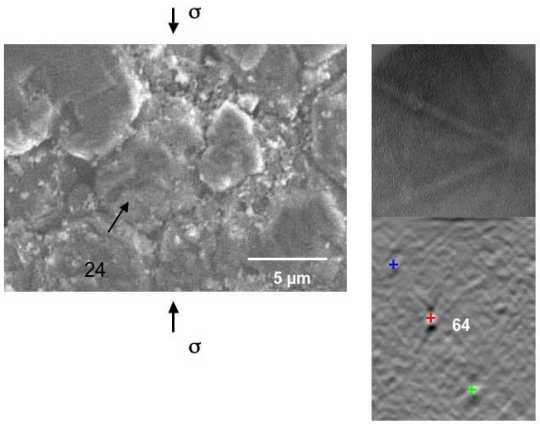

(b)

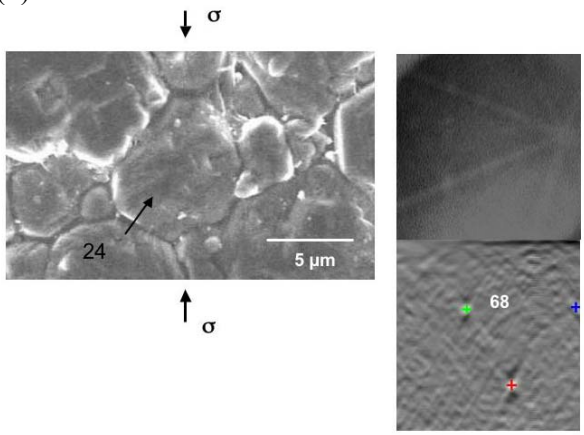

(c)

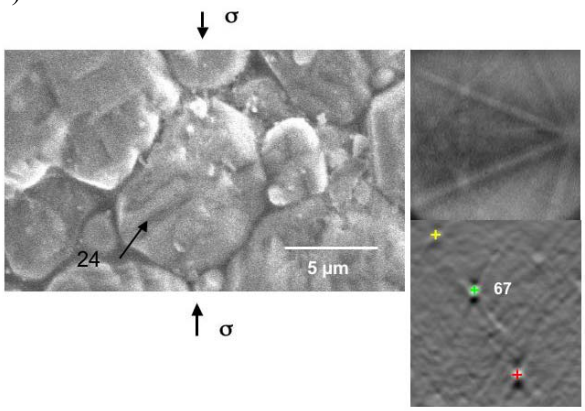

Figure 5. SEM micrograph, diffraction bands, and its corresponding Hough transform for a specific grain deformed to strains of (a) 2%, (b) 4%, and (c) 6%.

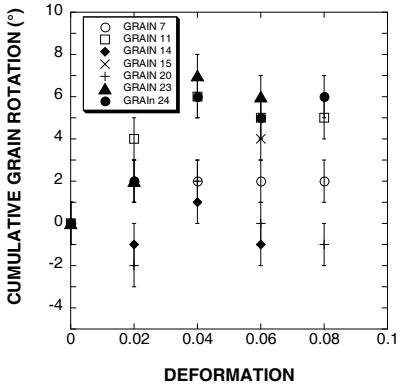

Figure 6. Cumulative grain rotations as a function of applied strain measured on seven grains in $SrTiO_3$ deformed at 1280°C and 5×10^{-6}/s.

Discussion

Polycrystalline $SrTiO_3$ has been shown to deform in a plastic manner at temperatures >1200°C and strain rates as high as 1×10^{-5}/s. This behavior is analogous to the high-temperature deformation behavior in other polycrystalline ceramics and composites such as Al_2O_3 [20], 3Y-TZP (3 mol % Y_2O_3-stabilized tetragonal zirconia),[2] and ceramic matrix composites.[3] It is generally accepted that the mechanism by which deformation or plastic flow occurs in these materials is by diffusion-assisted GBS.[2,3] Conditions conducive to deformation by plastic flow are reasonably high test temperatures and fine and equiaxed grain structure to accommodate the displacements of individual grains.[7]

The steady-state creep equation, as represented in Eq. (1), adequately defines the deformation behavior of $SrTiO_3$ for temperatures >1200°C and strain rates ranging from 2×10^{-6}/s–1×10^{-5}/s. A stress exponent of $n\approx1$ is indicative of a diffusion-controlled deformation process.[7] Further, the absence of any deformation-induced dislocation structures in the TEM analysis (as shown in Figure 4) indicates that $SrTiO_3$ deforms by GBS. Park et al. also observed no change in grain shapes in their study of a relatively large-grain (19–50 μm) $BaTiO_3$ ceramic and concluded that high-temperature deformation was controlled by GBS.[13] The stress exponent in their study was reported to be ≈1. The higher stress exponent value (n=1.6) for tests on $SrTiO_3$ conducted at 1200°C is not clear. This observation could be due to the onset of microfracture or a change in the deformation mode.

Insight into the possible deformation mechanism(s) can be obtained from the activation energy measurements. Activation energy for deformation of $SrTiO_3$ ceramic was 628 ± 42 kJ/mol, as determined from the Arrhenius plot of Figure 3. This value is quite similar to an activation energy of 620kJ/mol reported by Wang et al.[12] on the creep deformation of a $SrTiO_3$ single crystal deformed along {100} <010> orientation. The stress exponent for single-crystal $SrTiO_3$ was 3.5, and the deformation mechanism was controlled by diffusion-assisted-dislocation climb and was independent of temperature. Furthermore, Wang et al.[12] point out that this activation energy is similar to that of the diffusion of Ti^{+4} ions, which is the slowest and rate-controlling species in the titanate perovskites.[21,22]

For layered perovskites, such as superconductors, it has been shown that creep is controlled by diffusion of A site cations.[23,24] For $SrTiO_3$, the A-site cation is an Sr ion. The activation energy of Sr diffusion in polycrystalline $SrTiO_3$ is reported to be 293 kJ/mol,[25] which is significantly lower than the activation energy determined from the present study. It is quite possible that, in polycrystalline $SrTiO_3$, diffusion of the B-site cation or titanium ion is the deformation controlling species because of its +4 valence state and octahedral coordination with oxygen ions, as suggested by theoretical defect studies and experimental measurements for Ti^{+4} diffusion in titanates.[21,22] A similar possibility that diffusion of B-site cation or titanium ion is the deformation controlling specie has been suggested by Park et al. in their work on polycrystalline $BaTiO_3$.[13] Furthermore, the role of zirconium ion impurity (≈4 wt %) in the deformation and hence the measured activation energy was not explored.

The activation energy determined for polycrystalline $SrTiO_3$ is on the lower end compared with the activation energies of other complex-structured perovskite-type ceramics, as shown in Table 1. Normalized activation energy [Q/RT_m, (R=gas constant and T_m=melting point)] allows one to compare the activation energy for various other material systems. Moreover, for these complex oxides, it is known that n≈1 and the deformation mechanism is GBS. It is clear from Table 1 that there is a wide distribution for the normalized activation energies for the various perovskites.

Table 1. Activation energies for deformation of various oxide ceramics

Material	Q (kJ/mol)	Q/RTm	Reference
$BaTiO_3$	*720*	46	Park et al. (13)
$CaTiO_3$	840	45	Yamada (33)
$SrZrO_3$	710	29	Nemeth (34)
$SrTiO_3$ single crystal <100>	750	39	Wang et al. (12)
	620	32	
<110>			
$SrTiO_3$	628	33	This work

There are numerous examples of observance of grain rotation during deformation, grain growth[26] or texture evolution in metallic systems.[27] It is generally accepted that during plastic deformation, grain rotation is a consequence of a net torque on the grain.[15] However, in concert with grain rotation, an accommodating process needs to occur so that no voids or cavities are created. This accommodation is accomplished by GBS that, in the case of $SrTiO_3$, is assisted by cation diffusion.

Evidence of grain rotation in $SrTiO_3$ ceramics as a function of applied strain is clear from Figures 5 and 6. From SEM and TEM analysis of the deformed samples there was no evidence of cavitation. In addition, the form factors or the grain shapes of the specific grains for which rotation was measured did not change within the accuracy of the experimental measurements. Thus to accommodate the plastic strains, the grains must rotate.[9] Ashby and Verrall[9] have shown that plastic strains can be accommodated by diffusion-assisted GBS that involves grain translation and rotation and little or no change in grain shape or size. Based on the Ashby-Verrall model, large strains are accommodated by neighbor-switching events, and the degree of grain rotation is dependent on the surrounding grains.[9] This model is fundamentally different from Nabarro-Herring[28] and Coble[29] creep models that predict grain shape changes with no grain rotations.

Gifkin[3*] pointed out that strain rate predictions from the Ashby-Verrall model were on the lower end of the experimental measurements and that the grain size dependence did not agree with the experimental observations. Further, a simple 2-dimensional Ashby-Verrall model does not account for the changes in the surface area. Gifkin[3*] showed

in his model that changes in the surface area can be accounted for by considering the grains emerging from subsurface or surface grains disappearing into the bulk. This effect was first observed and reported by Rachinger.[31] Gifkin's model[3*] also predicts grain rotation. Evidence of grain disappearing into the bulk was also observed in the present study. Thus it appears that in addition to diffusion-assisted GBS, there is movement of grains from subsurface to interior and vice versa to account for the surface area changes as predicted by Gifkin.[3*]

Recently, there have been several meso-scale simulation efforts to quantify grain rotation during plastic deformation. Notably, Ding et al.[32] have simulated grain rotation for a model material with 5000 grains. They assumed equiaxed grains with a log normal grain size distribution and varying diffusive fluxes. However, no grain sliding resistance was considered. Grain-boundary diffusion or Coble creep accommodated deformation. They found that at 50% plastic strain, grain rotations ranged from −10° to +10°, with almost 40% of the grains showing no rotation. Another 40% of the grains showed rotations between −5° and +5°. These simulations are qualitatively similar to the experimental observations made on grain rotations as a function of plastic strain in $SrTiO_3$ in this study. It is recognized that the number of grains followed for rotation in this study are too small to provide a statistically meaningful comparison.

Grain rotation measurements were conducted in an ex-situ manner. Reloading of the specimen at each strain level is expected to create a somewhat different stress state at the microstructure level. In addition, the rotations measured are only for the surface grains. It is expected that grains in the sample interior will be exposed to different stresses as well as different diffusion conditions. In this regard, an in-situ experiment will be definitive where the grains in the bulk can be tracked for rotation.

Conclusions

High-temperature compressive deformation behavior of a polycrystalline strontium titanate ($SrTiO_3$) ceramic has been investigated between 1200 and 1345°C at strain rates ranging from 5×10^{-6}/s to 5×10^{-5}/s. Stress exponents of ≈1 indicated a viscous diffusion-controlled deformation mechanism with an activation energy of ≈628 kJ/mol. GBS was identified as the principal deformation mechanism. Comparison of activation energy with literature data on single-crystal $SrTiO_3$ suggests that diffusion of titanium ions is rate controlling. The EBSD technique was used to determine grain orientation as a function of applied strain in $SrTiO_3$. Grain rotations were both positive and negative, and rotations as large as 7° were measured. The magnitudes of grain rotation angles were qualitatively similar to those predicted from simulations.

References

1. W. R. Cannon and T. G. Langdon, "Creep of Ceramics—1. Mechanical Characteristics," *J. Mater. Sci.* **18** (1), 1–50 (1983).
2. F. Wakai, S. Sakaguchi, and Y. Matsuno, "Superplasticity of Yttria-Stabilized Tetragonal Zirconia," *Adv. Ceram. Mater*. **1,** 259 (1986).
3. A. H. Chokshi, A. K. Mukherjee, and T. G. Langdon, "Superplasticity in Advanced Materials," *Mater. Sci. Eng*. **R10** 237 (1993).
4. J. Ye and A. Domininquez-Rodriguez, "Joining of Y-TZP Parts," *Scripta Metall. Mater*. **33**, 441–6 (1995).
5. F. Gutierrez-Mora, A. Dominguez-Rodriguez, J. L. Routbort, R. Chaim, and F. Guiberteau, "Joining of Yttria-tetragonal Stabilized Zirconia Polycrystals using Nanocrystals," *Scripta Mater*. **41**, 455–60 (1999).
6. K. C. Goretta, F. Gutierrez-Mora, J. J. Picciolo, and J. L. Routbort, "Joining Alumina/Zirconia Ceramics," *Mater. Sci. & Eng*. **A341**, 158–162 (2003).
7. T. G. Langdon, "The Characteristics of Superplastic-Like Flow in Ceramics," in *Plastic Deformation of Ceramics*, eds. R. C. Bradt, C. A. Brookes, and J. L. Routbort, Plenum Press, New York, pp. 251–268 (1995).
8. F. Gutierrez-Mora, K. C. Goretta, S. Majumdar, J. L. Routbort, M. Grimdisch, and A. Domínguez-Rodriguez, "Influence of Internal Residual Stresses in Superplastic Joining of Airconia Toughened Alumina," *Acta Mater.* **50**, 3475–3486 (2002).
9. M. F. Ashby and R. A. Verrall, "Diffusion-Accommodated Flow and Superplasticity," *Acta Metall*. **21**, 149–163 (1973).
10. D. Singh, F. Gutierrez-Mora, N. Chen, K. C. Goretta, and J. L. Routbort, "Joining of Advanced Materials by Plastic Deformation," *Ceram. Eng. Sci.* **25**(3), 113–119 (2004).

11. F. Jona and G. Shirane, in *Ferroelectric Crystals*, Dover, New York, 1993
12. Z. Wang, S. Karato, and K. Fujino, "High Temperature Creep of Single Crystal Strontium Titanate ($SrTiO_3$): A Contribution to Creep Systematics in Perovskites," *Phys. Earth & Planet. Inter.* **79**, 299–312 (1993).
13. E. T. Park, P. Nash, J. Wolfenstine, K. C. Goretta, and J. L. Routbort, "High-temperature Creep of Polycrystalline $BaTiO_3$," *J. Mater. Res*. **14**(2), 523–528 (1999).
14. C. Carry and A. Mocellin, *J. Am. Ceram. Soc*. **69**, C215 (1986).
15. D. Moldovan, D. Wolf, and S. R. Phillpot, "Theory of Diffusion-Accommodated Grain Rotation in Columnar Polycrystalline Microstructures," *Acta Mater.* **49**, 3521–3532 (2001).
16. E. E. Underwood, in *Quantitative Stereology*, Addison-Wesley, Reading, MA (1970).
17. F. J. Humphreys, "Review: Grain and Subgrain Characterization by Electron Backscatter Diffraction," *J. Mat. Sci.* **36**, 3833–3854 (2001).
18. X. Tao and A. Eades, "Errors. Artifacts, and Improvements in EBSD Processing and Mapping," *Microsc. Microanal*. **11**, 79–87 (2005).
19. T. Bretheau, J. Castaing, J. Rabier, and P. Veyssiere, "Dislocation Motion and High-Temperature Plasticity of Binary and Ternary Oxides," *Adv. Phys.* **28**, 835 (1979).
20. L. A. Xue and I. W. Chen, "Deformation and Grain Growth of Low-Temperature-Sintered High-Purity Alumina," *J. Am. Ceram. Soc.* **72**, 3518 (1990).
21. W. H. Rhodes and W. D. Kingery, "Dislocation Dependence of Cationic Diffusion in $SrTiO_3$," *J. Am. Ceram. Soc*. **49(**10), 521–526 (1966).
22. K. Wright, *Rheology of Perovskites and Its Implications for Mantle Dynamics*, Ph.D. Thesis, Department of Geological Science, University College, London (1991).
23. A. Dominguez-Rodriguez, J. Castaing, K. C. Goretta, and J. L. Routbort, in *Point Defects and Related Properties of Ceramics*, eds. T. O. Mason and J. L. Routbort, p. 139, American Ceramic Society, Westerville, OH, (1991).
24. M. Jimenez-Melendo, A. R. De Arellano-Lopez, A. Dominguez-Rodriguez, K. C. Goretta, and J. L. Routbort, "Diffusion-controlled Plastic Deformation of $YBa_2Cu_3O_x$," *Acta Metall. Mater*. **43**, 2429 (1995).
25. P. Turlier, P. Bussiere, and M. Prettre, *Compt Rend. Acad. Sci*., **250**, p. 1649, Paris (1960).
26. P. G. Shewmon, in *Recrystallization, Grain Growth and Textures,* ASM, Metals Park, OH, 1966.
27. T, Yamaskai, Y. Demizu, and Y. Ogino, *Mater. Sci. Forum* **461**, 204–206 (1996).
28. C. Herring, *J. Appl. Phys.* **21**, 437 (1950).
29. R. L. Coble, *J. Appl. Phys.* **34**, 1679 (1963).
30. R. C. Gifkin, "Grain Rearrangements during Superplastic Deformation," *J. Mat. Sci.* **13**, 1926–1936 (1978).
31. W. A. Rachinger, *J. Inst. Metals* **81**, 33 (1952–53).
32. R. Ding, D. Moldovan, V. Yamakov, D. Wolf, and S. R. Phillpot, "Effects of Microstructural Inhomogeneity on Dynamic Grain Growth during Large-Strain Grain Boundary Diffusion-Assisted Plastic Deformation," *Modelling Simul. Mater. Sci. Eng.* **13**, 1129–1151 (2005).

B. Attachment Techniques for Heavy Truck Composite Chassis Members

Principal Investigator: Barbara Frame
Oak Ridge National Laboratory
P.O. Box 2008, Oak Ridge, TN 37831-6053
(865) 576-1892; fax: (865) 574-8257; e-mail: framebj@ornl.gov

Chief Scientist: James J. Eberhardt
(202) 586-9837; fax: (202) 587-2476; e-mail: james.eberhardt@ee.doe.gov
Field Technical Manager: Philip S. Sklad
(865) 574-5069; fax:(865) 574-6098; e-mail: skladps@ornl.gov

Contractors: Oak Ridge National Laboratory, Pacific Northwest National Laboratory
Contract Nos.: DE-AC05-00OR22725, DE-AC06-76RL01830

Objectives

- Overcome the technical issues associated with joining composite materials in heavy vehicles by developing technically robust and economically attractive joining techniques.
- Develop and validate one or more joint designs for a composite structural member attached to a metal member that satisfy the truck chassis structural requirements both economically and reliably.
- Solicit input from truck original equipment manufacturers (OEMs) and suppliers on the technical hurdles and needs associated with joining structural composite members in heavy vehicles. Use this information to guide the joint design and development activities.
- Publish information on the design, modeling, and testing methodologies that are developed to support the incorporation of composite materials into other chassis components.

Approach

- Collaborate with the National Composites Center (NCC) and its OEM partners to identify and address technical needs related to the manufacturing, joining, and implementation of a composite chassis component.
- Design attachment components and configurations in close coordination with the composite structural component development.
- Use modeling techniques to predict the performance of various joint designs, taking into account damage mechanisms and fatigue/life requirements.
- Characterize various composite materials and mechanical joint configurations through mechanical testing, considering variables such as hole size, hole fabrication method, bolt preload, inserts, combined loading, vibration, fatigue, and durability.
- Validate joint design for the composite structural member through shaker and track testing.

Accomplishments

- Conducted constant amplitude and block loading fatigue of candidate three-dimensional (3-D) glass fiber reinforced composites.
- Conducted double lap shear tensile and fatigue tests to investigate changes in bolt preload resulting from through-thickness creep of the composite and damage progression.

- Developed data acquisition software to calculate and monitor energy expended per cycle during tension-tension fatigue tests and initiated evaluation with commercial-grade carbon fiber composite.
- Conducted environmental tension-tension fatigue tests of bolted 3-D glass fiber reinforced composite/steel lap shear joints under conditions of water and salt water exposure.
- Conducted finite element analyses (FEAs) of 3-D glass fiber reinforced composite/steel bolted double lap joints.

Future Direction

- Continue bolt bearing and fatigue tests using thicker (¼ – ½ in.) fiberglass composites to investigate design modifications, adhesive bonding, and acceptable hole clearance levels to minimize damage progression in the composite and improve the fatigue life of a composite-to-steel joint.
- Continue environmental fatigue tests with 3-D glass fiber reinforced composite and incorporate vehicle cleaning fluid and elevated temperature into the environment test matrix.
- Continue tension-tension fatigue tests with developed data acquisition software and commercial-grade carbon fiber composite to evaluate capabilities to estimate fatigue life using an energy dissipation approach.
- Continue FEA modeling with input from the composite and joint tests to further optimize and predict the performance of the composite/steel joint.

Introduction

In May 2003, researchers at Oak Ridge National Laboratory (ORNL) and Pacific Northwest National Laboratory (PNNL) began collaboration on a 4-year research effort focused on developing technically robust and economically attractive joining techniques to overcome the technical issues associated with joining lightweight materials in heavy vehicles.

This project has been conducted in close partnership with the NCC and two truck industry OEMs. These partners have contributed significantly toward many previous accomplishments in the project by providing guidance regarding the service environment, manufacturing processes, and end user expectations. Some of the testing work was even done in an OEM partner's plant, so that it could simulate real manufacturing conditions as closely as possible.

These partners were working on a cost-shared, partially DOE-funded project that serendipitously served as a "focal project" for the team. Major reductions in the HSWR program necessitated a major reduction in the DOE funding for the industry project, and the research team experienced a corresponding decrease in interaction with its industry partners. Consequently, this year the team has addressed joining issues of general interest, with increased attention to problems that may arise throughout the truck chassis, but with decreased industry feedback regarding the practical and specific implementations of those solutions.

Composite Material Testing

Variable Amplitude Fatigue

Components in a truck chassis undergo complex random variable fatigue loading during their lifetime. Previous studies reported in the literature indicate that standard methods employed for variable amplitude fatigue life prediction can overestimate the actual experimentally measured life. The inaccuracy is due in part to the different failure mechanisms and property degradation in fiber-reinforced composite materials.

For example, the Palmgren-Miner linear relationship assumes that if a block of loading cycles at a given stress amplitude (n_1) is followed by a subsequent block of cycles at different stress amplitude (n_2), that overall damage accumulation is determined as a sum of the ratios of the loading cycles (n) to the failure cycles (N) at each stress level. Failure is predicted when the sum of the ratios equals 1:

$$n_1/N_1 + n_2/N_2 + \ldots = 1$$

The Palmgren-Miner linear relationship assumes that fatigue cycles at a specific load level always result in the same damage regardless of the loading history. The literature suggests that the model yields acceptable results for metals and is used for life predictions in many practical applications for metallic structures.

Block loading fatigue tests were conducted to characterize the behavior of 3-D glass fiber–reinforced epoxy and 3-D glass fiber–reinforced polyurethane composite. A comparison of measured fatigue life with the Palmgren-Miner's prediction was made and some deviation was evident.

Quasi-static tensile tests indicated that the 3-D glass fiber–reinforced polyurethane specimens had an average tensile strength of 378.6 MPa and modulus of 24.0 GPa. The 3-D glass fiber–reinforced epoxy specimens had a slightly higher average tensile strength of 421.9 MPa and a modulus of 23.8 GPa.

Figure 1 is a plot of constant amplitude tension-tension fatigue test results for the 3-D glass fiber reinforced epoxy and 3-D glass fiber–reinforced polyurethane composite. Although the number of data points is limited, the plots in Figure 1 indicate that the constant amplitude fatigue results of the two materials are similar.

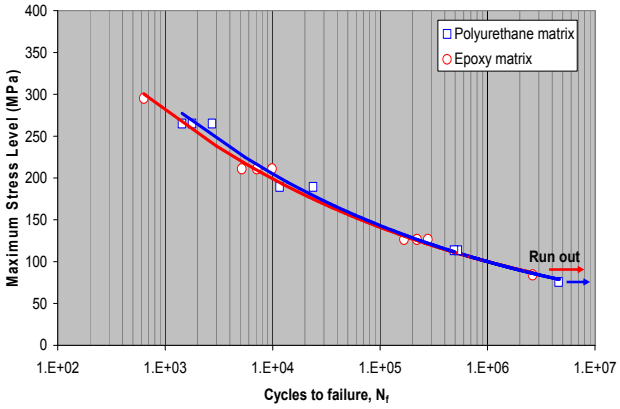

Figure 1. Constant amplitude fatigue test results for 3D glass-fiber–reinforced epoxy and polyurethane matrix composite specimens.

Figures 2 shows block loading fatigue results for the 3-D glass fiber–reinforced polyurethane and 3-D glass fiber–reinforced epoxy composites. The two-block maximum fatigue loads as a percentage of ultimate tensile strength are 50% and 30%. The 3-D

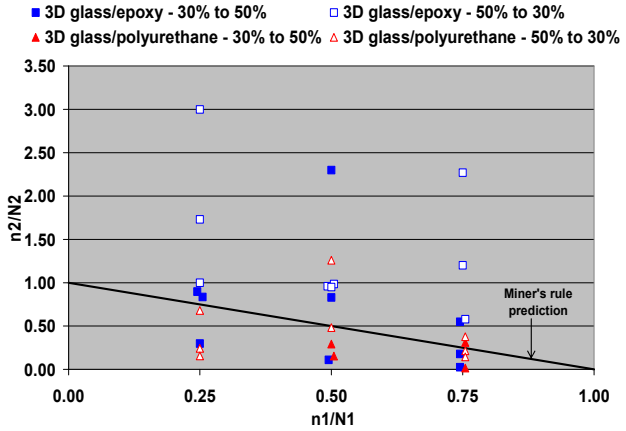

Figure 2. Block loading fatigue results for 3D glass-fiber–reinforced epoxy and 3D glass-fiber–reinforced polyurethane matrix specimens. The two-block maximum fatigue loads as a percentage of ultimate tensile strength are 50% and 30%.

glass/polyurethane composite data suggest that the two-block amplitude load sequence is more damaging for these specimens than would be predicted by the Palmgren-Miner model. The 3-D glass fiber–reinforced epoxy matrix specimens showed less deterioration of predicted fatigue life from the two-block amplitude load sequence, and data points from the high-to-low sequences exceed predicted life significantly.

For both epoxy and polyurethane matrix composites, the lower stress level applied prior to the high stress level was more damaging than when the higher stress level was applied first.

It is hypothesized that the difference in performance between the polyurethane and epoxy composite specimens with block loading fatigue may be attributable to the properties of the polyurethane and epoxy matrix resins, the quality of the fiber-matrix interface, and specimen geometry. The level of statistical confidence in this study is also shaped by the small number of replicates available for each testing condition.

These tests demonstrated that the 3-D glass fiber–reinforced composite specimens can become visibly whitened and opaque with evidence of fatigue damage (attributed to microcracks, matrix crazing, and failure of the fiber-resin interface) but still retain sufficient load-bearing capability to continue cycling for some period of time before eventual failure. That is, the presence of some visible damage does not signal that catastrophic failure

is imminent. It is speculated that the 3-D reinforcement may be beneficial in this regard by helping keep the sample together (intact).

This research team has been working closely with Alpha Star to integrate a damage model into Genoa that will take into account the deviation from the Palmer-Miner prediction. Additionally, the progressive failure analysis in Genoa may assist in developing an understanding of the damage development and evolution which may result in the different behavior based on the loading sequence. The ultimate goal would be to have a predictive tool that could be used for a more realistic random amplitude fatigue spectrum. This would be helpful to reduce the high cost of material characterization associated with fatigue testing, but this research is beyond the scope of this program.

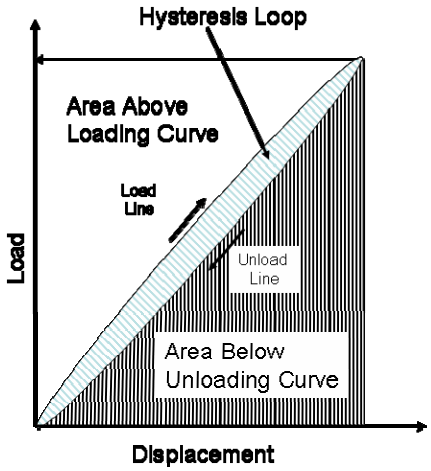

Figure 3. Schematic of load-displacement hysteresis.

Fatigue Energy Dissipation Study

It is hypothesized that a relatively simple relationship may exist between fatigue amplitude and damage accumulation leading up to catastrophic failure. Such a relationship could be better used to predict structural survival in composites than traditional methods such as S-N curves or the Palmgren-Miner model adopted from high cycle fatigue of metals. An exploratory study was therefore initiated with a commercially available carbon fiber–reinforced cross-ply laminate to investigate the fundamental relationships between energy dissipation and damage accumulation, and their utility in making fatigue life predictions.

A typical load displacement record for an individual fatigue cycle consists of a loading curve and unloading curve as depicted in Figure 3. In the case of a viscoelastic composite under load control, the associated displacement may lag the applied load, resulting in a hysterisis loop that will remain constant within the elastic range of the material. However, any damage accumulation should be evident by observing changes in specimen stiffness (increased displacement) under the constant amplitude loading, which will change the area contained within the hysteresis loop.

The proposed approach assumes that the cumulative damage energy from each cycle is simply the work or the area under the load-displacement curve for each fatigue cycle summed over the life of the structure. At failure, the total accumulative energy and the number of cycles may be easily measured from a fatigue test. This total energy would represent the energy capacity of the material in question. With this information, it is reasonable to assume that the number of cycles to failure may be predicted for different fatigue amplitudes and loading scenarios, based on the cumulative damage energy results obtained from earlier tests. The key to this approach is to determine the energy component responsible for damage.

Although this approach may appear simplistic, it requires determining energy levels for each cycle of a fatigue test, which may last for millions of cycles. This poses a data acquisition and computational challenge. The second challenge is determining the precise energy component(s) that correlate with the damage progression in the composite.

For example, the total potential energy for a single cycle will include the (1) elastic strain energy, (2) energy dissipated due to heating, (3) any plastic-like permanent deformation, and (4) dissipative energy associated with damage. It is the latter of these energy terms which must be discerned from each load-displacement curve associated with each fatigue cycle. If this can be accomplished, it is reasonable to assume that it would be possible to establish an energy capacity for a given material by accumulating all of the dissipative damage energy for a particular material over a series of fatigue cycle loadings leading to failure.

Fatigue tests are being conducted under several constant amplitude load ranges with the areas under

the loading and unloading curves being recorded for every fatigue cycle in the test up until specimen failure. These data can be used to determine the area enclosed in the hysterisis loop and other associated information to establish any correlation between these energy levels and the required number of cycles to failure. Strongly correlated data would suggest a relation between energy accumulation and the fatigue life of the material and provide phenomenological evidence to explore any correlation at a more fundamental, rigorous level.

Static and Fatigue Double-Lap, Shear-Joint Testing

A testing methodology has been developed to study the effects of bolt preload with composite to steel joints. The double-lap, shear-bolted composite/steel assembly in combination with an interface load cell to monitor the bolt-clamping force during testing is being used to evaluate the effect of changes in the torque level on static strength and fatigue life. Specimen size is 76.2 mm wide × 177.8 mm long × 2.5 mm thick. Holes (12.7 mm diam) are drilled using a Forstner bit, and assembly was with 12.7-mm (½-in.) grade-8 bolts. The torque is applied by hand with a torque wrench adjusted to the proper setting.

Bolt Preload and Quasi-Static Strength

Quasi-static tensile tests conducted with 2.54–3.17-mm thick fiberglass-reinforced composites show that the tensile load-bearing capability of the composite/steel assembly increases as bolt preload increases. Failure modes shift from bearing type failures at the lower preloads, typified by local composite crushing at the hole perimeter, to composite material tensile failures initiating at the hole. This is attributed to the higher clamping forces enabling a more effective transfer of tensile load between material adjacent to the hole perimeter and the surrounding (bulk) composite.

Materials evaluated to date include 3-D glass fiber–reinforced epoxy and 3-D glass fiber–reinforced vinyl ester composites molded by the NCC, and a commercial pultruded fiberglass Extren® sheet product. Figure 4 shows the maximum joint break load of specimens prepared with a specified composite material as a function of bolt torque.

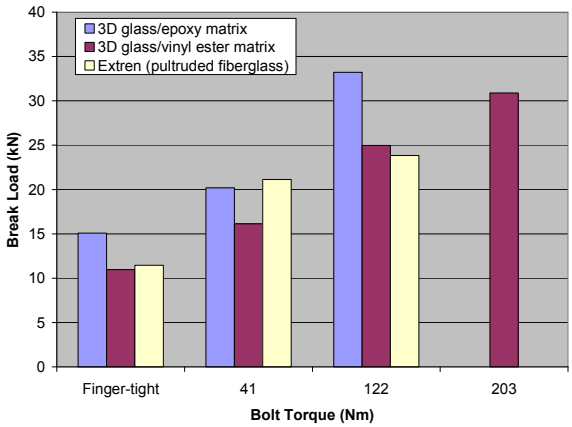

Figure 4. Tensile break loads of bolted double lap shear composite/steel assemblies as a function of bolt pre-load.

Through-thickness Creep and Loss of Bolt PreLoad

An important component of a bolted composite/steel joint design is the bolt preload at assembly, which is selected to achieve the desired clamp load for proper function of the joint throughout the service life of the assembly. A minimum clamping force is required to overcome vibration-induced loosening, joint separation, slippage, fatigue, leakage and other similar failures. The maximum clamp force should be below a threshold value that would cause bolt yielding, joint crushing, stress cracking, premature fatigue failure, or other related service failures.

The low through-thickness properties typical of most composite architectures suggest that bolted composite assemblies will experience a loss of preload over time due to the relaxation or creep of the softer composite material.

Tension-tension fatigue joint tests were conducted with 3-D glass fiber–reinforced epoxy specimens provided by the NCC. For these tests, the torque level was maintained at 41 Nm (30 ft-lb). This torque nominally produces a bolt clamping force of 15–17 kN as measured directly by the interface bolt load cell. The maximum fatigue load was established as a percentage of the ultimate tensile break load of comparably prepared specimens. The fatigue tests were run with a stress cycle R factor of 0.1 and a frequency of 5 Hz.

Figure 5 is a plot of the representative loss of bolt preload data as a function of the fatigue cycle number, and measured for fatigue levels of 70%,

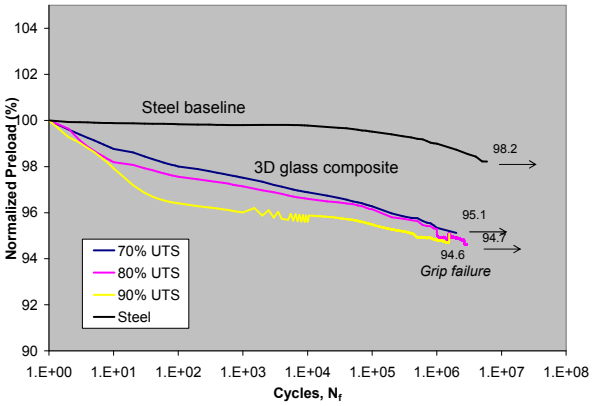

Figure 5. Normalized loss of pre-load for 3D glass-fiber–reinforced epoxy composite and steel baseline specimens during joint tension-tension fatigue test.

80% and 90% of the ultimate failure load. Data from a steel baseline specimen in which a steel plate was substituted for the composite are included for comparison. The data show that the loss of the preload of the bolted steel/steel assembly during tension-tension fatigue is considerably less than that of the composite/steel assemblies. The higher loss of bolt preload measured with the composite assemblies is attributed to through-thickness creep of the composite.

Fatigue joint testing with nominal 2.5-mm (0.10-in.) 3-D glass fiber–reinforced epoxy specimens provided by the NCC shows that the double lap shear composite/steel assemblies withstand reasonably high fatigue load levels without failure, provided that the initial bolt clamping force is at least 15–17 kN. For instance, one specimen achieved run-out with over 2.6 million cycles at a fatigue level of 95% of the ultimate failure load.

Other failures occurred at over 1 million cycles at a fatigue level of 90% of the ultimate failure load, but it did not initiate at the hole. These failures occurred either in the bulk composite or at the grip. This suggests that the fatigue life of the bolted composite/steel assembly is currently on par with that of the 2.54-mm fiberglass composite, provided that adequate clamping force is maintained for the duration of the test (i.e., no loss of preload occurs due to through-thickness creep of the composit.

Recommendations are that further composite/steel assembly fatigue investigations be conducted using thicker (and more robust) fiberglass specimens. A specimen thickness that is representative of the projected fiberglass chassis component is highly desirable for these investigations.

Environmental Fatigue Tests

Environmental fatigue testing is being conducted to evaluate the durability of bolted composite/steel joints with exposures to water, miscellaneous chemical fluids, and temperature extremes likely to be encountered during the long-term operation of a truck. Testing is conducted with bolted composite/steel lap shear specimens and the composite material is the 3-D glass fiber–reinforced epoxy composite provided by the NCC. Specimen size is 25.4-mm wide × 101.6-mm long × 2.5-mm thick. Holes (6.4-mm diameter) are drilled using a Forstner bit and assembly is with 6.4-mm (1/4-in.) grade 8 bolts. The torque is 20 Nm applied by hand with a torque wrench adjusted to the proper setting.

Environmental fatigue tests to date have been conducted at room temperature in ambient air, distilled water, and 5 wt % salt water environments. The maximum fatigue loads are established as a percentage of the ultimate tensile load of comparably assembled specimens tested in air and at room temperature. Fatigue tests were run with a stress cycle R factor of 0.1 and a frequency of 5 Hz.

Figure 6 is a plot of the environmental fatigue test results to date. The data suggests that water immersion does not significantly reduce fatigue life of the 3-D glass fiber–reinforced epoxy composite. Specimens immersed in water achieved run-out with over 2 million cycles at a fatigue level of 60% to 70% of the ultimate failure load. Specimens tested in 5 wt % salt water exhibited a reduced fatigue life compared to the specimens tested in air and distilled water.

Comparable 3-D glass fiber–reinforced epoxy composite coupons (25.4-mm wide × 101.6-mm long × 2.5-mm thick with a 6.4-mm diameter hole) were immersed in distilled water, 5 wt % salt water, and a commercial car wash solution to measure weight change with time immersion. Results are summarized in Figure 7. Weight increases of less than 0.20% were measured with coupons immersed in distilled water and salt water immersions after 27 days and with coupons immersed in a car wash solution for 21 days. This suggests that there is not appreciable “wicking” of fluid into the composite

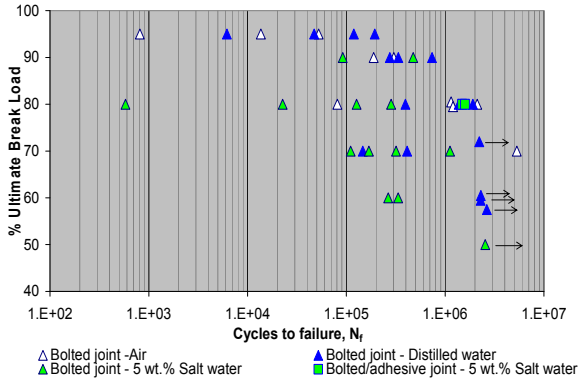

Figure 6. Environmental fatigue test results for bolted 3-D glass fiber–reinforced epoxy composite/steel lap shear specimens.

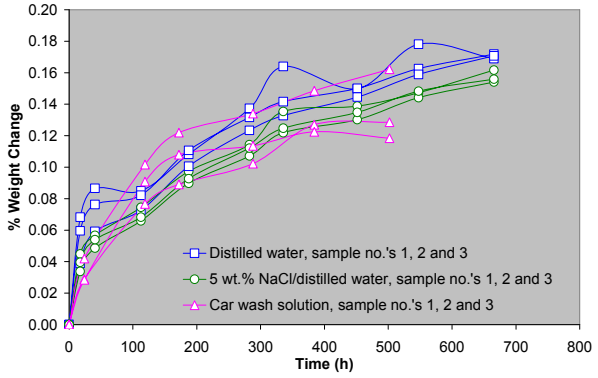

Figure 7. Weight gain versus immersion time for 3-D glass fiber–reinforced epoxy composite coupons.

through the machine edges and hole perimeter when the coupons are in a static (un-stressed) condition.

Quasi-static tensile tests were conducted with sets of bolted composite/steel lap shear specimens prepared from 3-D glass fiber–reinforced composite coupons that had been immersed in distilled water and 5 wt % salt water for 8 days at room temperature. No reduction in joint tensile break loads was detected with either group of specimens.

Structural Adhesives

Data presented in the FY 2005 Annual Progress Report showed that the fatigue life of bolted composite/steel assemblies can be enhanced by the addition of a structural adhesive to the joint. In this effort, commercially available structural adhesives were evaluated for their ability to bond well with both 3-D glass fiber–reinforced composite and steel substrates, and for ease of processing.

Composite-to-steel lap shear specimens were used to evaluate epoxy and polyurethane adhesives and included Pliogrip 7779 polyurethane, Betamate 4601 and Betamate 2096 epoxy, Hysol E-20HP epoxy, and 3M 2214 aluminum-filled epoxy. Cohesive failures were obtained with specimens preheated slightly (35°C–65°C) to enhance adhesive flow and wet-out of the steel and composite surfaces. "Room temperature" curing adhesives also responded well to the application of some heat to ensure full cure of the adhesive. Lap shear strengths for these type specimens are on the order of 20–24 MPa.

Modeling

Adhesively bonded joints can often be designed to be stronger, stiffer, and lighter than their mechanical counterparts in many applications. However, constraints on the design envelope, manufacturing processes and the cost of a final product often prevent designers from considering adhesively bonded joints.

Bonded joints are susceptible to peel stresses, and care must be taken to eliminate and/or minimize peel loading near the edges of the joint. Design envelope constraints may preclude the design modifications necessary to minimize peel stresses, thereby eliminating bonded joints from consideration. Hart-Smith analyzed single-lap joints and concluded that joints with thin adherends and large overlap areas exhibited failure of the adherends with a high joint efficiency. Joints with thicker adherends failed due to peel or shear stresses, and the joint efficiency was significantly lower. Joint efficiency with thick adherends is possible using scarf or stepped-lap joint techniques. However, these methods significantly increase the manufacturing cost and complexity of the joint. For these reasons, adhesive bonding of thick adherends is generally not considered a viable option in automotive and heavy truck applications.

Mechanical (bolted) joints have several advantages that make them attractive for heavy vehicle applications. Unlike bonded joints, bolted joints can withstand significant peel stresses, and loads can be transferred more efficiently through thick components using simple joint geometries such as single- and double-lap configurations. In addition, bolted joints can be easily inspected, repaired, require minimal surface preparation prior to assembly, and have lower production costs.

Two load-transfer modes can be idealized for a bolted joint loaded in shear such as the double-lap specimen. These are hole loading and contact surface loading. The dominant mode type is primarily dependent on the bolt preload and is affected by material properties and joint geometry. The hole-loading mode occurs when the preload is low and components are allowed to slip under load. This scenario is not desirable in heavy truck applications because vibration and reversal of loads would result in movement of the components, quickly resulting in material wear near the bolt due to friction. Higher bolt preload results in load transfer through friction at the component (contact) surfaces. "Failure" of these joints occurs when either the interfaces slip or the material incurs damage. The ultimate load is strongly dependent on the force and contact area.

Finite element analyses (FEA) were conducted for the case of a symmetric double-lap joint consisting of a 3-mm-thick 3-D glass fiber–reinforced vinyl-ester composite joined to two steel plates of 3, 5, 7 and 11-mm thickness via a 12-mm (½-in.) bolt. The joint assembly prepared with the 3-mm thick steel plates is a representation of an actual setup tested in this project and described earlier in this report. The detailed geometry of the joint was idealized and only one-half of the setup was analyzed due to its symmetry (Figure 8).

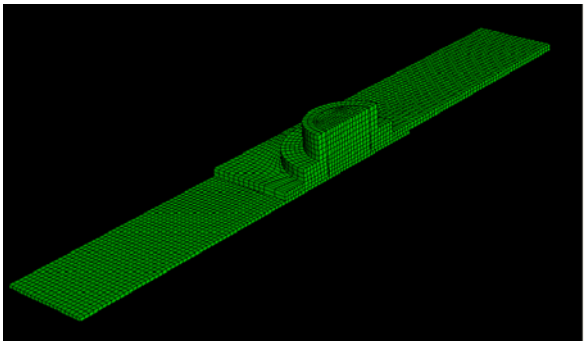

Figure 8. Idealized representation of double-lap joint.

Preloads (i.e., the clamping force applied to the assembly after tightening the bolt) of 0.44, 2.22, 4.45, 8.90, 13.34, and 22.24 kN (100, 500, 1000, 2000, 3000, and 5000 lb-ft) were applied to each geometry setup for a total of 24 analyses performed. The objective was to inspect the contact area between the components as a function of the thickness of the steel plates and the applied preload. Von-Mises stresses in two cross sections are depicted in Figure 9.

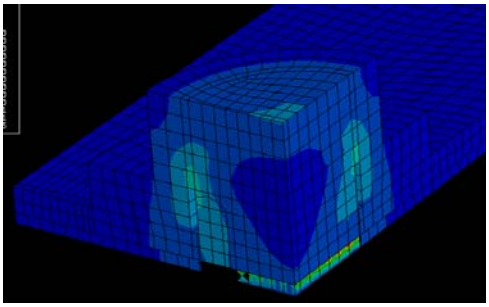

Figure 9. Graphical representation of Von–Mises stresses due to preloads.

Figure 10 shows the limit cases of the joint. The conclusion is that while the magnitude of the contact pressure changes as a function of applied preload, the contact area remains virtually unaffected for thinner steel plates and increases only modestly for thicker substrates. The contact area can be assumed constant and equal to the area of the washer inserted between the plates and the bolt or nut for the case of the 3-mm-thick steel plates (Figure 10.-a). For thicker steel plates, the contact area is greater and increases with applied preload as illustrated in Figure 10b.

Summary

This project is a 4 year research effort focused on the development of technically robust and economically attractive joining techniques to overcome the technical issues associated with joining composite chassis components in heavy vehicles. This report discusses the FY 2006 research activities.

A variable amplitude fatigue testing has been conducted with 3-D glass fiber–reinforced epoxy composites. An exploratory study was initiated with a commercially available carbon fiber–reinforced, cross-ply laminate to investigate the fundamental relationships between energy dissipation and damage accumulation, and their utility in making fatigue life predictions.

Loss of bolt preload due to through-thickness creep of the composite has been monitored for composite/steel joints under static and fatigue loading,

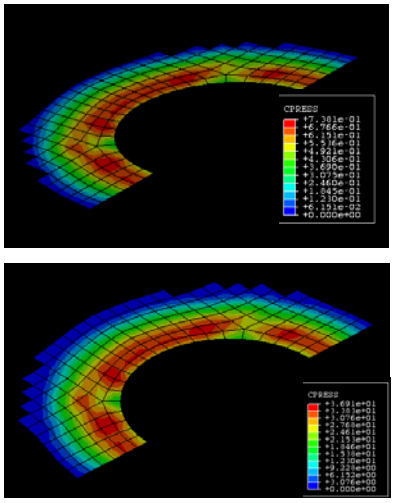

(a) 3-mm-thick steel plates.

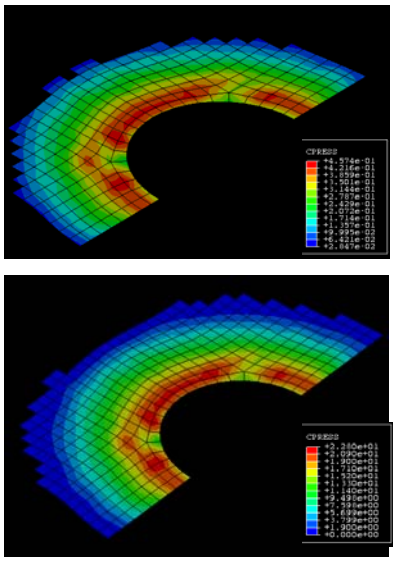

(b) 11-mm-thick steel plates

Figure 10. Contact area and pressure for (a) 3-mm-thick and (b) 11-mm-thick steel plates with preloads of, respectively, 0.44 and 22.24 kN (100 and 5000 lb-ft)

and commercially available structural adhesives were evaluated for their ability to bond well with 3-D glass fiber–reinforced composite and steel substrates as well as for ease of processing. Environmental fatigue testing has been conducted to evaluate the durability of bolted 3-D glass fiber reinforced composite/steel joints with exposure to air, water, and salt water environments.

Finite element analyses were conducted for the case of a symmetric double lap joint consisting of a 3-D glass fiber–reinforced composite joined to two steel plates to inspect the contact area between the components as a function of the thickness of the steel plates and the applied preload.

Acknowledgements

The principal investigators would like to acknowledge the valuable contributions of the members of the research team, including Don Erdman, Vlastimil Kunc, and Tom Battiste of ORNL.

C. Friction-Stir-Joined Aluminum Sheet Materials for Heavy Vehicle Cab Structures

Principal Investigator: Glenn J. Grant
Pacific Northwest National Laboratory
P.O. Box 999, Richland, WA 99352-0999
(509) 375-6890; fax: (509) 375-4448; e-mail: glenn.grant@pnl.gov

Chief Scientist: James J. Eberhardt
(202) 586-9837; fax: (202) 587-2476; e-mail: james.eberhardt@ee.doe.gov
Field Technical Manager: Philip S. Sklad
(865) 574-5069; fax:(865) 574-6098; e-mail:skladps@ornl.gov

Participants:
Elizabeth Stephens, Karl Mattlin, and Mike Dahl, Pacific Northwest National Laboratory
Scott Wazny and Brian Fulbright, Freightliner LLC
Douglas Waldron and Keith McTernan, Advanced Joining Technologies, Inc.
Tom Sanor, Magna Drive Automotive
Alcoa

Contractor: Pacific Northwest National Laboratory
Contract No.: DE-AC06-76RL01830

Objective

- Develop and deploy friction stir joining (FSJ) as a weight and cost-saving manufacturing technology for heavy vehicle cab structures

Approach

- Demonstrate the use of aluminum tailor-welded blanks (TWBs) for heavy vehicle applications.
- Develop weld process parameters to lower manufacturing cost, increase joint reliability, and explore dissimilar material blanks that can afford additional weight savings.
- Develop and prototype lightweight cab-in-white structures, including door inner liners, door opening panels, back- wall, and floor structures for Class 7–8 trucks using FSJ technologies.
- Address manufacturing issues to lower blank fabrication cost and other barriers to implementation of aluminum TWBs.

Recent Accomplishments

- Began conducting a design of experiments on tool development and process design for high-speed welding (+150 in. per min) to lower the cost of the initial blanking operation.
- Developed three tool designs for high-speed welding of dissimilar aluminum alloys of different thicknesses (5182-O and 6111-T4 aluminum alloys).
- Developed two tool designs for high-speed welding of dissimilar aluminum alloys of similar thicknesses.

- Completed setup of digital image correlation for use with limited dome height tests to track strain localization and strain variation of welded parts during forming.
- Characterized and completed strength and formability tests for the 5182/6111 TWBs fabricated for high-speed welding.

Future Direction

- Continue with the weld process and tool development for dissimilar alloy combinations and hard alloys (6xxx, 5xxx H3x, etc.) that would result in greater cost and weight savings.
- Develop and optimize the welding process parameters of dissimilar aluminum alloys of different thicknesses (5182-O and 6111 aluminum alloys).
- Focus on FSJ as a low-cost enabler of lightweight, low-cost vehicle assembly (non-TWB).

Introduction

This work is a collaborative effort between Pacific Northwest National Laboratory (PNNL), Freightliner, LLC, Advanced Joining Technologies, Inc. (AJT), Magna Drive Automotive, and Alcoa. This project aims to develop and deploy FSJ as a weight- and cost-saving manufacturing technology for heavy vehicle cab structures. To date, the project has focused on (1) developing the appropriate FSJ process parameters to create high-reliability joints that survive stamping operations; (2) prototyping full cabs using FSJ technologies and testing for durability and crash performance; and (3) addressing manufacturing issues, including lowering blank fabrication cost, and other barriers to implementing the technology. The challenge is to develop stamped panels that can meet the unique strength and durability requirements of heavy vehicle cab structures.

Aluminum TWBs consist of multiple-thickness and multiple-alloy sheet materials welded together into a single, variable-thickness blank. Figure 1 shows a typical fusion-welded TWB before and after a stamping application. A TWB is assembled as a series of flat sheets joined together, which are then submitted to a stamping process. The technology allows production of a weight-optimized, variable-thickness vehicle body component. TWB technology gives automotive and truck designers the ability to selectively vary body panel thickness to optimize the use of material. Successful use of the technology ultimately results in reducing vehicle weight without compromising final strength, stiffness, and durability. The manufacture of TWBs and their application in body panels requires that the weld material deform under biaxial loading during sheet metal stamping. The deformation of weld materials and their limits of formability are important aspects of TWB technology.

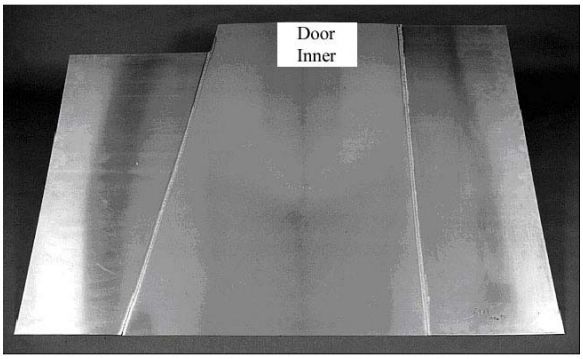

(a)

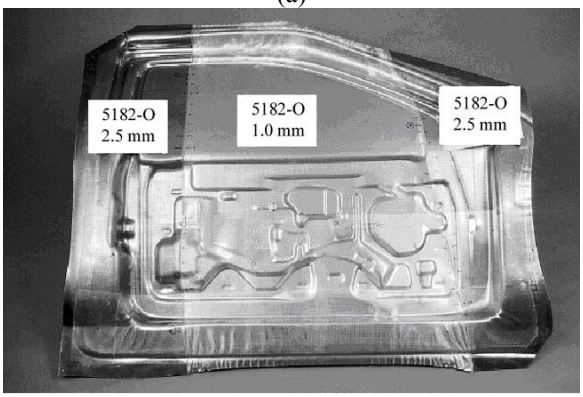

(b)

Photos courtesy of Reynolds Metals Company and Ogihara America Corp.

Figure 1. (a) A TWB viewed in the as-welded condition, ready for submission to the stamping process. The shape shown is typical for a door inner stamping operation. (b) Aluminum TWB after stamping to produce a door inner panel.

The primary challenge of using aluminum TWBs in the past has been the relatively low quality of aluminum fusion welds. It often results in premature fracture or a lack of reliability of weld materials

during stamping. Improving aluminum weld quality, understanding and describing the formability of the weld region, and predicting its formability are the primary technical challenges in using aluminum TWBs.

FSJ is a revolutionary joining technology that employs severe plastic deformation to create solid state joints between wide varieties of different materials. Invented by TWI, Ltd., about 12 years ago, FSJ is capable of producing aluminum alloy welds as good as (or significantly better than) fusion welds in terms of joint efficiency, mechanical properties, and environmental robustness. The advantage of using this solid state joining technique is the ability to avoid liquid metal during joining. Aluminum has low molten viscosity, high reflectivity, and a relatively high propensity to form internal porosity during joining because of the high solubility of hydrogen in liquid aluminum.

FSJ also can eliminate hot cracking and minimize heat-affected-zone (HAZ) issues in 6000-series heat-treatable aluminum alloys. Avoiding the liquid phase of the materials also avoids the formation of various large eutectic constituent particles or other undesirable intermetallic particles that develop in particular alloys or with certain types of weld or materials contamination.

The use of FSJ also better facilitates welding of heat-treatable materials, since the HAZ is normally smaller or less pronounced than with fusion welding. The use of solid state joining enables a variety of types of dissimilar aluminum alloy joining not normally possible using fusion welding methods. The goal of producing a highly formable weld joint may be achievable with friction stir welding because of the wide range of weld heat, plastic work, and weld metal grain-size manipulation that is possible.

High-Speed Welding

Although the industrial partners consider the program research and engineering a success, there are still barriers to implementation of the FSJ technology for aluminum TWBs. While many material combinations were successfully stamped, others that would have had stronger manufacturing arguments (cost and weight savings) were not successfully stamped (i.e. 6xxx and 5xxx H3x alloys). In addition, the cost models were close but were still below cost parity with monolithic sheet stampings. A low-cost, fast process will be the driver for implementation of the technology. Joint reliability and speed of blank fabrication are two barriers to overcome.

To overcome the blank cost, high-speed welding, >150 in. per min (ipm), of 5182-O and 6111-T4 TWBs is being investigated (2 and 1.5mm thick, respectively). Currently, a design of experiments (DOE) on tool development and process design is being performed. Three tool designs were developed for high-speed welding of the dissimilar aluminum alloys of different thicknesses. A 2-level factorial design was chosen to study the joint effect of process parameters on formability. Two rounds of experimental testing will occur. The first round of testing is designed to hone in on one tool design for high-speed welding; the second round of testing is to continue with optimizing the welding process parameters with the selected tool.

For the first round of testing, the two factors considered for the 2-level factorial were travel speed and tool rotation speed. A low-level and high-level speed for each factor were determined. For tool travel speed, a low level of 150 ipm and a high level of 300 ipm were chosen. For tool rotation speed, a low level of 2000 rotations per minute (rpm) and a high level of 3500 rpm were chosen.

These levels were chosen for the 2-level factorial because previous work indicated these values as the feasible ranges for these materials. Table 1 is representative of the DOE matrix created. A 5182-O/6111-T4 TWB panel was friction stir welded for each run (at the determined process parameters) in the DOE matrix. The matrix consists of six weld runs, and replicates of each run will be performed.

Table 1. DOE matrix developed for tool design

Run	Matrix			Travel speed (ipm)	Rotation speed (rpm)
1	–1	+1	→	150	3500
2	–1	–1	→	150	2000
3	+1	–1	→	300	2000
4	+1	+1	→	300	3500
5	0	0	→	225	2750
6	0	0	→	225	2750

In the DOE, each weld run (including replicates) is treated as an independent experiment. Each weld run must be conducted randomly to rule out any variability and influences. All material alloys used for the weld runs come from the same source (i.e.,

same supplier, same sheet of metal). We will be able to ensure uniformity among the materials and be able to determine that any differences observed in formability performance from subsequent testing are due to the tool and not to the material used.

Test coupons were prepared from the TWB panels made from each weld run and were subsequently tested for strength and formability. Tensile tests and limited dome height (LDH) tests were performed. Further investigation of the optimum joining process parameters will occur in the second round of testing, in which a second DOE matrix will be created to establish the optimum weld conditions. Test coupons will be prepared from the welded panels and subsequently tested and characterized to determine the set of parameters that produces a TWB with the best formability.

Forming Strain Characterization Using Digital Image Correlation

During this reporting period, digital image correlation (DIC) has been applied for use with limited dome height formability tests to overcome the barrier of joint reliability. DIC is a data analysis method that uses an algorithm to analyze digital image data taken when a sample is subjected to mechanical strain. Displacement and strain are measured. This technique uses white-light speckle correlation, where two similarly speckled images captured by a video camera represent the state of the object before and after deformation. Consecutive images are captured during testing, and the image correlation will register a change in surface characteristics as the specimen is affected by stresses imposed upon it. The actual object movement is measured and the Lagragian strain tensor is available at every point on the surface.

This technique will help us further understand strain localization in a non-homogenous gage such as a weld. We will be able to track strain localization and strain variation of the welded parts during forming. These incremental strains acquired during forming will be entered into finite element analysis (FEA) models. This technique will allow us to comprehend the stresses required for forming. The use of FEA models will allow us to re-create the loading or stress paths that occur during deformation. Figure 2 illustrates the major strain observed in a monolithic 6111 sheet during LDH testing.

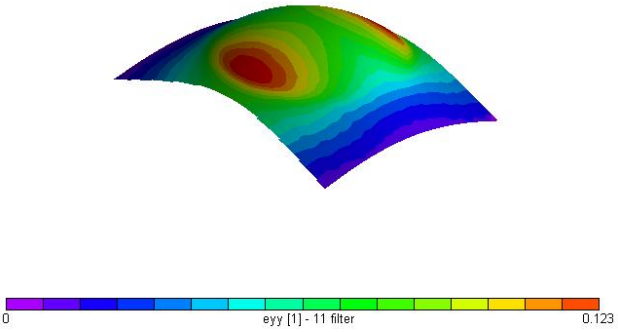

Figure 2. An illustration of the major strain characterization of a 6111-T4 monolithic sheet during LDH testing. Note that image was taken prior to reaching peak height.

Tool Designs and Blank Fabrication

Maximum weld traverse speed is very much a function of tool design. Three tool designs were developed for high-speed welding of the dissimilar aluminum alloys of different thicknesses to address the speed of blank fabrication. Following is a description of each tool design used for the DOE.

Tool A: AJT proprietary tool

Tool B: Threaded, three-flat pin tool with flats equally spaced, convex scrolled shoulder

Tool C: Threaded, three-flat pin tool with flats equally spaced, flat scrolled shoulder

All blanks were fabricated with a lead angle of one degree in the direction of weld travel.

Formability and Strength Performance of High-Speed Welds

Limited dome height testing has shown that welded blanks with the highest dome heights can be correlated with those that have minimal property gradients across the weld zone. Minimal property gradients delay the onset of necking instability. Changes in process parameters will change the local mechanical properties and provide a way to "customize" the weld to the parent sheet. Picking process parameters that match flow stresses between the sheet and the weld zone may be a strategy to increase stamping performance.

In the limited dome height evaluations, two specimens per weld run and tool design in the DOE were tested. Similar trends were observed. All the specimens tested, regardless of tool design and weld travel speed, failed at low loads and "unzipped" on the weld center-line. The weld splitting indicates a poorly consolidated weld. Based on the DIC analysis, the strain accumulated in the parent sheets next to the weld prior to failure ranged from 3–6% depending on the weld process parameters and tool design. Figure 3 is a representative photo of a specimen during testing illustrating the failure mode observed. Figure 4 is a comparison of the weld speed versus failure load of process parameter data from earlier studies and the recent tool design limited dome height test data.

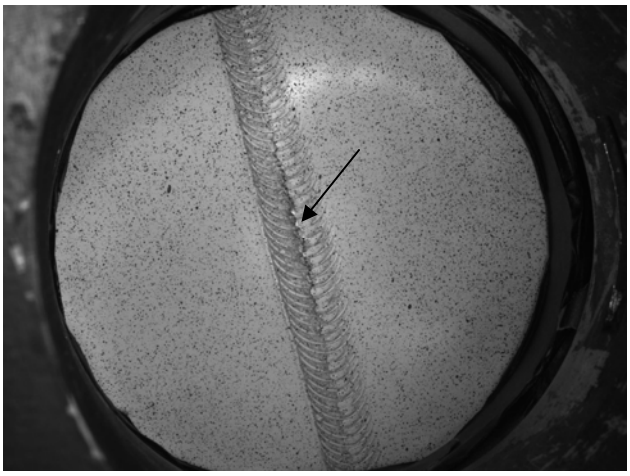

Figure 3. Representative photo of a limited dome height specimen during testing. Unzipping of the weld at the weld centerline can be observed.

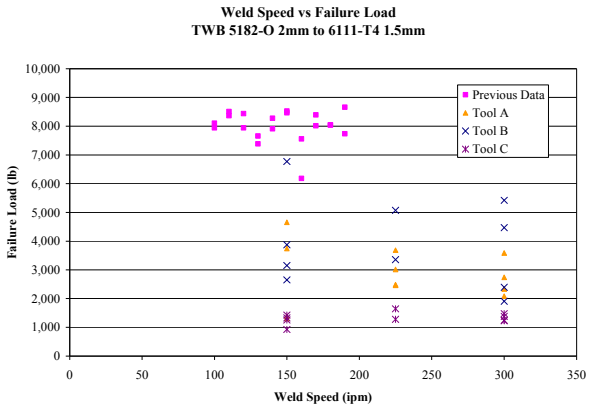

Figure 4. Comparison of the weld speed versus failure load of process parameter data from earlier studies and the recent tool design limited dome height test data.

For the tensile tests, ASTM E-8 sub-size specimens were used. Four specimens were tested for each weld run and tool design in the DOE. The peak load strengths varied among the specimens depending on the tool and process parameters. All the specimens fabricated from Tool C, regardless of welding speed, failed in the weld centerline. Most specimens fabricated from Tool A, except three, also failed in the weld centerline. Two of the four specimens fabricated at 150 ipm and 2000 rpm and one of the four specimens fabricated at 225 ipm and 2750 rpm failed in the 6111 thin sheet material near the HAZ. As with Tool A, most specimens fabricated from Tool B, except three, failed in the weld centerline. Two of the four specimens fabricated at 150 ipm and 3500 rpm and one of the four specimens fabricated at 225 ipm and 2750 rpm failed in the 6111 thin sheet material near the HAZ. Figure 5 is a representative photo of the two failure modes observed among the tensile specimens.

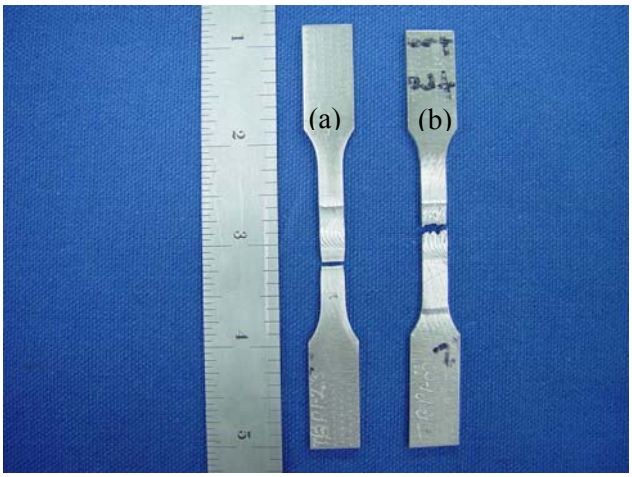

Figure 5. Photo representative of the specimen failure modes observed after tensile testing: (a) in the 6111-T4 thin sheet material near the HAZ and (b) unzipping in the weld centerline.

Overall, the formability and strength results of the high-speed welds in this current work were poor. The results are significantly below those from previous work, as illustrated in Figure 4. It is speculated that a weld defect was generated during welding of the blanks (this will later be verified through microstructural analysis) and contributed to the "unzipping" of the welds observed during testing. In addition, the welding setup conditions were not optimum for Tool B and Tool C. These two tools were designed with longer pin lengths to ensure full con-

solidation of the weld and were designed to be used with a transverse tilt (a rake angle perpendicular to weld travel) to accommodate the dissimilar sheet thicknesses. The pin lengths were also shortened during fabrication of the blanks.

To continue with the investigation of high-speed welding, new welded specimens will be fabricated with the same three tool designs; however they will implementing a transverse tilt with no modification to the pin lengths. The DOE test matrix will be repeated. All results from the limited dome height and tensile tests will be fed into the DOE to hone in on one tool design for high-speed welding. Further investigation of the optimum joining process parameters will occur in a second round of testing, in which a second DOE matrix will be created to establish the optimum weld conditions.

Conclusions

From this investigation, the following conclusions were derived:

- FSJ is suitable for fabricating aluminum TWBs.
- The FSJ process is "customizable" for mechanical properties, and the weld process parameters can be optimized for formability.
- Further investigation of tool design and weld process development is needed to determine optimum joining process parameters for high-speed welding of 5182-O /6111-T4 TWBs.

Publications

G. J. Grant, R. W. Davies, E. V. Stephens, et al., "The Formability of Friction Stir Welds in Automotive Stamping Environments," *SAE Transactions Journal of Materials & Manufacturing* **114**(5), 619–629 (2006).

D. Friction Stir Joining and Processing of Advanced Materials including MMCs

Principal Investigator: Glenn J. Grant
Pacific Northwest National Laboratory
P.O. Box 999, 902 Battelle Blvd., Richland, WA 99352
(509) 375-6890; fax: (509)375-44; e-mail: glenn.grant@pnl.gov

Project Manager: Moe Khaleel
Pacific Northwest National Laboratory
P.O. Box 999, 902 Battelle Blvd., Richland, WA 99352
(509) 375-2438; fax: (509) 375-6631; e-mail: moe.khaleel@pnl.gov

Chief Scientist: James J. Eberhardt
(202) 586-9837; fax: (202) 587-2476; e-mail:james.eberhardt@ee.doe.gov
Field Technical Manager: Philip S. Sklad
(865) 574-5069; fax: (865) 574-6098; e-mail: skladps@ornl.gov

Participants:
Bill Arbegast, Stan Howard, Casey Allen
Advanced Materials Processing Center
South Dakota School of Mines and Technology
Rapid City, S.D.

Contractor: Pacific Northwest National Laboratory
Contract No.: DE-AC06-76RL01830

Objective

- Develop friction stir joining and processing (FSJ/P) to enable widespread use of lightweight, advanced materials in heavy vehicle manufacturing.

Approach

- Develop new technologies within the broad topic area of FSJ/P that facilitate lightweight manufacturing methods and new materials for use in heavy vehicle application.
- During 2006 the project focused on two primary areas:
  - Using FSJ to join sheet materials for superplastic forming applications
  - Developing fundamental process models using a new approach: smooth particle hydrodynamics (SPH)

Accomplishments

- Developed FSJ weld metal with superplastic properties to facilitate large, multisheet SPF or integrally stiffened panel applications for heavy vehicle cab structures.
- Fabricated proof of concept multisheet panels joined together by FSJ and SPF formed into stiffened structural panels.
- Developed unique computational code based on SPH to predict material flow, mixing and defect formation in FSJ/P.
- Collaborated with researchers at the South Dakota School of Mines and Technology (SDSMT)in a numerical modeling study of the strength and dampening characteristics of fabricated multisheet panels.

Future Direction

- Develop weld process parameters that enhance superplasticity in joined assemblies to allow for part consolidation in lightweight SPF cab structures.
- Test multisheet and integrally stiffened panel for strength, modulus, and other mechanical performance metrics.
- Parallelize SPH computational code to run on supercomputers to improve the ability of the model to define fine features of flow, defect formation, and tool designs in friction stir joined or processed material.

Introduction

Friction Stir Joining

One of the key strategies for making a vehicle energy-efficient is to manufacture it from lighter materials. Structural and functional requirements, however, lead to a situation in which no single lightweight material is appropriate for all applications. A modern, weight-optimized vehicle structure is a hybrid of many materials. A critical problem that has emerged in the development of these hybrid structures is that for many material combinations, traditional joining technologies (e.g., fusion welding or mechanical fastening) are not appropriate. For some highly specialized materials, like aluminum metal matrix composites (MMCs), titanium, and advanced high-strength steels, a better joining technology can have significant impact on whether these materials have a role in future vehicle structures.

In the past 15 years, the new joining technology, FSJ, has emerged and has the potential to join many lightweight materials. Invented by TWI, Ltd., FSJ is a solid-state process that employs severe plastic deformation to create joints between wide varieties of different materials. A typical FSJ butt joint is depicted in Figure 1. The weld is created by clamping the materials to be joined and plunging a spinning tool into the surface. The spinning tool is then translated down the joint line, leaving behind a weld zone characterized by a fine-grained, dynamically recrystallized microstructure. Typically, the tool is spun at 400 to 2000 rotations per minute (rpm) and translated down the joint line at a rate of 4 to 300 in./min (ipm), depending on tool design, base material, and thickness. As the tool rotates and translates, complex flow patterns develop in the base material that create an intimate mixing of materials from both sides of the weld. Heat input during plastic deformation generally creates a temperature in the weld between 0.6 and 0.8 of the absolute melting temperature so that no liquid phase is generated.

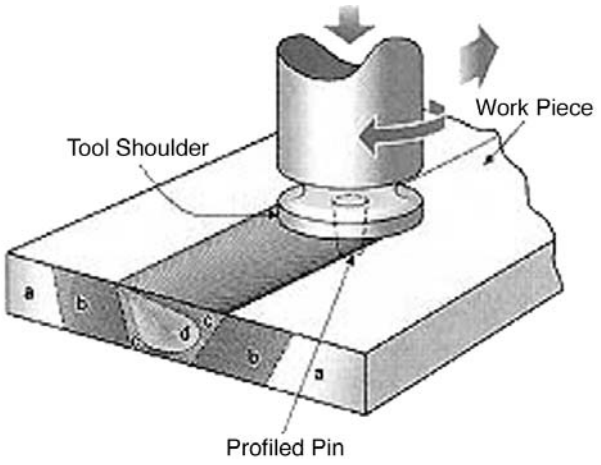

Figure 1. Friction stir joining and processing are accomplished by plunging a spinning tool into a material and translating the tool across the surface to form either a joint or a surface processed region (*Source:* TWI, Ltd.).

FSJ is capable of producing aluminum and magnesium alloy welds as good as, or better than, fusion welds in terms of joint efficiency, mechanical properties, and environmental robustness. A significant advantage of the process, for application to hybrid structures, is that since there is no melting during the process, a large variety of dissimilar material joints are possible, including dissimilar aluminum and magnesium joints that are not possible with conventional fusion welding.

In the past 10 years, FSJ has been shown to be a commercially important, energy-efficient, and environmentally friendly process for joining aluminum. However, there are many opportunities for other higher-strength lightweight materials to be considered if good joining technologies existed for these materials as well. The objective of this project is to investigate how FSJ can be applied to advanced materials including AL-MMCs, titanium, steels, cast iron, superplastic materials, and materials that display graded structures with unique surface properties.

Approach

The basic objective of this project is to investigate and develop FSJ and FSP as viable industrial techniques for advanced lightweight materials. During 2006, the project concentrated on two main task areas: (1) development of FSJ/P as a process to join sheets that will be subjected to superplastic forming, and (2) development of numerical, physics-based modeling strategies to help define the fundamental process and predict process conditions.

The primary task in 2006 was the application of FSJ to superplastic forming environments. Numerous opportunities exist to use this manufacturing technology to reduce weight on heavy vehicles. One barrier to SPF manufacturing is that hang-on truck components are complex and often very large—larger than the standard coil widths. If sheets are joined together to make a large part by fusion welding, the weld region does not deform superplastically because of the coarse microstructure of fusion weld metal. FSJ produces a weld region that is formable by SPF and may be an enabler for complex or large structures that are joined, then later hot gas formed in single operations to form cab structures and panels.

The second task investigated was continued development of a numerical modeling process using SPH. This modeling approach has not been previously applied to FSJ/P, but our preliminary work suggests that it may be able to provide significant insight into the fundamental nature of the heat generation and material flow that occurs during the FSJ/P process.

Results

Task 1 — FSJ/P for SPF manufacturing

Superplastic forming (SPF) is a lightweight manufacturing technology that has shown to be cost effective and produce weight-optimized structures through reduction in part count and through the use of lightweight materials.

One important factor that is relevant to the particular problems of heavy vehicle SPF is that truck parts are large. The parts are modulus (stiffness) driven, not strength driven, because of aero flutter and shear size. Big parts need stiffeners. This requires a complex assembly. One cost effective and lightweight option is to join multiple flat sheets together, then use SPF to join the entire multisheet pack together in one operation. This incorporates the stiffener into the assembly. The problem with this strategy revolves around the method chosen to join the sheets together. If the sheets are fusion welded, the microstructure of the fusion weld region will not deform superplastically. Figure 2 shows the coarse microstructure of a fusion welded aluminum sheet. When these joints are subjected to superplastic forming, the joint remains undeformed. These undeformed areas also have very poor postforming mechanical properties. In contrast, FSJ leaves behind a weld microstructure that is highly deformable at SPF conditions.

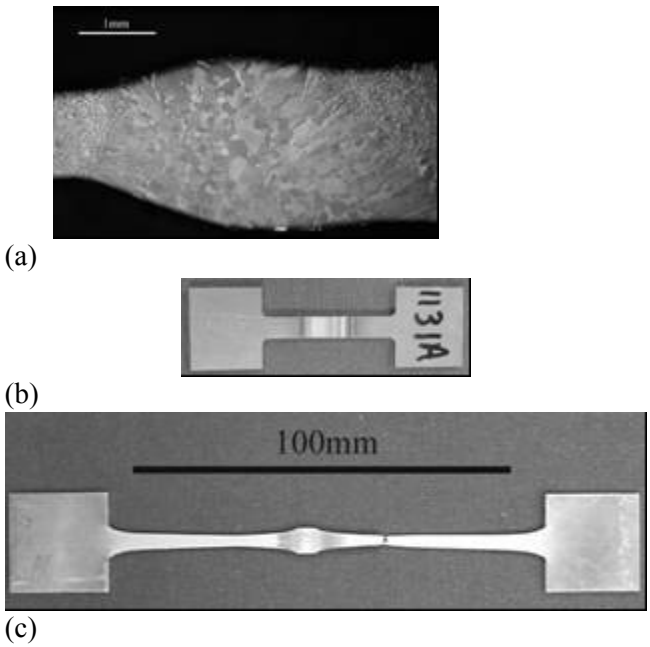

Figure 2. (a) Weld nugget region in a butt weld between aluminum sheet materials showing coarse, cast microstructure of a fusion weld. (b) Transverse tensile specimen. (c) Transverse tensile test at SPF conditions shows the undeformed nature of the fusion weld metal.

This project is investigating the particular weld process parameters and part geometries that could produce an integrally stiffened panel for a heavy vehicle cab application. The work to date involves fabricating multisheet assemblies as shown in Figure 3. These assemblies have been SPF formed into structural panels in three configurations, “egg crate,” “hat stiffened,” and “doughnut.” The purpose of the test forms is to discover the correct FSJ process parameters and the best SPF deformation possible in these geometries. The panels are made using both linear FSJ and friction stir spot welding (FSSW)

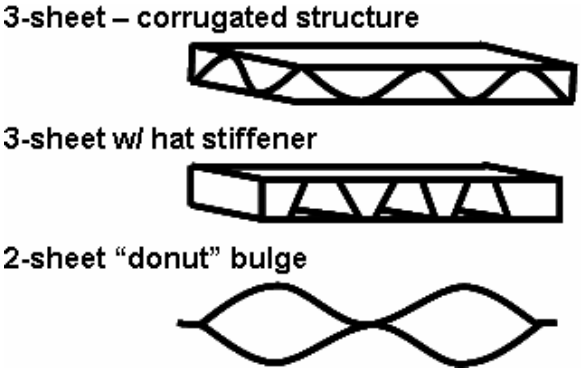

Figure 3. Geometries of test panels fabricated for this program

(Figures 4 and 5). The FSSW joints are of particular interest because they are made using a new process that does not leave an exit hole after the spot joint is made. This process, called the "refill" method was invented by GKSS (Riftec) and the panels were fabricated at the facilities of our project partner, SDSMT.

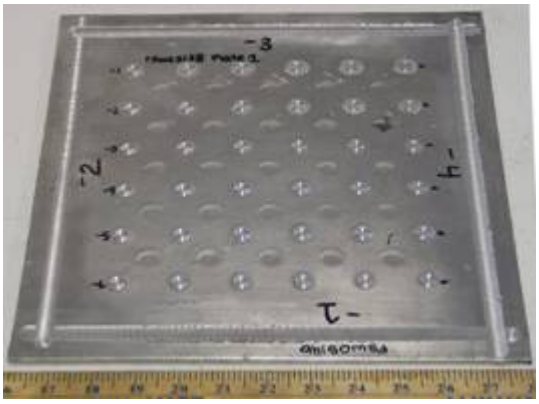

Figure 4. Friction stir spot welded three-sheet multisheet pack prior to SPF testing. This configuration is designed to produce the corrugated structure. Alternating spot welds are made from each side of the multisheet pack using the "Refill" (GKSS-Riftec) FSSW method at the SDSMT.

Structural panels like those shown in Figures 6, 7, and 8 were successfully formed by SPF at 530ºC, both with and without die constraint. Offset linear friction stir joints on the multisheet pack produce a truss structure, and offset friction stir spot welds produce an egg crate structure (truss on the diagonal).

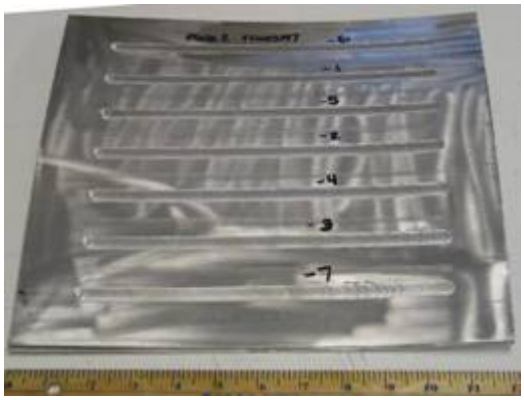

Figure 5. Linear friction stir welded multisheet pack prior to SPF testing. This configuration is designed to produce the "three sheet with hat stiffener" structure. Alternating linear welds are made from each side of the multisheet pack using a pin that penetrates only through the upper two sheets.

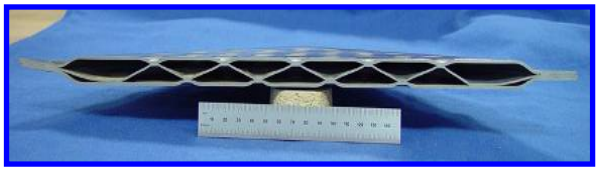

Figure 6. Structure formed from multisheet packs joined together as sheets then subsequently hot-gas formed into a lightweight structural panel

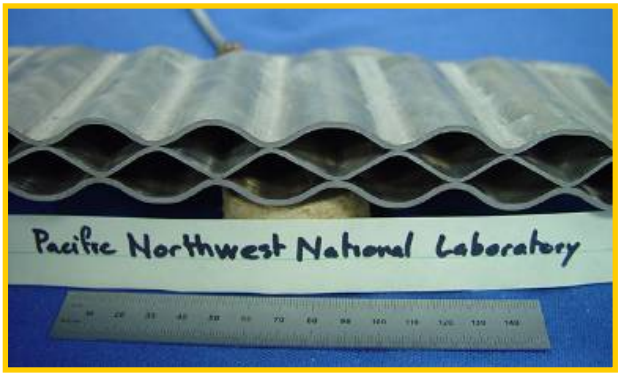

Figure 7. Sheet pack cross section after SPF. This structure was fabricated with no constraining die platens.

A particular advantage of shapes like those shown in Figure 8 is that they are hollow with interconnected channels between the outer sheets. This shape gives the panel a 3-D structural stiffness, but

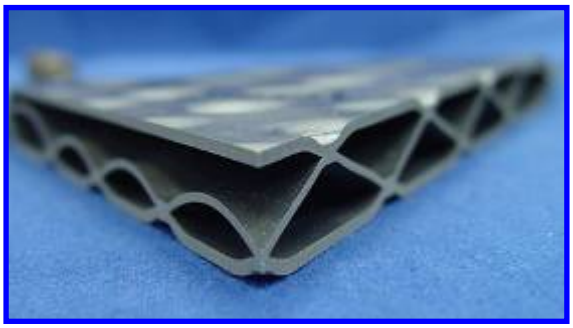

Figure 8. Two side cross section of a friction stir spot welded multisheet structure using die platens with a 1-in. standoff.

it also gives it particular properties for dampening, vibration, energy absorption, and thermal conductivity. Essentially, the airspace and shape of the structure acts to isolate one side of the sheet from another. This allows these panels to have very good properties as noise, vibration, harshness (NVH) resistant structures. They also can be used to thermally isolate one area from another as is might be required for a firewall structure, or used as a crash energy absorption structure. The inclusion of space filling foams either metallic or polymeric can further enhance these properties.

To investigate the effects of different internal shapes on the static, vibrational, and energy absorbing characteristics, researchers at the facilities of our project partners at SDSMT have completed a numerical model of the static stresses and modal frequencies of the different panels fabricated at PNNL (Figure 9). The results of this work illustrate the positive advantages that "sandwich" panels can have as compared with monolithic sheet.

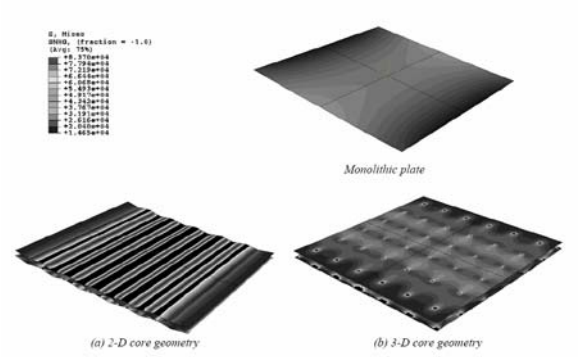

Figure 9. Von Mises contour plots of the sandwich panels from static analysis. (*Source:* Karim H. Muci-Kuchler, et al., 2007)

Task 2 — FSJ/P Numerical Modeling

Work continued in FY 2006 on a new modeling approach to investigate the fundamental flow and heat generation properties of the friction stir process. The industry has struggled with modeling this process for 10 years because the high strains and high strain rates are very difficult to capture in conventional modeling approaches. Conventional modeling techniques such as finite element modeling and computational fluid dynamics suffer from many issues, mostly surrounding the need for the model to track huge variations in strain, temperature-dependent flow stress, strain rate, and heat generation.

The modeling approach we have started to investigate in this program is a departure from other approaches and involves the use of SPH. This is a fully Lagrangian particle method, so no grids are required. The code solves 2-D and 3-D equations for continuity, momentum, and energy balance. The model uses a temperature-dependent shear stress equation (Johnson Cook formulation) to track stress/strain response so material databases are easier to incorporate as input parameters.

The model currently can explicitly model mixing of materials, predict temperature generation at the surface of the tool as well as that due to viscous dissipation, and produce temperature and strain histories for any material point in the field. This may allow it to make microstructural prediction at different parts of the weld since temperature and strain history can be tracked, although this has not as yet been implemented in the code. Figure 10 shows some example output from the model.

Fully implemented, the code should be able to make predictions on the effects of tool shape and changing process parameters and help to provide a fundamental physical understanding of the FSJ process.

Conclusions

FSJ/P technologies will enable the application of many lightweight materials in the next generation of transportation systems. It is envisioned that structural multisheet panels can play a key role in making vehicles lighter weight. In addition, these panels hold opportunities for multiuse structures, such as metal or polymeric foam filled sheet packs with buckle resistance or internal dampening for better NVH performance.

The results of this work will allow designers to anticipate and implement structures that are a hybrid of many different materials, facilitate the application of lightweight superplastically formed structures, and suggest new materials and engineered surfaces that can help deliver lighter and more fuel-efficient vehicles.

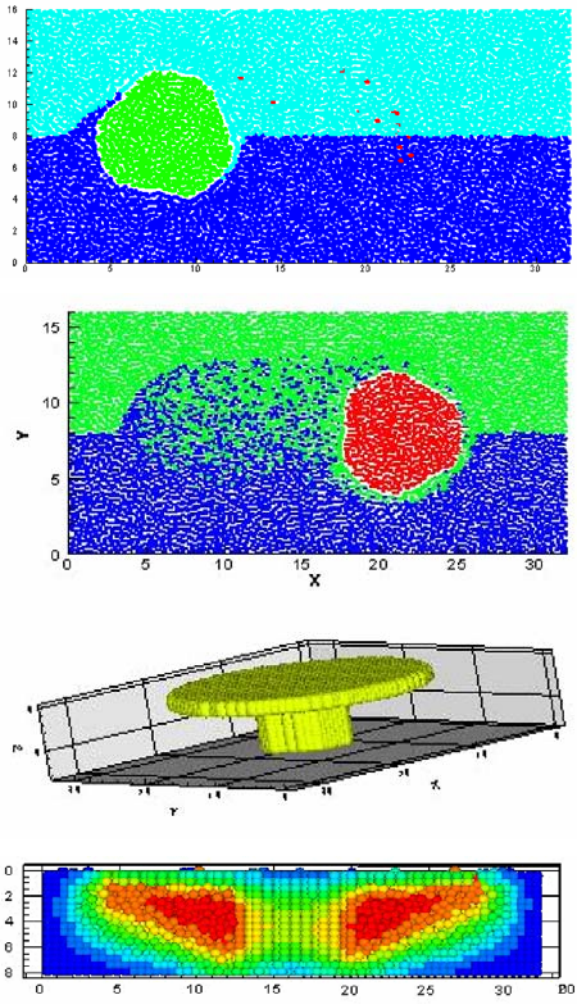

Figure 10. Model output. Upper two figures show mixing of dissimilar materials using a tool with three flats on the pin. (Only the tool pin is shown in this 2-D simulation.) The lower two figures show arrangement of 3-D model and a temperature distribution. Highest temperatures are in a region near the pin root away from the pin surface, due to heat generated by plastic work and conduction into the pin.

Presentations/Publications/Patents

1. Tartakovsky, A., Grant, G., Sun, X., and Khaleel, M., "Modeling of Friction Stir Welding (FSW) Process with Smooth Particle Hydrodynamics (SPH)," *Welding and Joining and Fastening and Friction Stir Welding,* SAE Special Publication SP-2034, SAE, 2006.
2. Grant, G.J., Herling, D., Arbegast, W., Allen,C., Degan,C., "Superplastic Forming of Aluminum Multisheet and Integrally Stiffened Structures Fabricated Using Friction Stir Welding and Friction Stir Spot Welding," (abs) *9th International Conference on Superplasticity in Advanced Materials (ICSAM 2006),* Chengedu, China, June 2006.
3. Grant, G.J., Herling D., "Friction Stir Welding to Facilitate Superplastic or Quick Plastic Forming of Complex Automotive Structures," (abs) *Society of Automotive Engineers 2006 World Congress*, Detroit, April 2006.
4. Tartakovsky A.M., G.J. Grant, X. Sun, S. Hong, and M.A. Khaleel, "Smooth Particle Hydrodynamics (SPH) Model For Friction Stir Welding (FSW) of Dissimilar Materials." In *6th International Symposium on Friction Stir Welding, Saint-Sauveur,* Canada, October 10, 2006. PNNL-SA-52321, 2006.
5. Muci-Kuchler, K.H. S.K. Annamaneni, D.R. Herling, and W.J. Arbegast, "Numerical Simulation of the Static and Dynamic Response of Corrugated Sandwich Structures made with Friction Stir Welding and Superplastic Forming," In *Friction Stir Welding and Processing IV*, Eds. R.S. Mishra, M.W. Mahoney, T.J. Lienert, and K.V. Jata, TMS (The Minerals, Metals and Materials Society), to be published in 2007.

E. Friction Stir Welding and Processing of Advanced Materials

Principal Investigator: Zhili Feng
Oak Ridge National Laboratory
1 Bethel Valley Road, Oak Ridge, TN 37831
(865) 576-3797; fax: (865) 574-4928; e-mail: fengz@ornl.gov

Chief scientist: James J. Eberhardt
(202) 586-9837; fax: (202) 587-2476; e-mail: james.eberhardt@ee.doe.gov
Field Technical Manager: Philip S. Sklad
(865) 574-5069; fax: (865) 574-6098; e-mail: skladps@ornl.gov

Participants:
Michael L. Santella, Oak Ridge National Laboratory
Tsung-Yu Pan, Ford Motor Company

Contractor: Oak Ridge National Laboratory
Contract No.: DE-AC05-00OR22725

Objective

- Develop the technological basis for friction stir welding and processing (FSW/P) of advanced high-strength and lightweight materials for the automotive industry.
- Gain fundamental understanding of the relationships between workpiece and tool material properties during FSW/P.
- Characterize the mechanical properties and microstructures of joints.
- Correlate the proprieties and microstructures produced by FSW/P to the process conditions.

Approach

- Conduct experimental welding and processing tests on advanced materials using the state-of-the-art FSW/P process development system.
- For particular workpiece materials, select the tool material based primarily on high-temperature strength, wear resistance, and chemical compatibility.
- Evaluate mechanical properties and their correlation with microstructures produced by FSW/P.
- Develop predictive modeling capability to study the properties as a function of process conditions.

Accomplishments

- Completed a study of FSP to improve properties of cast magnesium (Mg) alloy AM60B.
- Demonstrated the feasibility of friction stir spot welding (FSSW) of Mg alloy AZ31.
- Completed further process development to improve the properties of FSSW of aluminum (Al) alloy.

Future Direction

- Investigate the effects of heat treatment on the fatigue life of FSP cast Al alloys.
- Develop new approaches for FSSW without an exit hole to improve structural properties of the joint.
- Carry out FSSW of other lightweight materials and dissimilar welds.

Introduction

Friction stir welding (FSW) is a novel solid state joining method that was described in detail in previous reports. The uniqueness of the process is creating new opportunities for welding both mature alloys and newer alloys, as well as enabling their consideration in a wider range of applications.

The use of FSW for many wrought Al plate alloys has been a great success. Nevertheless, the technology is still rapidly evolving. There is tremendous interest in and efforts to extend the technology to welding a wide range of both high-performance lightweight alloys and high-melting-temperature alloys. In addition, novel applications of the process other than welding are emerging. For example, it can be used to thermomechanically process (FSP) a material for microstructure refinement and property enhancements.

This program aims at advancing FSW/P technology to promote the increased use and adoption of high-strength lightweight materials in automotive structures, particularly heavy vehicles. It supports the goals of the Office of Heavy Vehicle Technology to increase fuel efficiency and reduce emissions of heavy trucks by weight reduction without sacrificing strength and functionality.

In FY 2006, we continued studies on FSP of cast Mg alloys and FSSW of wrought Mg alloys and Al alloys. Part of the project involves a cooperative research and development agreement (CRADA) with Ford Motor Company on FSW of wrought and cast Al and Mg alloys for vehicle structure applications. An effort related specifically to tool material development is also continuing.

Feasibility of Spot Friction Welding AZ31 Magnesium

Magnesium alloys are receiving a great deal of attention in the automotive industry because of the weight-saving potential they offer compared with both steel and Al alloys. Most current Mg parts are produced from cast Mg alloys, such as AZ91 and AM60; however, wrought Mg alloys such as AZ31, AZ61, AZ80 and ZK60 are beginning to draw attention for body and chassis parts.[1]. Among these wrought alloys, AZ31 is the most common Mg alloy available in sheet form. They are produced by direct-chill casting, followed by hot rolling, or by a twin-roll continuous casting process.

There have been relatively few studies on the joining of wrought Mg alloys. Fusion welding—such as gas metal arc welding, gas tungsten arc welding, resistance welding, laser welding, and e-beam welding—can be used with wrought Mg alloys, but it can cause the formation of a brittle inter-metallic phase ($Mg_{17}Al_{12}$) in the welds,[1] causing reduced weld strength.

In comparison, FSW offers a significant quality advantage over the conventional fusion welding processes for Mg alloys. Fusion welding requires parent metal to melt and solidify, causing potential defects such as voids, trapped gas, and solidification cracking. FSW does not require melting of the parent metal and thus eliminates the formation of these defects.

Experimental

Magnesium alloy AZ31B-H24 sheets, 1.58 mm thick, were obtained from Magnesium Elektron N.A. The nominal composition was 3.0 wt.% Al, 1.0 wt.% Zn, 0.2 wt.% Mn, and balance Mg. The sheets were heated to 0 temper at 412°C for 10 minutes before spot friction welding experiments. Sheets were cut to 100×30 mm coupons. The spot-friction-welded specimens were prepared in lap-shear configuration with 30-mm overlap. Two different sample surface conditions were prepared. One was as-received with a dark-gray oxide layer on the surface. The second group was cleaned and wire-brushed to remove most of the surface oxides.

The spot friction welding process was carried out using an MTS Systems FSW system at Oak Ridge National Laboratory. The SFW tool was a fixed-pin probe-type tool with a 15-mm diameter at the tool shoulder. The 15-mm-diameter spot friction

welding tool was chosen because it was close to the recommended electrode diameter (15.9 mm) for resistance spot welding of 1.6-mm-thick AZ31B.[2,3] The process used a displacement-control algorithm with an insertion depth of either 2.4 or 2.8 mm and four different rotational speeds—500, 1,000, 1,500 and 2,000 rpm. The process time was fixed at 2 s for each joint, which was considered to be typical of a production operation. Tensile tests of lap shear coupons were conducted on an Instron mechanical testing machine with a crosshead speed of 12.5 mm/min. Three replicates were produced for each joining condition.

Results and Discussion

Lap Shear Strengths

Maximum tensile loads, identified as lap shear strengths, of spot-friction-welded AZ31 versus tool rotational speed are presented in Figure 1 with the standard deviation associated with each averaged data point. In general, the specimens with surface oxides removed had higher strength than the as-received specimens. The highest lap shear strength achieved was 4.75 kN with oxide-removed specimens at 2.4-mm insertion depth and 1000 rpm. Specimens with surface oxide cleaned showed failure occurring as circumferential cracking around the weld button, whereas for the as-received specimens, bond failure occurred between the two sheets at the spot weld location (interfacial), as shown in Figure 2.

The lap shear strength was also dependent on the rotational speed and the insertion depth. Increasing the rotational speed for the specimens with surface oxide removed from 1000 to 2000 rpm reduced the lap shear strength from 4.75 to 3.9 kN. The low rotational speed of 500 rpm produced the weakest spot-friction-welded joints. The as-received specimens produced with a 2.4-mm insertion depth and 500-rpm rotational speed had an average lap shear strength of 2.6 kN, much lower than those made at 1000 (3.9kN), 1500 (4.1 kN) and 2000 (3.4 kN) rpm. The results indicate that the slower rotational speed could not generate enough frictional heat and/or stirring to produce satisfactory joints.

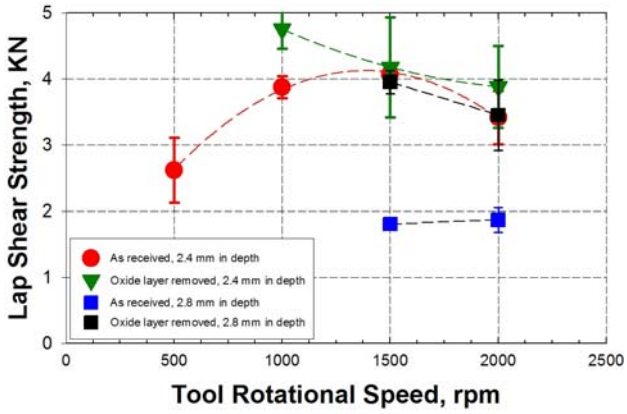

Figure 1. Lap shear strength vs tool rotational speed in spot friction welding of AZ31 at two different insertion depths (2.4 and 2.8 mm) and two different surface conditions (as received and oxide layer removed).

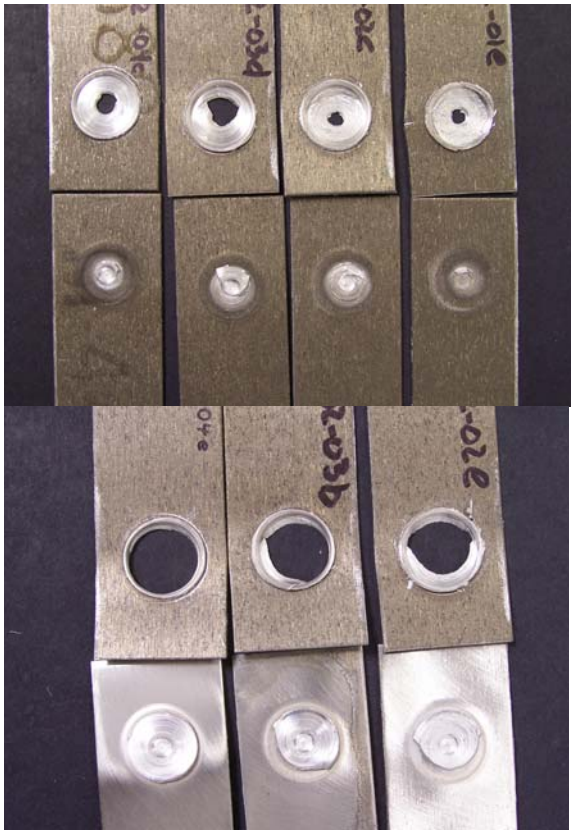

Figure 2. Tension-tested lap-shear specimens (top, as-received and bottom, oxide layer removed). The number shown on each figure refers to the tool rpm. The insertion depth was 2.4 mm.

Spot-friction-welded joints produced from specimens with surface oxide cleaned had higher lap shear strength than did as-received specimens. This was especially evident on the specimens with a

2.8-mm insertion depth. The differences were approximately 2 kN (at 1500 rpm) to 1.5 kN (at 2000 rpm); however, the difference was less for the specimens with a 2.4-mm insertion depth.

Comparison with Resistance Spot Welding

The most widely published spot joining method for wrought Mg is resistance spot welding (RSW). The study was first pioneered in 1953 by Klain et al.[4] and later adopted as an industrial standard with recommended equipment, electrodes, and process parameters.[2,3] The Resistance Welder Manufacturers Association (RWMA)[2] lists the minimum average tensile shear strength requirements for various Mg alloys and thicknesses. The data were generated using two different RSW equipment setups, including a 3-phase frequency converter machine and a single-phase alternating current machine (Figure 3). The minimum average tensile shear strength, using RSW for Mg specimens 1.58 mm thick, was between 2.4 kN (single-phase A/C machine) and 3.6 kN (3-phase machine with post-heat). All data for spot friction welding joint strength from this study are overlaid and presented in Figure 3. It is shown, without optimization in this study, that joint strengths as high as 4.75 kN are possible using the spot friction welding process.

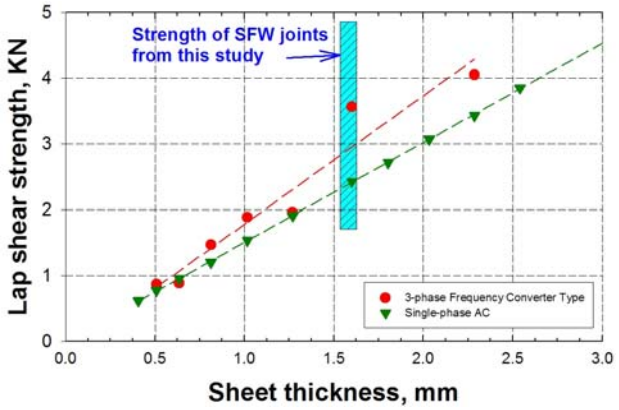

Figure 3. Comparison of lap shear strengths of spot-friction-welded and resistance-spot-welded AZ31. (Data for resistance-spot-welded joint strength are from ref. 4.)

The lap-shear strength, t-peel strength and fatigue performance of spot friction welds of Al are as good as or better than those of RSW, self-piercing rivets (SPR), or clinching.[5,6] In a recent cost analysis, costs were favorable for spot friction welding compared with RSW and SPR. Spot friction welding does not require a large power source, cooling water, or a compressed air supply as does RSW. The electrical consumption of spot friction welding is less than 1/20 th that of RSW.[7,8] Other merits of SFW include long tool life, high productivity, high reliability, and better working environment.[7]

Conclusions

Lap joints of 1.58-mm-thick Mg alloy AZ31B-O sheet were produced by spot friction welding. Tensile-shear testing showed that joint strengths of up to 4.75 kN were obtained. The spot friction weld strengths agree favorably with minimum spot weld strengths specified by the RWMA for similar Mg alloy sheet using the recommended 15.9-mm-diameter RSW. The removal of surface oxides from the sheets prior to welding increased lap shear strengths by about 50% at the 2.4-mm insertion depth, and it promoted failure by nugget pullout rather than by interface separation.

Friction Stir Surface Modification of AM60B Magnesium Die Castings

Experimental

Die-cast plates with dimensions of 127×25×6 mm were made of the AM60B by a cold chamber casting process under protective atmosphere. The nominal chemical composition of the plates was (5.4–6.1) Al + 0.13 Mn wt%. They contained about 5% porosity on average from entrapped gas, which is typical of the HPDC process used to cast them. The surfaces were left in the as-cast condition rather than being ground or polished before FSP.

FSP was conducted on a Bridgeport milling machine fitted with a 1.1-kW electric motor. The position of the milling machine spindle was fixed relative to its table so that the stir processing was conducted in a displacement-control mode. The stir tool was made of H13 steel with a shoulder diameter of 8 mm. The pin was cylindrical with a hemispherical tip; its dimensions were 3 mm diameter × 2 mm length. The working surfaces of the stir tool were smooth. Two tool rotation speeds were used: 1250 and 2500 rpm. The translation speed was fixed at 1.7 mm/s throughout the experiments. These conditions were used to make stir passes with lengths of about

100 mm. Some testing and analysis was done using single stir passes. Other plates were processed with 5–6 passes overlapped on intervals of about 2 mm. Overlapping the passes created relatively consistent stir-processed volumes in the plates with dimensions of about 1.5–2×10×100 mm.

The room temperature properties of the FSP surfaces were measured by Vickers microhardness testing and tensile testing. The microhardness measurements were made on metallographically prepared specimens taken to view the surfaces of stir passes. The indentations were made under a 50-g load in 200×200 μm arrays extending from the stir zones into the base metal.

The bars with the overlapped passes were used to make tensile specimens. For the tensile specimens, blanks were cut by electrical discharge machining (EDM) from the stir zones using the shape specified in ASTM E8 for rectangular subsize specimens. Slices 2 mm thick were then EDM cut from both surfaces of the blanks to provide one specimen of base metal and one specimen where the gage section was entirely within the FSP material. The gage dimensions were 1 mm thick × 6.2 mm wide × 25 mm long. The nominal strain rate for the tensile tests was 1×10^{-3}/s.

Results and Discussion

A cross-sectional view showing the appearance of a single-pass surfacing layer made at 2500 rpm is shown in Figure 4(a), and a similar view of a multipass layer made at 1250 rpm is shown in Figure 4(b). In both cases, some relatively large pores are visible in the base metal, but none were found in the stir zone. The base metal pores are characteristic of those commonly found in die-cast AM60. This indicates that the heat from FSP was not sufficient to promote the growth of pores in the heat-affected zone regions or the reheated stir zones of prior passes. The microstructure in the stir zone of the single-pass layer is shown in Figure 4(c). The stir zone consisted primarily of very fine equiaxed grains with sizes in the range of 5–10 μm. There is no evidence of solidification structure, and the material in the stir zone appears to contain only relatively small second phase particles. This grain

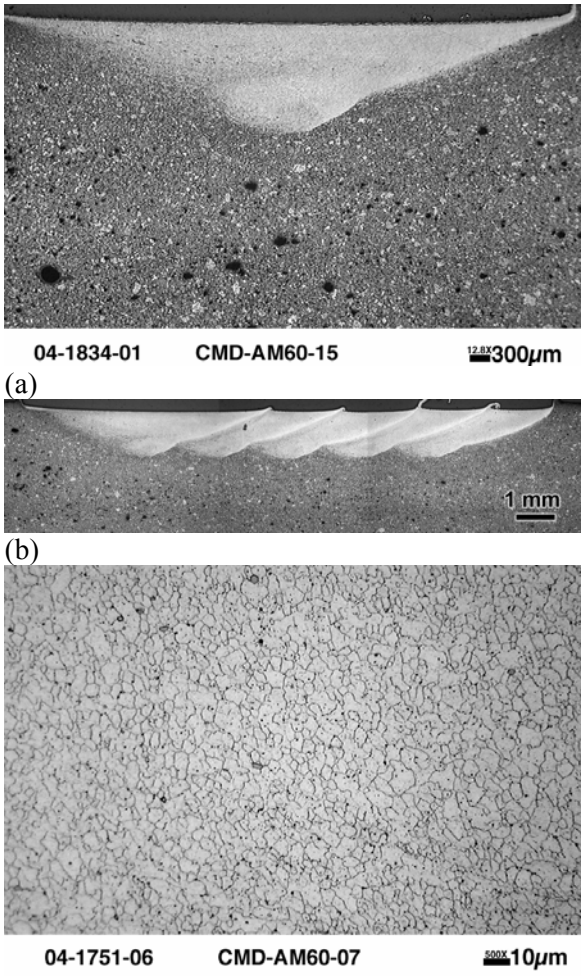

Figure 4. Optical micrographs showing cross section views of (a) a single stir pass in AM60B made at 2500 rpm; (b) five overlapped stir passes made at 1250 rpm, and (c) the microstructure of the single stir pass.

structure was also typical of that observed in the multipass layers.

Stir zones were also examined in a scanning electron microscope (SEM). The micrographs presented in Figure 5 more clearly illustrate the effects stir processing had on the AM60B microstructure. The base metal microstructure [Figure 5(a)] shows the two major phases expected in AM60B die castings, the Mg matrix that forms the continuous phase plus large particles of $Mg_{17}Al_{12}$.

The microstructure near the horizontally oriented boundary between the base metal and the stir zone is shown in Figure 5(b). At this location the shape change of the $Mg_{17}Al_{12}$ particles indicates the

extensive deformation associated with the stir processing. In addition, the amount of $Mg_{17}Al_{12}$ decreases as the boundary between base metal and stir zone is traversed. The microstructure in the stir zone is shown in Figure 5(c). At this level of examination, only a very small number of the large $Mg_{17}Al_{12}$ particles were visible in the stir zone microstructure, as most of this phase was apparently dissolved in the Mg matrix by the combination of heat and deformation during the stir processing.

Limited examinations of stir zone microstructures were also conducted by transmission electron microscopy (TEM). The overall microstructure of a single-pass layer at this higher level of detail is illustrated by Figure 6(a). The TEM examinations confirmed that the stir zones consisted largely of an equiaxed Mg solid solution phase with grain size in the range of 5 μm. Also, numerous particles at a size range of several tenths of microns were distributed throughout the microstructure. These were not uniquely identified, but their number and relatively wide distribution indicate that they must be $Mg_{17}Al_{12}$. More detail of the stir zone microstructure is presented in Figure 6(b). At this location several relatively large particles are visible, some situated on grain boundaries. In addition, smaller particles can be seen distributed more uniformly in the matrix phase. Based on the work of Clark,[9] it can be concluded that the smaller, more uniformly distributed particles are also $Mg_{17}Al_{12}$. The general features of the stir zone microstructure regarding grain size and the disappearance of large $Mg_{17}Al_{12}$ particles are consistent with those made by Esparza et al.[10] in thixomolded AM60B.

The results from microhardness testing of a 5-pass surfacing layer are presented in Figure 7. An optical micrograph is shown on the top and an image representation of microhardness distribution on the bottom. The arrays of indents used for the microhardness measurements are also visible in the micrographs and the image representations. For the surface of the 5-pass layer, the average hardnesses were 53.0 ± 7.2 kg/mm^2 in the base metal and 66.2 ± 5.3 kg/mm^2 in the stir zone. For this case, the stir zone experienced an increase in hardness of 25% over that of the base metal. Similar measurements

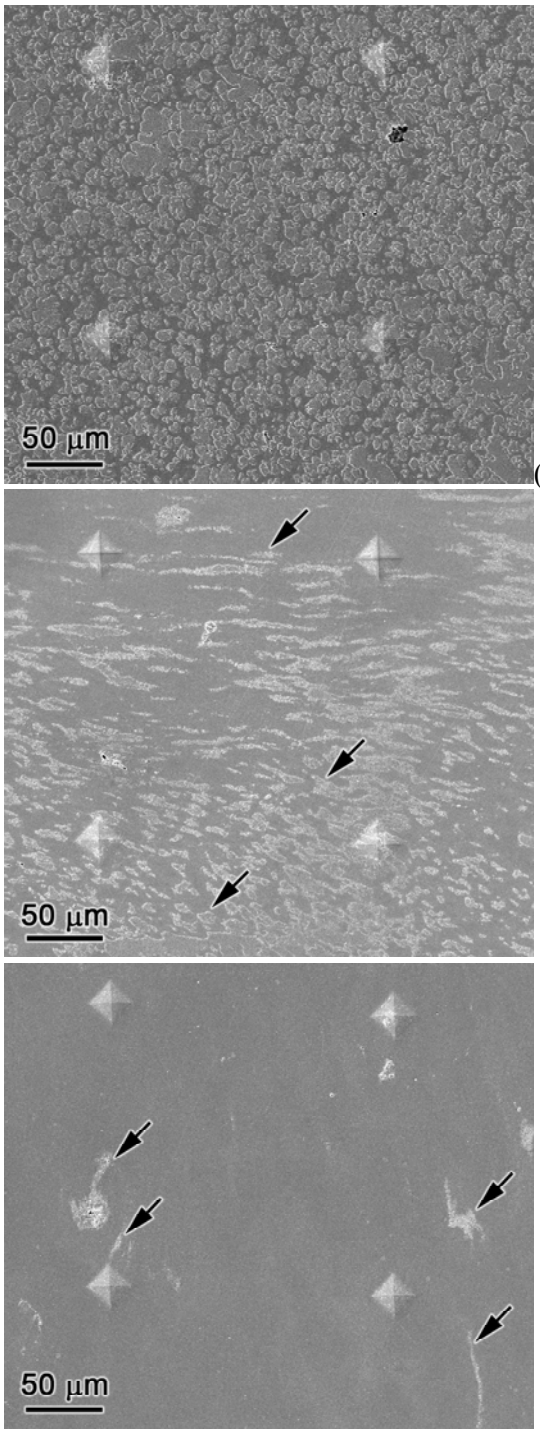

Figure 5. Scanning electron micrographs showing the AM60B microstructure in (a) base metal, (b) near the boundary between the base metal (bottom) and the stir zone (top), and (c) the stir zone. Specimen is unetched. Paricles of $Mg_{17}Al_{12}$ are indicated by arrows in (b) and (c). Indentations from the hardness testing are also visible.

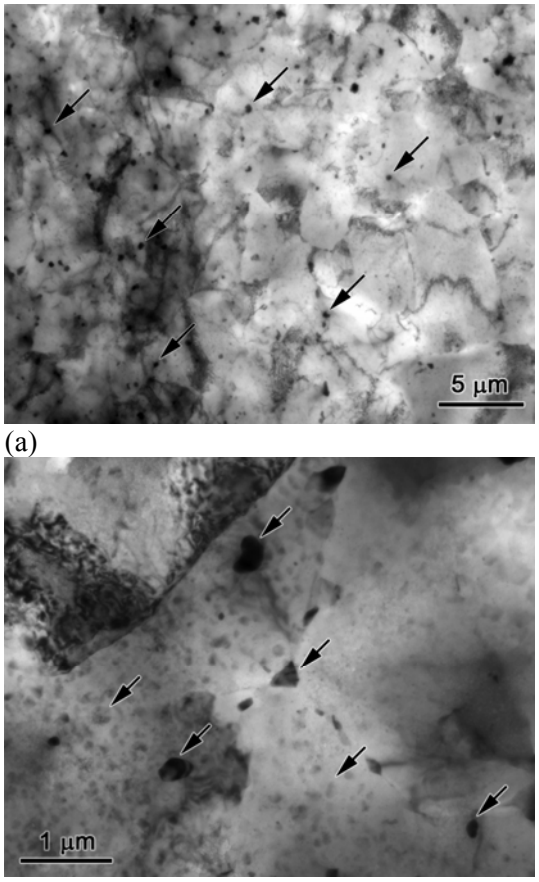

Figure 6. Transmission electron micrographs in a single-pass surfacing layer on AM60B. General structure of equiaxed grains containing $Mg_{17}Al_{12}$ particles (arrowed) is shown in (a). Details in (b) show some larger particles on grain boundaries as well as smaller particles distributed throughout the matrix.

were also made on the surface of a 5-pass layer made with 2500 rpm. The hardness values for this processing condition were 56.9 ± 6.8 kg/mm^2 in base metal and 66.0 ± 5.7 kg/mm^2 in the stir zone.

Summary

The ability of FSP to produce stir passes of high integrity on AM60B was demonstrated. Grain structure in the stir zones was largely equiaxed, with grain sizes of 5–10 μm. Optically, the grains appeared to be all of a single phase. TEM observations revealed a homogeneous microstructure comprising Mg solid solution grains containing small second-phase particles. Based on metallographic evidence and previously reported thermodynamic considerations, the stir zone microstructures were concluded to consist mainly of the Mg matrix containing much smaller $Mg_{17}Al_{12}$ particles than those found in the as-cast material. Microhardness testing indicated that stir processed regions experienced hardness increases up to 25% above base metal.

CRADA with Ford Motor Company: FSW of Lightweight Vehicle Structures

The purpose of this CRADA is to establish the FSW process as a viable candidate for construction of lightweight substructures for trucks and cars, including engine cradles, suspension sub frames, instrument panel supports, and intake manifolds.

The approach is to conduct welding trials to establish acceptable process parameters for producing quality joints that maximize the mechanical performance appropriate for specific applications (e.g., strength, fatigue). The work will be conducted primarily on castings and extrusions of Al and Mg alloys. The project is structured in three phases: coupon testing is used to establish basic behaviors, concept testing to demonstrate commercial viability, and component testing to verify that the processing is developed sufficiently for deployment in production.

Summary

The major technical issues currently being addressed include shortening weld cycle times and maximizing weld joint tensile-shear strength. For lap welds of 2-mm-thick material, weld times of less than 5 s are desired. The target value for tensile-shear strength is a minimum of 4 kN. Another major component of the effort relates to establishing the influence of tool geometry and tool surface features on the process adaptability and joint appearance.

The material being used in this initial effort is the Al alloy 5754, which is under consideration for a variety of structural components. Both 2-mm and 3-mm-thick sheets are being spot welded using several tool designs, including a tool designated as a reversed shoulder spiral tool (RSST), shown schematically in Figure 8. There are two unique features of the RSST. One is that the shoulder tapers away from the pin tip, opposite to the more conventional shape where the shoulder taper forms a shallow cav-

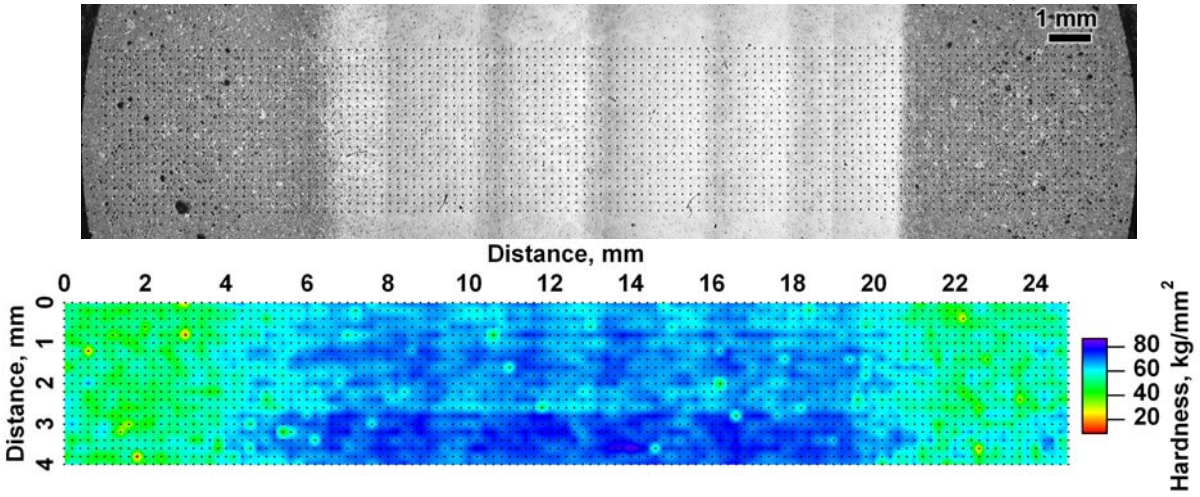

Figure 7. Optical micrograph showing top view of a 5-pass friction stir layer on the surface of an AM60B plate. An image representation of the microhardness distribution is shown on the bottom.

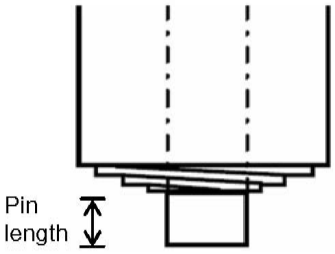

Figure 8. Schematic of reversed shoulder spiral tool shape.

ity. The second important feature is that the length of pin extension is adjustable.

Example results from the evaluation of the influence of process (i.e., weld cycle) time and pin length on shear strength are shown in Figure 9. These spot welds were made in 2-mm-thick 5754 using insertion depths of 2.6 and 3.0 mm. Three pin lengths were used, 1.4, 1.2, and 1.0 mm. The overall shoulder diameter of this tool is 10 mm. These results indicate that at the shorter processing times, the intermediate pin length of 1.2 mm produced the strongest welds. For the 1.2-mm pin, the effect of insertion depth was insignificant. Although additional testing is required to build statistical confidence in the results, the joint strengths were relatively insensitive to processing time. This suggests that increasing weld cycle time may not be necessary for meeting minimum strength require-

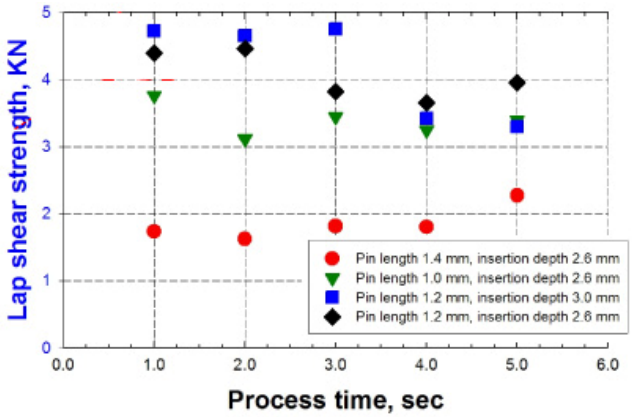

Figure 9. Variation of lap-shear strength with process (welding) time for joints of 2-mm-thick 5754 spot welded with an insertion depth of 2.6 mm and pin lengths of 1.0 and 1.4 mm.

ments, a finding somewhat contrary to the expected result.

Figure 10 shows a compilation of results on the effects of insertion depth and pin length on lap-shear strength. All of these spot weld joints were made with a 5 s weld time. Figure 10 indicates that for each pin length from 0-2 mm, a peak occurred in the variation of lap-shear strength with insertion depth. However, these strength peaks occurred over narrow ranges of insertion depth. It appears that it is feasible to obtain a joint strength that exceeds the desired minimum of 4 kN. The narrow range of insertion depths over which the peaks occur means

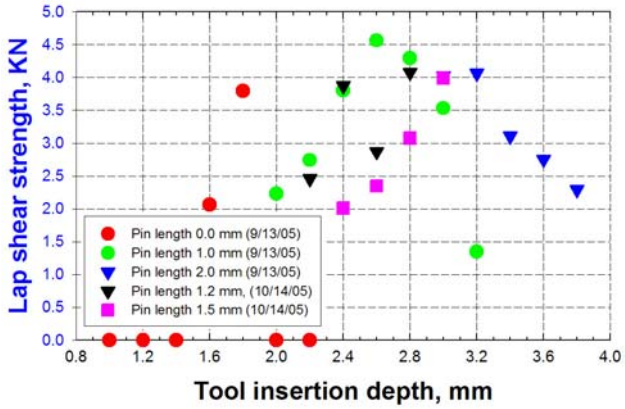

Figure 10. Variation of lap-shear strength with insertion depth for a weld time of 5 s and pin lengths of 0-2 mm.

that the process must be very closely controlled. This is undesirable from a production perspective, and efforts to increase strength while broadening the strength peak are continuing.

The strength data presented in Figure 9 are also replotted in Figure 11, where the reaction forces on the stir tooling are included. This plot shows that the tool reaction forces decreased as processing times increased from 1–5 s. The effect of processing time on the reaction force is significant because it will be a factor in determining the sizes of robots needed for producing welds using portable welding heads. The 13-18 kN reaction forces measured at lower processing times are quite high compared with the levels used for RSW robots. The implications of these observations are being discussed with manufacturers of robotic equipment.

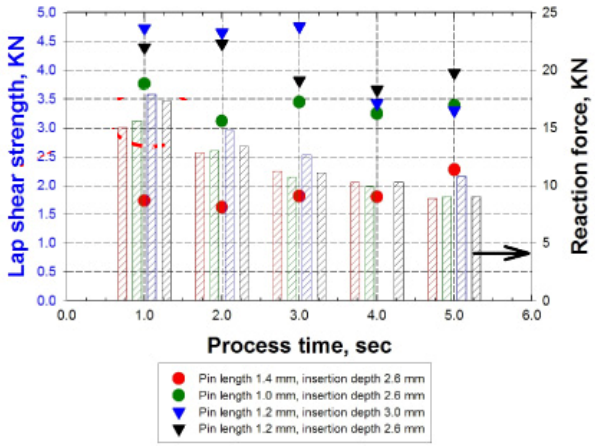

Figure 11. Variations of both lap-shear strength and stir tool reaction forces with process (welding) time for spot welds of 2-mm-thick 5754.

Conclusions

Progress has been made in FY 2006 in FSW/P of lightweight materials for automotive structure applications. It has been demonstrated that, for both Mg and Al alloys, friction stir spot welding was capable of producing welds exceeding the strength requirements for RSW of the same material and thickness. The influence of tool geometry and process conditions on the weld joint strength of Al5754 was investigated, and the relatively high process load to meet the strength requirement needs to be considered in the design and fabrication of welding robots for assembly line application of the friction stir spot welding process.

The ability of FSP to produce a high-integrity surface layer on AM60B was demonstrated. In addition to removing the solidification porosity of the cast AM60B, FSP regions experienced hardness/strength increases of up to 25% above base metal, suggesting the possibility of considerable improvement of mechanical properties (strength, ductility and fatigue life) in the FSP region.

Presentations/Publications

Z. Feng, M. L. Santella, S. A. David, R. J. Steel, S. M. Packer, T-Y Pan, M. Kuo, and R. S. Bhatnagar, "Friction Stir Spot Welding of Advanced High-Strength Steels—A Feasibility Study," *SAE 2005 Congress*, SAE-International, Detroit, 2005-2001-1248, 2005.

M. Awang, V. Mucino, Z. Feng, and S. A. David, "Thermo-Mechanical Modeling of Friction Stir Spot Welding (FSSW) Process: Use of an Explicit Adaptive Meshing Scheme," *SAE 2005 Congress, SAE-International*, Detroit, 2005-2001-1251, 2005.

S. G. Arul, T-Y Pan, J. Pan, P. C. Lin, Z. Feng, and M. L. Santella, "Microstructures and Failure Mechanisms of Spot Friction Welds in Lap-Shear Specimens of Aluminum 5754 Sheets," *SAE 2005 Congress*, Detroit, 2005-2001-1256, 2005.

M. L. Santella, Z. Feng, C. Degen, and T-Y Pan, "Modifying AM60B Magnesium Alloy Die Cast Surfaces by Friction Stir Processing," in *7th International Conference on Trends in Welding Research*, S. A. David. Ed., TMS, Pine Mountain, GA, 2005.

M. L. Santella, Z. Feng, C. Degen, and T-Y Pan, "Friction Stir Processing to Improve the Surface Properties of Aluminum and Magnesium Castings,"

Materials Science & Technology 2005 Conference, ASM International, Pittsburgh, 2005.

M. L. Santella, T. Engstrom, D. Storjohann, and T-Y Pan, "Effects of Friction Stir Processing on Mechanical Properties of the Cast Aluminum Alloys A319 and A356," *Scripta Materialia* **53**(2), 201–206 (2005).

Z. Feng, T-Y Pan, M. L. Santella, and S. A. David, "Friction Stir Spot Welding and Its Applications," *AeroMat 2005*, ASM International, Orlando, FL, 2005.

W. Woo, P. K. Liaw, H. Choo, D. W. Brown, Z. Feng, S. A. David, and C. R. Hubbard, "D-41 Two-Dimensional Mapping of Residual Stresses in 6061-T6 Aluminum Friction Stir Welds," *Powder Diffraction* **19**(2), 202 (2004).

M. L. Santella, A. Frederick, C. Degen, and T-Y Pan, "The Use of Friction-Stir Technology to Modify the Surfaces of AM60B Magnesium Die Castings," *JOM* **58**(5), 56–61 (2006)

M. L. Santella, T-Y Pan, and C. Degen, "Modifying AM60 Magnesium Alloy Die Cast Surfaces by Friction Stir Processing," presented at SAE 2006 World Congress, Detroit, April 6, 2006.

T-Y Pan, M. L. Santella, P. K. Mallick, A. Frederick, and W. J. Schwartz, "A Feasibility Study on Spot Friction Welding of Magnesium Alloy AZ31," in *Proceedings of 2006 World Magnesium Conference*, 2006.

References

1 A. Luo, "Wrought Magnesium Alloys and Manufacturing Processes for Automotive Applications," SAE Technical Paper 2005-01-0734, Society of Automotive Engineers, Warrendale, PA, 2005.

2 *Resistance Welding Manual*, revised 4th ed., Resistance Welder Manufacturers' Association, 2003.

3 Metals and Their Weldability, pp. 418–424 in *Welding Handbook*, 7th ed., vol. 4, American Welding Society, Miami, 1982.

4 P. Klain, D. L. Knight, and J.P. Thorne, "Spot Welding of Magnesium with Three-Phase Low Frequency Equipment," *Welding Journal* **32**(1), 7–18 (1953).

5 S. Kallee and D. Nicholas, "Application of Friction Stir Welding to Lightweight Vehicles," SAE Technical Paper 982362, Society of Automotive Engineers, Warrendale, PA, 1998.

6 M. Fujimoto, M. Inuzuka, M. Nihio, Y. Nakashima, "Development of Friction Spot Joining (Report 2): Mechanical Properties of Friction Spot Joints," Preprints of the National Meeting of Japan Welding Society, no.74, pp.6–7, 2004.

7 "Mazda Develops World's First Aluminum Joining Technology Using Friction Heat," Mazda Media Release, February 27, 2003.

8 R. Hancock, "Friction Welding of Aluminum Cuts Energy Cost by 99%," *Welding Journal* **83**, 40 (2004).

9 J. B. Clark, "Age Hardening in a Mg-9 wt% Al Alloy," *Acta Metallurgica* **16**, 141–152 (1968).

10 J. A. Esparza, W. C. Davis, and L. E. Murr, "Microstructure-property Studies in Friction-stir-welded, Thixomolded Magnesium Alloy AM60, *Journal of Materials Science* **38**, 941–952 (2003).

F. Basic Studies of Ultrasonic Welding for Advanced Transportation Systems

Principal Investigator: Zhili Feng
Oak Ridge National Laboratory
1 Bethel Valley Road, Oak Ridge, TN 37831
(865) 576-3797; fax: (865) 574-4928; e-mail: fengz@ornl.gov

Chief Scientist: James J. Eberhardt
(202) 586-9837; fax: (202) 587-2476; e-mail: james.eberhardt@ee.doe.gov
Field Technical Manager: Philip S. Sklad
(865) 574-5069; fax:(865) 574-6098; e-mail: skladps@ornl.gov

Participants:
X. Zhang and M. L. Santella, Oak Ridge National Laboratory
W. Zhang and K. Li, Oakland University

Contractor: Oak Ridge National Laboratory
Contract No.: DE-AC05-00OR22725

Objective

- Develop a fundamental understanding of the ultrasonic welding (UW) process.
- Establish process conditions to optimize joint properties of aluminum (Al) alloys and other lightweight materials for auto body applications.
- Explore opportunities for joining dissimilar materials.
- Explore the feasibility of ultrasonic processing in other novel and unique situations in materials processing, such as consolidating metal powder, producing functionally graded components, and modifying surface properties.

Approach

- Perform UW experiments to develop correlations of process parameters with joint properties.
- Characterize details of joint microstructures.
- Model the fundamental interactions of ultrasonic waves with solids.

Accomplishments

- Demonstrated UW of magnesium (Mg) alloys.
- Developed an efficient computational model to study the acoustic energy distribution in the welded workpiece.
- Investigated the geometric effects on ultrasonic energy generation and dissipation during the welding process.
- Initiated experimental study on residual stress distribution in the bonding region.

Future Direction

- Continue welding process development for dissimilar materials.
- Study the structure-property relationship of joints.

Introduction

Ultrasonic welding (UW) uses high-frequency mechanical vibrations to produce a solid-state metallurgical bond (weld) between metals. The basic process setup is illustrated in Figure 1 for typical spot weld configurations. An electro-mechanical converter converts high-frequency electric current to mechanical vibration. The mechanical vibration is then modulated and amplified by the booster/horn before it is applied to the overlapping workpiece through the vibration of the sonotrode. A moderate clamping force is applied to ensure the mechanical vibration is transferred to the sheet-to-sheet interface (the faying surface) where the weld is created. Typically, the mechanical vibration is at 20–40 kHz with an amplitude range of 5–50 μm. The power delivered to the workpiece is in the range of several hundred to several thousand watts.

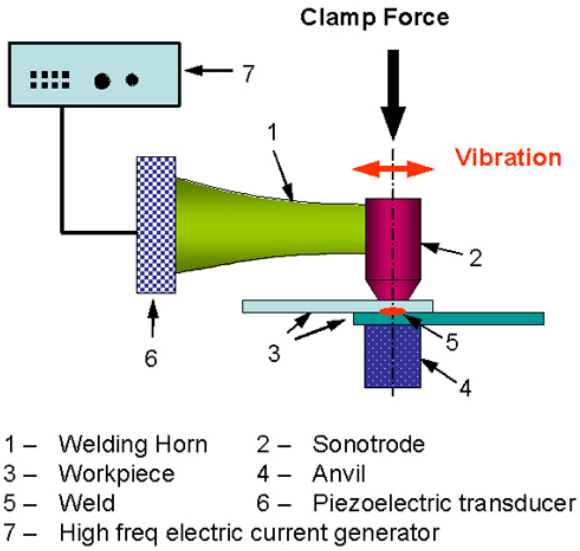

Figure 1. Schematic setup of UW process.

Figure 2 illustrates the essential underlying mechanisms involved in the formation of the metallurgical bond at the workpiece interface during UW. The combination of normal clamp pressure and lateral mechanical vibration results in several important effects at the workpiece interface. The lateral mechanical vibration introduces relative motion at the interface. The frictional action at the interface due to the relative motion and the normal pressure breaks the surface oxides and other contaminants. As a result, clean metal surfaces are brought into contact with each other under pressure. Frictional

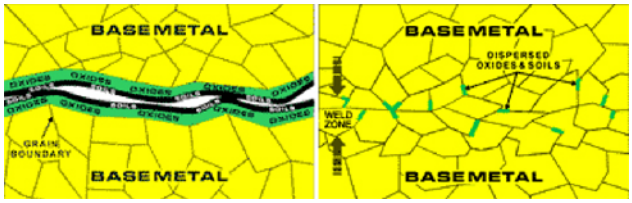

Figure 2. Schematic representation of bond interface before (left) and after (right) UW.

heating also occurs at the bond interface. The heating promotes both localized deformation and diffusion in the region where the pressure is applied. When the process conditions are right, a metallurgical bond is formed without melting at the bonding interface. The self-cleaning nature of UW and its ability to form metallurgical bonds without melting are two important advantages of the process.

UW creates a joint without bulk melting. Thus, UW is inherently immune to welding defects associated with the solidification in various fusion welding processes (electric resistance spot welding, arc welding, laser welding, etc.). Solidification-induced defects such as solidification cracking and porosity can be a major quality problem for a number of high-performance lightweight structural materials used in automotive body structures. In addition, UW offers the possibility for joining dissimilar metals such as Al to steel and Al to Mg, metal-to-metal composites that have been extremely difficult for conventional fusion welding processes. Because melting is avoided, the UW process is much more energy efficient. UW has attracted considerable attention in the auto industry as an important enabling joining technology for assembling structural components made of Al alloys, Mg, and other high-performance lightweight materials.

Progress before FY 2006

UW of Al alloys was successfully demonstrated in FY 2003, the first year of the program. UW of other materials was also explored. Studies on dissimilar welds between Al2024 and Al6061 revealed a number of important phenomena at the interface under different process conditions.

The FY 2004 research involved studying the relationship between the weld quality of Al alloys and weld process conditions. It was observed that the ultrasonic weld quality strongly depends on a number of geometric factors, such as the weld location, the

shape and size of the workpiece, and the sonotrode vibration direction relative to the workpiece. Under certain circumstances, cracking occurs at unexpected locations. Destruction of prior welds by subsequent welding was also observed. These observations suggested that the acoustic wave propagation and reflection in the workpiece being welded are very complicated and would result in considerable weld-to-weld quality variations.

In FY 2005, the program focused on investigating the acoustic energy distribution during welding. By utilizing a real-time infrared (IR) thermography technique, localized temperature rise in the workpiece during UW was observed and recorded as a function of time. The influence of the geometry factors on the energy distribution was experimentally investigated to elucidate possible causes for the observed weld quality variations. The causes for the formation of unforeseen hot spots and cracking were identified, and the factors contributing to the acoustic energy generation and dissipation in welded samples determined. In addition, we began to formulate an efficient computational modeling approach to further the understanding of the acoustic energy distribution in the workpiece. This model makes it possible to investigate the localized acoustic energy distribution and heat generation during ultrasonic welding process.

The research activities in FY 2006 included investigating the feasibility of UW of Mg alloys, because Mg alloys used for auto body structure material received increased attention in the automotive industry. We also completed the development of the computational model for acoustic energy distribution in the workpiece during UW. In addition, the residual stresses in the UW joint were studied using an interferometric strain/slope rosette (ISSR) stress measurement technique.

Joining of Mg Alloys

Two Mg alloys (AZ31B and AM50) were studied. AZ31B rolled sheet had a nominal thickness of 1 mm, and the die-cast AM50 sheet was 2 mm thick. The weld coupons were 25 mm wide. A standard 25-mm overlap between the two workpieces was used in the welding trials.

All welding tests were performed on a Sonobond ultrasonic welder. The machine operated at 20 kHz and had maximum rated power output of 2500 W. A series of welding tests were performed. The welding time varied from 0.7 to 1.75 s, and the welding energy varied from 980 to 2400 J.

In addition to same-alloy welding (AZ31B to AZ31B and AM50 to AM50), welding between AZ31B and AM50 was also performed. Figure 3 shows the appearance of typical welds made in this study.

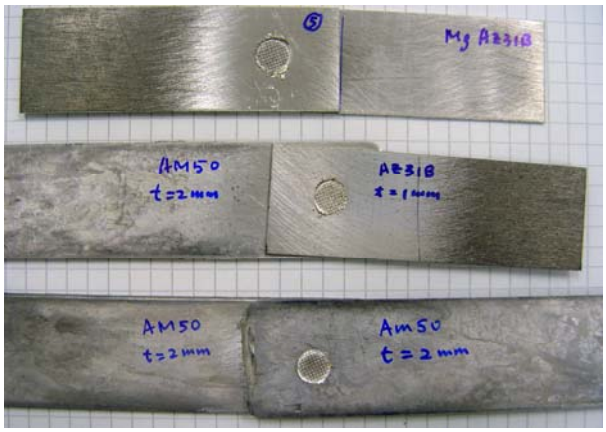

Figure 3. Appearance of ultrasonic welds. Top weld: AZ31B to AZ31B (t=1 mm); middle: 2 mm AM50 to 1 mm AZ31B; bottom: AM50 to AM50 (t-2 mm).

Excellent metallurgical bonding was obtained for both Mg alloys. Figure 4 shows the defect-free 4-mm-wide bonding interface of AM50. At higher magnification (Figure 5), severely elongated grains are formed along the bonding interface because of the extensive deformation of interface during UW. The width of the deformed grain zone is very narrow, approximately 20 μm, indicating UW involving very localized deformation at the interface. This was consistent with UW of other materials such as Al alloys studied in the past.

Outside the bonding region, randomly distributed solidification porosity/voids are clearly visible in the base metal of AM50, as shown in Figures 4 and 5. Such solidification porosity/voids are common and associated with the die-casting process.

Figure 6 shows the bonding interface of the dissimilar weld between AZ31B and AM50. It is evident that metallurgical bonding between the two different Mg alloys was produced by the UW process.

While we did not perform mechanical testing to determine the joint strength (planned in FY 2007), the peel test commonly used to test resistance spot

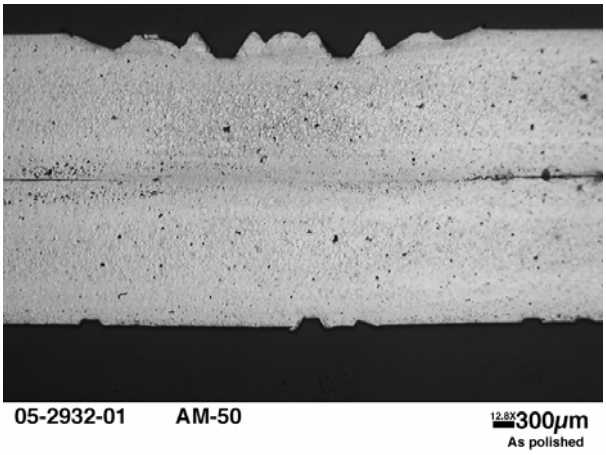

Figure 4. Weld cross-section of AM50.

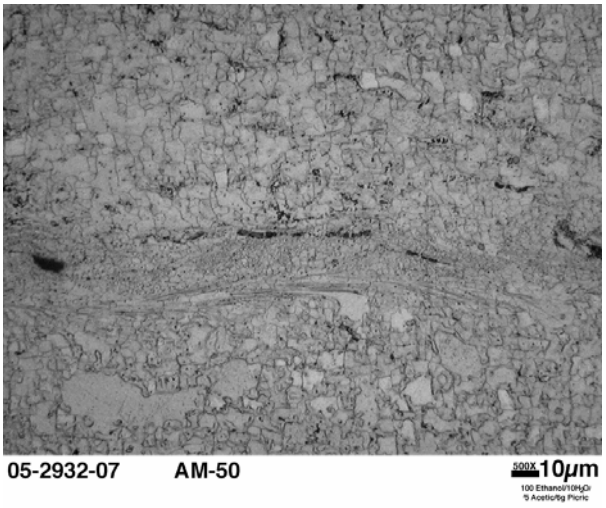

Figure 5. Microstructure at the bonding interface of AM50**.** Note the solidification porosity in the base metal region.

welds was conducted to determine the quality of ultrasonic weld. As shown in Figure 7, the ultrasonic welded joint failed in the base metal adjacent to the weld, indicating that the ultrasonic weld had adequate strength.

Modeling UW by Means of Time Domain Elastic Wave Solution Technique

We have completed the development of a UW model based on the time-domain elastic wave solution technique. The theoretical basis and modeling results are summarized here.

Wave propagation and the vibration modes in elastic plates and cylinders have been model problems for solutions of elastic wave equations. Early

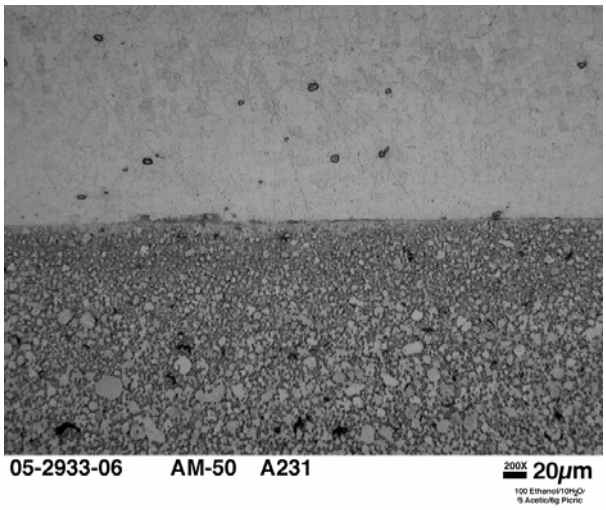

Figure 6. Microstructure at the bonding interface between AZ31B (top) and AM50 (bottom).

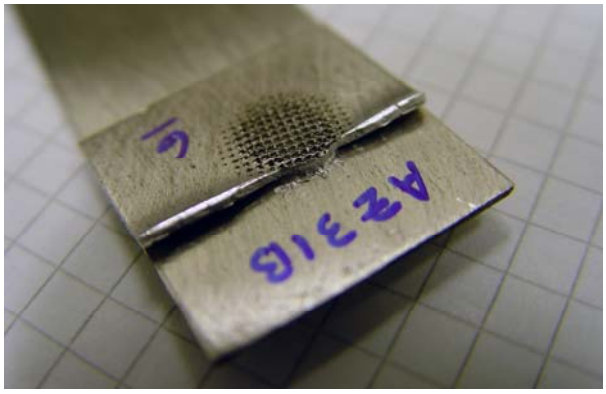

Figure 7. Base metal failure during peel test AZ31B ultrasonic weld.

works by Lord Rayleigh[1,2] considered cases where the thickness H of a plate is much smaller than the dimensions in the other two directions; and the extensional modes, which involve wave propagation along the thickness of the plate, can be neglected. In the more general case of thin plates with finite thickness, a series expansion in the thickness of the plate can be obtained, which can be solved numerically.[3,4] These early studies focused on free vibrations.

For thin plates driven by external periodic forces, the solutions are often expressed in terms of a summation over different frequency modes.[5,6] Research of driven plates so far has mostly focused on the steady-state problems. Little attention has been given to non-steady-state cases.

The short duration of the UW process, a fraction of a second, contains only tens of thousands of cy-

cles at the driving frequency. This is not long enough to establish steady-state vibrations in the plates. A detailed study of a driven elastic plate in the time domain is necessary.

Although the welding process itself is not an elastic process and cannot be described by linear elastic equations, the distribution of the acoustic energy over the driven plate can be described reasonably well by the linear equations, if we approximate the energy dissipation by a damping parameter over the entire plate. For the simplicity of the model, we also neglect the effect of heating and the transfer of energy from the top plate to the bottom plate. Again, this energy can also be modeled by an appropriately chosen damping term within the linear theory. These approximations yield a time-dependent linear acoustic problem for a single driven plate that can be readily solved using a finite-element numerical technique.

Governing Equations of Elastic Vibration of Thin Plates pertaining to UW

Consider a thin plate situated in a three-dimensional (3-D) rectangular coordinate system, (x, y, z), with the thickness in z direction. The plate is bounded by the planes z = h and z = – h and the thickness of the plate is H = 2h at the start. Let U, V, W be the displacements of the plate in x, y, z directions respectively. We followed the elastic modeling approach for high-frequency extensional vibrations of plate by Kane and Mindlin.[3] It was assumed that the displacements in x and y directions are independent of the thickness of the plate and the displacement in z direction varies linearly along z with no displacement at the middle plane of the plate. Hence, the three displacements follow the formulas

$$\begin{aligned} U(x,y,z,t) &= u(x,y,t) \\ V(x,y,z,t) &= v(x,y,t) \\ W(x,y,z,t) &= \frac{z}{h} w(x,y,t) \end{aligned} \tag{1}$$

In Eq. (1), the equation of motion can be solved in the reduced domain (x, y, t). The corresponding plate-displacement system of equations of motion is

$$\begin{aligned} &(\lambda+2G)u_{xx} + Gu_{yy} + (\lambda+G)v_{xy} + \frac{\pi}{\sqrt{3}H}\lambda w_x + \frac{T_1}{H} = \rho u_{tt} \\ &Gv_{xx} + (\lambda+2G)v_{yy} + (\lambda+G)u_{xy} + \frac{\pi}{\sqrt{3}H}\lambda w_y + \frac{T_2}{H} = \rho v_{tt} \\ &G(w_{xx}+w_{yy}) - \frac{\sqrt{3}\pi}{H}\lambda(u_x+v_y) - \frac{\pi^2}{H^2}(\lambda+2G)w + \frac{3T_3}{H} = \rho w_{tt} \end{aligned} \tag{2}$$

where λ, G are Lame's constants; ρ is the mass density; H = 2h is the thickness of the plate; T_1, T_2, T_3 are the components of surface traction in x, y and z directions.

We represent the driving vibration of the sonotrode by a simple temporal harmonic oscillation of surface traction with exponentially decaying amplitude in the spatial domain. The choice of a continuous surface traction is to avoid difficulties in solving Eq. (2) arising from spatial discontinuities. In an UW process, strong friction exists between the workpiece interface. A simple friction term is used in each equation of motion to represent the friction effect. This leads to Eq. (3), the elastic model for UW.

In Eq. (3), ω is the vibration angular frequency of the force applied to the weldment, (x_c, y_c) is the center of the sonotrode on the workpiece, and $C_1, C_2, C_3, \alpha, \gamma$ are nonnegative constants.

There are two physical origins of the damping coefficient γ in Eq. (3). The first is the obvious source, the dissipation of the elastic energy into heat on the plates. The second is less obvious but equally important. This is the energy leak due to imperfect impedance match between the sonotrode, the workpiece, and the supporting anvil.

Boundary Conditions

We consider a rectangular plate $[0, A]\times[0, B]$, corresponding to the upper workpiece in the UW experiment. In the UW process, the sides of weldment are free. Hence, at the four sides of the rectangular plate, we propose zero normal stresses. Since the plate is thin, we propose zero shear stresses along the z-direction (the thickness direction). Since

$$\begin{aligned} &(\lambda+2G)u_{xx} + Gu_{yy} + (\lambda+G)v_{xy} + \frac{\pi}{\sqrt{3}H}\lambda w_x + C_1 e^{-\alpha\left[(x-x_s)^2+(y-y_s)^2\right]}\sin\omega t = \rho u_{tt} + \gamma u_t \\ &Gv_{xx} + (\lambda+2G)v_{yy} + (\lambda+G)u_{xy} + \frac{\pi}{\sqrt{3}H}\lambda w_y + C_2 e^{-\alpha\left[(x-x_s)^2+(y-y_s)^2\right]}\sin\omega t = \rho v_{tt} + \gamma v_t \\ &G(w_{xx}+w_{yy}) - \frac{\sqrt{3}\pi}{H}\lambda(u_x+v_y) - \frac{\pi^2}{H^2}(\lambda+2G)w + C_3 e^{-\alpha\left[(x-x_s)^2+(y-y_s)^2\right]}\sin\omega t = \rho w_{tt} + \gamma w_t \end{aligned} \tag{3}$$

the plate is clamped along the z-direction at the sonotrode and the vibration in the surface traction is in the xy-plane, the rotation movement of the displacement vector <U, V, W> about the z-axis is negligible at the boundary. Hence, we propose the irrotational condition of the displacement vector <U, V, W> about the z-axis. The resulting boundary conditions for Eq. (3) are

$$\begin{aligned} &(\lambda+2G)u_x+\lambda v_y+\frac{\pi\lambda}{h\sqrt{12}}w=0\\ &u_y-v_x=0\\ &w_x=0 \end{aligned} \tag{4}$$

at the boundaries x = 0 and x = A, and

$$\begin{aligned} &\lambda u_x+(\lambda+2G)v_y+\frac{\pi\lambda}{h\sqrt{12}}w=0\\ &u_y-v_x=0\\ &w_y=0 \end{aligned} \tag{5}$$

at the boundaries y = 0 and y = B. The compatible boundary conditions at a corner of the rectangular domain require

$$\begin{aligned} &u_x=v_y=-\frac{\pi\lambda}{h(\lambda+G)2\sqrt{12}}w\\ &u_y-v_x=0\\ &w_x=w_y=0 \end{aligned} \tag{6}$$

The initial conditions for Eq. (3) in our UW model

$$\begin{aligned} &u(x,y,0)=v(x,y,0)=w(x,y,0)\\ &=u_t(x,y,0)=v_t(x,y,0)=w_t(x,y,0)\\ &=0 \end{aligned} \tag{7}$$

Eqs. (3)–(7) form a closed mathematical system of an initial boundary problem of a system of linear partial differential equations.

The direction of the applied vibration in UW is controlled by the parameters C_1, C_2, C_3 in Eq. (3). For vibration along the length of the plate (in x direction), we assign $C_1 = 0.035, C_2 = C_3 = 0$. For vibration along the width of the plate (in y direction), we assign $C_1 = 0, C_2 = 0.035, C_3 = 0$. The coefficient of the decay of the applied vibration in Eq. (3) is set as α = 32000 so that the applied force vanishes quickly away from the welding spot centered at (x_c, y_c).

Finally, the following material properties were used for the Al alloy workpiece.

$$E = 7.0404172\frac{N}{m^2}, \sigma = 0.34, \rho = 2700\frac{kg}{m^3},$$
$$\lambda = \frac{\sigma E}{(1+\sigma)(1-2\sigma)}\frac{N}{m^2}, G = \frac{E}{2(1+\sigma)}\frac{N}{m^2},$$
$$H = 0.001m, A = 0.1m, B = 0.025m,$$
$$x_s = 0.065m, y_s = 0.0125m, \omega = 169646.01Hz$$

Numerical Simulations and Comparisons to the Experimental Results

A variable-coefficient ODE solver, DVODE_F90[7,8] was used in the computation. The stiff backward differentiation formulas were adopted as the integration method.

Consistent with the UW experiments conducted in FY 2005, the Al alloy workpiece was 0.025 m wide and 0.1 mm long. The sonotrode was located at x_c=0.075 m and y_c=0.0125 m.

We assume that the temperature distribution during UW as observed in IR measurement is in proportion to the sum of the kinetic and potential energy distributions on the plate. With an applied periodic vibration force, the solution and energies change approximately periodically. Hence, we define a time averaged energy sum as

$$E(x,y)=\frac{1}{T}\int_0^T (K(x,y,t)+P(x,y,t))dt = E_K + E_P \tag{8}$$

where $K(x,y,t), P(x,y,t)$ are the kinetic and potential energies and T is a sufficiently long time. In our simulations, it was found that the potential energy dominates the kinetic energy. Hence, the distribution of the averaged energy sum, E, is much closer or similar to that of the time averaged potential energy, E_P.

First, the UW model was applied to the case in which the direction of the driving vibration from the sonotrode was along the width of the rectangular plate (in y-direction), with damping coefficient $\gamma = 20\rho/s$. Figure 8 shows the out-of-plane motion of

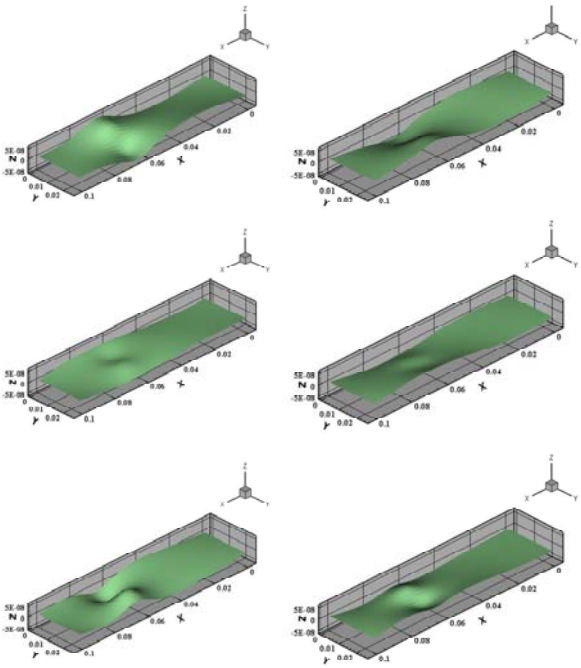

Figure 8. Snapshots at different time instances of the plate vibration in the thickness direction (z-axis) during UW. The driving vibration is in the direction of the y-axis. Damping coefficient $\gamma = 20\rho/s$. Acoustic excitation locates at x = 0.065 m and y = 0.0125 m.

the plate in one cycle. The oscillations of the surface were mainly confined at two spots near the long edge of the plate, away from the applied vibration location ($x = 0.065m$, $y = 0.0125m$).

Figure 9 shows the distribution of the time-averaged energy. We observe that two high-energy spots appeared on the long edges of the plate, contributed largely by the potential energy. The locations of the high-energy spots qualitatively agree to the IR thermography image reported in FY 2005. Since the potential energy is high at those spots, cracks are likely to develop there.

Second, the same vibration force was applied along the length of the rectangular plate (in x-direction), with the same damping coefficient $\gamma = 20\rho/s$. Figure 10 shows the distribution of the time-averaged energy. A completely different energy distribution was observed. There is only one high-energy spot located at the mid-width of the plate. Furthermore, the magnitude of the high-energy spot is much smaller than that shown in Figure 9. Such energy distribution is consistent with the IR thermograph observation where no hot spots were observed and no crack developed under this testing condition.

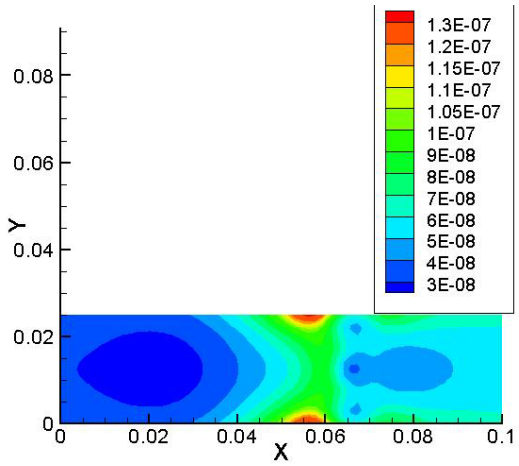

Figure 9. Distribution of the time-averaged sum of the kinetic and potential energy density in the plate during UW when the driving vibration is in the direction of the y-axis. Damping coefficient $\gamma = 20\rho/s$.

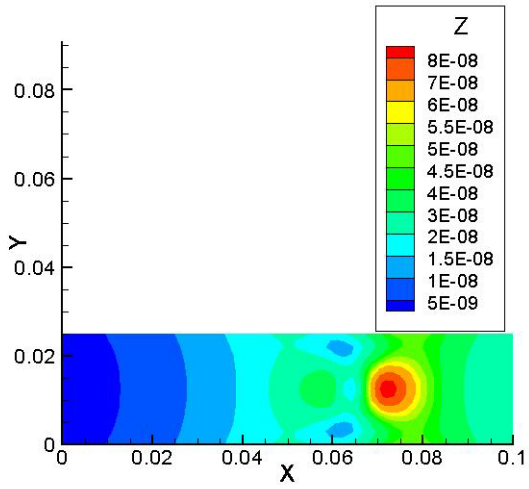

Figure 10. Distribution of the sum of the kinetic and potential energies on the plate during UW when the driving vibration is in the direction of the x-axis. Z represents the amount of the energy sum. Damping coefficient $\gamma = 20\rho/s$.

Third, the model was used to study the effect of acoustic impedance by changing the damping coefficient. Small damping means that most of the energy is trapped within the plate, while large damping means that a large portion of the energy is leaked to the anvil. Therefore, the damping parameters can be used to simulate the effect of acoustic impedances of the workpiece. In particular, two plates with a frictional interface correspond to a relatively small

damping, whereas a single plate corresponds to a large damping.

For the impedance study, the vibration force was applied along the width of the plate (in y-direction). Figure 11 shows the distributions of the time-averaged energy when using a smaller damping coefficient, $\gamma = 2\rho/s$. This corresponds to larger interface impedance. The high-energy spots appeared at the corners of the plate away from the welding spot. There is no high-energy spot around or close to the welding spot.

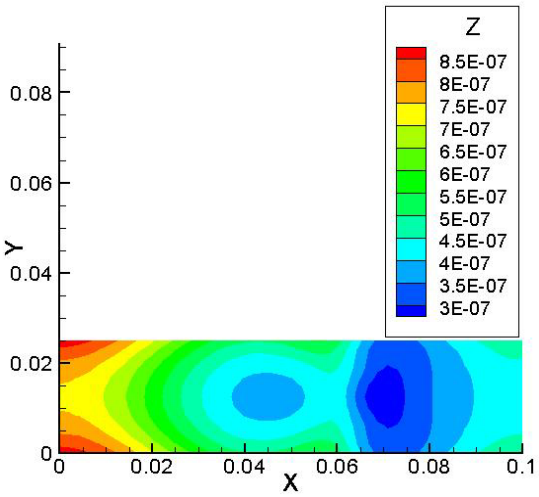

Figure 11. Distribution of the sum of the kinetic and potential energies on the plate during UW when the driving vibration is in the direction of the y-axis. Damping coefficient $\gamma = 2\rho/s$.

Figures 12–14 show the cases of larger damping coefficients ($\gamma = 80\rho/s$, $160\rho/s$ and $320\rho/s$). As the damping coefficient increases, more elastic energy leaked to the anvil. The effect of the plate geometry plays less and less of a role since the motion is quickly damped out away from the welding spot. In Figure 12, as the damping increases to $\gamma = 80\rho/s$, four main high-energy spots occurred at the long edges of the plate surrounding the welding spot as a center. There are also four small secondary high-energy spots closer to and on the paths of the welding spot. As the damping coefficient increases to $\gamma = 160\rho/s$ (Figure 13), the four high-energy spots on the long edges of the plate become secondary high-energy spots, while two main high-energy areas are located inside the plate and on the two sides of the welding spot along the direction of the applied vibration. As the damping coefficient increases to $\gamma =$

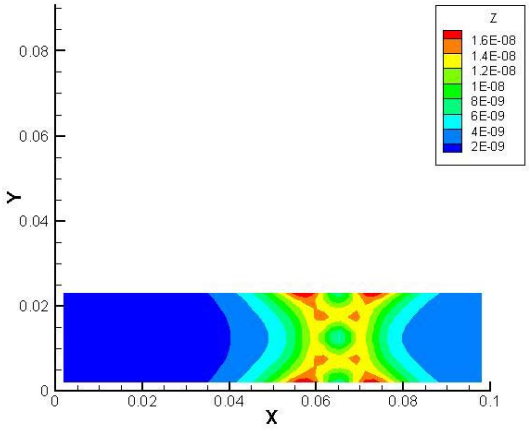

Figure 12. Distribution of the sum of the kinetic and potential energies on the plate during UW when the driving vibration is in the direction of the y-axis. Damping coefficient $\gamma = 80\rho/s$.

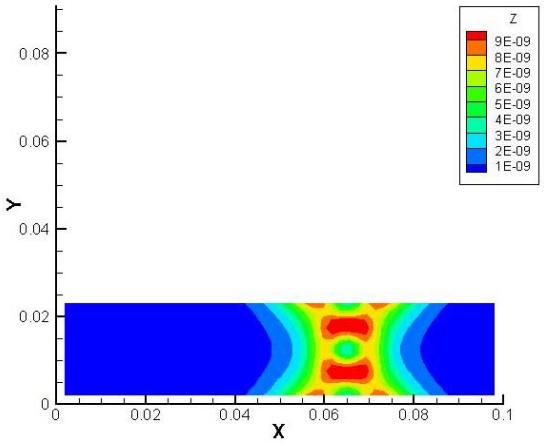

Figure 13. Distribution of the sum of the kinetic and potential energies on the plate during UW when the driving vibration is in the direction of the y-axis. Damping coefficient $\gamma = 160\rho/s$.

$320\rho/s$ (Figure 14), high-energy spots disappear from the edges of the plate and from the two high-energy spots formed on the side of the welding spot along the direction of vibration. The last figure is very similar to the experimental image of a single plate.

Conclusions

1. Two Mg alloys, AM50 and AZ31B, have been successfully welded using the ultrasonic welding process. Metallurgical bonding was produced. Peel tests revealed that the weld joint

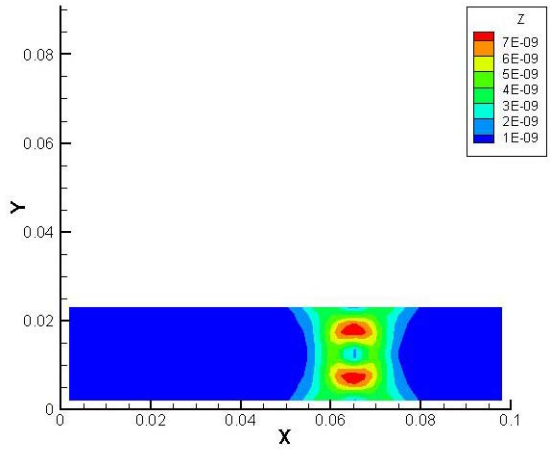

Figure 14. Distribution of the sum of the kinetic and potential energies on the plate during UW when the driving vibration is in the direction of the y-axis. Damping coefficient $\gamma = 320\rho/s$.

failed in the base metal region adjacent to the spot weld, demonstrating sufficient strength of the ultrasonic welds produced in this study.

2. An efficient computational modeling approach based on the time domain elastic wave propagation principle has been developed to further the understanding of
3. The acoustic energy distribution in the workpiece. This model makes it possible to investigate the localized acoustic energy distribution and heat generation during UW process.

References

1 S. H. Crandall, "Rayleighs Influence on Engineering Vibration Theory," *Journal of the Acoustical Society of America* **98**(3), 1269–72, 1995.

2 A. E. H. Love, *A Treatise on the Mathematical Theory of Elasticity*, New York, Dover, 1944.

3 T. R. Kane and R. D. Mindlin, "High-Frequency Extensional Vibrations of Plates," *J. Appl. Mech.* **23,** *Trans. ASME 78*, A-277–283, 1956.

4 S. S. H. Chen and T. M. Liu, "Extensional Vibration of Thin Plates of Various Shapes," *Journal of the Acoustical Society of America* **58**(4), 828–831, 1975.

5 C. T. Sun, and J. M. Whitney, "Forced Vibrations of Laminated Composite Plates in Cylindrical Bending," *Journal of the Acoustical Society of America* **55**(5), 1003–8, 1974.

6 N. H. Farag and J. Pan, "Free and Forced In-plane Vibration of Rectangular Plates," *Journal of the Acoustical Society of America* **103**(1) 408–13, 1998.

7 http://www.radford.edu/~thompson/vodef90web.

8 P. N. Brown, G. D. Byrne, and A. C. Hindmarsh, "VODE: A Variable Coefficient ODE Solver," *SIAM J. Sci. Stat. Compu*. **10**, 1038–51, 1989.

5. LIGHTWEIGHT VEHICLE STRUCTURES

A. Application of Superplastically Formed Aluminum for Truck Body Panels

Principal Investigator: Nirmal M. Tolani
International Truck and Engine Company
2911 Meyer Road, Fort Wayne, IN 46803
(260) 461-1238; fax: (260) 428-3661; e-mail: nirmal.tolani@nav-international.com

Chief Scientist: James J. Eberhardt
(202) 586-9837; fax: (202) 587-2476; e-mail: james.eberhardt@ee.doe.gov
Field Technical Manager: Philip S. Sklad
(865) 574-5069; fax: (865) 574-6098; e-mail: skladps@ornl.gov

---

Contractor: International Truck and Engine Company
Contract No.: 4000026691

Objective

- Investigate applications of superplastic aluminum for low to moderate volume (up to 30000/year) body panels to provide a lightweight and low-tooling-cost alternative to steel and sheet molding compound.

Approach

- Select a large exterior truck body panel having a complex shape and moderate production volumes.
- Develop part design, conduct forming simulation and finite element analysis (FEA).
- Build prototype parts to demonstrate process capability and develop realistic part cost data.
- Evaluate the performance of the parts in the real vehicle environment.

Accomplishments

The program was initiated in March 2005. To date, the following tasks have been completed.

- Selected appropriate exterior truck body part.
- Completed part design and developed the part support structure design concepts.
- Completed forming simulations to verify manufacturability
- Completed FEA of part design and support structure.
- Completed second-iteration FEA of part support structure with the exception of joint between mounting structure and superplastic forming (SPF) bumper panels.
- Completed prototype SPF tooling.
- Completed prototype forming trials and development.
- Completed trial of a lower-cost SPF material from a domestic supplier to reduce cost.
- Made six prototype parts for preliminary assembly and test trials.

- Reassessed and revised cost data for production parts
- Ran a preliminary cab shaker test to assess the interface between SPF panel and mounting structure.

Future Direction

- Productionize the prototype tool and run the part in the production process to gain a better understanding of the inconsistencies noted in the prototype forming trials.
- Evaluate surface quality and material thickness variations of the product's representative parts.
- Get a true assessment of production cycle times and costs under the production environment.
- Develop a robust interface between the SPF panel and mounting structure.
- Perform cab shaker test and/or vehicle test to assess part durability for possible implementation in production.

Introduction

Traditionally, commercial truck (Class 5–8) cabs have been made from two materials—steel and aluminum. To stay profitable, the truck industry has been going through product rationalization. To reduce the tooling cost associated with two different cabs, there appears to be a trend to standardize to a single higher-volume steel cab. This trend will make the Class 7–8 vehicles cabs heavier and reduce the fuel efficiency.

This trend toward conversion from aluminum to steel in heavy-duty trucks can be reversed if the formability of aluminum for producing future aerodynamic shapes is improved and the tooling cost to produce aluminum cab panels can be significantly reduced. Deployment of SPF technology offers the opportunity to do so.

SPF of certain aluminum alloys offers the ability to produce complex aerodynamic shapes for truck body applications using lower-cost tooling. This technology allows the production of lightweight, highly integrated, net-shape components that often consolidate many parts in one. It reduces the number of parts, fasteners, and assembly operations required for complex truck body parts and enables the use of aluminum in place of steel at competitive costs.

A typical SPF process is illustrated in Figure 1. The process uses a single-sided die rather than a matched two-sided die. The sheet blank is clamped in the die and blow-formed. Complex-shaped parts can be formed that are not otherwise possible.

International Truck and Engine Company studied the feasibility of using the SPF process for large truck panels in 1985. At that time, the SPF aluminum process cycle times and superplastic aluminum material costs were high; also, the Class A surface finish required for exterior body panels could not be achieved. Although the tooling costs were low, the part costs were very high. It was determined that SPF was economically viable only for very low volumes (<1000 pieces).

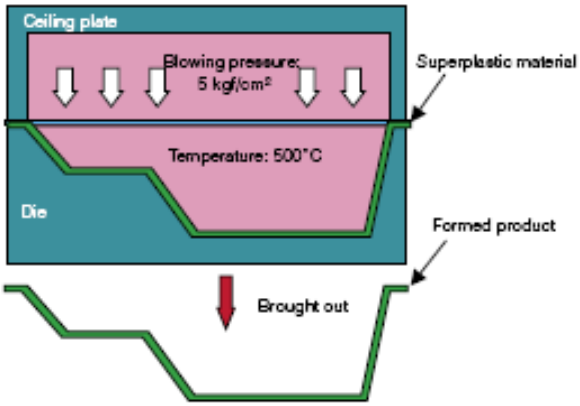

Figure 1. Illustration of typical SPF process.

In recent years, significant new developments in SPF materials and processes have been reported. It is reported that these developments have made higher production volumes feasible, matching those of Class 7–8 truck volumes, through a combination of increased forming rates and lower material cost. It is also reported that for moderate levels of forming, the Class A surface condition required for exterior body panels is achievable.

These recent developments make SPF technology increasingly attractive for heavy-vehicle applications. However, there is a strong need to validate the claims made about the forming cycle

times, part costs, tooling costs, Class A surface capability, and fatigue properties as they apply to large cab panels and structural parts. The only way to convince the heavy truck industry to deploy this relatively new technology is to demonstrate its feasibility for a large exterior body part.

Project Goal

The project goal is to initially demonstrate the feasibility of SPF technology for a large exterior body panel as phase 1. If the results look promising, in the second phase, application of SPF will be expanded to making more complex body sub-assemblies and/or the entire truck cab, depending on the funding level provided.

Project Plan

Phase 1 of the project involves the design, analysis, prototyping, and testing of the large exterior truck body part. The following task descriptions were proposed to address the key issues related to the use of SPF in heavy-duty vehicle applications.

Design and analyze parts: This task has helped to understand design and tooling considerations and limitations. It helped develop guidelines for future designs with SPF aluminum.

Build prototype parts: The production of prototype parts will help evaluate tooling issues, forming process cycle times, part wall thickness variations, and the capability of SPF aluminum to provide a Class A surface.

Perform durability tests: This will help evaluate the assembly, stiffness and durability of SPF aluminum in Class 8 truck applications.

Conclusions

The application of SPF for truck body panels is well under way. An initial set of prototype parts was produced for "show and tell." The ability to form such complex-shaped parts in lightweight aluminum was received very positively. However, based on the prototype trials and the increase in material cost, the cost data for the production parts were revised by the supplier.

Production of additional prototype parts was delayed because of a lack of material. After some delay in obtaining the SPF material from the current Japanese supplier and a domestic supplier, the prototype forming trials were restarted.

Trials with material supplied by the domestic supplier and a thinner-gauge material from the Japanese supplier were unsuccessful.

During the prototype part development trials, it became apparent that the part could not be made consistently without splitting in some area because of the variations in the manually controlled forming process parameters. There was a very significant scrap rate. Also, some of the design radii may have been too sharp in view of the material thickness.

The only way to determine if the selected part can be consistently made without significant problems is to run the part in a production process. A decision was made to modify the prototype tool to be production-capable by incorporating heating elements, polishing, and coating for friction reduction and by changing some of the design radii to make them better suited for the process.

Since this decision to productionize tooling increases spending funds for material, the funding remaining for the validation testing will be reduced. If needed, International will fund the additional testing.

Presentations

Nirmal Tolani, Heavy Vehicle Materials Program Review, Oak Ridge, Tennessee, September 14, 2005.

B. Advanced Composite Support Structures

Principal Investigator: Brian Knouff
National Composite Center
2000 Composite Drive
Kettering, OH 45420
(937) -297-9458; fax: (937) 297-9440; e-mail: bknouff@compositecenter.org

Project Manager: Jay Batten
Delphi Corp.
3900 Holland Rd
Saginaw, MI 48601-9494
(989) 757-3895; fax: (989) 757-42950; e-mail: jay.batten@delphi.com

ORNL Project Manager: Cliff Eberle
(865) 574-0302; fax: (865) 574-8257; e-mail: eberlecc@ornl.gov

Chief Scientist: James J. Eberhardt
(202) 586-9837; fax: (202) 587-2476; e-mail: james.eberhardt@ee.doe.gov
Field Technical Manager: Philip S. Sklad
(865) 574-5069; fax: (865) 574-6098; e-mail: skladps@ornl.gov

---

Contractor: Oak Ridge National Laboratory
NCC/ORNL Contract No.: 4000039214

Objective

- Lead the rapid implementation of lightweight composite materials in Class 7/Class 8 vehicles via the development of advanced composite support structures, specifically chassis lateral braces, which can number up to six per vehicle. Mass reductions are targeted for 50%.

Approach

- Continue to model composite support structures using finite element analysis (FEA).
- Include part, subsystem, and system analyses and optimizations.
- Model failure mechanisms with progressive failure analysis (PFA).
- Work with original equipment manufacturer (OEM) customer to organize potential supplier list for production:

  — Develop criteria with weighting factor on selecting final suppliers.
  — Assemble manufacturing team to interview potential supplier candidates.

Accomplishments

- Finalized design approach to composite center piece only to reduce risk at joint to primary beams.
- Generated first model to accompany this approach.

- Met with OEM supplier to assemble a potential supplier list for production:
  - Assembled criteria ranking list for potential suppliers.

Future Direction

- Determine if OEM partners would like to continue program without DOE assistance:
  - National Composite Center (NCC) reduced the cost of the program and offered to pay for tooling costs to alleviate engineering budget.

Introduction

The purpose of this effort is to lead the rapid implementation of lightweight composite materials in Class 7/Class 8 vehicles via the development of advanced composite support structures. This task specifically addresses lateral braces; primary beams are being targeted for future work. The mass reduction target is 50% and the minimum requirement is 30%. The benefits of mass reduction in commercial vehicle applications are well known. They include increased fuel economy and a larger payload, which translate into fewer total trips and thus fewer vehicles on the road. This leads to less traffic, which aids highway safety, and decreased emissions. Support structures offer an opportunity for significant weight savings. However, this area of the vehicle also represents a large hurdle in terms of composite applications and market acceptance.

The application that is the focus of this report is a Class 8 tractor lateral brace. The estimated total annual usage of Class 8 lateral braces could exceed 1 million by 2007. Many are simple stamped parts that do not qualify for composite replacement on a per-component basis. However, some are heavy duty and can benefit greatly from a composite redesign, as in the present case. The application currently being studied has a production volume of about 50,000 per year. The total weight of the current design is 24 kg. A minimum weight savings of 30% is 7.2 kg per part. There are normally two of these braces per vehicle, for a minimum potential weight savings of 14.4 kg (31.7 lb) per vehicle.

To facilitate this work and future endeavors, advanced FEA and PFA softwares are being employed and developed. The FEA software contains a unique optimization algorithm that allows for the rapid optimization of such design variables as part thickness, fiber angle, fiber type, and even part shape while minimizing mass, strain, or even cost.

PFA, although still in development for composites, provides the ability to model composite behavior in durability and fatigue situations.

Modeling

The design scenarios previously chosen were narrowed down to one: a composite center piece attached to current end brackets. Although this scenario does not offer the biggest mass reduction, it was chosen to reduce the risk at the joint to the primary beams.

The first approach considers the shape of the center piece. Figure 1 shows the designable zones that were inserted in the composite center piece to reduce the thickness from the end bracket joint (where it is needed) to the center section (where it is not needed).

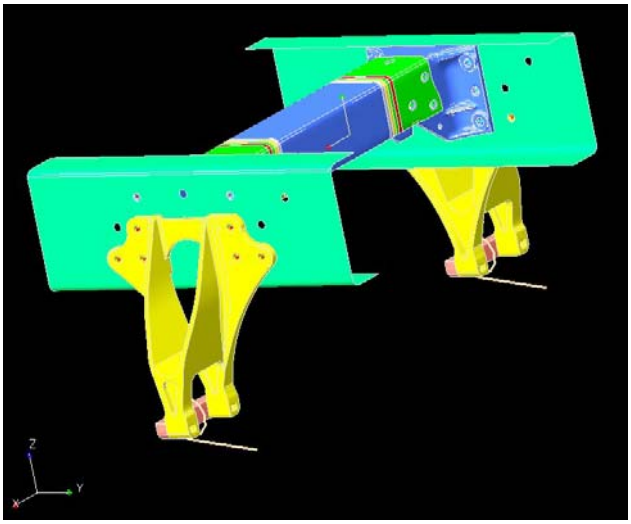

Figure 1. Subsystem FEA model showing thickness reduction zones between green and blue areas in composite center piece.

Figure 2 shows the results. The end section required a composite thickness of about 26 mm, while the center section narrowed down to 1 mm.

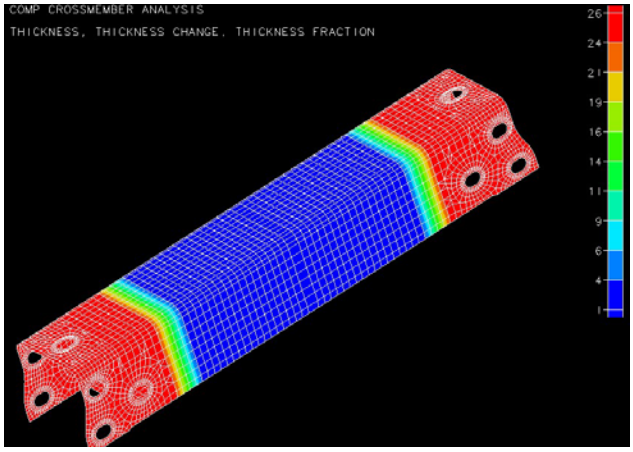

Figure 2. Results in first approach showing the thickness reduction.

The resulting normal stresses shown in Figure 3 are acceptable with maximums of +119 MPa and –139 MPa. However, the resulting shear stresses may be of some concern with maximums of +48 MPa and –59MPa, as shown in Figure 4.

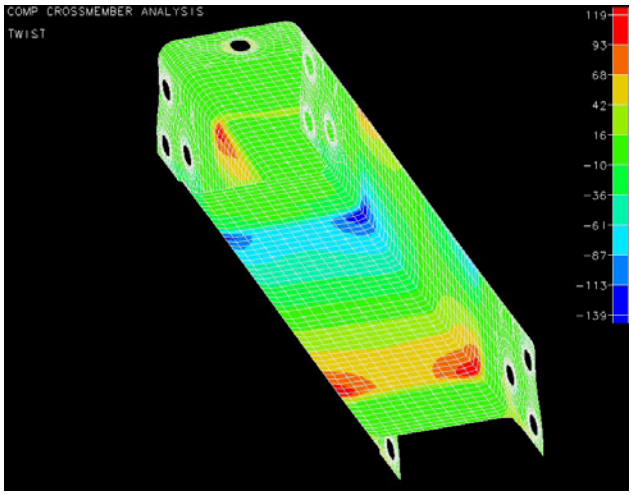

Figure 3. Resulting normal stresses show maximums of 119 MPa in tension and –139 MPa in compression, which are well below the predicted failure stresses.

Production Readiness

To prepare for production, a meeting with the OEM supplier was conducted to initialize a potential supplier list for production of this product. Table 1 shows the criteria and weighting factor for each as the potential suppliers were rated.

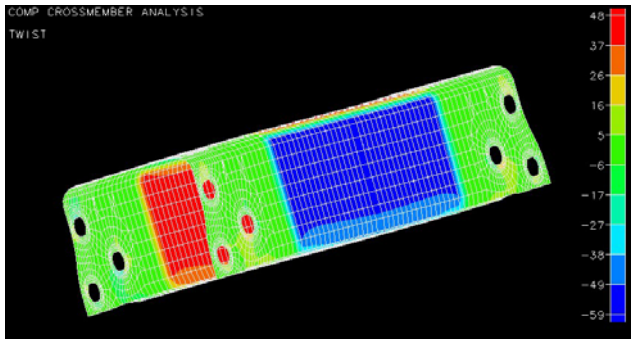

Figure 4. The resulting shear stresses of +48 MPa and –59 MPa are actually of more concern.

Table 1. Criteria and weighting factor for ranking suppliers

1. Process experience (thermoset only)	
• RTM/RIM/VARTM w/fabric or performs	
• Filament winding/compression molding	
• Prepreg	10
— Unilayers (laminate)	
— Woven fabrics	
• Hybrid insert molding	
2. Cost transparencies	8
3. Mfg. engineering support records (e.g., FMEAs, PPM record)	8
4. Program management structure	7
5. Quality control records/audits	6
6. Commercial transportation OEM tier 1 experience	5
7. Cost improvement plan	5
8. Warranty policy	4
9. Proof of customer satisfaction (awards, recognitions)	3
10. Subcontractor list (if any)	
11. Tool support/maintenance relationships	2

Conclusions

Accomplishments for FY 2006 include the following:

Modeling

- Narrowed the design scenarios to one: composite center piece with current end brackets
- Determined the thickness reduction from the ends to the center section
- Finalized design plans using Genesis and ABAQUS for production

Production Readiness

- Assembled manufacturing team from OEM and NCC personnel
- Identified a list of nine potential suppliers
- Developed a criteria list to rank potential suppliers

Future Direction

Modeling

Had the program continued, the two load cases of racking and twisting would be used to determine appropriate loads applied at the same places as deflections to generate duplicate stress profiles. Those loads would then be used to optimize composite design in Genesis (we found previously that enforced displacements did not work for optimization). Those results would then be transferred to ABAQUS to optimize the metal corner flange design for contact stresses. March 7 was the expected deadline to have the finalized design delivered to potential suppliers.

Production Readiness

A program to visit the main suppliers was being put together to give them the overall design and answer questions they may have had. The list would be narrowed to four suppliers who would give request for quotation presentations to the OEM customer.

Each supplier would be given 90 minutes to present while focusing on addressing the criteria. The presentations were to be scheduled April 1–11. On April 13, the manufacturing team would meet with the OEM to reduce the candidates to four. The design team would then visit each of the four candidates to answer specific detailed questions for production. The manufacturing team would then visit each supplier for its request for quotation final presentations the week of June 12.

Proposal for Continuation

NCC developed a plan that was presented to the OEM for continuing this program. To lessen costs, the PFA part of the design was eliminated and the focus was on safety factors in the elastic design. Previously, the main OEM had committed to funding up to $200,000 in tooling costs. To help alleviate engineering expenses for the OEM, NCC offered to pay for up to $200,000 for tooling costs using Ohio state capital funding. The requirement, however, was that all tooling and prototyping be performed in the state of Ohio. Unfortunately, the OEM was not able to transfer tooling budget to engineering, and the program has now been indefinitely suspended.

C. New-Generation Frame for Pickup/Sport Utility Vehicle Application

Principal Investigator: Curt A. Lavender
Pacific Northwest National Laboratory
P.O. Box 999, M/S K2-03, Richland, WA 99352
(509) 372-6770; fax: (509) 375-4448; e-mail: curt.lavender@pnl.gov

Kurt M. Knop
DaimlerChrysler Corporation
14250 Plymouth Road
Detroit, MI 48227
(313) 659-6076; fax: (313) 635-5221; e-mail: kmk4@daimlerchrysler.com

Chief Scientist: James J. Eberhardt
(202) 586-9837; fax: (202) 587-2476; e-mail: james.eberhardt@ee.doe.gov
Field Technical Manager: Philip S. Sklad
(865) 574-5069; fax: (865) 574-6098; e-mail: skladps@ornl.gov

---

Contractor: Pacific Northwest National Laboratory
Contract No. DE-AC06-76RLO 1830

Objective

- Evaluate the design of an optimized hybrid materials frame that represents a new generation of pickup/sport utility vehicle (PU/SUV) frame applications and vehicle architecture.

Approach

- Apply high-risk manufacturing and design methods to the PU/SUV frame to reduce mass while meeting cost goals consistent with a high-production vehicle.

Accomplishments

- Established performance, packaging, and weight targets for the second iteration of the new-generation frame, the "next-generation frame" (NGF).
- Created a design for the NGF that projects greater weight reduction and a decrease in the number of parts compared with the current steel baseline frame.
- Created a computer-aided engineering (CAE) model of the NGF and evaluated impact; noise, vibration, and harshness (NVH); and durability of the NGF.
- Completed CAE and design iterations to meet requirements for a DCX 5-Star crashworthiness rating.
- Created a complete bill of materials for the prototype and initiated procurement.
- Assembled the prototype frame into a full-size vehicle and road tested it at the DCX Auburn Hills Technical Center.
- Performed extensive analysis of the crush tip mechanical properties (the results will be the subject of a presentation co-authored by DCX at the Society of Automotive Engineers annual meeting).

Future Direction

- Have the frame evaluated by DCX for torsion
- In support of DCX crush tip testing, evaluate the effect of hydroforming on tip mechanical properties.

Introduction

Increased consumer demand for PU/SUVs has resulted in increased fleet fuel consumption. The fuel demand for this class of vehicle has exceeded that of passenger automobiles and now consumes approximately 27% of the oil used in the United States.[1] The objective of this project is to explore manufacturing methods and materials to reduce the mass of the SUV/PU frame, thereby reducing fuel consumption for this class of vehicle.

During the second quarter of FY 2003, DaimlerChrysler completed vehicle testing at the DCX Proving Grounds using an SUV/PU platform equipped with a hybrid frame. Results of the accelerated testing have proved that (1) the hybrid frame design had sufficient strength and durability to meet the vehicle performance requirements; and (2) the frame was probably somewhat overbuilt and heavier than required, even with a substantial weight savings from the current baseline steel frame.

The next phase of the project will evaluate the use of a lighter frame, the NGF. The NGF uses a CAE approach and higher-risk manufacturing technologies. The NGF is projected to weigh less than the previously tested new-generation frame and require 35% fewer components.

Approach

A CAE model of the NGF will be created and design iterations performed to meet the NVH, impact, and durability requirements for a DCX 5-Star rating. A prototype of the frame will be fabricated and evaluated by frame flexure and road tests.

Progress

CAE analyses of the frame are complete and satisfy all of DCX requirements for 5-Star crashworthiness, NVH, and durability. The frame has been completed and delivered to DCX and Magna for full-scale automotive testing. Figure 1 shows the frame being fabricated in the assembly fixture.

Figure 1. NGF components and assembly fixture before final assembly.

The completed frame was assembled into a Dodge Durango and evaluated using a vehicle simulator at the DCX Auburn Hills Technical Center. The frame successfully completed a satisfactory lifetime. Figure 2 is a photograph of the Dodge Durango undergoing vehicle testing with the NGF.

Figure 2. Dodge Durango undergoing vehicle testing with the NGF.

Future Direction

All vehicle testing of the frame has been completed and is being evaluated by DCX and PNNL staff.

Reference

1. *Light Duty Vehicle Trends: 1975 through 2004*, EPA 420-R-04-00, United States Environmental Protection Agency, Washington, D.C.,April 2005.

D. Advanced Superplastic Forming Development for Heavy Vehicle Structures

Principal Investigator: Curt A. Lavender
Pacific Northwest National Laboratory
P.O. Box 999, M/S K2-03, Richland, WA 99352
(509) 372-6770; fax: (509) 375-4448; e-mail: curt.lavender@pnl.gov

Don Trettin
PACCAR Technical Center
Farm to Market Road
Mount Vernon, WA
(360) 757-5241; fax: (360) 757-5370; e-mail: don.trettin@paccar.com

Nirmal Tolani
2911 Meyer Road
PO Box 1109
Fort Wayne, IN 46801-1109
(260) 461-1238; fax: (260) 428-366; e-mail: nirmal.tolani@nav-international.com

Chief Scientist: James J. Eberhardt
(202) 586-9837; fax: (202) 587-2476; e-mail: james.eberhardt@ee.doe.gov
Field Technical Manager: Philip S. Sklad
(865) 574-5069; fax: (865) 574-6098; e-mail: skladps@ornl.gov

---

Contractor: Pacific Northwest National Laboratory
Contract No. DE-AC06-76RLO 1830

Objective

- Evaluate the use of superplastic forming (SPF) for heavy vehicles

Approach

- Focus on demonstrating the technology, using mutually agreed-on truck components, with the goal of developing the SPF design and material property knowledge base to the point where the individual companies have the ability to implement it for their new vehicle designs.

Accomplishments

- Performed room-temperature tensile properties tests of 5083 sheet superplastically formed to a biaxial strain of 0.45.
- Performed superplastic tensile tests on the baseline 5083 aluminum alloy.
- Designed a die to evaluate the elimination of secondary operations.
- Performed initial tests on the 6013 alloy to determine if a heat-treatable alloy may be used in a low-cost SPF process. Results indicate that a post-SPF aging treatment will be required.

Future Direction

- Form additional trays and develop an S-N fatigue curve.
- Perform tests with the new die.
- Develop a process for a low-cost high-strength SPF alloy.

Introduction

Replacement of low-strength glass-fiber-reinforced plastics with aluminum in heavy vehicle hoods and other cab components can significantly reduce the weight of Class 6-8 truck components. Although the use of aluminum has been viewed as a desirable weight savings approach for some time, the complex shapes of aerodynamic hoods, bumpers, and fairings; the limited room-temperature formability of aluminum; and the high cost of forming tools have restricted its use. SPF, in the context of this proposal, is an elevated-temperature gas pressure forming technology that has been widely used in aerospace applications and was more recently introduced by General Motors (in a modified form) for selected aluminum automotive components. Advantages of SPF include inexpensive tooling, the ability to form complex aerodynamic shapes, simplified die design compared with traditional stamping and the opportunity for significant part count consolidation. Although SPF is traditionally viewed as a slow-forming process, recent advances in aluminum alloys and forming process procedures have reduced typical forming times to the point where SPF appears well suited for typical heavy truck production volumes. However, a number of technical barriers remain, including the ability to form Class A surfaces, the availability of suitable SPF sheet materials for large components, and the performance of SPF components and structures in heavy-duty truck applications.

Approach

The objectives of this project are to evaluate current production SPF capabilities and limitations through parallel truck original equipment manufacturer (OEM) demonstration components, to develop cost and design allowable tools that allow the OEMs to select proper applications for SPF, and to advance SPF materials and processing capabilities for heavy vehicle applications. The project team involves collaboration between two major truck manufacturers, International Truck and PACCAR Technical Center (PTC) (parent company of Kenworth and Peterbilt). Because of the competitive nature of truck manufacturing, the project will focus on demonstrating the technology using mutually agreed-on truck components; however, it will have the goal of developing the SPF design and material property knowledge base to the point where the individual companies have the ability to design and implement it for their new vehicle designs.

Progress

International and PTC have identified candidate components for SPF prototypes. International has initiated manufacturing of the components, and PTC is completing a stress analysis of the selected component.

To facilitate design of the components, Pacific Northwest National Laboratory (PNNL) superplastically formed samples of the 5083 aluminum alloy sheet to be used, and measured tensile properties normal and parallel to the rolling direction after a biaxial strain of 0.45 at 850°F and 1.3×10^{-3} s^{-1} strain rate. Room-temperature tensile samples were removed from the long dimension of the formed tray (shown in Figure 1) and tested according to ATSM E8. Additional samples were subjected to the 850°F thermal cycle only and compared with the tensile tests from formed trays.

The results of the tensile tests conducted in the rolling direction indicate that after forming to 0.45 at 1×10^{-3} s^{-1} at 850°F ,the sheet properties were similar to the as-annealed properties. Yield strength, ultimate strength, and elongation were 23,000 psi, 44,000 psi and 32% for annealed materials and 22,000 psi, 43,000 psi, and 31% for formed materials.

The results of tensile tests conducted transverse to the rolling direction indicate that after forming to 0.45 at 1×10^{-3} s^{-1} at 850°F, the sheet properties were

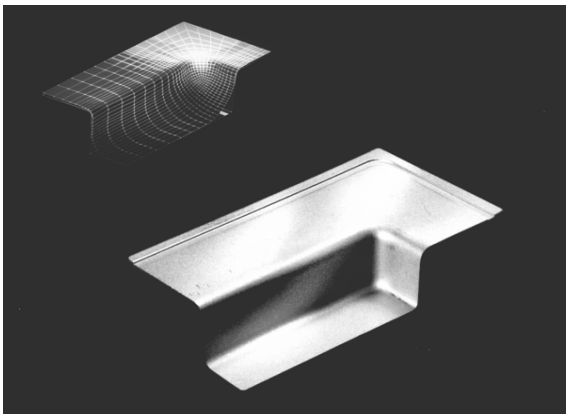

Figure 1. Sample SPF part used to characterize tensile properties from 0.047-in. 5083 aluminum sheet.

similar to the as-annealed properties. Yield strength, ultimate strength, and elongation were 23,000 psi, 42,000 psi, and 30% for annealed materials and 21,000 psi, 41,000 psi, and 29% for formed materials. The results of the tensile tests are summarized in Table 1.

The 5083 alloy used for SPF generally has a very fine grain structure, developed by high levels of cold work, that results in a low flow stress under controlled temperature and strain rate conditions. The material supplied to PNNL was tested in tension at room temperature and was found to have a 57,000 psi yield and 66,000 psi ultimate strength and an elongation of 10%. The high-strength sheet material can be beneficial prior to SPF because of high scratch and dent resistance forming; however, it can result in higher material costs if the sheet cannot be coiled, particularly in thick gage.

The sheet material was tested for superplasticity at 850 and 950°F and exhibited tensile ductility and strain-rate sensitivity, m-value, expected from fine grain superplasticity in the 5083 alloy.[1] The samples were tested using constant strain rate as approximated by an exponentially increasing crosshead velocity[2] at 5×10^{-4}, 1×10^{-3}, and 5×10^{-3} s^{-1}. At a strain of 0.15, the crosshead velocity was increased by 20% and the stress increase was used to determine the strain-rate sensitivity, m-value, using the relationship

$$m = \log(\sigma_2 / \sigma_1) / \log(\dot{\varepsilon}_2 / \dot{\varepsilon}_1) \ .$$

A typical stress-strain curve derived for an SPF tensile test has been included here for illustration purposes as Figure 2. The superplastic tensile test results are summarized in Table 2.

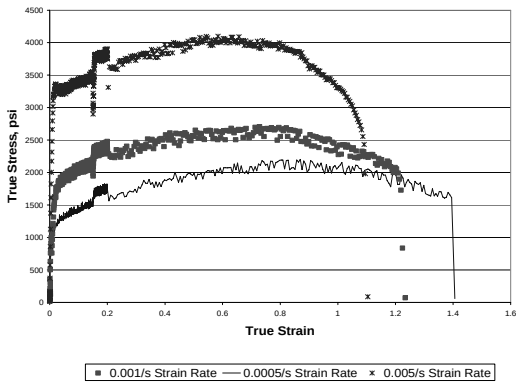

Figure 2. Typical superplastic tensile test curve performed at constant strain rate with a 20% velocity bump at 0.15 strain to determine strain rate sensitivity, m. The results shown in Figure 2 were from tensile tests performed at 850°F from 0.047-in. 5083 aluminum sheet.

The m-values ranged from a low of 0.33 at 850°F at 5×10^{-3} s^{-1} to a high of 0.55 at 950°F at 5×10^{-4} s^{-1}. The elongation was relatively insensitive to testing conditions and was 230 to 300% except for the 850°F 5×10^{-3} s^{-1} test condition, where elongation values dropped to below 200%. Consistent with the high strain rate sensitivity of superplastic materials, the initial flow stress of the sheets was dependent upon test conditions and ranged from a low of 500 psi at 5×10^{-4} s^{-1} and 950°F to a high of 3500 psi at 5×10^{-3} s^{-1} and 850°F. Recent developments in the automation of SPF have significantly reduced the cycle time required to load, form, and unload an SPF part. The newly reduced cycle time and transfer presses may enable the use of higher-strength alloy that has a heat treatment response analogous to “paint baking” in steels. Therefore, a brief study was initiated to determine if alloy 6103, which has higher strength and lower susceptibility to stress corrosion cracking, could be used. The study used hardness data to determine if a solution heat-treated sheet subjected to a rapid heatup to 850 and 950°F could exhibit an aging response, and if a sheet formed at 850 to 950°F

Table 1. Summary of room-temperature tensile tests performed on samples machined from superplastically formed trays made from 0.047-in. 5083 aluminum sheet; all trays were formed at an average strain rate of 1.3×10^{-3} s^{-1} and 850°F with a total cycle time (heat up to cool down) of 12 minutes

Sheet condition	Orientation	Yield strength (0.2% offset) (1000 psi)	Ultimate strength (1000 psi)	Elongation (%)
As-received sheet	Rolling direction	57	65	10
	Transverse	57	67	9
Annealed at 850°F for 12 minutes	Rolling direction	23	44	32
	Transverse	23	42	30
Formed tray	Rolling direction	23	42	30
	Transverse	21	41	29

Table 2. Superplastic tensile properties measured for the 0.047 inch 5083 aluminum sheet.

Temperature (°F)	Strain rate (s^{-1})	Orientation	m-value	Initial flow stress (psi)	Elongation (%)
850	5×0^{-4}	Rolling	0.54	1200	300
		Transverse	0.50	1200	300
	1×10^{-3}	Rolling	0.49	1800	240
		Transverse	0.45	1800	240
	5×10^{-3}	Rolling	0.34	3300	190
		Transverse	0.33	3500	180
950	5×10^{-4}	Rolling	0.55	500	260
		Transverse	0.51	540	250
	1×10^{-3}	Rolling	0.50	1000	250
		Transverse	0.43	1000	230
	5×10^{-3}	Rolling	0.35	2000	260
		Transverse	0.37	2100	230

and removed rapidly from a die could have a post-SPF age response without a water quench.

Initial results showed that the hardness of a sheet heated and held at 850 and 950°F, even for only 1 minute, was less than 10 HRB, indicative of a fully annealed sheet. This suggests that it is unlikely that the rapid heatup and short cycle time associated with an automated SPF process could result in a "paint bake" for a solution heat-treated 6013 sheet. However, 6013 sheets heated to 850 and 950°F, removed quickly from a furnace and air- cooled, exhibited an age response when held at 350°F. The hardness achieved in the air-cooled sample was less than that of a sample that was water-quenched; however, it did indicate that a post-SPF aging treatment could result in a higher hardness without a water quench. Figure 3 shows the aging curves.

The favorable results found in the hardness testing were followed up with tensile tests and, as predicted, tensile yield strengths of slow-cooled and aged samples were in excess of 34,000 psi. This significant finding will allow for additional weight savings. A stress analysis for the PTC demonstration part showed that if an alloy with 34,000 psi can be made cost-effectively, the mass savings over external sheet moulding compound panels can be in excess of 40%, compared with approximately 20% for commercial 5083.

A survey of the existing literature regarding 6××× was performed. The data [3,4] indicate that the 6013/6111 alloy could be made superplastic by

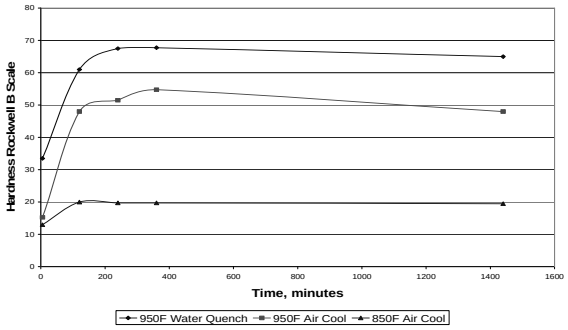

Figure 3. The age hardening response, measured in Rockwell B scale, of the aluminum alloy 6013 at 350°F after being subjected to air-cooling and water quenching at temperatures typical of SPF.

controlled thermomechanical processing. However, the processes used required extended aging times that would be prohibitively costly for heavy vehicle sheet products. A variant was developed at PNNL that simply uses cold work of annealed or heat-treated sheet to produce the fine grain size required from SPF. The grain sizes achieved at PNNL were less than ASTM size 11 (Figure 4) and exhibited superplastic elongations of greater than 200% at flow stresses typical of commercial fine-grained 5083. The 6013 samples had m-values greater than 0.4, indicating a relatively diffuse necking material that should produce high-quality parts. See Figure 5 for superplastic tensile test results for a fine-grained 6013.

A thermomechanical process developed at PNNL was used to produce sheet materials large enough to form an SPF component and allow for the evaluation of tensile properties using standard E8 tensile specimens. For the tensile strength

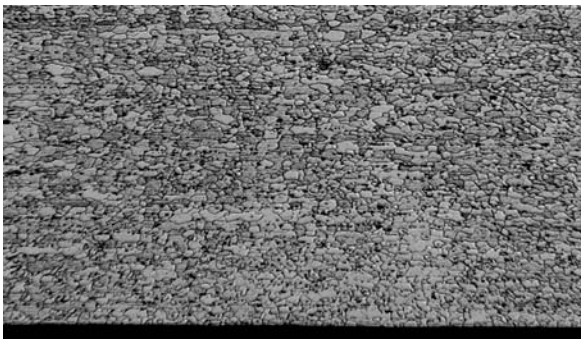

Figure 4. Typical ASTM 11 grain size found in 6013 alloy subjected to 60% or greater reduction of area at room temperature.

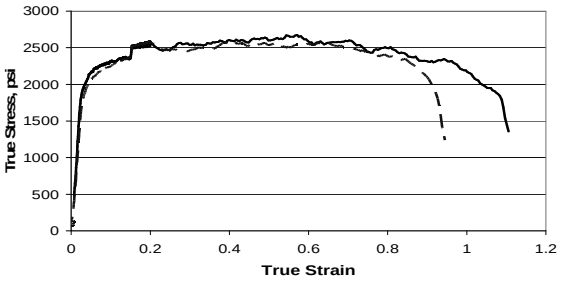

Figure 5. Superplastic tensile test performed on 6013 cold-rolled 60% (solid line) and 90% (dashed) line showing a relative insensitivity to processing conditions. Tested at 5×10^{-3} s^{-1} at 960°F.

evaluation, PNNL used the tray die shown in Figure 1 and removed samples as shown in Figure 6.

To simulate production cycles required for heavy production, the trays were formed using a total cycle time limit of 15 minutes (including heating and cooling) and a strain of 0.7 (100% elongation). The typical cross-section of a formed tray is given in Figure 7. In order to achieve the maximum strength levels found in the previous heat treatment study, the trays were formed above the solid solution temperature of 950°F.

Typically, in heat treatable aluminum alloys, maximum strengths are achieved by water quenching from a sufficiently high temperature to produce a metastable solid solution that forms fine (submicron) precipitates during a low-temperature thermal treatment (aging). For large sheet parts, such as those required for heavy vehicles, water quenching is not possible as a result of distortion and costly straightening and re-strike operations.

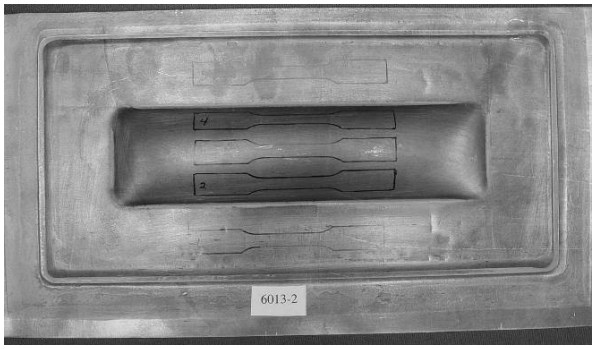

Figure 6. Tensile sample layout for 6××× alloy SPF trays formed at PNNL.

Figure 7. Typical formed 6××× alloy tray representing 100% elongation (0.7 strain).

Therefore, the trays were formed at 1022°F and subjected to three cooling rates—water quench, forced air, and static air—and then aged at 350°F for 8 hours. Tensile results are summarized in Table 3.

As expected, the tensile properties measured from the trays were found to be a strong function of the post-SPF cooling rate. The maximum 0.2% offset yield strength of 47,000 psi was found in the tray subjected to the water quenching, and strengths of 44,000 and 42,000 psi were found in the forced-air and static air-cooled trays, respectively. All strength levels measured were in excess of the target value established by PACCAR and indicate that a low-cost high-strength SPF 6××× alloy is viable for heavy vehicle production.

Table 3. Tensile values from superplastically formed trays subjected to different cooling rates from the SPF temperature of 1022°F

Quench condition from forming temperature	Yield strength (1000 psi)	UTS (1000 psi)	Elongation (%)
Water	44	59	18
Forced air	42	56	15
Air cooled	40	53	12

Future Direction

The development of data for use in SPF component design will continue. Fatigue data from superplastically formed 5083 aluminum sheets will be determined.

The evaluation of a low-cost, high-strength alloy process for high-rate SPF will continue with the development of a low-cost thermomechanical process.

References

1. J. S. Vetrano et al., "Superplastic Behavior in a Commercial 5083 Aluminum Alloy," *Scripta Metallurgica* **30**, 565–570 (1994).
2. K. I. Johnson et al., "The Effect of Specimen Geometry on the Accuracy of Constitutive Relations in Superplastic 5083 Aluminum Alloy," in *Proceedings of the 1994 International Conference on Superplasticity in Advanced Materials* ((ICSAM-94), Moscow, Russia, May 24–26, 1994.
3. L. P. Troeger and E. A. Starke, "Particle Stimulated Nucleation of Recrystallization for Grain Size Control and Superplasticity in an Al-Mg-Si-Cu Alloy," *Mat. Sci. and Engr.* **A293**, 19–29 (2000).
4. R. Kaibyshev et al., "Effect of Liquid Phase on Superplastic Behavior of a Modified 6061 Aluminum Alloy," *Scritpa Metallurgica* **47**, 569–575(2002) .

E. Development of Magnesium for Heavy Vehicle Powertrain Components

Principal Investigator: Darrell R. Herling
Pacific Northwest National Laboratory
P.O. Box 999, Richland, WA 99352
(509) 376-3892; fax: (509) 376-6034; e-mail: darrell.herling@pnl.gov

Chief Scientist: James J. Eberhardt
(202) 586-9837; fax: (202) 587-2476; e-mail: james.eberhardt@ee.doe.gov
Field Technical Manager: Philip S. Sklad
(865) 574-5069; fax: (865) 574-6098; e-mail: skladps@ornl.gov

---

Contractor: Pacific Northwest National Laboratory
Contract No.: DE-AC06-76RL01830

Objective

- Develop magnesium (Mg) composite casting technology and associated low-cost tooling for manufacturing of ultra-lightweight heavy vehicle powertrain components. The project is focused on three development tasks:
  - — Assess the potential to use Mg for vocational and long-haul trucks through technology development, evaluation of full-scale prototype components, and economic analysis.
  - — Develop advanced Mg materials and processing capabilities for heavy vehicle applications.
  - — Develop a low-cost shape-forming process that combines casting and in situ compositing for metal matrix composite (MMC) components.

Approach

The following is a project outline and general approach. The underlying focus is on process development and economical manufacturing methods for Mg and its composites. The approach and cost analysis will consider product design, material-specific characteristics, and component performance.

- Address technical challenges for the use of Mg:
  - — Develop high-strength, low-cost Mg MMC—PNNL/supplier.
  - — Current Mg alloys will have limited application for heavy vehicles.
  - — High-strength Mg MMC can improve strength while minimizing cost.
  - — Increase durability; fatigue life is more demanding than in automobiles and operating temperature/creep resistance are needed.
  - — Develop economical manufacturing/casting/compositing method.
    - Develop stir-cast Mg process.
    - Demonstrate hybrid lost-foam/pressure infiltration casting.

- Apply Mg to heavy vehicles:
  - — Determine how and where it is best to use Mg—PNNL/original equipment manufacturer (OEM).
    - Develop design guidelines and properties database.
  - — Work to reduce manufactured part cost—OEM/supplier/PNNL.
    - Address issues with integration of Mg into vehicle manufacturing process.

Accomplishments

- Designed, fabricated, and installed a new rapid compositing mixer at PNNL specifically for Mg MMC composites.
- Initiated experimental trials for stir-cast Mg-MMC production and modeled lost-foam casting molds.

Future Direction

- Develop the compositing ability to in situ cast and mix an Mg composite casting.
- Evaluate a modified lost-foam casting process that combines casting and compositing into one process step.

Introduction

Ultra-lightweight, high-performance Mg MMCs can improve fuel utilization while increasing component durability for heavy vehicles. As a rule of thumb, lightweighting can contribute to an increase of roughly 6–7% in fuel economy for every 10% reduction in mass. An estimated 3000 lb of mass can be targeted for reduction in the heavy vehicle powertrain and chassis. There is the potential for roughly 200–500 lb of weight savings through redesigning and replacing specific aluminum and cast iron components with Mg MMCs.

Downsizing of ancillary fixtures can result in additional mass and fuel savings. Increased component durability in applications, where wear is a factor, can also lead to improved vehicle operating costs. This is an incentive for fleet owners and independent truckers to embrace the new technology.

The objective of this project is to enhance the properties of Mg alloys by creating a Mg-ceramic composite. This class of material is an MMC in which ceramic particles or short fibers are added to the metal matrix. The resulting composite has very high specific strength and stiffness and significantly improved wear resistance. Thin cast sections are still possible; and, in the case of Mg, noise, vibration, and harshness (NVH) and load carrying capacity improve beyond the basic alloy. This is especially beneficial for vocational trucks, where load capacity and noise/vibration are two of the more common design problems facing engineers.

Approach

Development of low-cost Mg alloys and processing technologies is a major technical hurdle to widespread application of Mg in the heavy vehicle manufacturing industry. Therefore, the approach taken for this project includes active participation by a truck OEM, as well as by suppliers where appropriate. The philosophy of this teaming approach is to ensure meaningful technology transfer of enabling and new technical developments.

This project is a collaborative effort with Mack Trucks, Driveline Division. The project goal is to develop Mg composite casting technology and associated low-cost tooling for manufacturing ultra-lightweight heavy-vehicle powertrain components. The project scope is broken down into three tasks:

1. Assess the potential to use Mg for vocational and long-haul trucks through technology development, evaluation of full-scale prototype components, and economic analysis
2. Develop advanced Mg materials and processing capabilities for heavy vehicle applications
3. Develop a low-cost shape-forming process that combines casting and in situ compositing for MMC components.

Metal Compositing Method

Stir-casting techniques are currently the most common commercial method of producing aluminum MMC materials. This approach uses mechanical mixing of the reinforcement particulate into a molten metal bath. The resulting metal composite is cast, typically, by low-pressure die or sand casting. This process is effective in making high-quality parts. The process, coupled with a low-cost MMC feedstock material, can be an economical manufacturing method. However, combining the compositing and casting processes into a single process reduces the cost of producing an MMC component by an estimated 6%.

We have initiated an experimental investigation of the stir-cast Mg MMC production method as one

of the two technical development thrusts of this project.

A hybrid system that consists of combining evaporative pattern (lost-foam) casting techniques and low-pressure infiltration to create the metal-ceramic composite during the shape forming (casting) operation is currently being modeled. This second process, though a higher technical risk for success, would significantly reduce component-manufacturing cost. We expect it to allow easy, selective reinforcement of cast components because the reinforcement particles would be placed only where they would be of the greatest benefit to part performance. The key to achieving this approach is the ability to co-mix the second-phase particulate with the foam beads prior to expanding into the mold pattern, followed by a controlled burnout rate of the pattern during casting and infiltration of that particulate by the liquid metal front.

Once this process is modeled and the casting parameters are estimated, various part geometries will be cast in order to validate the process. Initially, tensile bars will be cast for mechanical property evaluation.

Magnesium MMC Development

In order to develop proper Mg MMC materials for powertrain components, it is necessary to investigate which alloy-reinforcement combinations will work best to achieve the mechanical performance goals as well as the environmental performance goals. To accomplish this task, a stir-cast metal composite mixer, shown in Figure 1, has been designed by PNNL and MC-21 Inc., constructed, and installed at PNNL.

The micro-mixer's design is based on MC-21's rapid mixing technology for aluminum MMCs, with provisions to safely melt Mg. This technology is unique in that it is a highly efficient means of mixing together (compositing) ceramic and molten metal, resulting in a metal composite material. The unit is capable of melting, mixing, and casting 10 kg of Mg or aluminum metal in a single batch. With this capability, multiple combinations of alloy-reinforcement chemistry can be produced and evaluated.

Figure 1. New PNNL rapid mixing and casting system.

Conclusions

Magnesium MMCs have outstanding specific strength and stiffness properties as well as NVH dampening characteristics—greater than Mg alloys alone. They also have enhanced wear and creep resistance over unreinforced alloys. One drawback to Mg and its MMC is that the supply base has all but disappeared in North America, requiring OEMs and specialty/prototype casters to assume production roles. The focus of this project is to develop manufacturing technologies that allow for the production of low-cost Mg MMC components. The intent is to allow an OEM to apply the low-cost process or transfer the technology easily to a supplier. The development of Mg composite casting technology will include low-cost tooling approaches for manufacturing of ultra-lightweight heavy-vehicle powertrain components, as well as the development of a low-cost shape-forming process that combines casting and in-situ compositing for MMC components.

F. Lightweight Stainless Steel Bus Frame—Phase III

Principal Investigator: J. Bruce Emmons
Autokinetics Inc.
1711 West Hamlin Road, Rochester Hills, MI 48309
(248) 852-4450; fax: (248) 852-7182; e-mail: jbemmons@autokinetics.com

Chief Scientist: James J. Eberhardt
(202) 586-9837; fax: (202) 587-2476; e-mail: james.eberhardt@ee.doe.gov
Field Technical Manager: Philip S. Sklad
(865) 574-5069; fax:(865) 574-6098; e-mail:skladps@ornl.gov

Contractor: Autokinetics Inc.
Contract No.: 4000010114

Objectives

- Investigate and demonstrate the mass-saving potential of ultra-high-strength stainless steel as applied to the structure and chassis of a full-size urban transit bus.
- Finalize design and analysis and build a full-scale prototype of the body structure and chassis.
- Investigate all of the fundamental feasibility issues related to the structure and chassis:
    1. Fabricate and test large lightweight stainless steel sandwich panels
    2. Fabricate roll-formed, high-strength stainless steel sections
    3. Test the feasibility of lightweight stainless steel cantilever seats
    4. Design and fabricate lightweight stainless steel independent suspension
    5. Integrate the traction motors into the suspension design

Approach

- Execute the basic body structure, including the floor/roof sandwich panels, pillar assemblies, longitudinal rails, and suspension subframes.
- Choose prototyping techniques that emulate the intended production process as closely as possible to aid in developing robust but cost-effective manufacturing techniques essential to meeting the objectives of the project.
- As computer-based design and analysis details of the bus develop, conduct hands-on physical experimentation in parallel to support the concepts and methods.

Accomplishments

- Installed exterior side panels.
- Made progress on steering system components.
- Received all window glass.
- Installed windows.
- Completed emergency exit windows.
- Completed prototype driver's station (mock-up).
- Received batteries.

- Installed batteries.

Future Direction

- Complete the fabrication and installation of suspension, steering, and spring components.
- Assemble propulsion components.
- Prototype two seats.
- Test structure.

Introduction

Advanced-technology transit bus concepts have made significant advancements in terms of light weight and fuel economy. However, these gains have come at the expense of higher manufacturing costs. In spite of attempts to use life-cycle costs to justify their purchase, initial cost remains a major obstacle to the introduction of fuel-efficient buses.

DOE's OFCVT approached Autokinetics in an attempt to solve this problem and asked Autokinetics to develop concepts for a lightweight urban transit bus based on the use of high-strength stainless steel. In the passenger car field, Autokinetics had developed structural and manufacturing techniques for the cost-effective use of stainless steel in spaceframes and suspensions. OFCVT wanted to determine whether this approach could be applied to transit buses as well.

The program was structured in three phases:

- Phase I—Initial Concept Development
- Phase II—Concept Verification and Initial Design
- Phase III —Final Design and Prototyping of Body and Chassis

Phases I and II have been successfully completed. Phase III will result in a full-size body structure and suspension that will be tested statically and dynamically. The development of an optimized hybrid powertrain and other vehicle systems will be addressed in a separate project.

This project was unusual in that no formal mass or cost targets were given. The object was to save as much mass and cost as possible.

Current State of Progress

With the installation of exterior side panels and glass, the overall body structure is now nearly complete. Much of the remaining work will focus on the final design and fabrication of suspension components. Relatively few tasks remain, and it is expected the project will be completed by mid-2007.

Exterior Side Panels

The body side panels (Figure 1) were assembled to the basic body structure during this reporting period. Because the side panels are intended to be an integral part of the overall structure, it was necessary to install them with their material in tension. This requirement was complicated by the fact that the 0.030-in. stainless steel sheet material to be used displayed pronounced waves due to coil-set. A special technique was developed to position and pretension the side panels as they were spot-welded to the structure. This technique worked very well, was straightforward to accomplish, and resulted in very little surface deviation in the installed side panels.

Steering System Components

Additional progress was made in the steering system. Various communications and meetings took place with Pailton Steering Systems, ZF Lemforder, and TRW to discuss the somewhat unusual, low-floor-compatible steering system design and necessary components. As of the end of this reporting period, all necessary components have been identified and are in the process of being delivered.

Figure 1. Exterior side panels.

Figure 2. Body side glass.

Body Glass

As reported previously, laminated glass was chosen for all glazing positions because it provides a number of advantages compared with tempered glass. During this reporting period, Fox Fire Glass (Pontiac, Michigan) completed fabricating and delivered the prototype glass for all side windows and the two-part windshield.

The fixed-position glass was installed by Troy Auto Glass Inc. (Troy, Michigan), a local automotive glass installer. It is shown in Figure 2. The installation was accomplished using standard processes and materials. It is interesting to note that a couple of windows were installed prematurely and had to be removed to allow access for other operations. Troy Auto Glass removed these windows using industry-standard equipment and reinstalled them when appropriate. This exercise provided the opportunity to evaluate the glass replacement procedure. It was found that replacement of the bonded side glass could be accomplished quickly and efficiently using only standard equipment, materials, and processes.

Figure 3. Emergency exit window.

Emergency Exit Windows

In addition to the two doors, five windows located throughout the bus are designated as emergency exits. One such window is shown in Figure 3. Since the vehicle structure incorporates bonded-in-place side glass, the five exit windows required a different attachment and sealing approach. These windows are of a frameless design and are attached to the structure through a standard piano- type hinge bonded to the upper edge of the glass. The body side of the hinge is bolted rather than spot-welded to aid replacement. A standard profile bulb seal pressed onto the flanges around the perimeter of the window opening provides the sealing function as well as protection from the raw edges of the sheet metal.

A latch-bar, which carries the two side-position latches, was then bonded to the inside of the glass panel. This joining procedure uses the same bonding material as the standard glass installation. The use of a latch-bar allows for subassembly of the latch system, greater dimensional control, and a wide distribution of the 03566e stress imposed by the latch.

Driver's Station

A prototype driver's station mock-up was assembled to physically locate the relative positions of all driver station components. A plywood "buck" was fabricated to which the physical components such as the driver's seat, steering column, and pedals were attached. It also allowed for the flexibility to reposition the various elements of the driver's environment. This mock-up provided a basis for evaluation and was used in the development of the driver's station design task covered under a separate project. The completed driver station derived from this mock-up is shown in Figure 4.

Figure 4. Driver's station.

Received Batteries

During this reporting period, Autokinetics received delivery of nine Zebra Z37 batteries from MES-DEA (Switzerland). Eight of these batteries were purchased under a DOE Systems project. One battery was purchased to fulfill the requirements of this project in place of a bank of 25 lead-acid batteries as originally proposed. The additional cost of the Zebra battery was absorbed by Autokinetics. It is felt that this more advanced battery technology will result in a much more meaningful first trial of the bus prototype. This first battery was connected to the vehicle control network and the motor controllers to enable testing and debugging of the prototype electric drive propulsion system.

Battery Installation

During this reporting period, a battery arrangement was developed and mounting hardware designed and fabricated to secure the batteries to the vehicle. Overall mass balance, length of conductors, and high-voltage safe practices were all important factors in determining the configuration and placement of the batteries and their supporting components.

Once preliminary testing of the control network was completed, the battery was installed into the vehicle along with its charger, cooling fan, and a motor controller. This installation is shown in Figure 5.

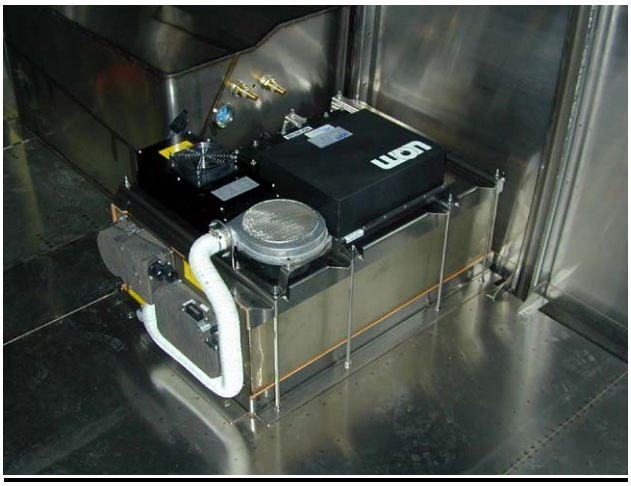

Figure 5. Battery installation.

Dissemination and Commercialization

9/23/05—Meeting with ZF Lemforder. Attended by Paul Donnelly and Cliff Eschelman.

11/22/05—Meeting with Solutia, Inc. Attended by Jay Pyper and others.

11/30/05—Informal review meeting with Lee Slezak (DOE); Donald Hillebrand, Argonne National Laboratory (ANL); Tim Murphy and Jim Francfort, Idaho National Laboratory.

2/23/06—Meeting with Utilimaster. Attended by Rob Fairchild (Fairchild and Associates) and John Knudtson (Utilimaster)

3/15/06—Meeting with Pailton Steering Systems. Attended by Rob Kilhefner, Andy Rose, and James Wiles.

5/23/06—Meeting with City of Rochester Hills, MI, to discuss "Smart Zone." Attended by Dan Casey (City of Rochester Hills).

8/24/06—Systems project review. Attended by Lee Slezak (DOE) and Jules Routbort (ANL).

Conclusions

Autokinetics remains confident that high-strength stainless steel has the potential to achieve substantial mass reductions in bus structures. The bus body structure is now nearly complete; most of the identified technical risk issues have been resolved; and structural and chassis mass estimates remain nearly unchanged compared with early predictions. Ongoing fabrication of the physical prototype has provided concrete mass numbers, and it is now expected the actual mass reduction of the complete battery electric vehicle will be close to 50%.

It is also hoped that practical commercialization can be achieved in the not too distant future. Low capital investment and an ample knowledge base are key enablers for this. Much has been learned thus far about processing and assembling of the body structure and many useful techniques have been developed. Given the relative ease of constructing this prototype within our own facility, it is quite apparent that capital requirements for commercializing this technology will be relatively small.

The independent cost analysis commissioned by DOE supports this as well as the predicted mass and unit cost savings.

6. APPLICATION OF INNOVATIVE MATERIALS

A. Application of Carbon Fiber for Large Structural Components

Principal Investigator: Kevin L. Simmons
Pacific Northwest National Laboratory
P.O. Box 999, MSIN: K2-44, Richland, WA 99352
Phone 509-375-3651; fax: 509-375-2186; e-mail: kl.simmons@pnl.gov

Technology Development Manager: Dr. James Eberhardt
(202) 586-9837; fax: (202) 586-1600; e-mail: james.eberhardt@ee.doe.gov
Field Technical Manager: Philip S. Sklad
(865) 574-5069; fax: (865) 574-6098; e-mail: skladps@ornl.gov

---

Contractor: Pacific Northwest National Laboratory
Contract No.: DE-AC06-76RL01830

Objective

- Develop selective reinforcement technology that can be applied to large cab components to improve specific stiffness and strength while reducing overall component weight.

Approach

- Determine how well low-cost carbon fibers can be hybridized with glass fibers to provide substantial weight and cost reductions in large cab components.
- Develop a system for preforming carbon and glass fibers together that will allow components to take maximum advantage of the capabilities of selective reinforcement alignment and property contribution.
- Develop models for the analysis of hybrid chopped fiber preforms and composites that allow the thermal and structural properties to be developed and compared with experimental analysis.
- Perform structural testing to define the limits of applicability of the carbon/glass hybrid reinforcement materials to the large structures and develop guidelines for applications that may be used by original equipment manufacturers (OEMs).
- Design and develop critical sub-section components of large structures to use in correlation with the predictive models, and to validate the structural application criteria. Determine the capability of the materials to be fabricated in full-scale components and determine the performance of these full-scale components in real application scenarios.

Accomplishments

- Developed short fiber composite models for predicting properties of hybrid composite structures.
- Completed experimental testing of hybrid composite panels for model correlations.
- Developed a method of measuring fiber angles to determine the level of anisotropy in chopped fiber composites.
- Completed a set of design experiments on a new resin system for use with the hybrid composites.
- Completed initial runs on a large test tool with short fiber composite preforms.

- Developed a large-scale, sub-component tool specifically to mimic design attributes applicable to several structural and appearance components.
- Performed initial runs on a large test tool with short fiber composite preforms at a tier-one supplier.
- Developed hybrid fiber preforms for test tool and demonstrated initial successful molding with hybrid fiber and resin system.
- Prepared samples for testing from large structural components.
- Developed the first Class A structural carbon composite panels for truck applications.
- Demonstrated impact performance 2–3 times better than that of standard structural composites.
- Developed hybrid carbon composite with improved impact performance over fiberglass composites.
- Demonstrated thin (2.5-mm) panel fabrication and resin transfer molding capability.
- Demonstrated panel molding with varying cross-sections from 2.5 to 7 mm in a single component.
- Performed panel molding with various filler types and loadings and selected optimum fillers for achieving a Class A surface.
- Performed mechanical and impact tests on a range of panels.
- Developed and performed process trials with a new tooling system that allowed the system to work together. This included improving the thermodynamic control necessary for achieving mechanical and impact properties.
- Optimized the resin system using different fillers.
- Tested and validated thickness constraints on panels for achieving structural performance on surface-coated thin hybrid panels.
- Tested and validated the barrier coat and optimized it for surface profile.
- Modeled tooling resin flows into fiber perform.
- Evaluated the feasibility of large-scale part production.
- Determined the cost spread among tooling approaches compatible with this system.
- Evaluated the dimensional stability of the hybrid composite material under various environmental conditions.
- Evaluated the paint bakeout cycle for changes in adhesion and surface appearance.

Introduction

The purpose of the project is to develop the design and material processing technology that will facilitate the use of low-cost hybrid glass fiber and carbon fiber reinforcements in large composite components, which will reduce weight and improve structural performance. The project will also seek to advance low-cost carbon fiber materials developed by industry by advancing the introduction of low-cost resin systems that are compatible with current heavy vehicle structural composites.

Our approach was to determine the feasibility of hybridizing low-cost carbon fibers with glass fibers to provide substantial weight and cost reductions in large cab components. A system was developed for preforming carbon and glass fibers together that would allow the components to take maximum advantage of the capabilities of selective reinforcement alignment and property contribution. Models were developed for the analysis of hybrid chopped fiber preforms and composites that allow the thermal and structural properties to be developed and compared with experimental analysis.

Structural testing was performed to define the limits of applicability of the carbon/glass hybrid reinforcement materials to the large structures and develop guidelines for applications that may be used by OEMs. We evaluated the design and development of critical sub-section components of large structures to use in correlation with the predictive

models, and to validate the structural application criteria. The project goal was to determine the capability of the materials to be fabricated in full-scale components and determine the performance of these full-scale components in real application scenarios.

The use of selective reinforcements with higher-stiffness fibers has the potential to reduce both costs and weight simultaneously, even at today's price points. However, their introduction is hindered by the lack of understanding of the fibers in existing processes, the cost, and the need to develop robust methods of preforming glass and carbon fiber materials together. In addition, the capability to provide a Class A surface finish is required; developing that capability will require the potential development of bonding agents and the ability to model thermal and structural performance of the materials in a hybrid system. The recent development of composite systems combining carbon fiber reinforcement with low-cost automotive and marine resin systems provides the opportunity for selective reinforcement of a broad range of structural composite components.

Predictive Modeling

Summary of the Modeling Approach

A computational tool called EMTA, which uses the Eshelby/Mori-Tanaka approach, has been developed to predict the elastic and thermal properties (thermal conductivity, thermal expansion coefficients) as well as the elastic-plastic responses for short-fiber composites.[1] The EMTA model makes use of the Eshelby equivalent inclusion method in which fiber characteristics (inclusion shape) are accounted for through the so-called Eshelby tensor while the constituents' properties and volume fractions and the interactions of fibers are taken into account through the homogenization procedure. EMTA can handle two types of fibers, which are mixed and embedded together in a resin matrix (hybrid composites). Planar orientation is assumed and obeys the fiber orientation distribution density of the form $\rho(\theta) = \lambda e^{-\lambda\theta}$, where λ is the orientation angle measured with respect to the major fiber alignment axis (or fiber orientation distribution axis), and θ denotes a parameter governing the randomness. When λ is very small ($\theta \to 0$) the fibers are randomly oriented, while they are aligned for large values of θ. Between these two limiting cases, a given value of θ designates a fiber orientation distribution that can be rather random or rather semi-oriented. EMTA can be used as a stand-alone code to predict the basic homogenized composite properties. It has also been introduced into ABAQUS by means of the user subroutine UMAT of this code for structural analyses.

The value in developing this code is that it helps the designers of large structures design shapes and do analyses using hybrid composites. There is very little modeling capability that can predict properties for short-fiber composites. Models that combine both fiber types, based on randomness of each, are not available.

Figure 1 illustrates an unsymmetrical hybrid composite made of different composite layers, which are not symmetrical through the thickness. These are of particular concern because of the mismatch of coefficients of thermal expansion (CTEs) between the layers, which can lead to unacceptable structural deformations. On the other hand, adjusting the CTEs by means of trial-and-error approaches is time-consuming and expensive. Therefore, numerical methods to predict the CTEs of the composite layers and the governing *microstructural parameters* (e.g., fiber volume fraction, aspect ratio, orientation distribution) are helpful in the design of unsymmetrical hybrid composite laminates.

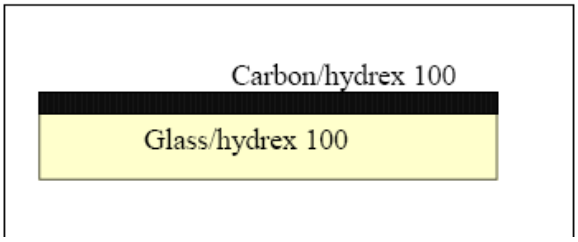

Figure 1. Schematic of a hybrid laminate

Table 1 compares the CTEs for different materials and the prediction in the composite forms. When the material constituent properties are combined with the processing orientations that a machine may bias, the EMTA model is able to predict the part behavior.

Figure 2 shows the predicted deflection (displacement u_3) resulting mainly from the mismatch of the in-plane CTEs (α_1, α_2) between the carbon

Table 1. Thermal expansion coefficients of the constituent materials and of the fiber tows filled with Hydrex 100

	α_1 (xE6/°C)	α_2 (xE−6/°C)	α_3 (xE−6/°C)
Carbon[a]	–0.7	10	10
E-glass[a]	5.4	5.4	5.4
Vinyl ester[b]	70	70	70
Carbon/vinyl ester[c]	–0.011935	38	38
Glass/vinyl ester[c]	7.7081	36.525	36.525

[a] ASM *Handbook of Composites*.[2]
[b] Based on the values of thermoset polyester given in ref. 2.
[c] EMTA prediction.

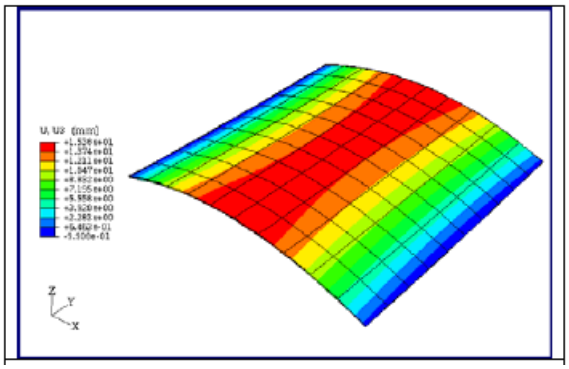

Figure 2. Prediction of the deformed shape an dout-of-plane deflections for the analyzed hybrid panel after molding.

and glass layers. The predicted deformed shape agrees well with the experimental shape shown in Figure 3. Predicted and experimental deformed configurations are presented in Figure 4 in terms of the spatial coordinates *X*, *Y,* and *Z*. In both configurations, the *Z*-coordinates were determined on the top surface of the hybrid panel. The predicted values correlate well with the experimental results.

To reduce the mismatch of CTEs, the first remedy is to realize the same orientation distribution for the carbon and glass fiber tows. Consider, for instance, that the carbon tows' orientations are also completely random. Such orientations will lead to the predicted variations of the in-plane CTE as a

Figure 3. Warpage of the hybride panel after molding.

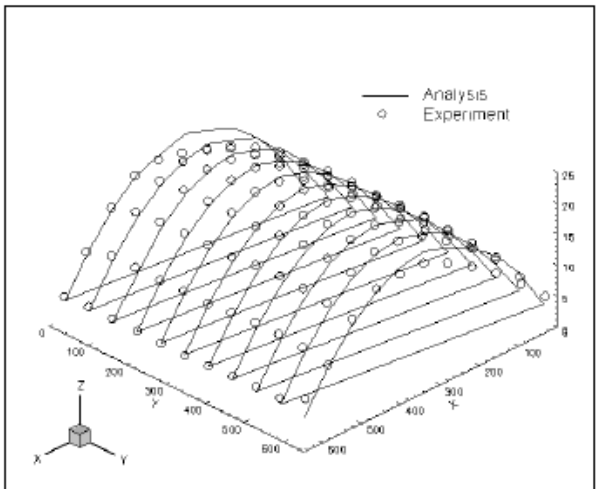

Figure 4. Experimental and predicted deformed coordinates for the analyzed hybrid panel after molding.

function of the fiber tow volume fraction shown in Figure 5.

For a given glass tow volume fraction, the curves provide the corresponding carbon tow volume fraction, which must be realized so that the mismatch of CTEs is zero. These values were determined for the proper fiber volume fractions of the glass layer and of the carbon layer, as well as the fiber volume fractions of the tows. Finally, Figure 6 shows the simulation results for the adjusted case. The deflection is reduced practically to zero as a result of suitable adjustments of fiber orientation and of the carbon tow volume fraction in the carbon layer.

Preform Materials

Experimental preform test panels have been fabricated using a variety of methods. The initial stud-

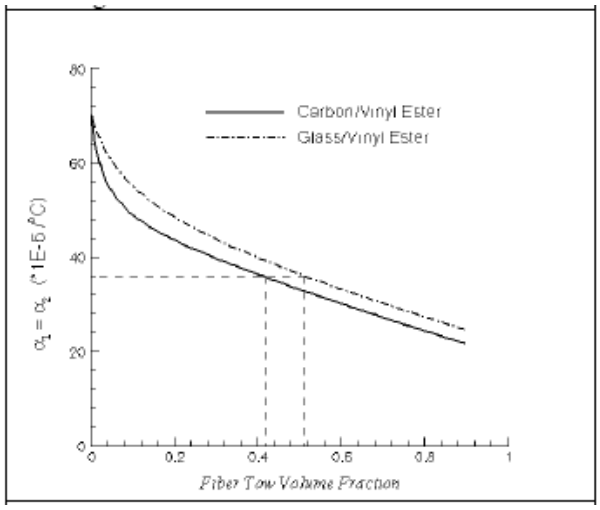

Figure 5. Variations of the in-plane CTEs of the carbon and glass layers with the fiber tow volume fraction.

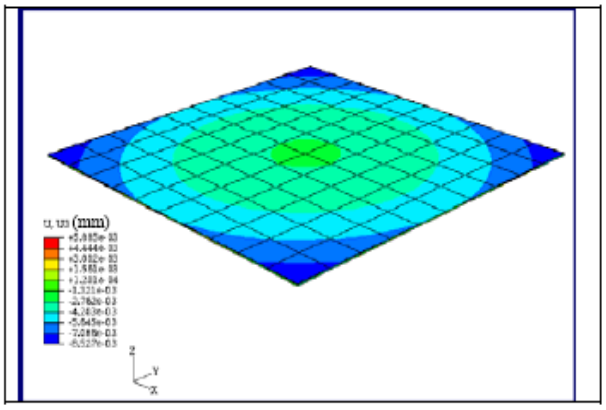

Figure 6. Prediction of the deformed shape and out-of-plane deflection for the analyzed hybrid panel after adjustments of fiber orientation distribution and fiber volume fraction for the carbon layer.

ies attempted to use preforms by the National Composites Center (NCC). These panels (Figure 7 show a typical carbon/glass hybrid panel using 3% carbon) had variations in the volume fractions of glass and/or carbon. The hybrid panels also had four levels of carbon fiber in addition to the glass. Carbon volume levels were 3%, 9%, 15%, and 45%, with the balance being random glass, and were made in two nominal thicknesses of 2.5 mm and 4.0 mm. There were also fiber-directed preforms of carbon fiber for comparing how well the properties could be controlled for a specific orientation. The panels were then formed in a resin transfer mold (RTM)

Figure 7. Composite hybrid perform with 3% carbon fiber chop.

with a standard polyester RTM resin from Reichhold Corporation.

Fiber orientation measurements were made for determining the randomness factor for the EMTA model. Figure 7 shows a 3% carbon fiber preform that was used to determine the random pattern of the chopped material applied to the preform.

The preform digital image was then used in a Scion Image software package from which fiber orientation was measured relative to the bottom edge. The orientation was from 0 to 180°. Figure 8 shows the output data from the Figure 7 panel. The data show very good randomness with no defining pattern.

NCC also provided some fiber-directed preforms for evaluation. The panels were to have 0° and 90° directed fibers. The panels used in these measurements proved to be more challenging because of the higher fiber volume fraction of carbon, which presented a darker background and little con-trast. The lighting was extremely important for enhancing the fiber tows on the surface.

Figure 9 shows the histogram data of the oriented fiber measurements. A pattern is developed by the preferential orientation of the chopped fiber pattern program from the chopper gun. The histogram shows a bimodal distribution of fibers at approximately +45° and –60°.

The NCC panels did not perform well for processing. The use of a low-pressure RTM through a low-porosity preform created a slow process time that was not conducive to large part applications.

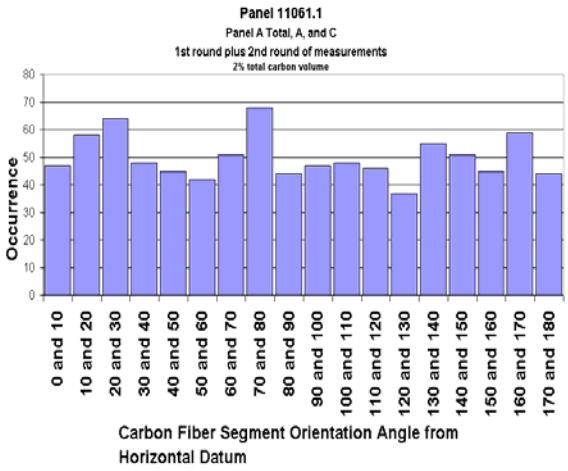

Figure 8. Histogram of fiber orientation.

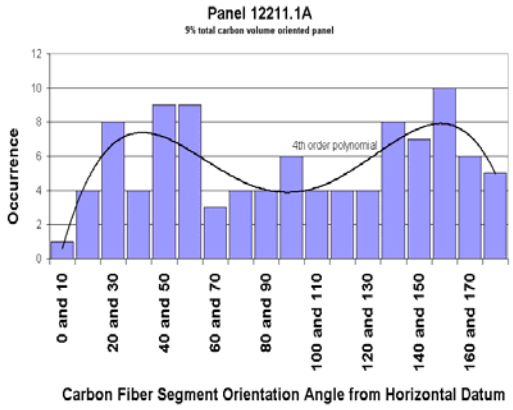

Figure 9. A bimodal distribution of carbon fiber.

This process was not deemed useful for further study, given the hybrid materials approach and large part format we were considering. The development of a hybrid system with a flow media core significantly increased the processing speed and created an improved part. Two vendors provided commercially available glass materials that were modified with our hybrid carbon fiber approach.

The vendor-supplied materials were evaluated based on core thickness and core types. Several binder formulations for binding chopped carbon fibers to the glass and flow media material were evaluated, and a final formulation was chosen for all of the experiments. The significance of the flow speed was a key criterion if the end use was to be large structural components. The time to fill was reduced from 5–6 min down to less than 1 min for our model experiment. The significance of this time is that it allows for the tool cavity to fill with resin before the resin begins to gel and build a high enough viscosity that the resin will not wet out fibers and stops flowing in the cavity.

Resin Evaluation

Initial evaluations of the EMTA model used a traditional low-cost polyester resin system. The resin system did not perform satisfactorily with hybrid fiber combinations, so the program worked with Reichhold Chemical to come up with a low-cost hybrid resin. Current interest in the attractive properties arising from the combination of polyester and urethane resin chemistries has prompted investigation into efficient manufacturing methods using a blended polyester/urethane system. By mating this material to a glass/carbon hybrid fiber perform, an optimization of properties from all of the constituents can be achieved at a relatively low cost, especially if the laminate production can occur within a short cycle time.

The resin system chosen was a hybrid resin chosen for its ability to bond to both glass and carbon fiber surfaces. Traditional polyester resins bond well to glass fibers but are substandard for bonding to carbon fiber. Other resin systems that bond well to carbon fibers exceed the price points for a low-cost composite system. Those systems would not be cost-effective for manufacturers to implement. The hybrid system underwent a set of experiments to determine the controlling variables for processing. Several catalyst types were evaluated; temperature ranges, promoter types, and levels were investigated. A Minitab design of experiments (DOE) was run using a full factorial design with two levels and three factors. The interest in the experiments was to help determine which components gave the most control over the gel time. The factors of interest were temperature, cobalt content, and catalyst. The output measurements were gel time, peak exotherm time, and peak temperature.

The experiments were run on a Haake Rheocord 90 mixer using Brabender medium-shear mixing blades. The new hybrid resin from Reichhold was used. The catalyst, cobalt promoter, and temperature were controlled for the experiments.

The data were collected based on time, temperature of the resin, and torque value during the mix. The gel time was taken as the first inflection of the torque curve. This is based on the torque value be-

ginning to climb during resin gelling. The resin temperature also begins to increase relative to the same point as the gel time. The peak exotherm time is taken at the peak temperature that the mixture reaches before cooling down.

Figure 10 is a Pareto chart that illustrates the standardized effects from the experiments. The Minitab output compares the different factors and combinations of effects. The Pareto chart clearly indicates that temperature has the most effect on gel time, followed by the cobalt content. The combined effect of cobalt and temperature is a key contributor to the gel time. The catalyst showed very little effect on the gel time, and the trend was for the lower catalyst content to trend higher in peak exotherm temperature. However, the difference in peak temperatures is not statistically valid and is not considered as a concern.

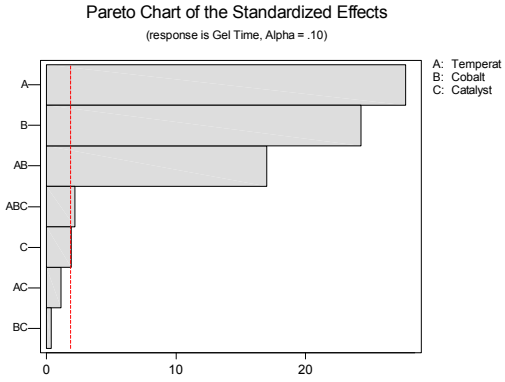

Figure 10. Pareto chart for gel time.

This set of experiments gave us the controlling parameters needed for molding large structures. It provided the controls to slow down the reaction and minimize the time to cure. The experiments also showed what temperature expectation would occur during curing so that tooling can be designed to control the temperature. This would allow for part-to-part processing consistency without heat buildup in the tooling, which would create greater variability.

The development effort remained focused on using a carbon- and fiberglass-compatible resin system. This has proven to be a valid selection based on impact test data that indicate excellent performance with carbon fiber systems, as well as glass and other systems. The resin is tailored for use in an RTM process. The resin supplier has mentioned several features of the development project as being unique and beneficial based on the project. The capability to develop a truck-quality Class A surface without low-profile additives (which compromise toughness) and to achieve consistent molding is new to the industry. The excellent toughness seen in carbon hybrid composites is also an industry first, described with enthusiasm by the resin supplier as "ballistic performance." Figure 11 illustrates the significant increase in impact energy compared with industry standards of sheet moulding compound (SMC) and liquid molding. One significant issue with carbon composites is their lack of toughness and brittle failure nature. The team had concerns about the minimum achievable panel thickness owing to this issue. Limiting panel thickness would severely hinder cost competitiveness but would provide desirable weight savings. Resin and process evaluation indicated a need for a system with close temperature control and required development of tight tolerances on the process and equipment.

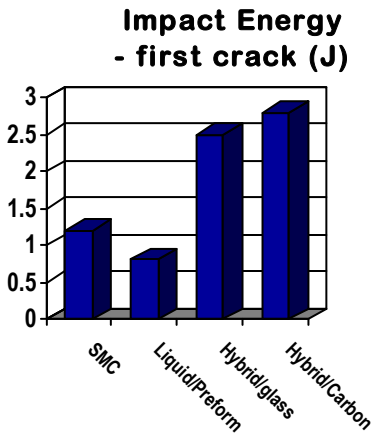

Figure 11. Resin system allowing excellent impact energy.

Filler Optimization in Hybrid Resin

Filler optimization is important in minimizing viscosity for the lowest achievable fill pressures on large structures. Likewise, maximum filler loading is an important aspect of reducing resin shrinkage for achieving the best possible surface finish (Class A).

The results of the DOE to optimize filler loading with viscosity included four factors: resin blend (20/80 to 30/70), filler load (25 pph to 45 pph). The filler ratio (15% to 35% filler A to filler B) meas-

ured at 2 and 12 min after mixing, as a function of viscosity, showed that there is an optimal region of filler ratio and filler loading within the tested ranges. In Figure 12, the Pareto chart of the effects, not including mixing time, shows resin blend as the largest determinant of viscosity at a given mix time. Therefore, the most sensitive component of final mix viscosity is the isocyanate-to-polyester ratios, with some dependence on filler load.

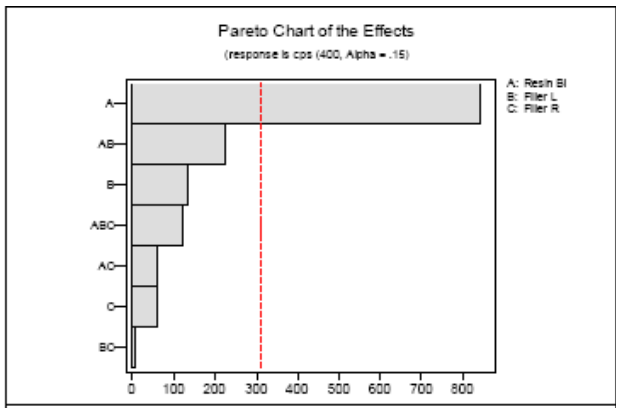

Figure 12. A Pareto chart illustrating the combined and individual effects of the different constituents of the mixes.

The other non-setting factors show narrow ranges of minimum viscosity. The filler load seems to have the second largest effect on mix viscosity, and in general, viscosity increases with increasing filler load. Filler load shows a decreased viscosity response between 30 and 40 pph and a resin blend ratio below where an interaction may be occurring with the filler ratio.

Filler ratio, the percentage of filler A within the blend of filler A and filler B, gives a minimum viscosity within the range of 20% to 25% depending on the total filler load in the mix and set-time. This interaction resulted in a shift in the viscosity minimum from 25% to 20% in filler ratio as the filler load shifted from 30 to 40 pph. It is also affected by the setting of the resin over time by shifting the optimum filler ratio back from 20% to 25%. This same shift with set-time can be seen in the resin blend vs. filler ratio above. Is this shift an interaction between the surface of one of the fillers and a resin component?

The approach to this screening study was intentionally broad within the area we now know as a more optimal range for the factors tested. The next step needed to verify and improve the resolution of the data is a full factorial concentrated around a focal point of a filler ratio of 23%; a filler load of 35%; a resin blend minimizing isocyanate but controlled for its effects on the final composite properties; and mixing times of 2, 7, and 12 min.

Model and Experimental Correlation

A representative region of the specimens was used and discretized in 3-dimensional finite elements for the simulation of the tensile stress/strain responses.

The panels were then laid out for specimen orientation and cutouts. Figure 13 shows the layout for the specimens. The specimens were oriented with one referenced edge of the panel and specimens were then removed; one set was parallel (0°) and the other was perpendicular (90°) to the referenced edge.

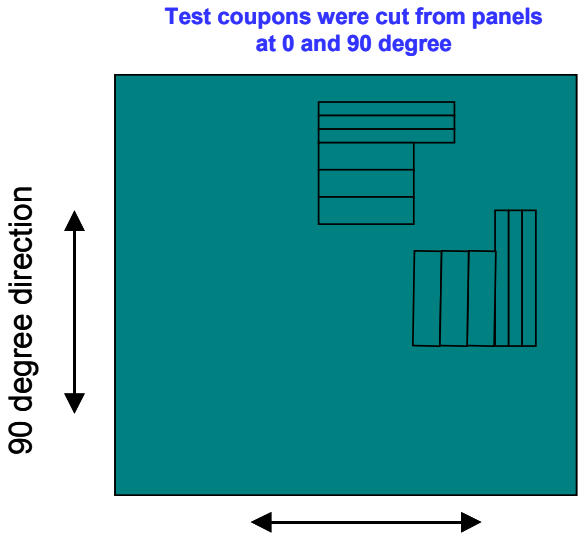

Figure 13. Specimen layout on panels.

Tensile and flexural specimen geometry followed the ASTM D638 Type I Tensile and ASTM D790 Four-Point Bending standards, respectively. Specimen profile measurements, including width and thickness, were taken and recorded for each specimen. The specimens were also asymmetric in the panel through-thickness.

The double extensometers were then used to measure the axial elongation and the width strain during axial loading during tensile testing. From this double extensometer measurement, a 3-dimensional

strain response can be calculated. These data are then used to develop the elastic stiffness matrix and constitutive equations for model development. The flexural specimens were tested in 4-point bending. This allowed the modeler to be able to compare how well the prediction correlated with experimental data.

Figures 14 and 15 present the simulated tensile stress/strain responses compared with the experimental results for the glass/vinyl ester and carbon/vinyl ester specimens tested until failure. The simulated curves were obtained using the elastic EMTA model (dashed line) and the incremental elastic-plastic EMTA model (solid line) implemented in ABAQUS. The glass/vinyl ester specimens could undergo higher deformations than the carbon/vinyl ester ones. In the former case (Figure 14), after linear behavior at small strains, the responses become nonlinear at higher applied stresses; whereas the non-linearity of the responses is negligible in the latter case (Fig. 15). The non-linearity results mainly from two different material origins. The first origin is damage by matrix cracking, fiber/matrix de-cohesion, and fiber pullout and breakage at the final stage. The second cause is the plastic deformations of the matrix material. In this report, damage was not modeled, and only the plasticity of the polymer matrix was accounted for. Figures 14 and 15 show good correlations of the predicted results with the experimental values, except around the final loading stage in which excessive accumulations of damage have led to failure of the specimens.

Flexural tests (based on the ASTM D790 standards) were conducted for glass/vinyl ester, carbon/vinyl ester, and carbon/glass/vinyl ester specimens. The latter are made of two layers: one carbon/vinyl ester and one glass/vinyl ester layer. In all specimens, the major fiber alignment axis is parallel to the width direction. Figures 16 and 17 show the predicted load/deflection curves compared with the experimental values also presented on the same figures for the glass/vinyl ester and carbon/vinyl ester specimens. Good correlations with the experimental results were obtained with the use of the

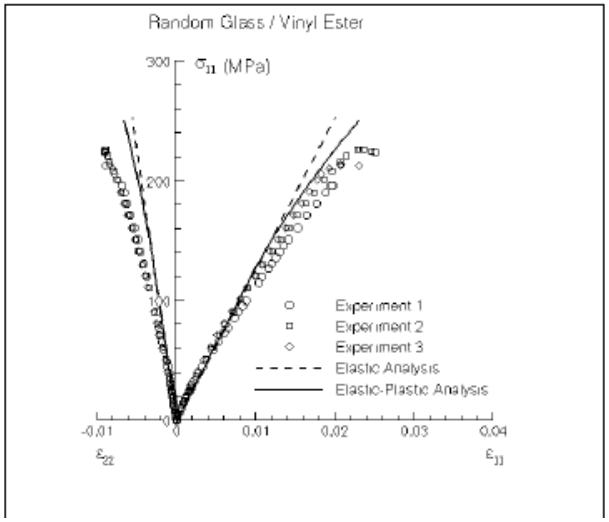

Figure 14. Tensile stress/strain responses of the random glass/vinyl ester specimens.

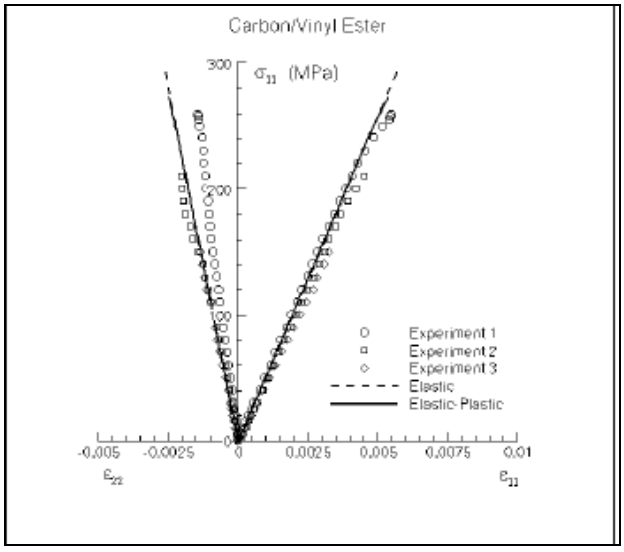

Figure 15. Tensile stress/strain responses of the random carbon/vinyl ester specimens.

elastic-plastic EMTA model. In order to determine the effect of large displacements (which occur around the end of the loading) on the overall responses, we also carried out an elastic-plastic analysis using the large displacement (geometric non-linearity) option in ABAQUS. The corresponding solution for the carbon/vinyl ester specimen is denoted as "NLG elastic-plastic" and is presented in Figure 17. Compared with the elastic-plastic solution of the same problem, it is noted that the geometric non-linearity is negligible. This is because the maximum deflection is of the same order of

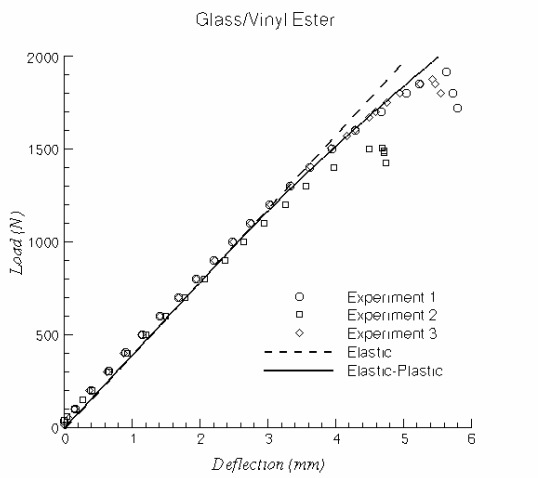

Figure 16. Flexural load/deflection responses of the random glass/vinyl ester specimens subjected to four-point bending.

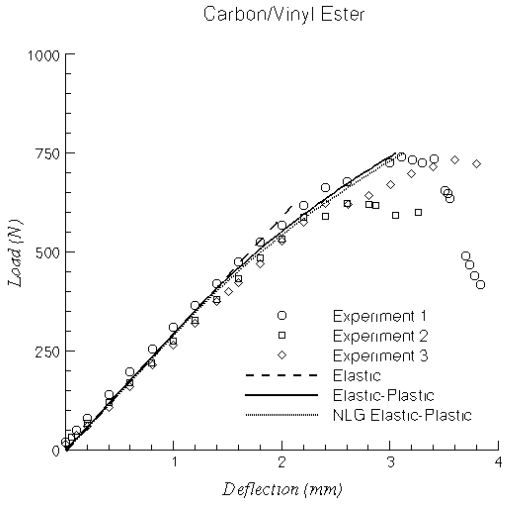

Figure 17. Flexural load/deflection responses of the random carbon/vinyl ester specimens subjected to four-point bending.

magnitude as the specimen thickness. Consequently, it is not necessary to carry out elastic-plastic analyses accounting for geometric non-linearity for these specimens.

Preform Development and Evaluation

Several different preform styles have been considered and evaluated for the program to date. These include commercial and development variations to achieve the goals for fiber hybridization.

Using the DOE/Automotive Composites Consortium P4 preforming cell at the NCC, hybrid flat preforms were made in a continuous process by modifying equipment to meet requirements. This was a distinctly different approach from the previous efforts where separate preforms of carbon and glass were made and later bonded together by NCC. Issues were seen in the distribution of binder in this approach, especially given the preferred flat tow form of carbon fiber being used. Molding of these panels indicated a lack of binder and/or a lack of fully developed strength for interlayer adhesion, especially in the glass fiber layer. Preforms were later developed for a multi-sided test tool, as well as the large test mold for full-scale evaluation trials. These confirmed the lack of development of binder strength at the interface, as the all-carbon preforms molded extremely well while the glass preforms showed issues with fiber washout and lack of preform integrity.

The requirement for a discontinuous fiber preform that can accommodate multiple project objectives was a key issue in the project. Critical aspects included allowable loft and compressibility, capability to achieve a Class A surface, ease of fiber placement, ability to tailor for local additional carbon fiber reinforcement placement, minimum cost of processing, and repeatability of processing. The approach allows a given amount of loft to be available, yet is both compressible and able to provide a high-permeability resin flow path. The method and application of the surface fibers have provided benefits in tailoring fiber content and assisted in achieving success in the Class A arena.

A preform fabrication cell was developed to allow rapid changes to the preform structure, and subsequent molding trials, to allow more efficient and cost-effective evaluation of specific approaches. Hybrid preforms were developed that provided complete mold filling and wet-out capability and provided samples for mechanical property testing. Work to make this process repeatable and predictable continues.

Preforming development was completed on two fronts: (1) small test preforms for both the flat glass mold and multi-faceted test tools for determining permeability and resin/preform interactions and (2) large preforms for evaluation of scale-up factors and ability to meet design feature performance for subcomponent test tooling.

To supply the various molding trial requirements, different core densities and fiber surface densities were evaluated. Packing levels were from net to 60% compaction, which varied fiber loading in the composite from effective values of 25% to well over 45%. Fiber loading in the carbon fraction was approximately 50% and allowed excellent surface density and fabrication of a thin, high-stiffness panel. This is clearly seen in the test results for flexural properties vs. the results for tensile properties.

Figure 18 shows the surface available from the sample panel and several complex features that address draft angles, surface finish, and non-uniform thicknesses. The large tool evaluation will be explained in a separate section.

Figure 18. Molded preform indicating discontinuous fiber surface.

The alternative preform material showed significant improvement. Using combinations of the hybrid resin and the hybrid preforms, test panels were manufactured at different lengths to provide specimens and validate the feasibility of molding large (>5 ft) and thin (<3 mm) components. Close monitoring of developing manufacturing procedures provided valuable data concerning the behavior of both the resin and fiber hybrids in vacuum-assisted RTM (VARTM) and closed molding operations.

Two types of flat laminate panels were produced from two different mold sets. Initially, a 12×24 in. glass-top mold (Figure 19) was loaded with the preform and infused with both neat and filled blended resin systems using VARTM. The transparent mold allowed for visual confirmation of the location and flow path of the hybrid resin at any point during the infusion process. In addition, the mold was fitted with inlet and outlet pressure transducers to record pressure gradients during mold filling. The second mold was constructed and fitted to a hydraulic press operating at 2500°psi. Visual confirmation of resin flow was confirmed via short tube ports protruding from the upper mold half. The panel preforms were one of two types of cores, with and without chopped carbon fiber. In all cases, temperature was between 40 and 50°C;and the mold cavity was evacuated to 85 kPa prior to injection of the resin with an 11:1 custom piston pump, which kept the unmixed resin components at 45°C.

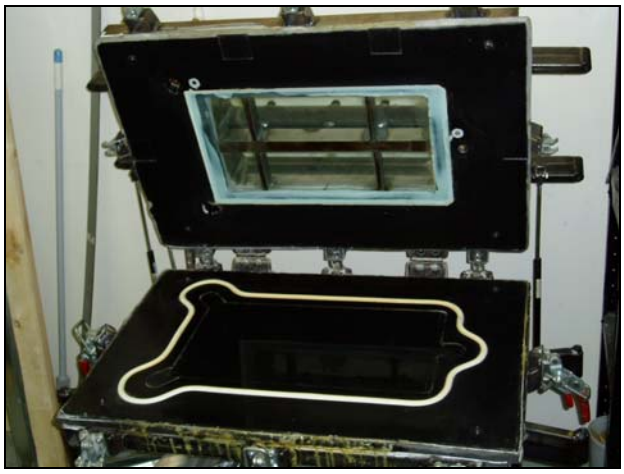

Figure 19. Glass top mold for test trials.

Working with material manufacturers, four cores of different thickness and architecture were examined as possible core materials for use with the highly viscous blended resin. CR-1, FM-1, S&F and "M-03" core materials were compared during initial testing. Only the S&F products were capable of providing fully wet-out panels of less than 5 mm. S&F and M-03 are 4-mm and 3-mm- thick fabrics, respectively, consisting of glass strand mat stitched to a "knitted" polypropylene core, which provides loft to create a flow path for the resin and reduce backpressure within the mold. S&F designed these mats specifically for the purpose of liquid injection molding with high-viscosity, highly filled resin systems; and the fabric has never been tested previously, ex-

cept during product development at S&F. Discontinuous carbon fibers were chopped from Toray 12-k tows directly onto the cores and held in place with polyester binder. In some cases, final placement and consolidation by hand was required to achieve full panel coverage and even fiber distribution. When filler was introduced to the matrix, calcium carbonate, in powder form, was added to the polyester side of the blended resin. The resin itself was supplied as a proprietary chemistry consisting of a polyester component, a compatible urethane component, and a catalyst.

The purpose of this investigation was to evaluate the processability of the blended resin and hybrid fiber/mat raw materials and characterize the required production cycle. During the early stages of testing, the S&F mats performed exceptionally well, allowing the matrix to fill and fully wet the glass and hybrid preforms in less than half the time taken by a competitor's core materials (Table 2). Figures 20 and 21 show the difference between inlet and outlet pressures recorded during the RTM process. Both the S&F and M-03 had equal gate and vent pressures in less than 100 seconds, with the thinner M-03 requiring slightly more time. It is important to note the design of the mold cavity itself is critical to both the fill time and the level of filler filtering. Resin must be injected directly into the polypropylene core of the mat, along the material plane. Otherwise, a layer of glass strand hinders the flow rate within the S&F and it behaves similarly to any other core material.

Table 2. Recorded fill times for core materials

Material	Time to fill 24×12× 0.12 in. cavity
CR-1	4:38
FM-1	5:20
S&F	1:43
M-03	0:34

The success of the 6-ft panel validates the use of the filled, blended resin system and S&F M-03 for the production of large components. The injection- took less than 4 min to complete, and the panel was demolded in less than 25 min from first injection. Resin ports along the length of the mold indicated an even flow rate along the full length of the panel. When demolded, the preform had been stretched

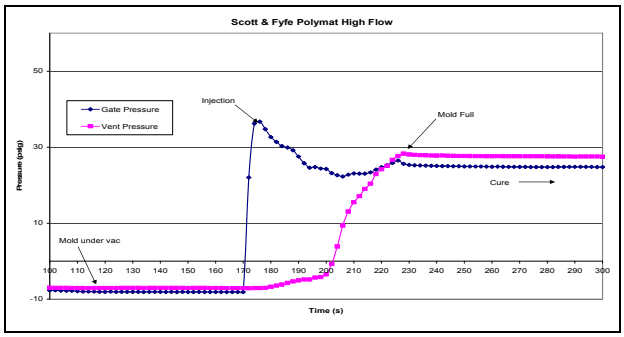

Figure 20. Pressure difference between gate and vent during injection cycle for S&F core material.

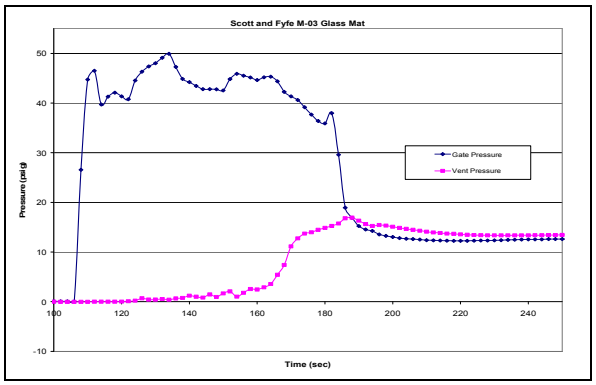

Figure 21. Pressure difference between gate and vent during injection cycle for M-03 core material.

slightly along the inlet width, a problem that was corrected by pinching the fiber along its edge and cutting a small section away directly in front of the resin gate.

The quality of the final panels was excellent in both the 2-ft and 6-ft panels. Panel surfaces showed no shrinkage or print–through, and thickness were as consistent as the molds would allow. Final panel thicknesses were between 2.5 and 3.25 mm when M-03 was used and between 3.5 and 4.5 mm when S&F was used. The nature of the S&F mat filling from "behind" the glass mat virtually eliminated washout of carbon fiber during RTM; however, polyester powder was still applied to ease preform handling. Filler improved the shrinkage characteristics slightly, although it would slow the rate of cure, possibly as a result of absorption of promoter over time. The resin system also performed admirably, wetting and bonding to both types of fibers, as well as the polypropylene core. The fast fill rates and high level of promoter reduced cycle times to less than 16 min for the short panels and 25 min for the

longer pieces, although the larger mold was frequently at a lower temperature than the glass-top.

Panels produced from the S&F mat and carbon chop were sectioned and subjected to flexural and tensile testing. The results agree quite well with the predicted material properties for hybrid fibers and blended resins. In addition, optical analysis of panel cross sections showed no signs of filtering out of fillers from the resin along the length of the panels.

Large Evaluation Tool

In order to evaluate the capability of the process and materials to meet demands of industry, a proof-test component tool was developed. The tool, which has all the features anticipated in designs, was used to evaluate the hybrid perform process for achieving performance given the requirements of these features. It is not expected that all features will be molded and perform as expected, since the goal of the development is to determine the limitations of the hybrid fiber system and to provide designers and OEMs with guidelines for where lightweight materials will be applicable and how to design and manufacture in those cases.

Project personnel ran the evaluation tool over a week-long period at a tier-one supplier, with support from the tier-one manufacturing floor personnel. Figure 22 illustrates the size of the test tool for evaluating complex preforms and mold filling. It was immediately apparent that this was not a desirable development process, as the systems for preforming, RTM, and resin optimization had to be developed independently and then brought in to the test. The P4 preforms developed at NCC showed great limitations. Alternative material systems were then evaluated that allowed the preforms to be modified.

Results from the trials showed issues with the binder capability of the preforms. Interaction of the resin system softened the binder over time (this was not observed to such an extent in smaller-scale test tools, as the resin had much shorter contact times with the preforms before the smaller tools were completely filled and flow stopped). All-carbon fiber preforms were much more successful than glass fiber preforms, and several test sections were useful for fabrication of coupons, etc. Indications from the test were that resin temperature and tool temperature control were critical for this system, which led to

Figure 22. Mold cell for test tool setup for large part molding.

the resin development experiments described. Mold temperature was seen to be a significant issue; this finding has led to new approaches to tool design and construction that are being evaluated.

A new cell was set up for R&D purposes to enable preforming and resin modification in a more appropriate environment. Also, several options for molding were built in that were not possible in the existing production environment but could easily be implemented once proven. In operating this cell, several successful test panel runs were made with hybrid preforms that met the requirements of the overall process.

The newly developed hybrid preforms using commercial materials and adapting them to hybridization not only proved to be cost-effective for the OEMs but also significantly improved fill and cycle cure time. Several tests were run using large tooling and comparing different materials and flow behaviors.

Based on the new material and test results, flow modeling was used for correlation in the large tool experiments.

Flow Modeling

Flow modeling used Polyworx software for simulations in the flat plate tools for determining preform permeability based on temperature, pressure, and viscosity. Figures 23a and 23b illustrate the pressure and flow patterns in the long, flat plate tool. The flow and pressure pattern was even. The

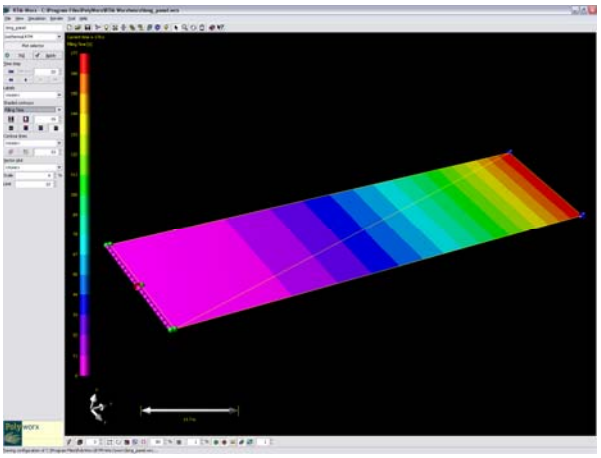

Figure 23a. Modeled flow pattern in 18×72 in. panel mold.

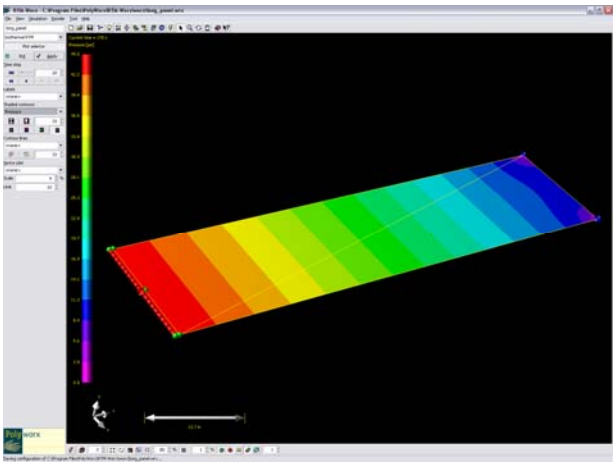

Figure 23b. Modeled pressure pattern in 18×72 in. panel mold.

data obtained from the flat panels were correlated with experimental data, which provided the information needed for inputting into the more complicated test tool.

The large, complex test tool was then modeled using the permeability numbers determined from the flat panels and the other resin input variables. The modeling of the test tool was used to show the correlation between the modeled and experimental results for scaling up complexity in the part. The simulations contributed to understanding of flow patterns and fill times with the current material configuration. This gave confidence that the modeling of the design will work prior to tool fabrication.

Mechanical Testing and Analysis

Testing and analysis were completed on all variations of material combinations. The project initially tested materials for the EMTA modeling that used the P4 preforms with varying levels of glass and carbon ratios with a low-cost vinyl ester resin system. The program then transitioned into the new hybrid resin materials and the hybrid preforms with the alternative performing approach. Tensile, flexural, and fatigue mechanical properties were tested for the different material combinations with some very satisfying results.

The analysis used microscopy and Archimedes measurements for determining the void volume, filler filtering, and interpenetration into the fiber tows. The Archimedes measurements were used to determine density of the materials and variations across the large parts. Figure 24 illustrates the fiber wet-out and the filler interaction with the fiber tows. This image shows great penetration of the filler into the tows that gives a Class A surface finish.

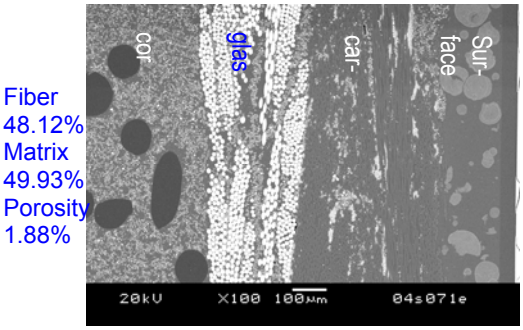

Figure 24. Microscopy of hybrid material with filler and surface coating.

The density of the hybrid resin and hybrid composite system used as the optimum setup was 25% less than that of SMCs used for semi-structural components and surface-finished parts and 15% less than the continuous strand mat (CSM) typically used in RTM of parts for OEMs. The tensile modulus was nearly 30% higher than that of the CSM. Flexural strength was approximately 50% higher than that of the CSM and equal to that of unsaturated polyester SMC. The flexural modulus, which is the key driver for designers in stiff driven parts, was three times that of CSM and 25% higher than that of SMC. Instrumented impact is over three times that absorbed by the unsaturated polyester SMC and compares

with that of a 50% glass loading SMC material that is nearly 25% heavier

The other outstanding property was fatigue strength in the composite. The OEM typically does not go past 10^6 cycles. The samples tested in the newly configured material were tested out to 10^7 cycles at a 60% stress factor. This test exceeds all expectations of the material design.

Tool Design Concept

A tooling method for application in rapid fabrication of thin-walled composite structures was developed under this program to help reduce the high cost of steel tooling.

During the investigation of layered hybrid composites, we investigated and proposed a low-cost, relatively rapid tooling system for RTM of polymer composites. The program evaluated the use of the MIT™ (multiple insert tooling) system. We requested and received verbal authority from the North American technology licensor—JHM Technologies—to use MIT on the non-commercial development program.

Our unique approach was to modify the MIT tooling and develop a MIT skin that achieved very high thermal conductivity, had responded rapidly to thermal excursions, had a near-zero CTE, and was stiffer than fiberglass skins. The rationale was that we needed to limit dimensional changes during the molding cycle and provide a system with increased durability in order to keep the surface of the tool in excellent condition over the tool life (or extended tool life), as well as provide for temperature control of the specific resin system chosen for the molding.

A tooling material approach was used in which the traditional thin molding surface skin (A-side or appearance mold skin) was fabricated with near-zero CTE and a high thermal conductivity. This skin replaces the typical skin of fiberglass composite in the MIT system (Figure 25).

The MIT skin uses a bolster to capture an independent skin that acts as a movable mold surface. This allows the operations associated with skin and fiber preparation to be done independently of the primary tool and press structure. Skins can be easily and cheaply fabricated from a pattern master, and multiple skins can be used to optimize the process, matching the press cycle to the number of skins required for the preparation cycle.

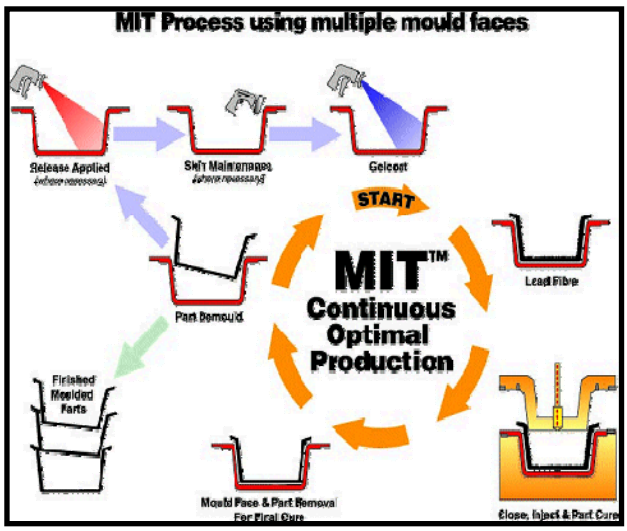

Figure 25. Multiple insert tooling approach using highly thermally conductive skins.

The approach of using a carbon MIT skin is novel in several ways. First, it provides a skin surface that is dimensionally similar at all temperatures. This ensures that the skin dimensions are similar during application of mold coat, fiber perform, installation in bolster, and molding and cool-down cycle. Internal stresses and surface dimensional changes are eliminated. Second, it provides for very rapid heat-up and cool-down of the mold cavity as heat is transferred very efficiently through the skins and into the part. This works in conjunction with the hybrid fiber and other fiber molding approaches to ensure consistent and repeatable process cycles and rapid processing capability. Third, the skins are 5–8 times stiffer than a typical glass fiber skin because of the improved fiber stiffness. Large, thin skins are more easily handled outside of the bolster, and their lower deflection leads to improved durability and less likelihood of surface cracking of the tooling surface coat. This is a major factor in mold surface quality deterioration and one that helps to resolve a related factor: deflection over time leads to "patterning through" in glass fiber molds, a process in which repeated flexing of the mold skin causes fibers near the surface to be forced against the surface and begin to appear in profile. This is eventually passed into the part.

Furthermore, high-temperature resin systems that have been modified offer better thermal conductivity and more uniform heating across the skin sur-

face for improved part process and controls. The high-temperature resin systems also provide higher heat deflection temperatures and resistance to preform fiber surface damage to the tool while the resin's exothermic reaction is taking place. The high-temperature resin system must be able to handle exothermic temperatures greater than 150°C.

The concept was also extended to the other components of the system, specifically the B-side tool and the bolster. Higher and more effective heat transfer rates and process lags of fewer than 3°C were noted, which improved the quality of molding significantly. A notable benefit of this approach is the capability to achieve consistent cure times and eliminate local hot spots caused by varying thicknesses of laminates. The process benefits translate into limiting pre-release from the tool surface and achieving better dimensional control and surface quality.

A set of durability tests was performed on some laminated test pieces with a surface coating that will allow us to achieve a Class A or near–Class A finish on the surface. The series included testing three specimens to failure in 4-point bending. This determined the first ply failure of the laminate and the load at which the surface coating cracked. Testing was then performed on the laminate in cyclic fatigue using the same 4-point bending setup and setting the peak load at 30%, 40%, and 50% of the first ply failure average of the previous testing to failure. These samples were then subjected to a 3-Hz cyclic fatigue. The samples reached 500,000 at 30%, 200,000 at 40%, and just under 100,000 at 50% when the test was terminated because surface cracking was observed. The durability of the carbon fiber laminate was very good, and there was little loss in the load for the set deflection.

Large Tool Scale-up

Two approaches were taken for tooling on a hood design. The first was an MIT approach that allowed for offline surface prep and de-molding separately from the press, which helped keep cycle times low and throughput high. The second approach was VARTM using lighter and lower-cost tooling to accomplish the same result while using the thermally conductive skins developed for the MIT approach.

The difference in cost between these two tools was nearly nine times, with VARTM being the lower-cost method. The challenge in doing very large structures is the weight of the tooling and the company's ability to handle such large, heavy tooling. Figure 26 illustrates the hood of a heavy truck that was planned for testing.

Figure 26. Proposed hood for tooling cost comparison.

The project had started building the hood tool with a tier-1 supplier to the OEM partner. The company went into receivership and the OEM's competitor took over the company. The tooling was removed and held in storage while the competitor was working on selling the company. The new owner of the company re-quoted the tooling, and the price was much higher than the initial tooling quote. The inflated cost eliminated any work with the new owners of the company. Figure 27 shows the progress that was made up to the point of receivership.

Figure 27. Master pattern for tool builds

The OEM tried several other tier-1 suppliers in its supply chain with little success. The supply chain

is extremely tight at the current production capacity in the trucking industry, and there is no shop time available to take on projects. The cooperative research and development agreement (CRADA) partner preferred to have a tier-1 supplier do the work so the partner could incorporate the technology into its product lines and be trained with the new technology.

An alternative supplier was found and a reasonable cost estimate given for demonstrating the technology with VARTM and our new skin technology. However, the CRADA partner management did not wish to engage any suppliers outside the preferred supplier base.

The current estimates for cycle times on a 72-ft^2 part are near 15–20 min. Estimated fill times are 4–9 min, depending on the volumetric flow rates of the pump. These cycle times compare with nearly 3 hours on a laminated hood and about 15 min on a preform hood (in steel molds at a cost factor of almost 5×).

Conclusions

The flow trials gave us valuable insight as to how fast the large panels will fill. The rheology studies indicate time sensitivity when the two resin components are mixed and have the largest influence on the viscosity. There is an optimum ratio of the two fillers at 25 pph that will help in reducing filler cost and viscosity. The viscosity data became very useful with the modeling, which illustrated the fill time and pressure gradients within the part. These models and the correlation data gave us the information needed to model large structures prior to tool fabrication, which helps reduce the risk of the unknown for large, complicated, and expensive tools.

Future work will model the large composite structure and build the tooling. An experimental correlation will be evaluated for the large molded parts. A large tool will be fabricated for testing the moldability and mechanical testing of the large parts. A series of factors associated with optimizing details of the process technology are being analyzed, and the CRADA partner is developing an approach to mold full-scale parts that will ultimately go on over-the-road trials. We chose the parts to demonstrate the most challenging aspects of the process capability, namely structural Class A surfaces in direct line-of-sight with some complex process details required for success. Tooling quotes and negotiations are ongoing; we anticipate that several aspects of the process will go forward for patent protection.

The program has generated a wealth of information. The goal of reducing weight reached a reduction of 40% of a replacement component comparison. The tooling cost competed with that for a single-sided chopper gun tool, which is several orders of magnitude lower than the steel tooling for SMC material processes. The cost of carbon fiber continues to be a serious problem for the adoption of new technologies. The cost of carbon fiber at the beginning of the program was $6.50/lb and climbed as high as $14/lb. Calculations for one part indicated that a break-even point for this new technology would be $6/lb. If the material price would return to reasonable levels, the adoption of new, lightweight hybrid systems would be an attractive investment.

Project accomplishments included

- predicting properties in chopped fiber composite RTM preform moldings using the newly developed EMTA modeling code
- modeling flow behaviors over large structures
- developing a unique approach to preform fabrication for increased fill speeds for large structures
- developing a hybrid resin for rapid cycle times
- developing new tooling skins for thermal control of exotherms, and class A surface finish that have combined to create increases in the mechanical properties

A computational tool using the EMTA approach was developed for thermo-elastic and elastic-plastic analyses of short-fiber polymer composites. It was created by implementing the EMTA-based constitutive models into ABAQUS. The simulations of tensile and flexural tests conducted on glass/vinyl ester, carbon/vinyl ester and carbon/glass/vinyl ester specimens provided good predictions of composite response and were in agreement with the experimental results. The computational tool can be used to determine the basic properties needed for the design of short-fiber polymer composites, such as effective thermal and elastic properties and tensile and flexural moduli of the composite laminate. Moreover, the ability to account for plastic deformations using the incremental elastic-plastic EMT model enables modeling of the composite behavior at high loading levels leading to deformations that exceed the elastic limit. The model inputs are fiber (or fiber tow) and

matrix properties, fiber (or fiber tow) volume fractions, aspect ratios, and the orientation parameter (θ). This computational tool offers the flexibility to adjust these parameters so that the resulting homogenized properties and responses satisfy the design criteria in terms of desired properties and deformation limits. The tool can therefore be used to assist in the design and manufacture of short-fiber composite structures.

The preform development started with a preforming process that would not work on large structures because of resin flow resistance. Development of a new preform system that used commercial materials was successful and helped achieve relative fill times nearly 10 times faster than those of previously used preform technologies.

The new hybrid resin system developed in the lab significantly improved the fiber wetting and bonding of two dissimilar fibrous materials. This helped improve mechanical properties by as much as 50% and increased the impact strength by three times compared with commercial materials.

Development of new tooling demonstrated that maintaining temperature control is extremely important, as the material exothermed during curing. Heat buildup in the tooling limits the fill time for the tool because of resin rheology changes. Tooling fatigue life was another important consideration: as large tools are handled and flexed, the fatigue can cause surface crazing and spider webbing that will impact the molded surface in the new part.

The OEM considered this program a technical success, but issues with tier-one suppliers and capacity limitations created by current high truck sales limited the transfer of technology to a supplier. The OEM is considering this material for future use in smaller parts as a result of the information gained from this program.

Presentations/Publications/Patents

B. N. Nguyen, K. L Simmons, G. J. Grant, and M. T. Smith, "A Computational Tool for Analysis and Design of Short-Fiber Polymer Composites," prepared for submission to *Composites Science and Technology*, 2003.

ASM International, *Engineered Materials Handbook: Composites*, ASM International, Metals Park, Ohio, 1987.

Three invention disclosures were submitted under this program.

B. Hybrid Composite Materials for Weight-Critical Structures

Principal Investigator: Curt A. Lavender
Pacific Northwest National Laboratory
P.O. Box 999 Richland, Washington 99352
(509) 372-6770; fax: (509) 375-4448; e-mail: curt.lavender@pnl.gov

Principal Investigators: Donald Trettin
PACCAR Technical Center
12479 Farm to Market Road, Mount Vernon, Washington 98273
(360) 757-5241; fax: (360) 757-5370; e-mail: don.trettin@paccar.com

Chief Scientist: James J. Eberhardt
(202) 586-9837; fax: (202) 587-2476; e-mail: james.eberhardt@ee.doe.gov
Field Technical Manager: Philip S. Sklad
(865) 574-5069; fax: (865) 574-6098; e-mail: skladps@ornl.gov

---

Contractor: Pacific Northwest National Laboratory
Contract No.: DE-AC06-76RLO1830

Objective

- Develop and demonstrate (1) the application of hybrid composites and composite/metal hybrids to heavy-duty vehicles and (2) the capability to integrate these materials choices into moderate-volume production.
- Develop and demonstrate the potential for major weight savings (>50% on a component basis) in critical structures applicable to truck cabs and support components.
- Demonstrate the basis for the use of hybrid metal-composite systems to reduce weight via proof-of-principle experimentation.
- Develop full-scale prototype components for vehicle testing and validation.

Approach

- Investigate the potential of new materials and manufacturing technologies to effect major weight reductions for heavy-duty vehicles.
- Assist in demonstrating the applicability of composites and composite/metal hybrids to operational vehicles with little or no cost impact.
- Provide the experience base to develop design and analysis tools, as well as the scientific understanding of the factors affecting molding and materials performance.
- Provide the materials suppliers with a market that can stimulate demand, leading to an increase in their production capacity. This will help reduce materials costs by creating higher volumes.
- Develop and assemble a full-scale prototype door system using hybrid material for heavy vehicle testing and evaluation.

Accomplishments

- Provided technical input to PACCAR for further implementation of the "hybrid" materials technology into a production vehicle.
- Provided technical information for the development of a PACCAR supply chain for the hybrid materials approach.
- Completed three sets of prototype hybrid door components, which were delivered to Pacific Northwest National Laboratory (PNNL) by the subcontractors. The key components include sand cast magnesium door inners (Style and Tech) and molded hybrid glass/carbon fiber upper door frames (Profile Composites).
- Developed bonding fixture, bonded the initial hybrid door components, and verified dimensional conformance.
- Assembled the first door and performed static load analysis. Initial results indicate that the hybrid door assembly exceeded the targeted 50% improvement and exhibited a 64% improvement.
- Assembled additional door for cab fit and function and full-length cab door durability testing.

Future Direction

- Support implementation of the hybrid materials system in a PACCAR production vehicle.
- Compile a final report at the conclusion of the prototype demonstration phase.

Introduction

Current materials and manufacturing technologies used for heavy vehicle door systems are often dictated by the high cost of tooling and the relatively low production volumes for Class 8 trucks. Automotive-style stamped door designs, whether of steel or aluminum, require multistage stamping dies that are generally cost-prohibitive at lower production volumes (<50,000 units per year). Alternate materials, such as glass-reinforced sheet moulding compound (SMC), require less expensive tooling and can provide a Class A finish, but the relatively poor specific properties of SMC tend to compromise design and result in a heavier door system. For many production truck cabs, a simple aluminum extrusion frame is used with a flat aluminum sheet riveted to the frame. Although this approach does not require expensive tooling, the use of constant cross-section extrusions in the frame is less than optimum, and it requires more assembly labor than other approaches. PACCAR, a world leader in Class 8 truck design and manufacturing, teamed with PNNL to explore alternate "hybrid" door system designs that minimize tooling cost and per/part door cost, while providing a lightweight, structurally stiff, automotive-style door.

Project Approach

The initial approach to development of the hybrid door system was to perform a structural analysis of an existing PACCAR door design and to determine what the design and performance goals should be for new-generation door systems. PACCAR provided a number of weight, cost, and performance parameters that it considered important for future door designs. PNNL was tasked with surveying existing and emerging materials and manufacturing approaches that could be applied to a new door design. Following completion of this survey and analysis of existing door designs, PNNL, with design assistance from Mercia, Ltd., developed a series of five door design concepts that included combinations of large die castings, extrusions, carbon- and glass-reinforced composites, and conventional SMC and stamped aluminum exterior panels.

Following a concept review meeting with PACCAR, an optimized hybrid door design concept was selected. The door concept was then defined using computer-aided-design tools and analyzed with finite element models to validate performance, weight, and cost. After determining that the prototype design met or exceeded all performance and projected cost targets, PNNL and PACCAR selected methods to produce prototype components for the full-scale assembly and testing phase of the project.

The finite element model of the prototype door system is shown in Figure 1.

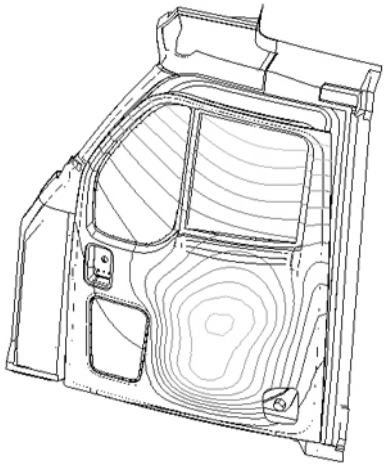

Figure 1. Finite element model of prototype door system under simulated loading conditions.

Following completion of the design selection phase of the project, full-scale hardware components were developed and shipped to PACCAR Technical Center for assembly and testing. In addition to conducting the static deflection tests, PACCAR assembled a complete door and mounted it in a Class 8 truck cab for fit and functional tests (Figure 2). Subsequently, the door was placed into a door durability cab test, which is currently being run to completion.

Figure 2. Prototype door assembled in Class 8 cab for functional testing.

The use of the hybrid materials approach is under evaluation by PACCAR for use in future vehicle systems. When required, PNNL has provided additional analysis and data to support implementation.

Conclusion

The team and its selected subcontractors completed the prototype development of hybrid door components for an advanced heavy truck door. The team has completed prototype assembly, including inspection and assembly fitting, as well as adhesive bonding development. The team assembled three prototype doors for cab testing and evaluation. Static testing and cab functional tests and evaluation have been completed. A prototype door has successfully completed durability testing, passing all requirements while reducing the mass by 37%.

C. High-Conductivity Carbon Foam for Thermal Management in Heavy Vehicles

Principal Investigator: B. L. Armstrong
Oak Ridge National Laboratory
P.O. Box 2008, Oak Ridge, TN 37831-6063
(865) 241-5862; fax: (865) 574-6918; e-mail: armstrongbl@ornl.gov

Principal Investigator: A. D. McMillan
Oak Ridge National Laboratory
P.O. Box 2008, Oak Ridge, TN 37831-6085
(865) 241-4554; fax: (865) 576-0003; e-mail: mcmillanad@ornl.gov

Chief Scientist: James J. Eberhardt
(202) 586-9837; fax: (202) 587-2476; e-mail: james.eberhardt@ee.doe.gov
Field Technical Manager: Philip S. Sklad
(865) 574-5069; fax: (865) 574-6098; e-mail: skladps@ornl.gov

---

Contractor: Oak Ridge National Laboratory
Contract No.: DE-AC05-00OR22725

Objective

- Develop an understanding of the demands for heat rejection for heavy vehicles and develop designs that utilize the superior performance of high-thermal-conductivity graphite foams.
- Coordinate efforts with an engine manufacturer so as to target the design(s) toward their concepts of the heat loads for heavy vehicles.

Approach

- Study fundamental mechanisms of heat transfer using graphite foam.
- Develop a testing method to evaluate the foams and designs using the foams.
- Work with an industrial partner to develop complete understanding of heavy-vehicle-related issues.

Accomplishments

- Achieved the production of graphite foam with homogeneous, controlled structure, allowing for tailorability for a given application, broadening the applicability of graphite foam in the marketplace.
- Developed a heat transfer model. It was determined that pressure drop across the foam is proportional to the flow length of the foam. In addition, permeability (and thereby, structure) of the foam plays a role in the thermal performance.

Future Direction

- Evaluate potential on-vehicle tests to be performed at industrial partner's facilities.

Introduction

A novel technique for creating pitch-based graphite foam was developed at Oak Ridge National Laboratory (ORNL). This technique uses mesophase pitch as a starting material but does not require the costly blowing or stabilization steps seen with typical carbon foams.

The ORNL foam is an open-cell structure with highly aligned graphitic ligaments; studies have shown the typical interlayer spacing (d002) to be 0.3356 nm, very near that of perfect graphite (0.3354 nm). As a result of its near-perfect structure, thermal conductivities along the ligament are calculated to be approximately 1700 W/m•K, with bulk conductivities ≥180 W/m•K. Furthermore, the material exhibits low densities (0.25–0.6 g/cm^3) so that the specific thermal conductivity is approximately four to five times greater than that of copper. The very high surface area (20,000 m^2/m^3) combined with the high thermal conductivity suggests that graphite foam has significant potential for application as a thermal management material.

One issue of importance with regard to the performance of the ORNL foam is homogeneity of density. Previous tests have shown that the density gradient usually observed in both experimental and commercial foams adversely affects performance. Efforts were undertaken to reduce or eliminate the gradient from ORNL foams so that a thermal model can aid in the design of a heat exchanger device using the graphite foam as well as predict the effectiveness of the device.

Experimental

Design and control of the structure of high-thermal-conductivity-graphite foam has been a technical hurdle since its development in the early 1990s. For some uses, it is desirable to have a more open structure (more and/or larger interconnected pores) while maintaining some mechanical strength and high specific thermal conductivity. By modifying processing parameters, such as foaming pressures and/or inorganic additives to the precursor material(s), such structure control can be realized, i.e., specific processing parameters can be tailored to specific performance properties (e.g., pressure drop, permeability), resulting in a high-thermal-conductivity graphite foam that is potentially less friable and has controllable pore and pore window sizes.

ORNL produced a volume of graphite foam pieces based on the needs of our CRADA partner's application. The foam material was processed in accordance with an ORNL proprietary process. This material was shipped to our partner's subcontractor, ThermalCentric, for evaluation and fabrication of a prototype heat exchanger. A combined total of 1524 in.^{3} was delivered to the CRADA partner and ThermalCentric.

Subsequently, ThermalCentric used the ORNL-produced graphite foam to assemble a prototype heat exchanger. The design of the heat exchanger was in response to performance parameters supplied by our CRADA partner. This device was subjected to the following test parameters in an air-to-air heat exchange test at our partner's facility. Hot-side inlet air flow was supplied at approximately 400°C and cool-side inlet air flow at approximately 30°C. The inlet temperatures and cold flow were held constant while the hot flow was varied through 50, 75, 125, and 150% of the design condition flow rate. This procedure was repeated, holding the hot flow constant and sweeping the cold flow through the same percentage range variation. Additional data were collected at the design condition at 200°C and 300°C.Results showed the hot-side inlet flow at 400°C was cooled to 37°C with a cold-side inlet flow of 25°C. Measurements of design-point performance were obtained at the beginning and end of the test program, and both results were identical. This demonstrates the heat exchanger was not damaged by internal thermal stresses despite the large temperature difference applied to its elements.

Conclusions

A variety of processing variables were evaluated in order to fabricate foam with controlled pore sizes and pore windows. A wide range of pore sizes and morphologies were made through control of these variables. Examples of the range of the pores size and morphology that are feasible through processing control are shown

in Figures 1–3. The micrographs taken on a scanning electron microscope (SEM), shown in Figures 1–3, represent three foams made at ORNL. A summary of their corresponding properties is provided in Table 1. A commercially available foam (Poco) is shown in Figure 4. Note the difference between the pore sizes in Figures 1–3 and the pore sizes in the Poco foam in Figure 4. Figure 1 (ORNL A) has the largest pore size but also the most uniform size across the thickness of the foam (not easily seen in this magnification). The pore windows of ORNL A are approximately the same size as the Poco pore size. Not only is the pore window size equivalent to that of the Poco foam in ORNL B, but the quantity of pore windows is also substantial higher, explaining the higher permeability seen in this foam structure. A biomodal distribution of pore size becomes more evident in the ORNL foams B and C, although it is not as evident in ORNL B. Also of interest in all the ORNL foam structures is the apparent absence of closed pores. The reduction of closed pores and the increase in pore window size and quantity directly relate to the increase in structure permeability. The average pore size and bulk and calculated thermal conductivity properties were measured at ORNL, and the permeability and Forchheimer coefficient were measured at ThermalCentric.

The four foams, ORNL A, B, and C and Poco, were tested at ThermalCentric using its thermal transfer rig. Testing details have not yet been disclosed by ThermalCentric. The results, as reported orally by Brian Thompson of ThermalCentric, showed that even in the slightly bimodal structure of ORNL B, approximately a 200% improvement over any other graphite foam was realized. This comparison is based on data from commercial vendors as well as those reported in the open literature. ORNL A had even more of an improvement in performance relative to ORNL B; however, the thin walls of the pores due to increased pore size and windows weakened the compressive strength of the foam structure so that it would not be useful according to the prototype design specifications.

The prototype design specifications were supplied by the partner to demonstrate a proof-of-concept application of foam. As a result, the partner commissioned a ⅛-scale heat exchanger prototype from ThermalCentric. The prototype was designed with a predicted effectiveness of 80% and achieved an effectiveness of ~94% at the design point. The repeatability of the points was very good. The pressure drop was also lower than modeled. The reasons for this may include better

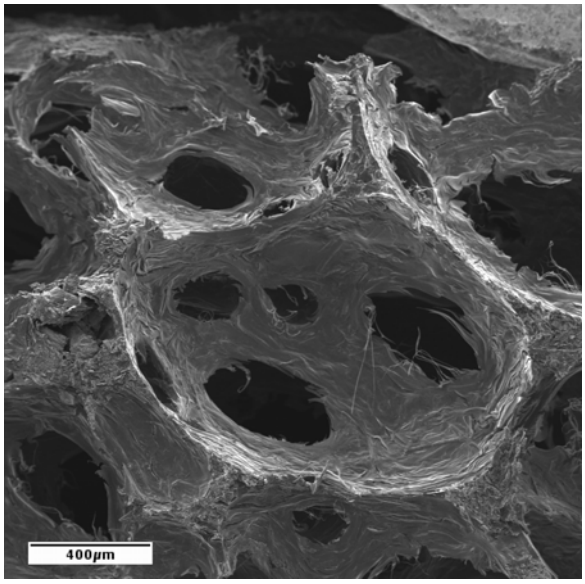

Figure 1. Scanning electron micrograph of ORNL foam A.

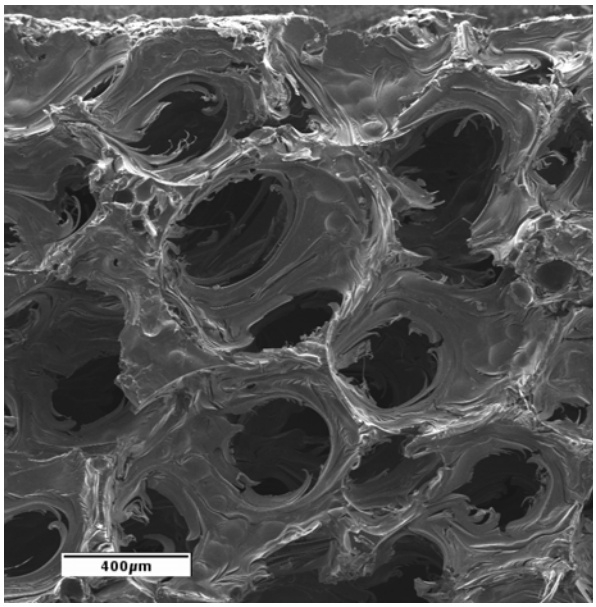

Figure 2. Scanning electron micrograph of ORNL foam B.

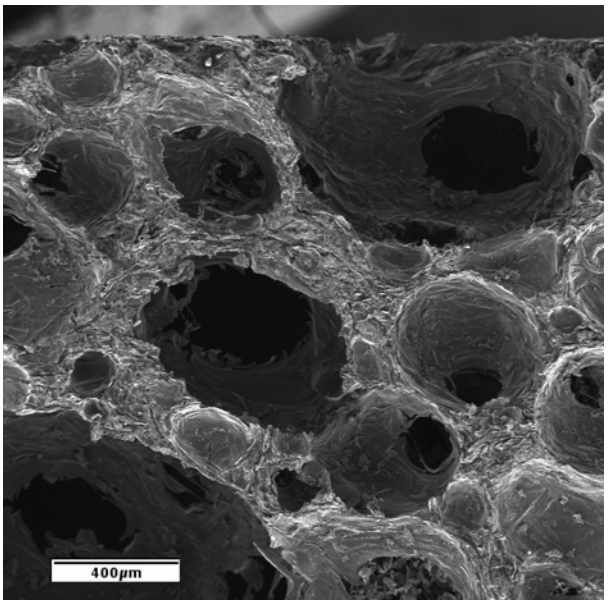

Figure 3. Scanning electron micrograph of ORNL foam C.

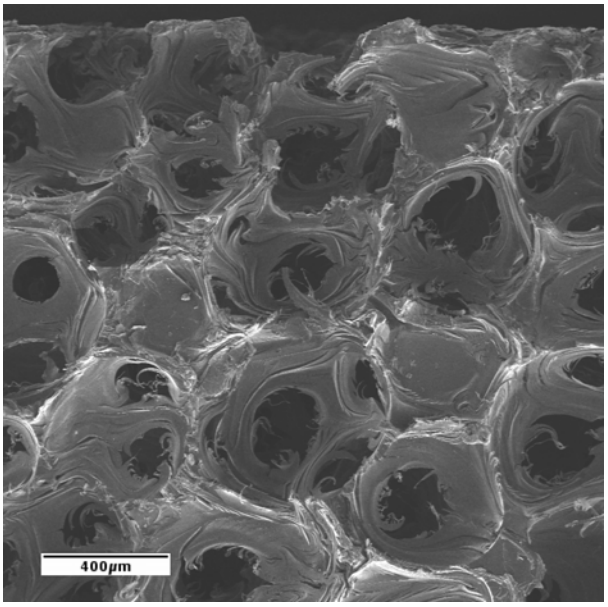

Figure 4. Scanning electron micrograph of commercial Poco foam.

Table 1. Properties of ORNL foams made using varying processing variables

Property	Foam ORNL-A	Foam ORNL-B	Foam ORNL-C
Avg. pore size (μm)	1131	714	978.5
Bulk calculated thermal conductivity (W/m K) X direction	19.7+/-1.8	34.7+/-2.9	36.5+/-2.2
Bulk calculated thermal conductivity (W/m K) Y direction	16.4+/-0.4	33.0+/-1.3	35.8+/-0.8
Bulk calculated thermal conductivity (W/m K) Z direction	26.8+/-1.2	79.1+/11.7	62.6+/-2.9
Permeability ($K\ m^2$)	2.05E-09	6.73E-10	Not reported
Forchheimer coefficient c_f	.3050	.8249	Not reported

convective heat transfer, higher fin efficiencies, advantageous longitudinal conduction through the foam, and lower contact resistance in the larger prototype than in smaller test coupons.

ORNL and its CRADA partner have successfully built and tested a graphite foam air-to-air heat exchanger. The heat exchanger transfers more heat than predicted, easily survived the rigorous test procedures, and demonstrated very good repeatability of the design point over time. The model underpredicts performance and pressure drop.

Presentations/Publications/Patents

"Controlling the Structure of Graphite Foam Using Secondary Inorganic Additives," ORNL invention disclosure.

"Design and Control of Structure of Graphite Foam," ORNL invention disclosure.

APPENDIX A: ACRONYMS AND ABBREVIATIONS

2-D	two-dimensional
3-D	three-dimensinoal
A	aging
AES	auger electron spectroscopy
AJT	Advanced Joining Technologies, Inc.
Al	aluminum
ANL	Argonne National Laboratory
APS	Advanced Photon Source
ASC	advanced squeeze casting
CAE	computer-aided engineering
CDM	continuum damage mechanics
CPM	cycles per minute
CR	cold rolling
CRADA	Cooperative Research and Development Agreement
CSM	continuous strand mat
CTEs	coefficients of thermal expansion
CT Scans	computed tomography scans
DARPA	Defense Advanced Research Projects Agency
DBSD	electron back-scattered diffraction
DIC	digital imaging correlation
DOE	Department of Energy, design of experiments
DTA	differential thermal analysis
EBSD	electron back-scatter diffraction
EDM	electrical discharge machining
EDX	energy-dispersive X-ray
EMTA	Eshelby/Mori-Tanaka approach
EPS	expanded polystyrene
FEA	finite element analysis
FE-SEM	field emission scanning electron microscope
FIB	focused ion bean
FSJ	friction stir joining
FSJ/P	friction stir joining and processing
FSP	friction stir processing
FSSW	friction stir spot welding
GBS	grain-boundary sliding
HAZ	heat affected zone
HDI	high-density infrared
HSWR	High-Strength Weight Reduction

ICP-AES	inductively coupled plasma–atomic emission spectroscopy
ICSAM	International Conference on Superplasticity in Advanced Materials
INEEL	Idaho National Engineering and Environmental Laboratory
IPM	inches per minute
IR	infrared
ISSR	interferometric strain/slope rosette
ITP	International Titanium Powder
LANL	Los Alamos National Laboratory
LDH	limited dome height
LPPM	low-pressure permanent mold
Mg	magnesium
$Mg_{17}Al_{12}$	brittle inter-metallic phase
MgO	magnesium oxide
Mg_2Si	magnesium silicide
MMC	metal matrix composite
Mo	molybdenum
NCC	National Composites Center
NGF	next-generation frame
NVH	noise, vibration, harshness
OEM	original equipment manufacturer
OFCVT	Office of FreedomCAR and Vehicle Technologies
ORNL	Oak Ridge National Laboratory
PFA	progressive failure analysis
PIVAC	pressure infiltrated vacuum assisted casting
PLI	pressureless infiltration
PNNL	Pacific Northwest National Laboratory
PTC	PACCAR Technical Center
PU/SUV	pickup/sport utility vehicle
R & D	research and development
RPM	rotations per minute
RSST	reversed shoulder spiral tool
RSW	resistance spot welding
RTM	resin transfer mold
RWMA	Resistance Welder Manufacturers Association
SAE	standard American equivalent
SC	squeeze cast
SDSMT	South Dakota School of Mines and Technology
SEM	scanning electron microscope
SMC	sheet moulding compound
SPF	superplastic forming
SPH	smooth particle hydrodynamics
SPR	self-piercing rivets
$SrTiO_3$	strontium titanate

SSBT	subscale brake testing
ST	solution treating
TEM	transmission electron microscopy
TTU	Tennessee Technological University
Ti	titanium
Ti-6Al-4V	popular alloy of Ti that contains additions of 6 wt % aluminum and 4 wt % vanadium
TWB	tailor welded blank
UW	ultrasonic welding
VAR	vacuum arc remelting
VARTM	vacuum-assisted resin transfer molding
VHP	vacuum hot pressing
WTI	Walford Technologies, Inc.

A Strong Energy Portfolio for a Strong America

Energy efficiency and clean, renewable energy will mean a stronger economy, a cleaner environment, and greater energy independence for America. Working with a wide array of state, community, industry, and university partners, the U.S. Department of Energy's Office of Energy Efficiency and Renewable Energy invests in a diverse portfolio of energy technologies.

For more information contact:
EERE Information Center
1-877-EERE-INF (1-877-337-3463)
www.eere.energy.gov